VYSOKÉ UČENÍ TECHNICKÉ V BRNĚ

BRNO UNIVERSITY OF TECHNOLOGY

STŘEDOEVROPSKÝ TECHNOLOGICKÝ INSTITUT VUT

CENTRAL EUROPEAN INSTITUTE OF TECHNOLOGY BUT

NANOSTRUKTURY PRO POKROČILÉ PLAZMONICKÉ APLIKACE

NANOSTRUCTURES FOR ADVANCED PLASMONIC APPLICATIONS

DIZERTAČNÍ PRÁCE
DOCTORAL THESIS

AUTOR PRÁCE
AUTHOR

Ing. Lukáš Kejík

ŠKOLITEL
SUPERVISOR

prof. RNDr. Tomáš Šikola, CSc.

BRNO 2023

ABSTRACT

Plasmonics, characterized by the coupling of free electron oscillations in metals with electromagnetic waves, has come to the forefront with advancements in nanotechnology. This synergy results in remarkable properties of nanoscale objects, characterized by confined and enhanced electromagnetic fields. These features pave the way for a wide array of nanostructure applications, spanning biosensing, emission enhancement, solar energy harvesting, and optical component substitution. This dissertation is centered on the application of plasmonic nanostructures, primarily focusing on planar optical components known as metasurfaces. Additionally, it explores their use in photocatalytic applications, harnessing the energetic hot charge carriers generated through plasmonics. The dissertation begins with an introduction to the theoretical foundations of plasmonics, highlighting key parameters governing plasmonic properties and providing an overview of its most compelling applications. Subsequently, it comprises four experimental sections which show the utilization of plasmonic nanostructures for various purposes, including the phase of light control, dynamic metasurfaces, investigations of inner crystallinity effects, and the utilization of hot charge carriers in photoelectrochemical systems. These studies share a common theme of employing advanced or less conventional materials, such as vanadium dioxide or transition metal dichalcogenides, within the realms of plasmonics and nanotechnology.

KEYWORDS

plasmonics, nanostructures, metasurfaces, electrochemistry, photoelectrochemistry, hot carriers, vanadium dioxide, tungsten disulphide, nanotubes

ABSTRAKT

Plazmonika, charakterizovaná spojením oscilací volných elektronů v kovech s elektromagnetickými vlnami, se dostala do popředí s pokroky v nanotechnologiích. Tato synergie vede k pozoruhodným vlastnostem objektů v nanoměřítku, vyznačujících se lokalizovaným a zesíleným elektromagnetickým polem. Tyto vlastnosti umožňují širokou škálu aplikací nanostruktur, zahrnujících biodetekci, zesilování emise, získávání solární energie a náhrazování optických komponent. Tato dizertační práce je zaměřena na aplikace plazmonických nanostruktur, primárně na plošné optické komponenty známé jako metapovrchy. Kromě toho zkoumá jejich použití ve fotokatalytických aplikacích, využívajících energetické horké nosiče náboje generované prostřednictvím plazmoniky. Dizertační práce začíná úvodem do teoretických základů plazmoniky, zdůrazněním klíčových parametrů řídících plazmonické vlastnosti a přehledem jejích nejpřesvědčivějších aplikací. Následně obsahuje čtyři experimentální části, které ukazují využití plazmonických nanostruktur pro různé účely, včetně ovládání fáze světla, dynamických metapovrchů, zkoumání efektů vnitřní krystalinity a využití horkých nosičů náboje ve fotoelektrochemických systémech. Tyto studie spojuje využití pokročilých nebo méně konvenčních materiálů, jako je oxid vanadičný nebo dichalkogenidy přechodných kovů, v oblasti plazmoniky a nanotechnologií.

KLÍČOVÁ SLOVA

plazmonika, nanostruktury, metapovrchy, elektrochemie, fotoelektrochemie, horké náboje, oxid vanadičitý, sulfid wolframičitý, nanotrubice

KEJÍK, Lukáš *Nanostructures for advanced plasmonic applications*: Brno University of Technology, Central European Intitute of Technology CEITEC, 2023. 159 p. Supervised by prof. RNDr. Tomáš Šikola, CSc.

Declaration

I declare that this dissertation was written under the supervision of prof. RNDr. Tomáš Šikola, CSc. and it is an original work with cited literature and other professional sources listed in the text and reference list.

Ing. Lukáš Kejík

Acknowledgement

I would like to thank Prof. Tomáš Šikola for his professional supervision, kind guidance, and for the careful proofreading of the text. I am also grateful that I could dive to scientific explorations in such a pleasant environment which he and Prof. Jiří Spousta helped to create at IPE FME BUT and at CEITEC BUT. Further, I want to thank Assoc. Prof. Miroslav Kolíbal for his scientific insights, valuable scientific discussions, and for his overall human kindness. Many thanks goes to my colleagues and friends from the plasmonic group at IPE – Michal Kvapil, Petr, Dvořák, Michal Horák, Jiří Liška, Vlastimil Křápek, Martin Hrtoň, Martin Konečný, Radek Kalousek, Zoltán Édes, Jiří Babocký, Tomáš Šamořil and others. All of them form a diverse team with huge knowledge base and it was a pleasure to work with them on various scientific projects. I also want to thank Lukáš Flajšman for helping with the automation of our apparatus for the photoelectrochemical experiments. Finally, I would like to thank Filip Ligmajer for a lot of deep scientific discussions, e.g., when trying to understand our photoelectrochemical results, and generally for the possibility of cooperation with him in several projects.

The results in this dissertation are a result of several collaborations which I had a chance to be a part of. The collaboration on phase imaging of metasurfaces was with a group of Prof. Radim Chmelík: Lenka Štrbková, Aneta Křížová, Jana Čolláková, and Petr Bouchal. Part of the work was also in collaboration with Prof. Dang Yuan Lei which started when I was in his group at Hong Kong PolyU, where I was introduced to VO_2, in a company of very welcoming students like Willis Ho, Tsz Wing Lo, and Steven Yeung. The last important collaboration was with the group of Assoc. Prof. Miroslav Fojta at IBP AS CR. Together with Luděk Havran, and especially Aleš Daňhel, they introduced us to electrochemistry, helped us with setting up the initial experiments, and with an interpretation of results.

I also want to thank the funding agencies. My research internship in the group of Dang Yuan Lei was supported by the Hong Kong PolyU under its Research Student Attachment Programme for Incoming Visiting Ph.D. students. Several other projects were funded by Grant Agency of the Czech Republic and Technological Agency of the Czech Republic. CzechNanoLab project LM2023051 funded by MEYS CR is also gratefully acknowledged for the financial support of the measurements/sample fabrication at CEITEC Nano Research Infrastructure.

The biggest thank you goes to my parents, my sisters, to my fiancée Andrea, and other members of my closest family, whose support and love made the successful finish of this journey possible.

Ing. Lukáš Kejík

CONTENTS

INTRODUCTION

The interaction of light with matter has always fascinated people as some materials let the light through while others cause its reflection. It became evident, that matter affects the light passing through it and careful shaping of the matter can bend the light to our will. This has led to advances in optics, the fabrication of lenses, and their assembly into optical devices like telescopes allowing discoveries of new worlds in far-away universe. Though our world was regarded as well-known, the invention of the optical microscope visualized the unknown worlds even within our grasp which were hidden due to our limited senses. The optical microscopes had soon reached their fundamental resolution limit on the order of wavelength of used light which hindered further probing of the micro-world. Nevertheless, plasmonics, where the free electron oscillations in the metals couple to electromagnetic waves, and advances in nanotechnology brought into focus the extraordinary properties of nano-sized objects. When interacting with such nanostructures, the electromagnetic wave is tightly confined to their vicinity thus surpassing the diffraction limit. The electromagnetic field confinement and its enhancement predestine a plethora of nanostructure applications ranging from sensing, therapy, and energy harvesting to optical components substitution and even computation.

The main aim of the dissertation is to provide an overview of plasmonic nanostructures with the necessary background and outline the benefits they can bring to several fields of application. Chapter 1 summarizes the behaviour of electromagnetic waves in materials and introduces basic models of solids. It is followed by a theoretical description of surface plasmon polaritons on metal–dielectric interface and a derivation of their dispersion relation. Localized surface plasmons induced in nanoparticles are theoretically described in a quasi-static regime as well as based on Mie theory, and some aspects of adjusting the resonance wavelength are explored via Mie theory calculations.

Chapter 2 focuses more on practical aspects of plasmonics starting with nanostructure fabrication methods. Next, various applications of plasmonic nanostructures are reviewed with a focus on metasurfaces which can substitute conventional optical components and biodetection which can be utilized to detect various antigens. Additionally, another beneficial aspect of plasmonic nanostructures, the generation of hot carriers via non-radiative plasmon damping, is reviewed and their benefits for application in energy harvesting are summarized.

The following chapters summarize the results obtained in projects where plasmonics was utilized in various scenarios. Chapter 3 establishes a novel method of metasurface performance analysis. The coherence-controlled holographic microscope, previously used for quantitative phase imaging of biological samples, was employed to analyze the phase of light modified by the presence of plasmonic nanostructures. After demonstrating the phase contrast on benchmark samples, our focusing metasurface function was confirmed by the phase mapping of its focal points in 3D.

Chapter 4 explores the tunability of plasmonic nanostructures based on phase-change material vanadium dioxide (VO_2). After the introduction of the material, two approaches to achieve tunable plasmonics using VO_2 are outlined. In the first case, the VO_2 is nanostructured itself by self-limited epitaxial growth exhibiting plasmon resonance in the NIR region at elevated temperatures and can function as a quarter-wave plate metasurface. In the second case, the epitaxial VO_2 serves as a substrate for conventional gold nanoantennas whose plasmon resonance can be easily tuned and it is affected by the underlying VO_2 anisotropy.

Chapter 5 highlights another aspect which can affect the plasmon resonance of metallic nanostructures, their crystal structure. Chemical synthesis of monocrystalline gold microplates directly on SiN_x membrane has been demonstrated. Gold nanorods from monocrystalline and conventional polycrystalline substrates were fabricated by a focused ion beam and analyzed by an analytical transmission electron microscope coupled with electron energy loss spectroscopy. Their structure revealed better shape reproducibility in monocrystalline nanorods when fabricated from the same monocrystalline substrate but they featured inclined boundaries. In terms of their optical properties, the results for both crystallinities were very similar hinting that the polycrystalline nature of nanostructures does not hamper their performance.

Chapter 6 deals with the introduction of plasmonic elements into a well-established field of electrochemistry and the interplay between light and electrons in photoelectrochemistry. First, the fundamental principles of electrochemistry are summarized and relevant experimental techniques are explained. The photo-induced phenomena of two systems utilizing plasmonic nanoparticles and semiconductor materials were studied. Bare WS_2 nanotube-based electrodes exhibited improved electrochemical characteristics when compared to bare ITO electrodes. Chemical decoration by gold nanoparticles introduced a plasmonic element to the small bandgap semiconductor and resulted in a significantly altered photo-induced response. Similarly, in another system with simplified geometry formed by a layer of large bandgap TiO_2 and gold nanoislands, the photo-response of electrodes is greatly enhanced especially in longer wavelengths. The thesis closes with a summary of all the results and future directions which the research can take.

1 INTRODUCTION TO PLASMONICS

1.1 Electromagnetic waves in matter

Generation and propagation of electromagnetic waves in matter can be completely described classically by a set of equations initially put together by J. C. Maxwell [1]. A set of four equations which are commonly referred to as Maxwell's equations were formulated by Heaviside [2]. The electric fields are described by the vectors **E** (the electric field) and **D** (the dielectric displacement) while the magnetic fields by **H** (the magnetic field) and **B** (the magnetic induction). In differential form, they can be expressed as

$$\nabla \cdot \mathbf{D} = \rho_{\text{ext}}, \tag{1.1a}$$

$$\nabla \cdot \mathbf{B} = 0, \tag{1.1b}$$

$$\nabla \times \mathbf{E} = -\frac{\partial \mathbf{B}}{\partial t}, \tag{1.1c}$$

$$\nabla \times \mathbf{H} = \frac{\partial \mathbf{D}}{\partial t} + \mathbf{J}_{\text{ext}}, \tag{1.1d}$$

where ρ_{ext} corresponds to the external charge density and $\mathbf{J}_{\text{ext}}$ to the external current density. The dielectric displacement **D** and magnetic field **H** can be further defined by

$$\mathbf{D} = \varepsilon_0 \mathbf{E} + \mathbf{P}, \tag{1.2a}$$

$$\mathbf{H} = \frac{1}{\mu_0}\mathbf{B} - \mathbf{M}. \tag{1.2b}$$

Vector **P** corresponds to the electric polarization inside the material (the average electric dipole moment per unit volume), **M** to the magnetization inside the material (the average magnetic dipole moment per unit volume), ϵ_0 and μ_0 to the electric permittivity and magnetic permeability of the vacuum, respectively. In a linear medium the **D** and **B** can be expressed as

$$\mathbf{D} = \varepsilon_0 \varepsilon \mathbf{E}, \tag{1.3a}$$

$$\mathbf{B} = \mu_0 \mu \mathbf{H}, \tag{1.3b}$$

where ε represents the relative permittivity and μ is the relative permeability of the material, the latter of which equals unity for non-magnetic materials. The relative permittivity is generally not constant as it depends on the frequency of electromagnetic waves in the material and it is commonly referred to as the dielectric function. Together with the complex index of refraction, the dielectric function represents a means to specify the optical properties of materials.

1.2 Optical properties of matter

The dielectric function describes the material's behaviour in the presence of an electromagnetic field and it is generally represented by a complex function $\varepsilon(\omega) = \varepsilon'(\omega) + \mathrm{i}\varepsilon''(\omega)$. This quantity is employed, e.g., in the theory of electromagnetic wave scattering by small particles and in Maxwell's equations in general. Another quantity used to characterize the optical properties of materials, typically in light beam propagation scenarios, e.g., Snell's law and Fresnel equations, is the complex index of refraction $N(\omega) = n(\omega) + \mathrm{i}k(\omega)$ which is related to the dielectric function

$$N(\omega) = n(\omega) + \mathrm{i}k(\omega) = \sqrt{\varepsilon'(\omega) + \mathrm{i}\varepsilon''(\omega)}, \tag{1.4}$$

where n is the index of refraction associated with the phase velocity of light in the material and k is the extinction coefficient associated with the absorption within the material. The relations between the individual components of the complex refractive index and the components of the dielectric function are the following

$$\varepsilon' = n^2 - k^2, \qquad \varepsilon'' = 2nk, \tag{1.5}$$

thus allowing an easy transition between the two quantities which can be retrieved experimentally, e.g., utilizing spectroscopic ellipsometry [3]. The dependence of the dielectric function on the frequency of electromagnetic waves is far from trivial. Nevertheless, it can be simplified by utilizing the classical models developed by P. Drude and H. A. Lorentz, respectively. Although these models don't account for quantum-mechanical effects, in most cases they are fully adequate to predict optical properties of materials. The Lorentz model [4] is frequently used to elucidate optical properties of dielectrics while its simplified version, the Drude model [5], is used for metals. The following models were described primarily using the Ref. [6].

1.3 Lorentz model

The Lorentz model originates from the notion of an electron bound to the positively charged ion aligned in a crystal lattice. The displacement of such atomic dipoles is then modelled as a damped harmonic oscillator with a single resonant frequency ω_0. The damping is included as a consequence of possible energy loss by collision processes, typically with phonons thermally excited in the crystal. The electric field of an electromagnetic wave then drives the dipole oscillation through the movement of electrons because of their much smaller mass when compared to the nuclei which we assume to be stationary. The displacement of the electron is then dictated by the following equation of motion

$$m_\mathrm{e}\frac{\mathrm{d}^2\mathbf{r}}{\mathrm{d}t^2} + m_\mathrm{e}\gamma\frac{\mathrm{d}\mathbf{r}}{\mathrm{d}t} + m_\mathrm{e}\omega_0^2\mathbf{r} = -e\mathbf{E}, \tag{1.6}$$

where m_e and e are the magnitudes of electron mass and electron charge, γ is the damping rate ($1/\gamma$ corresponds to the lifetime), and $\mathbf{E}$ is the electric field of the driving light wave. The terms on the left-hand side correspond to the acceleration, the damping, and the restoring force respectively. The term on the right-hand side corresponds to the driving force exerted by the oscillating electric field of the driving light wave.

If we consider the driving electric field $\mathbf{E}$ as harmonic with the frequency ω and amplitude $\mathbf{E}_0$ in the form $\mathbf{E}(t) = \mathbf{E}_0 \exp(-\mathrm{i}\omega t)$, the solution to the equation of motion for the displacement can be written as:

$$\mathbf{r}(t) = \frac{-e/m_\mathrm{e}}{\omega_0^2 - \omega^2 - \mathrm{i}\gamma\omega}\mathbf{E}(t). \tag{1.7}$$

The displacement of the electrons from the equilibrium positions therefore produces polarization effects within the dielectric. The dipole moment for a single atom can be expressed as $\mathbf{p} = -e\mathbf{r}$. If N is the number of atoms within a unit volume, the polarization is then given by $\mathbf{P} = -Ne\mathbf{r}$. Utilizing Eq. (1.7), the polarization can be rewritten as:

$$\mathbf{P}(t) = \frac{\omega_\mathrm{p}^2}{\omega_0^2 - \omega^2 - \mathrm{i}\gamma\omega}\varepsilon_0\mathbf{E}(t), \tag{1.8}$$

where $\omega_\mathrm{p} = \sqrt{Ne^2/m_\mathrm{e}\varepsilon_0}$ is known as the plasma frequency and is related to the natural resonant frequency of the free carrier gas of a given material. By combining Eq. (1.2a) and (1.3a) and comparing it with Eq. (1.8) we reach the final complex formula for the dielectric function of the material

$$\varepsilon(\omega) = 1 + \frac{\omega_\mathrm{p}^2}{\omega_0^2 - \omega^2 - \mathrm{i}\gamma\omega}. \tag{1.9}$$

We can also account for additional non-resonant contributions to the polarization with ε_∞ and modify Eq. 1.9 as:

$$\varepsilon(\omega) = \varepsilon_\infty + \frac{\omega_\mathrm{p}^2}{\omega_0^2 - \omega^2 - \mathrm{i}\gamma\omega}. \tag{1.10}$$

This formula can be split according to the $\varepsilon(\omega) = \varepsilon'(\omega) + \mathrm{i}\varepsilon''(\omega)$ into the real ε' and imaginary ε'' component as follows:

$$\varepsilon'(\omega) = \varepsilon_\infty + \frac{\omega_\mathrm{p}^2(\omega_0^2 - \omega^2)}{(\omega_0^2 - \omega^2)^2 + \gamma^2\omega^2}, \tag{1.11a}$$

$$\varepsilon''(\omega) = \frac{\gamma\omega\omega_\mathrm{p}^2}{(\omega_0^2 - \omega^2)^2 + \gamma^2\omega^2}. \tag{1.11b}$$

The dielectric function of a typical Lorentz oscillator is shown in Fig. 1.1 together with spring-mass oscillators as a mechanic analogue.

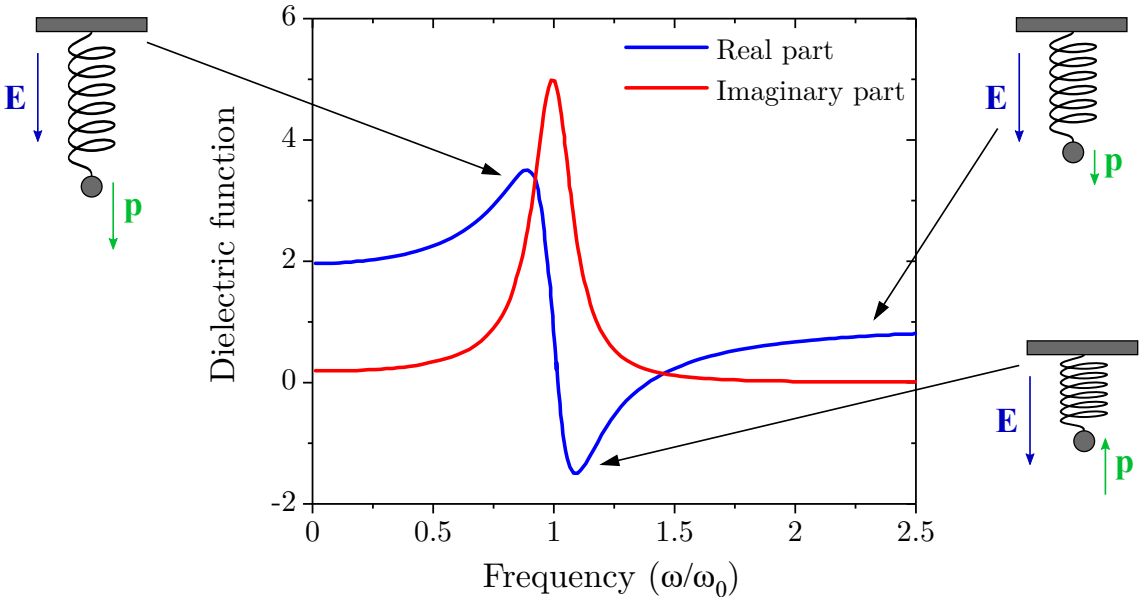

Fig. 1.1: The dielectric function of a typical Lorentz oscillator and the spring-mass oscillators as mechanic analogues. At the frequencies away from the resonance the response (the dipole moment $\mathbf{p}$) can follow the driving field $\mathbf{E}$ with no delay. Slightly below the resonance frequency, the ε' is increasingly positive and the response $\mathbf{p}$ is enhanced. Slightly above the resonance, the function has negative values, therefore the response is opposing the driving field. Modified from [7].

1.4 Drude model

When we disregard the restoring force acting on an electron in the Lorentz model in Eq. (1.6) we reach the Drude model which is generally used to describe the behaviour of metals and with small adjustments also of doped semiconductors [8]. The electrons can move freely within the material and experience only forces exerted by the driving electric field. The motion of such electrons is governed by the following equation:

$$m_\mathrm{e}\frac{\mathrm{d}^2\mathbf{r}}{\mathrm{d}t^2} + m_\mathrm{e}\gamma\frac{\mathrm{d}\mathbf{r}}{\mathrm{d}t} = -e\mathbf{E}. \tag{1.12}$$

Assuming the driving electric field is harmonic with the frequency ω, i.e., being described as $\mathbf{E}(t) = \mathbf{E}_0\exp(-\mathrm{i}\omega t)$, the solution to the equation of motion can be written as:

$$\mathbf{r}(t) = \frac{e/m_\mathrm{e}}{\omega^2 + \mathrm{i}\gamma\omega}\mathbf{E}(t). \tag{1.13}$$

For N as the number of atoms within a unit volume, the polarization is given by $\mathbf{P} = -Ne\mathbf{r}$ and consequently substituting the displacement for Eq. (1.13) we get

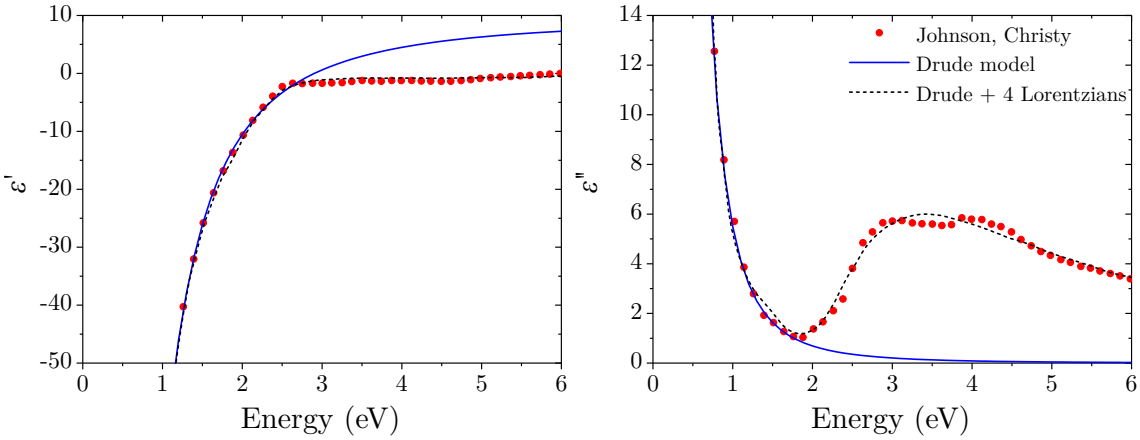

Fig. 1.2: Real (left) and imaginary (right) part of the dielectric function of gold. Red dots correspond to the experimental data obtained by Johnson and Christy [9], blue line represents a fit by the Drude model ($\varepsilon_\infty = 9.5$, $\omega_\mathrm{p} = 1.36 \times 10^{16}\,\mathrm{rad\,s^{-1}}$, $\gamma = 1.05 \times 10^{14}\,\mathrm{rad\,s^{-1}}$) [10], and the black dashed line corresponds to the Drude model combined with four Lorentz oscillators [11].

the polarization

$$\mathbf{P}(t) = -\frac{\omega_\mathrm{p}^2}{\omega^2 + \mathrm{i}\gamma\omega}\varepsilon_0\mathbf{E}(t). \tag{1.14}$$

By combining the Eq. (1.2a) and (1.3a), comparing it with Eq. (1.14), and accounting for other non-resonant contributions, we get the expression for the dielectric function

$$\varepsilon(\omega) = \varepsilon_\infty - \frac{\omega_\mathrm{p}^2}{\omega^2 + \mathrm{i}\gamma\omega}. \tag{1.15}$$

This complex formula can be split into real ε' and imaginary ε'' component

$$\varepsilon'(\omega) = \varepsilon_\infty - \frac{\omega_\mathrm{p}^2}{\omega^2 + \gamma^2}, \tag{1.16a}$$

$$\varepsilon''(\omega) = \frac{\omega_\mathrm{p}^2\gamma}{\omega(\omega^2 + \gamma^2)}. \tag{1.16b}$$

Note that for commonly used metals in higher optical frequencies, the damping γ in Eq. 1.15 can be neglected, thus getting to the simplified relation

$$\varepsilon(\omega) = 1 - \frac{\omega_\mathrm{p}^2}{\omega^2}, \tag{1.17}$$

which can be taken as the dispersion relation of an undamped free electron plasma.

The example of the Drude model for the dielectric function of gold is shown in Fig. 1.2 together with the experimental data obtained by Johnson and Christy [9]. The Drude model ($\varepsilon_\infty = 9.5$, $\omega_\mathrm{p} = 1.36 \times 10^{16}\,\mathrm{rad\,s^{-1}}$, $\gamma = 1.05 \times 10^{14}\,\mathrm{rad\,s^{-1}}$ [10])

fits the experimental data very well in lower energies below 2 eV where it starts to deviate significantly, primarily due to interband transitions inside gold.

The applicability of the Drude model can be extended even to the region of interband transitions by adding Lorentz oscillators into the formula of dielectric function in the following way [12]:

$$\varepsilon(\omega) = 1 - \frac{\omega_\mathrm{p}^2 f_0}{\omega^2 + \mathrm{i}\gamma_0\omega} + \sum_{j=0}^{k} \frac{f_j \omega_\mathrm{p}^2}{\omega_{0,j}^2 - \omega^2 - \mathrm{i}\gamma_j\omega}, \tag{1.18}$$

where k is the number of oscillators with the strength f_j, frequency ω_j, and damping rate γ_j related to the interband transitions, while the Drude term (intraband transitions) has been assigned the oscillator strength f_0 and the damping rate γ_0. The example of using four Lorentz oscillators to fit the experimental data in the regions affected by the interband transitions is also shown in Fig. 1.2 [11]. The agreement between the modelled and experimental dielectric function is significantly improved by these Lorentz terms which renders the model suitable for use in electromagnetic simulations.

1.5 Surface plasmon polaritons

Materials having the negative real part and the small imaginary part of the dielectric function, typically metals in the visible spectral range, can support a formation of surface plasmon polaritons (SPP) [13]. These are collective oscillations of surface conduction electrons, which can be excited using a coupling element (glass prism, grating) at the metal-dielectric interface by an electromagnetic wave [14]. The resulting SPP thus constitutes an electromagnetic wave coupled with the conduction electron movement which can then propagate along the interface. The SPP propagates along the interface typically for several μm depending on the metal layer material and SPP wavelength [15]. The electromagnetic field is confined to the interface and decays exponentially as an evanescent wave with the distance from the interface in both metal and dielectric half-spaces [16]. Fig. 1.3 illustrates the SPP propagating along the x-direction at the metal-dielectric interface characterized by ε_d and ε_m, respectively. The figure highlights the components of the propagating wave, its evanescent nature in the z-direction, and basic characteristics.

To derive the dispersion relation of the SPPs one must use Marwell's equations and apply their solution to the desired geometry. The geometry of the problem is highlighted in Fig. 1.3 where the dielectric with ε_d is above ($z > 0$) and the metal with ε_m below ($z < 0$) the interface which is set to $z = 0$. The electromagnetic wave corresponding to the harmonic solution and propagating in the described geometry

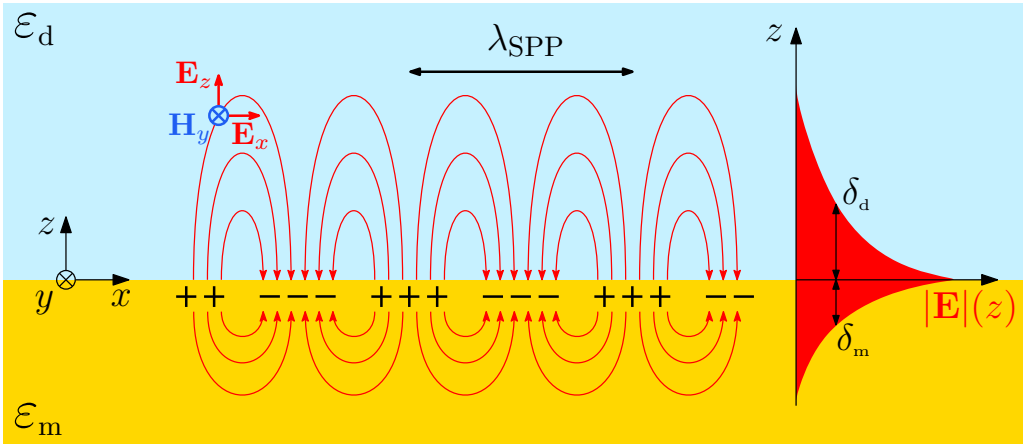

Fig. 1.3: SPP propagating at the metal-dielectric interface with related electromagnetic field components specific for TM wave. SPP can be characterized by the wavelength λ_SPP and the confinement of its electric field by the exponential decay in the z-direction away from the interface can be quantified by the penetration depths δ_m and δ_d [16].

along the x-axis can then be written in the form

$$\begin{Bmatrix} \mathbf{E}(\mathrm{r},t) \\ \mathbf{H}(\mathrm{r},t) \end{Bmatrix} = \begin{Bmatrix} \mathbf{E}(z) \\ \mathbf{H}(z) \end{Bmatrix} \exp[-\mathrm{i}(\omega t - \beta x)], \tag{1.19}$$

where $\beta = k_\mathrm{x}$ is called the propagation constant which corresponds to the projection of the wave vector to the (x-axis) direction. The validity of this solution has to be confirmed by plugging it into the so-called wave equation (Eq. 1.20). This type of equation can be obtained by combining two curl Maxwell's equations (1.1c and 1.1d) in homogeneous nonmagnetic media without external currents yielding the following equations:

$$\left(\nabla^2 - \varepsilon\varepsilon_0\mu_0\frac{\partial^2}{\partial t^2}\right)\begin{Bmatrix} \mathbf{E}(\mathrm{r},t) \\ \mathbf{H}(\mathrm{r},t) \end{Bmatrix} = 0. \tag{1.20}$$

We can substitute for $\mathbf{E}$ and $\mathbf{H}$ in Eq. 1.20 from Eq. 1.19, thus reaching the equations in the form of the Helmholtz equations [17]:

$$\left[\frac{\mathrm{d}^2}{\mathrm{d}z^2} + (k_0^2\varepsilon - \beta^2)\right]\begin{Bmatrix} \mathbf{E}(z) \\ \mathbf{H}(z) \end{Bmatrix} = 0, \tag{1.21}$$

where $k_0 = \omega/c$ corresponds to the wave vector of the wave propagating in vacuum and ε to the dielectric function of the medium. To further specify the components of the $\mathbf{E}(z)$ and $\mathbf{B}(z)$ fields, we can apply the presumed solution (Eq. 1.19) to the Maxwell's equations (Eq. 1.1c and 1.1d) with regard to the material relations (Eq. 1.3). The resulting equations can be assembled into two sets of self-consistent solutions

based on the polarization properties of the propagating waves. The first set of solutions is related to transverse magnetic (TM or p-) polarization modes with three nonzero components $E_\mathrm{x}, E_\mathrm{z}$, and H_y, while the second set is related to transverse electric (TE or s-) polarization modes where $H_\mathrm{x}, H_\mathrm{z}$, and E_y are nonzero. Note that in the following we will only work with TM polarization as TE polarization is not compatible with a bound wave at the interface based on the boundary conditions.

The solutions for TM wave can be written as

$$H_\mathrm{y}(z) = A_\mathrm{d}\exp(\mathrm{i}\beta x)\exp(-k_\mathrm{d}z), \tag{1.22a}$$

$$E_\mathrm{x}(z) = \mathrm{i}A_\mathrm{d}\frac{k_\mathrm{d}}{\omega\varepsilon_0\varepsilon_\mathrm{d}}\exp(\mathrm{i}\beta x)\exp(-k_\mathrm{d}z), \tag{1.22b}$$

$$E_\mathrm{z}(z) = -A_\mathrm{d}\frac{\beta}{\omega\varepsilon_0\varepsilon_\mathrm{d}}\exp(\mathrm{i}\beta x)\exp(-k_\mathrm{d}z) \tag{1.22c}$$

for $z > 0$ (i.e. in the dielectric half-space) and

$$H_\mathrm{y}(z) = A_\mathrm{m}\exp(\mathrm{i}\beta x)\exp(k_\mathrm{m}z), \tag{1.23a}$$

$$E_\mathrm{x}(z) = -\mathrm{i}A_\mathrm{m}\frac{k_\mathrm{m}}{\omega\varepsilon_0\varepsilon_\mathrm{m}}\exp(\mathrm{i}\beta x)\exp(k_\mathrm{m}z), \tag{1.23b}$$

$$E_\mathrm{z}(z) = -A_\mathrm{m}\frac{\beta}{\omega\varepsilon_0\varepsilon_\mathrm{m}}\exp(\mathrm{i}\beta x)\exp(k_\mathrm{m}z) \tag{1.23c}$$

for $z < 0$ (i.e. in the metal half-space). $A_\mathrm{d/m}$ represent the amplitudes of the surface wave and $k_\mathrm{d/m}$ represent the component of the wave vector perpendicular to the interface which can be specified based on the boundary conditions at the interface. To preserve the continuity of H_y and E_x at the interface, it is required that

$$A_\mathrm{d} = A_\mathrm{m}, \tag{1.24a}$$

$$\frac{k_\mathrm{d}}{k_\mathrm{m}} = -\frac{\varepsilon_\mathrm{d}}{\varepsilon_\mathrm{m}}. \tag{1.24b}$$

The waves bound to the interface with evanescently decaying fields in the z-direction away from the interface can only be achieved regarding Eq. 1.22 and 1.23 when $\mathrm{Re}\{k_\mathrm{d}\} > 0$ and $\mathrm{Re}\{k_\mathrm{m}\} > 0$, i.e., the real parts of the wave vectors are positive. If we consider media without losses (i.e., we assume only the real parts of permittivities and wave vectors), the condition in Eq. 1.24b can only be fulfilled for the two media with permittivities of opposing signs. Evidently, if $\varepsilon_\mathrm{d} > 0$ as is the case for dielectrics then $\mathrm{Re}\{\varepsilon_\mathrm{m}\} < 0$ which is a typical property of metals at frequencies $\omega < \omega_\mathrm{p}$. Therefore, surface waves can generally only exist at the interface between a conductor and an insulator.

Additionally, the component H_y in Eq. 1.22a and 1.23a must further satisfy the

wave equation (1.20) yielding

$$k_{\mathrm{m}}^2 = \beta^2 - k_0^2 \varepsilon_{\mathrm{m}}, \tag{1.25a}$$

$$k_{\mathrm{d}}^2 = \beta^2 - k_0^2 \varepsilon_{\mathrm{d}}. \tag{1.25b}$$

Combining Eq. 1.25 with 1.24b we arrive at the central result of this section, i.e., the dispersion relation of SPPs propagating at the interface between two media connecting their propagation constant to the frequency:

$$\beta(\omega) = k_0(\omega) \sqrt{\frac{\varepsilon_{\mathrm{m}}(\omega)\varepsilon_{\mathrm{d}}(\omega)}{\varepsilon_{\mathrm{m}}(\omega) + \varepsilon_{\mathrm{d}}(\omega)}}. \tag{1.26}$$

The dispersion relations for a Drude metal, either with or without losses, are plotted in Fig.1.4 with both axes normalized to the plasma frequency ω_{p}. The behaviour of light in a bulk metal in Fig.1.4(a,c) can be derived by recalling Maxwell's equation (1.1a) with no additional sources (i.e., $\nabla \cdot \mathbf{D} = 0$) and applying it to the general plane wave of the form $\exp[\mathrm{i}(\mathbf{k} \cdot \mathbf{r} - \omega t)]$ which gives

$$\varepsilon(\omega)\mathbf{k} \cdot \mathbf{E} = 0. \tag{1.27}$$

The first solution $\varepsilon(\omega) = 0$ corresponds to collective, purely longitudinal oscillations of the conduction electron gas in the background of positive ion cores. In the lossless material, this condition occurs at the plasma frequency ω_{p} and the oscillation is referred to as the bulk plasmon (BP). The second solution $\mathbf{k} \cdot \mathbf{E} = 0$ describes transverse waves which have to satisfy the following formula

$$k^2 = \varepsilon(\omega)\frac{\omega^2}{c^2} = \varepsilon(\omega)k_0^2, \tag{1.28}$$

representing the dispersion of a photon propagating in the medium characterized by $\varepsilon(\omega)$ [18]. Here, the use of the term polariton [19] is in place as it represents a quasi-particle where the photon is coupled with some fundamental excitation of the system [20]. In this case, the fundamental excitation is the bulk plasmon and the related quasi-particle can thus be termed bulk plasmon polariton (BPP). The region of $\omega > \omega_{\mathrm{p}}$ in Fig.1.4(a), where the metal no longer retains its metallic properties, allows propagation of electromagnetic waves and the dispersion curve approaches the free-space light line for high frequencies as the $\varepsilon_{\mathrm{m}} \to 1$. Nevertheless, for $\omega < \omega_{\mathrm{p}}$ the wave propagation is forbidden, i.e., the wave vector is purely imaginary. Upon including the losses [Fig. 1.4(c)] into the Drude model, this sharp distinction becomes blurred.

The dispersion relation of the SPPs at the interface between a Drude metal and vacuum is shown in Fig.1.4(b,d) and comes from Eq.1.26. In the region of $\omega > \omega_{\mathrm{p}}$ in Fig. 1.4(b) light can propagate through the metal, thus creating the so-called

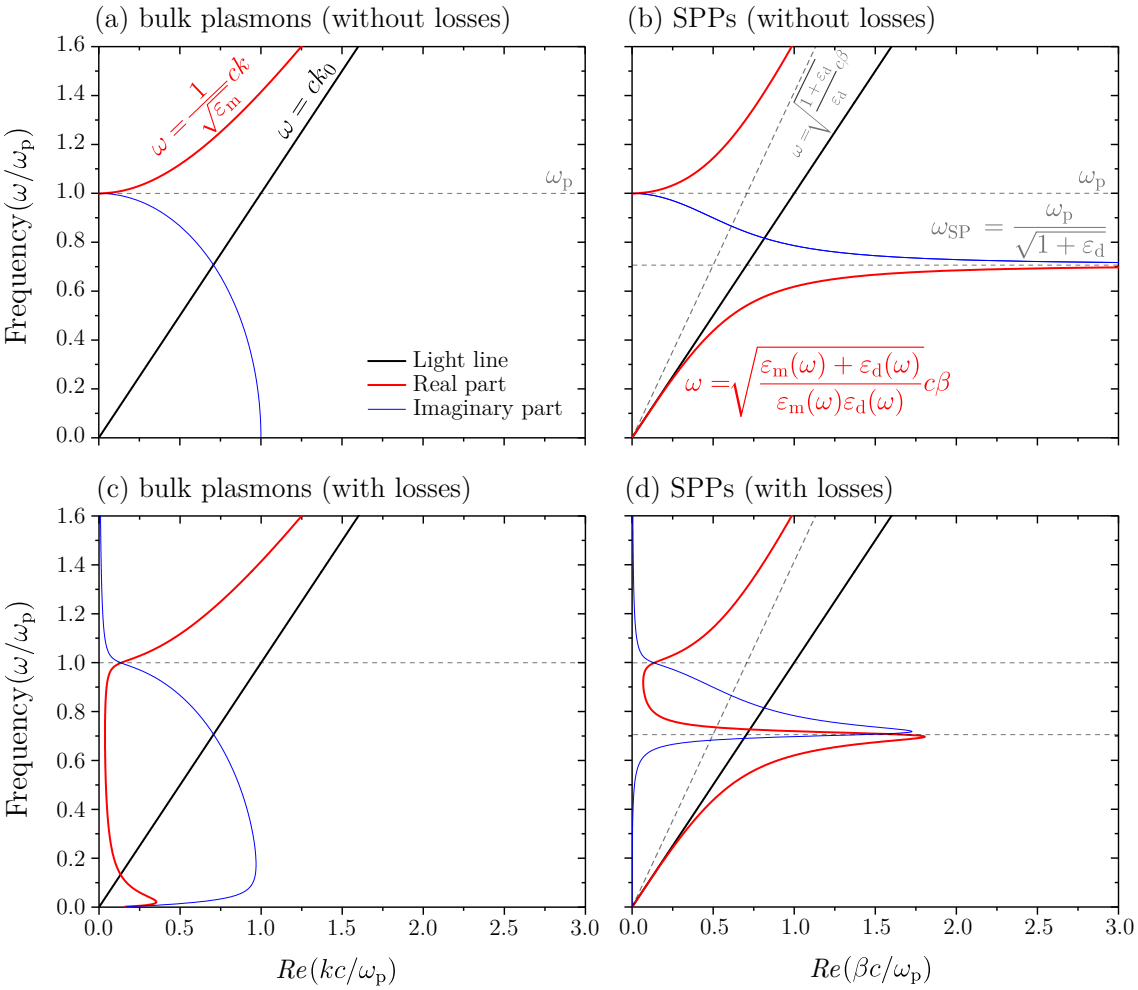

Fig. 1.4: The dispersion relations of plasmons showing both the real parts (red lines) and the imaginary parts (blue lines) of the wave vectors. The dispersion relation of light in a vacuum (black line) is shown as a reference. (a,c) Dispersion relation of bulk plasmons in a Drude metal (a) without losses and (c) with losses included. (b,d) Dispersion relation of SPPs propagating at the interface between the vacuum and the Drude metal (b) without losses and (d) with losses included. The loss-less Drude metal is characterized by Eq. 1.17 with $\omega_p = 1.36 \times 10^{16}\,\mathrm{rad\,s^{-1}}$ and the losses are included following Eq. 1.15 with the damping rate $\gamma = 0.5 \times 10^{15}\,\mathrm{rad\,s^{-1}}$ and $\varepsilon_\infty = 1$.

radiative modes, similarly as mentioned before in BPP. But unlike BPP, where the dispersion curve approaches the free-space light line, the SPP dispersion curve in this frequency region approaches the line defined by $\omega = \sqrt{(1+\varepsilon_d)/\varepsilon_d}c\beta$ as $\varepsilon_m \to 1$. For the metal-vacuum interface ($\varepsilon_d = 1$) the asymptote equation reduces to $\omega = \sqrt{2}c\beta$ [21]. For frequencies just below ω_p, there is a frequency gap with only an imaginary β where the light propagation is prohibited. Below this band gap, there is the region of bound modes where SPPs can exist. The bound modes of very low frequencies

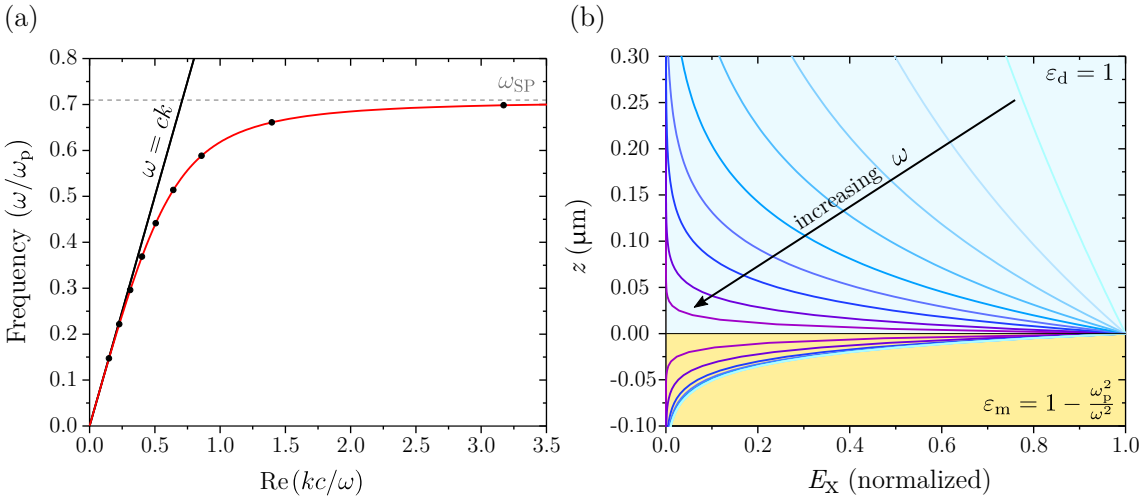

Fig. 1.5: (a) The bottom branch of the dispersion relation of SPP at the interface between the loss-less Drude metal and air (red), and the light line (black) for reference. The black dots highlight the frequencies used in (b). (b) Normalized tangential component of the SPP electric field (E_x) as a function of the distance z perpendicular to the interface. At lower frequencies (close to the light line) the electric field E_x of SPP penetrates much deeper to the dielectric than to the metal and is almost delocalized. At high frequencies (close to ω_p) the penetration depth into the dielectric is significantly reduced and it is almost the same as in the metal, stressing the strong localization of the electric field to the interface. Note that the loss-less Drude metal is characterized by $\omega_p = 1.36 \times 10^{16}\,\mathrm{rad\,s^{-1}}$ corresponding to gold.

(mid-infrared or lower) have the propagation constant β very close to the light wave vector k_0 and the waves extend significantly into the dielectric half-space. These waves, also known as the Sommerfeld-Zenneck waves, can be excited directly by electromagnetic waves under the grazing incidence [17].

In the region of higher frequencies (just below the band gap) the propagation vector tends to go to infinity as the frequency of SPPs reaches the so-called surface plasmon frequency

$$\omega_{SP} = \frac{\omega_p}{\sqrt{1+\varepsilon_d}}. \tag{1.29}$$

This formula can be derived looking at the SPP dispersion relation (Eq. 1.26) where for $\varepsilon_m = -\varepsilon_d$ the propagation vector β tends to go to infinity. Similarly, applying this condition to Eq. 1.17 for the loss-less Drude metal, we obtain the surface plasmon frequency formula (Eq. 1.29) which for a vacuum environment reduces to $\omega_{SP} = \omega_p/\sqrt{2}$. As opposed to the bulk plasmon modes, surface plasmons can't exist on their own, as they are always coupled with a photon in the form of surface plasmon polariton [18]. Once the losses are included, the low-frequency branch does not diverge close to ω_{SP} but bends back and then reconnects with the high-frequency

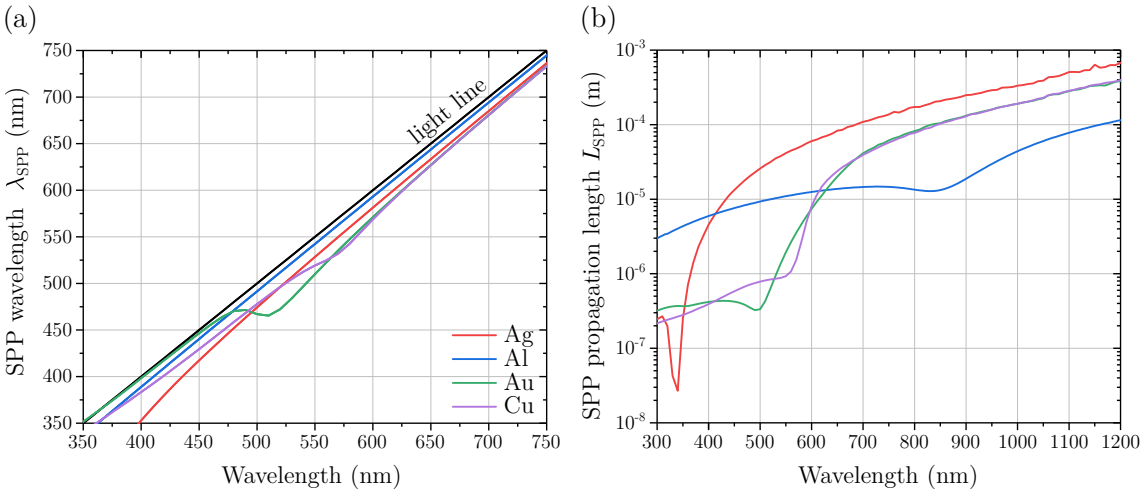

Fig. 1.6: SPP characteristics for a metal-air interface with four metals commonly used in plasmonics characterized by dielectric functions of real metals measured by McPeak [23]. (a) SPP wavelength related to the real part of the dielectric function. Note that λ_{SPP} always lays below the light line with some discrepancies in the regions of interband transitions. (b) SPP propagation length related to the imaginary part of the dielectric function of the respective metals. Note that the scale in (b) is logarithmic.

branch. Therefore, the frequency bandgap with purely imaginary wavevectors no longer exists as this region of anomalous dispersion contains the so-called quasi-bound modes [22].

The effect of localization of electric field in both half-spaces depending on frequency is highlighted in Fig. 1.5. At low frequencies, the electric field in the dielectric is almost delocalized and with increasing frequencies, the localization increases dramatically, while in the metal it stays localized with only slight dependence on the frequency. At the high-frequency limit, the localization in both media is the same. The field localization can be quantified using the penetration depth parameter δ based on Eq. 1.25 put into Eq. 1.22 and 1.23 as

$$\delta_{m/d} = \left|k_{m/d}\right|^{-1} = \frac{\lambda}{2\pi} \cdot \sqrt{\left|\frac{\varepsilon_m + \varepsilon_d}{\varepsilon_{m/d}^2}\right|}, \tag{1.30}$$

which corresponds to the perpendicular distance from the interface where the field intensity decays to 1/e portion of the maximum field at the interface. Another broadly used quantity, the propagation distance L_x, is related to the distance along the interface in the x-axis where the field intensity decays by 1/e, defined as $L_x = 1/\mathrm{Im}\{2\beta\}$. The wavelength of the SPP corresponds to $\lambda_{SPP} = 2\pi/\mathrm{Re}\{\beta\}$, which is always smaller than the wavelength of light, i.e., $\lambda_{SPP} < \lambda = \lambda_0/\sqrt{\varepsilon_d}$ [24]. These characteristic quantities of the SPP at the metal-air interface are displayed in Fig. 1.6

for four different metals often used in plasmonics. The input dielectric functions for the calculations were taken from McPeak *et al.* [23].

Recalling the dispersion relation of SPP, one notices that the lower SPP branch lies below the light line. This implies that $\beta > k_0$ for a fixed frequency, therefore, it is not possible to excite SPP directly by light (except the low-frequency Sommerfeld-Zenneck waves) even at a grazing incidence. This mismatch in momentum between light and SPP can be overcome by several approaches. The *prism coupling* scheme utilizes an attenuated total internal reflection inside a glass prism which is accompanied by a generation of an evanescent wave at the edge of the prism. The evanescent wave can then tunnel either through a thin metallic layer (Kretschmann configuration [25]) or a layer of air (Otto configuration [26]) and provide an excess momentum for the SPP to be excited on the nearby metal-air interface. Another way is to use *grating coupling* which overcomes the momentum mismatch by the diffraction effects on a grated metal surface [27], by *highly focused optical beams* with high numerical aperture immersion objectives [28], or even locally using *near-field excitation* via a metal coated tip with a sub-wavelength aperture generating an intense near-field suitable of SPP excitation [29].

Although the field localization is quite significant, due to the propagating nature of SPPs, it is spread along the interface which might be limiting for some applications such as biosensing. Nevertheless, by restricting the volume of the metal component, another kind of excitation, so-called localized surface plasmon (LSP), can be reached. The plasmon is no longer propagating but is localized within a small volume, with electrons oscillating in a standing wave manner and the merits of LSP will be thoroughly discussed in the following chapter.

1.6 Localized surface plasmons

In the previous section, we have described SPPs which were propagating electromagnetic waves coupled to the conduction electrons of a metal at a metal-dielectric interface. Localized surface plasmons (LSP), however, are non-propagating excitations of conduction electrons confined in metallic nanostructures coupled to an electromagnetic wave. The effect is shown in Fig. 1.7 where the electrons are driven out of equilibrium by the electric component of the external electromagnetic field. This generates a dipole moment and a restoring force on the displaced electrons inside the particle so that the resonance can occur amplifying the field components inside and near the particle. Another difference due to the curved surface dwells in the possibility of a direct excitation by electromagnetic waves as opposed to the SPP [17]. To understand this behaviour we need to consider a scenario where the electromagnetic wave is scattered by an object.

The scattering of an electromagnetic wave by an object has attracted a lot of attention even in ancient times, mostly related to colouring. Recently, we have relied on such scattering events in analysis on all kinds of scales ranging from celestial

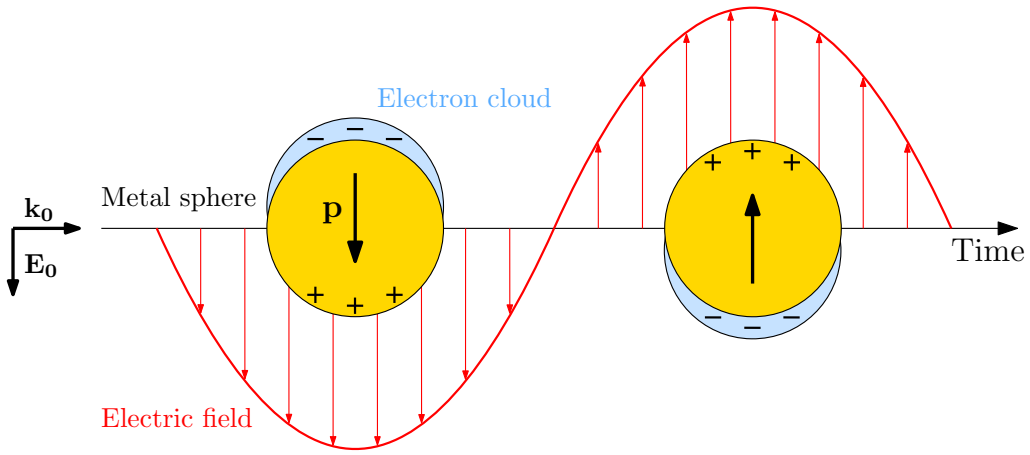

Fig. 1.7: Schematic image of localized surface plasmon (LSP) excited in a metal particle. The conduction electrons are displaced by an external electric field of an electromagnetic wave and the stationary positive ions generate the restoring force causing electron oscillations. Note that the arrow indicates the induced electric dipole.

bodies in astronomy to nanoparticles in material science. The scattering of electromagnetic waves where the energy of a photon is changed is called inelastic (e.g. Raman/Brillouin scattering) and its intensity is generally rather small. The other form of scattering, where the photon energy is unchanged, is called elastic with an intensity orders of magnitude higher than in the case of inelastic scattering. The following chapter will be focused primarily on the forms of elastic scattering on a spherical particle which is highly dependent on respective dimensions, i.e., the wavelength of the electromagnetic wave λ and the radius of the object R (see Fig. 1.8). We can define the size parameter x as the ratio between the dimension of the object and the wavelength of light as $x = 2\pi R/\lambda$ [30]. For $x \gg 1$ the occurring effects are governed by laws of geometrical optics, while for $x \ll 1$ the interaction is related to the Rayleigh scattering (also referred to as the quasi-static regime), and for comparable dimensions $x \sim 1$ the scattering is referred to as the Mie scattering (first described by Gustav Mie [31]). In the following text, we will focus only on the latter two cases, i.e., the Rayleigh and Mie scattering.

The interaction of an electromagnetic wave with a particle much smaller than the wavelength ($x \ll 1$), i.e., the Rayleigh scattering, can be analyzed using the simple quasi-static approximation. In this case, the phase of the oscillating electromagnetic field is practically constant over the particle volume, therefore, the problem can be re-framed to that of a particle in an electrostatic field. Neglecting these phase retardation effects simplifies the problem significantly and a harmonic time dependence can be added to the field distribution subsequently. This simplification of a full scattering problem describes well the behaviour of small particles (below 10 nm) and provides a decent approximation up to 100 nm when illuminated by visible light.

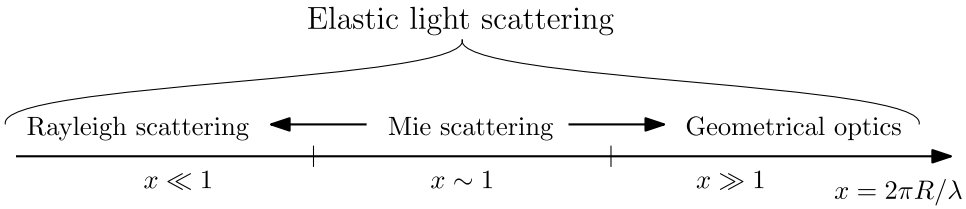

Fig. 1.8: Elastic scattering of an electromagnetic wave by a particle in different regimes based on the size parameter x. R represents the (effective) radius of the particle and λ is the wavelength of the electromagnetic wave [30].

The most convenient geometry for the analytical solution is a homogeneous, isotropic sphere of a radius R formed from a material whose dielectric response to the electromagnetic field is characterized by a complex dielectric function $\varepsilon_\mathrm{m}(\omega)$ (see Fig. 1.9). The sphere is located at the origin of the uniform, static electric field $\mathbf{E_0}$ oriented along the z-axis and the surrounding medium is isotropic and non-absorbing with a dielectric constant ε_d.

In the electrostatic approach, we can avoid solving more complicated Helmholtz equation $\nabla^2\Phi + k^2\Phi = 0$ and use Laplace equation $\nabla^2\Phi = 0$ instead. The obtained electric potential can then be used to calculate the electric field as $\mathbf{E} = -\nabla\Phi$. Solving the Laplace equation in spherical coordinates gives the electric potentials inside Φ_in and outside the sphere Φ_out as

$$\Phi_\mathrm{in}(r,\theta) = \sum_{l=0}^{\infty} A_l r^l P_l(\cos\theta), \tag{1.31a}$$

$$\Phi_\mathrm{out}(r,\theta) = \sum_{l=0}^{\infty} [B_l r^l + C_l r^{-(l+1)}] P_l(\cos\theta), \tag{1.31b}$$

where $P_l(\cos\theta)$ are the Legendre polynomials of the order l, θ is the angle between the position vector $\mathbf{r}$ of the point P and the z-axis. From the boundary conditions for $r \to \infty$ and at the sphere's surface $r = R$, the coefficients A_l, B_l, and C_l can be determined leading to the potentials in the form [32]

$$\Phi_\mathrm{in} = -\frac{3\varepsilon_\mathrm{d}}{\varepsilon_\mathrm{m} + 2\varepsilon_\mathrm{d}} E_0 r\cos\theta, \tag{1.32a}$$

$$\Phi_\mathrm{out} = -E_0 r\cos\theta + \frac{\varepsilon_\mathrm{m} - \varepsilon_\mathrm{d}}{\varepsilon_\mathrm{m} + 2\varepsilon_\mathrm{d}} E_0 R^3 \frac{\cos\theta}{r^2}. \tag{1.32b}$$

Using the formula $\mathbf{E} = -\nabla\Phi$ we get the following expressions for the electric field

$$\mathbf{E}_\mathrm{in} = \frac{3\varepsilon_\mathrm{d}}{\varepsilon_\mathrm{m} + 2\varepsilon_\mathrm{d}} \mathbf{E_0}, \tag{1.33a}$$

$$\mathbf{E}_\mathrm{out} = \mathbf{E_0} + \frac{3\mathbf{r}(\mathbf{r}\cdot\mathbf{p}) - \mathbf{p}r^2}{4\pi\varepsilon_0\varepsilon_\mathrm{d} r^5} = \mathbf{E_0} + \mathbf{E}_\mathrm{sca}. \tag{1.33b}$$

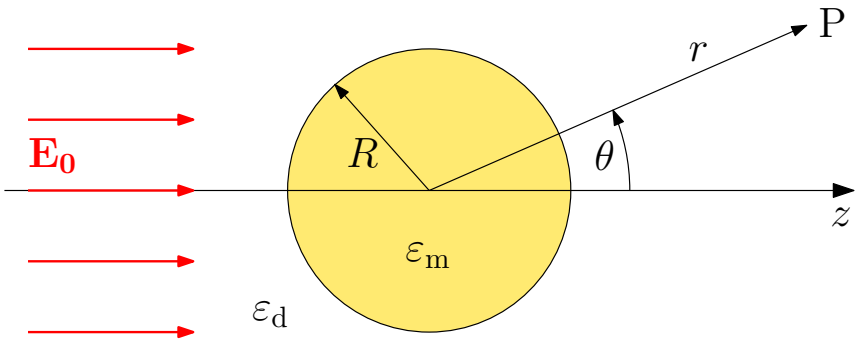

Fig. 1.9: Homogeneous isotropic sphere with the radius R and material property specified by $\varepsilon_{\mathrm{m}}(\omega)$ surrounded by an isotropic non-absorbing dielectric ε_{d} in an electrostatic field $\mathbf{E_0}$.

Thus we can see in the Eq. 1.33a that E_{in} is constant inside the sphere, while the Eq. 1.33b consists of the applied field and the scattered field which corresponds to an electric field generated by a dipole located at the sphere's centre. The dipole moment $\mathbf{p}$ induced inside the sphere is defined as

$$\mathbf{p} = 4\pi\varepsilon_0\varepsilon_{\mathrm{d}}R^3\frac{\varepsilon_{\mathrm{m}}-\varepsilon_{\mathrm{d}}}{\varepsilon_{\mathrm{m}}+2\varepsilon_{\mathrm{d}}}\mathbf{E_0} \tag{1.34}$$

and it is proportional to the applied electric field $|\mathbf{E_0}|$. An alternative form of the dipole moment utilizes polarizability α, which specifies the ease with which the sphere is polarized, via $\mathbf{p} = \varepsilon_0\varepsilon_{\mathrm{d}}\alpha\mathbf{E_0}$ as

$$\alpha = 4\pi R^3\frac{\varepsilon_{\mathrm{m}}-\varepsilon_{\mathrm{d}}}{\varepsilon_{\mathrm{m}}+2\varepsilon_{\mathrm{d}}}. \tag{1.35}$$

This function undergoes a resonant enhancement under the condition that $|\varepsilon_{\mathrm{m}}+2\varepsilon_{\mathrm{d}}|$ is minimal, which in the case of small or slowly-varying $\mathrm{Im}\{\varepsilon_{\mathrm{m}}(\omega)\}$ around the resonance reduces to $\mathrm{Re}\{\varepsilon_{\mathrm{m}}(\omega)\} = -2\varepsilon_{\mathrm{d}}$. This relation is referred to as the Fröhlich condition and for a sphere made of a Drude metal surrounded by a dielectric it is met at the frequency [33]

$$\omega_{\mathrm{LSP}} = \frac{\omega_{\mathrm{p}}}{\sqrt{\varepsilon_\infty+2\varepsilon_{\mathrm{d}}}}, \tag{1.36}$$

with ε_∞ corresponding to the dielectric response of bound valence electrons inside a Drude metal. Note that for an ideal free-electron gas with an air surrounding the formula simplifies to $\omega_{\mathrm{LSP}} = \omega_{\mathrm{p}}/\sqrt{3}$. Eq. 1.36 also highlights a very strong dependence of resonant frequency on the dielectric environment, red-shifting with increasing ε_{d}, making the metal nanoparticles an ideal platform for optical sensing of changes in the refractive index of the surrounding media.

Reaching the resonant condition is also intimately connected to the enhancement in both the internal and the dipolar electric field which is a property that a lot of

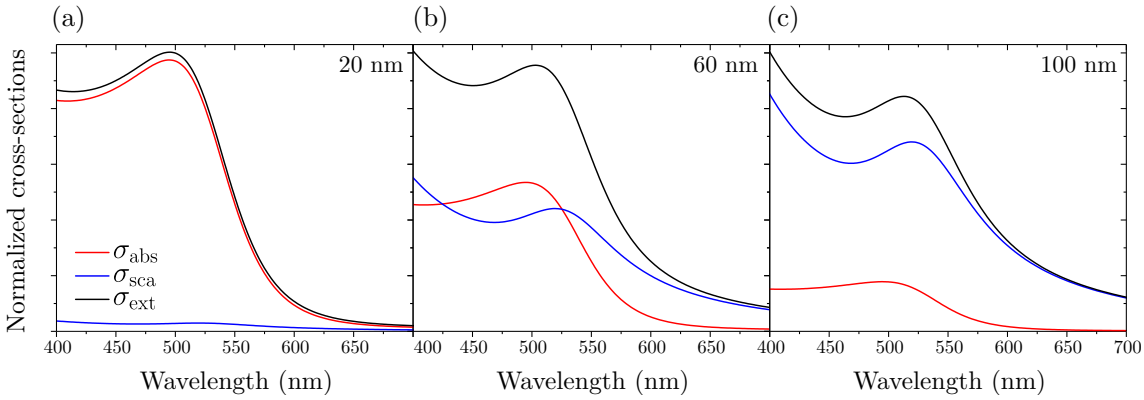

Fig. 1.10: Absorption, scattering, and extinction cross-sections of gold spherical nanoparticles with radii of (a) 20 nm, (b) 60 nm, and (c) 100 nm in air calculated within quasi-static approximation. The dielectric function of gold was taken from [9] and fitted by a modified Drude model with four Lorentz oscillators [11].

modern applications of metal nanoparticles make use of.

Upon a plane-wave illumination, its harmonic electric field induces an oscillating dipole moment. Radiation of the dipole leads to a scattering of the plane wave by the sphere which can be described as a point dipole radiation. Scattering by an ideal dipole with the moment $\mathbf{p}(t) = \varepsilon_0 \varepsilon_\mathrm{d} \alpha \mathbf{E_0} \mathrm{e}^{-\mathrm{i}\omega t}$ [34] allows the calculation of scattering and absorption cross sections via the Poynting vector [35]

$$\sigma_\mathrm{sca} = \frac{k^4}{6\pi} |\alpha|^2 = \frac{8\pi}{3} k^4 R^6 \left| \frac{\varepsilon_\mathrm{m} - \varepsilon_\mathrm{d}}{\varepsilon_\mathrm{m} + 2\varepsilon_\mathrm{d}} \right|^2, \tag{1.37a}$$

$$\sigma_\mathrm{abs} = k \mathrm{Im}\{\alpha\} = 4\pi k R^3 \mathrm{Im}\left\{ \frac{\varepsilon_\mathrm{m} - \varepsilon_\mathrm{d}}{\varepsilon_\mathrm{m} + 2\varepsilon_\mathrm{d}} \right\}, \tag{1.37b}$$

where k is the wavenumber. Note that the absorption efficiency, scaling with R^3, dominates over the scattering efficiency, which scales with R^6, in the case of very small particles. For larger particles, on the other hand, the scattering becomes more prevalent. Fig 1.10 demonstrates such effects for the case of spherical gold nanoparticles with various radii. The scattering and absorption cross-sections can be summed up into extinction cross-section as

$$\sigma_\mathrm{ext} = \sigma_\mathrm{sca} + \sigma_\mathrm{abs}. \tag{1.38}$$

Note that fulfilling the resonant condition in the nanoparticle is reflected in Fig 1.10 as a peak in extinction/scattering spectra and the wavelength corresponding to the peak maximum can be referred to as resonance wavelength λ_res which is a crucial characteristic of LSP resonance. For larger nanoparticles, where the phase changes over the particle volume start to appear, a more rigorous electrodynamic approach is required. This theory developed by Gustav Mie in 1908 [31], thereby often referred

to as the Mie theory, describes the complete scattering and absorption of an electromagnetic wave by a sphere. Using this approach it is necessary to find a solution of a full vector Helmholtz equation in spherical coordinates. Nevertheless, if the two proposed vectorial field solutions fulfil the conditions for being an electromagnetic wave, i.e., they satisfy the wave equation, and are linked together, the problem can be reduced to finding a solution of the scalar wave equation in spherical coordinates. From the scalar solution, the vector spherical harmonics corresponding to electric and magnetic modes can be calculated. If the planar electromagnetic wave interacts with the spherical object, it is necessary to expand the incoming wave into spherical harmonic functions as well. From that, we can then express all the relevant cross-sections [34]

$$\sigma_{\text{sca}} = \frac{2\pi}{|k|^2} \sum_{L=1}^{\infty} (2L+1)(|a_L|^2 + |b_L|^2), \tag{1.39a}$$

$$\sigma_{\text{ext}} = \frac{2\pi}{|k|^2} \sum_{L=1}^{\infty} (2L+1)\text{Re}\{a_L + b_L\}, \tag{1.39b}$$

$$\sigma_{\text{abs}} = \sigma_{\text{ext}} - \sigma_{\text{sca}}, \tag{1.39c}$$

where k is the wavenumber of the incoming electromagnetic wave, and L represents the integers specifying the modes of the scattering ($L = 1$ for dipole, $L = 2$ for quadrupole and further for higher modes). In the previous expressions, a_L and b_L correspond to the amplitudes of the electric and magnetic field, respectively, for the individual modes. These are composed of the Riccati-Bessel functions ψ_L and χ_L

$$a_L = \frac{m\psi_L(mx)\psi'_L(x) - \psi'_L(mx)\psi_L(x)}{m\psi_L(mx)\chi'_L(x) - \psi'_L(mx)\chi_L(x)}, \tag{1.40a}$$

$$b_L = \frac{\psi_L(mx)\psi'_L(x) - m\psi'_L(mx)\psi_L(x)}{\psi_L(mx)\chi'_L(x) - m\psi'_L(mx)\chi_L(x)}. \tag{1.40b}$$

Here, the parameter $m = n_{\text{m}}/n_{\text{d}}$, where n_{m} is the complex refractive index of the metal, and n_{d} is the real refractive index of the surrounding medium. $x = Rk_{\text{d}} = 2\pi R/\lambda_{\text{d}}$ represents the size parameter, where R is the radius of the particle, k_{d} and λ_{d} is the wavenumber and wavelength, respectively, in the surrounding medium [36].

The extinction cross-sections corresponding to gold spherical nanoparticles of radius R in an air environment calculated using the quasi-static approximation and using the Mie theory (calculated using the miepython module [37]), respectively, are shown in Fig. 1.11(a). In contrast to the quasi-static approximation results, the Mie theory provides spectra which exhibit a realistic red-shift of the resonance wavelength with an increasing size of the particle. The deviation of quasi-static approximation spectra from the Mie theory results increases with the nanoparticle size, confirming its validity only for smaller nanoparticles. Additionally, the Mie theory takes into account not only the ordinary electric dipole mode but higher-order

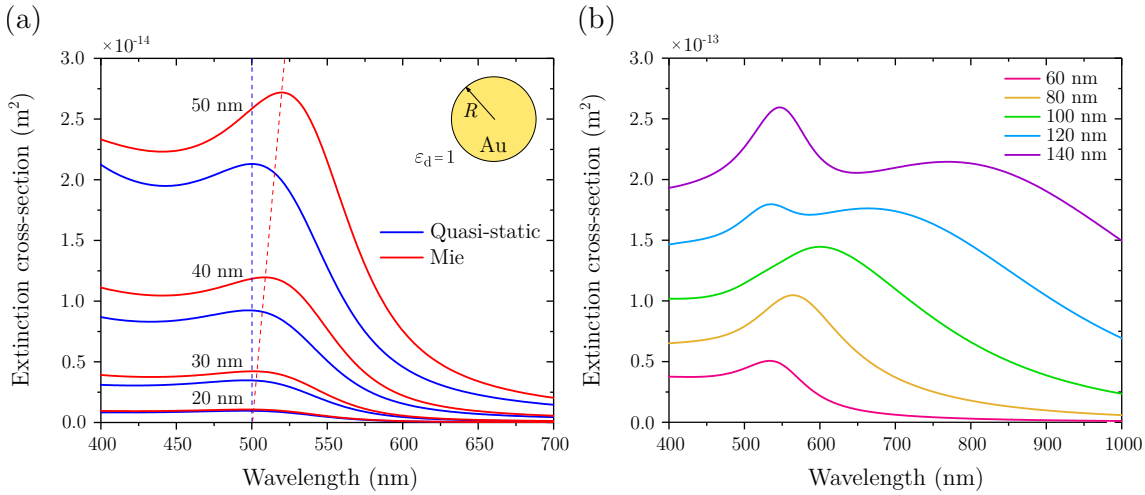

Fig. 1.11: Extinction cross-sections σ_{ext} calculated for gold nanoparticles with a radius R in air. (a) Comparison of σ_{ext} for small nanoparticles obtained from the quasi-static approximation and from the Mie theory, respectively, with the latter spectra showing noticeable red-shift in resonance wavelength of the electric dipole mode as the nanoparticle's size increases, highlighted by the dashed lines. (b) Mie σ_{ext} spectra calculated for larger nanoparticles with higher-order electric quadrupole mode appearing at shorter wavelengths next to the electric dipole mode. Note that the Mie theory calculations were done using the modification of the Python module miepython [37].

modes too, as well as the magnetic modes inside the particle. In metal nanoparticles, the magnetic modes are almost negligible due to a vanishing field inside the sphere. Thus, the additional mode appearing at shorter wavelengths upon further increasing the nanoparticle radius in Fig. 1.11(b) corresponds to the electric quadrupole mode. To get the magnetic response for the metallic particles, the shape needs to be altered, e.g., forming a split-ring resonator with the magnetic field enhanced in the ring centre [38].

Inside the dielectric nanoparticles there is a multitude of modes, typically referred to as Mie resonances which can be excited. As opposed to metallic nanoparticles [Fig. 1.11(b)], the magnetic modes in high-refractive-index dielectrics such as silicon are much more pronounced and the overall shape of the extinction spectra is rather more complex as shown in Fig. 1.12(a). The 100 nm silicon nanoparticle supports the existence of electric and magnetic dipole (ED and MD) and quadrupole (EQ and MQ) modes with higher-order modes being difficult to identify. Fiq. 1.12(b) depicts the electric field distribution of three major electric and magnetic modes which can be induced in a spherical dielectric nanoparticle including octupole modes (EO and MO). The resonant magnetic dipole response stems from the coupling of the impinging light to the circular currents of the electric field inside the particle. This situation occurs when the wavelength of light inside the particle is comparable to the

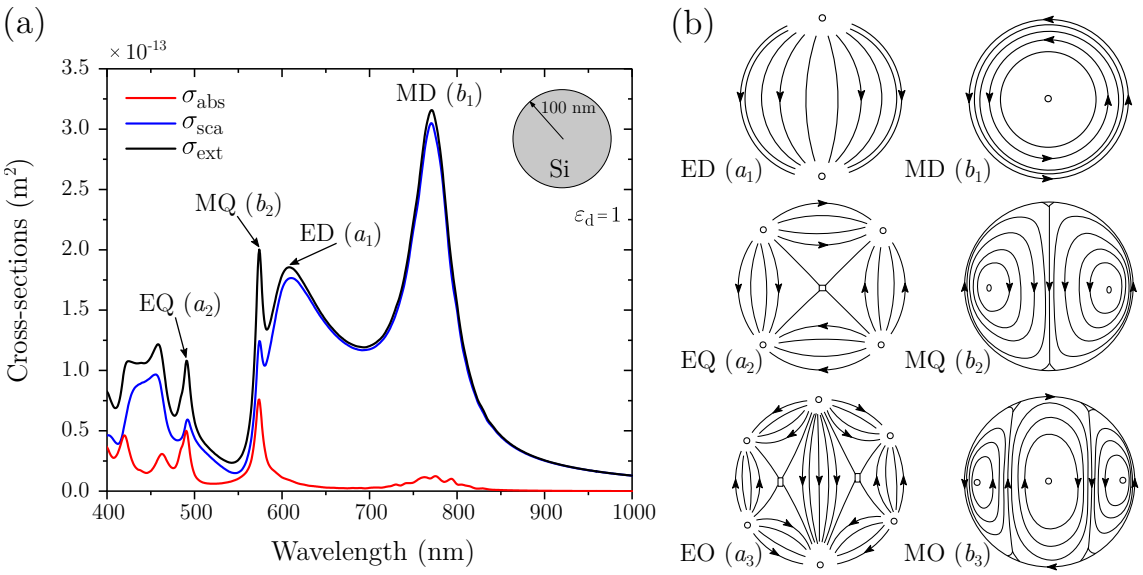

Fig. 1.12: (a) Mie theory calculated cross-sections corresponding to a silicon sphere of the 100 nm radius surrounded by air. The nature of the modes induced inside the particle is ascribed to the most pronounced peaks in the spectra. (b) Electric field distribution for the three lowest-order modes of electric and magnetic resonances supported by a spherical dielectric nanoparticle, modified from [35]. Note that ED and MD stand for electric and magnetic dipole modes, EQ and MQ for the quadrupole modes, and EO and MO for the octupole modes, while the parameters in the brackets reveal their amplitude indices in the context of Eq. 1.39. The data for Si were taken from [40] and [41] and the spectra were calculated using the modified miepython module [37].

nanoparticle diameter. Magnetic modes can even become the main contributor to the scattering behaviour of the nanoparticle [39]. Many effects similar to plasmonic ones observed for the lossy metal nanoparticles can also be achieved by low-loss high-refractive-index dielectric nanoparticles. The multitude of electric and magnetic modes which can be tuned independently by changing the nanoparticle's geometrical parameters present ideal building blocks, e.g., for a design of low-loss metasurfaces.

1.7 Tailoring the LSP response

The following figures of the calculated extinction cross-sections present a comparison of various materials used in nanophotonics to manipulate the light demonstrated on a spherical nanoparticle geometry. Fig 1.13 is dedicated to metallic materials used in conventional plasmonics such as silver, gold, and aluminium with an interesting candidate, particularly for the UV plasmonics, gallium [42]. The wavelength axis is fixed for all materials to highlight the differences in peak positions for all the materials, while the plotted range is limited by the available dielectric functions of

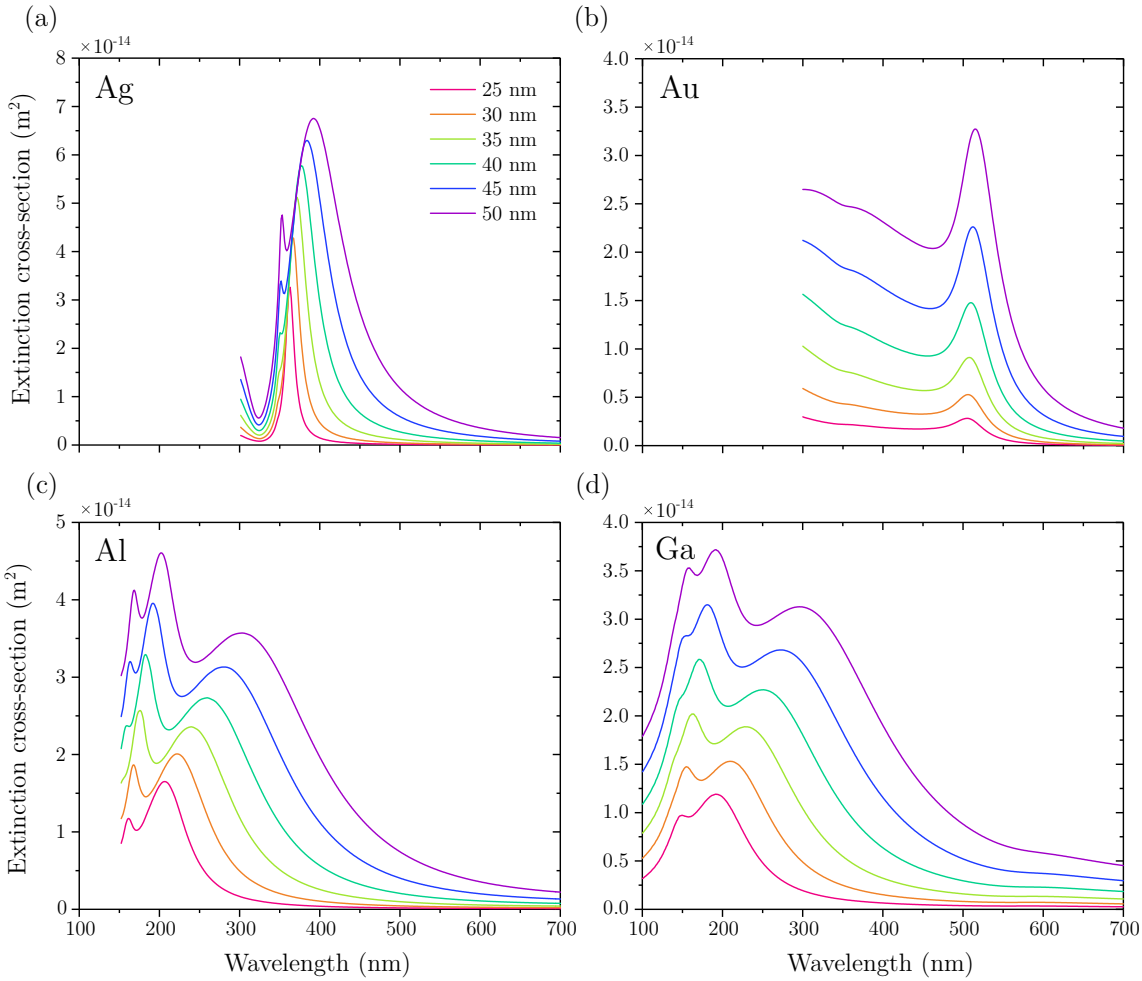

Fig. 1.13: Mie theory calculated extinction cross-sections corresponding to the spherical nanoparticles of various radii made of metals relevant in plasmonics: (a) silver, (b) gold, (c) aluminium, and (d) gallium, which are surrounded by air. The dielectric functions of Ag, Au, and Al were taken from [23], and Ga from [43] while the spectra were calculated using the modified miepython module [37].

the individual materials.

The main peaks in the spectra are generally related to the electric dipole mode with higher order modes appearing for larger nanoparticles at shorter wavelengths. For use in the UV range, gallium and aluminium are the best choices of materials, however, in the VIS and further, the losses inside these two materials increase dramatically. Silver NPs are usable roughly from 350 nm next to the region of interband transitions all the way to the IR region. Similarly, in gold NPs, the region of interband transitions ends around 500 nm and the resonance can go from this region to the IR. The red-shift of resonance wavelength with an increasing radius of the NPs is most pronounced in gallium and aluminium NPs while in silver and gold NPs it becomes more pronounced for larger radii of NPs.

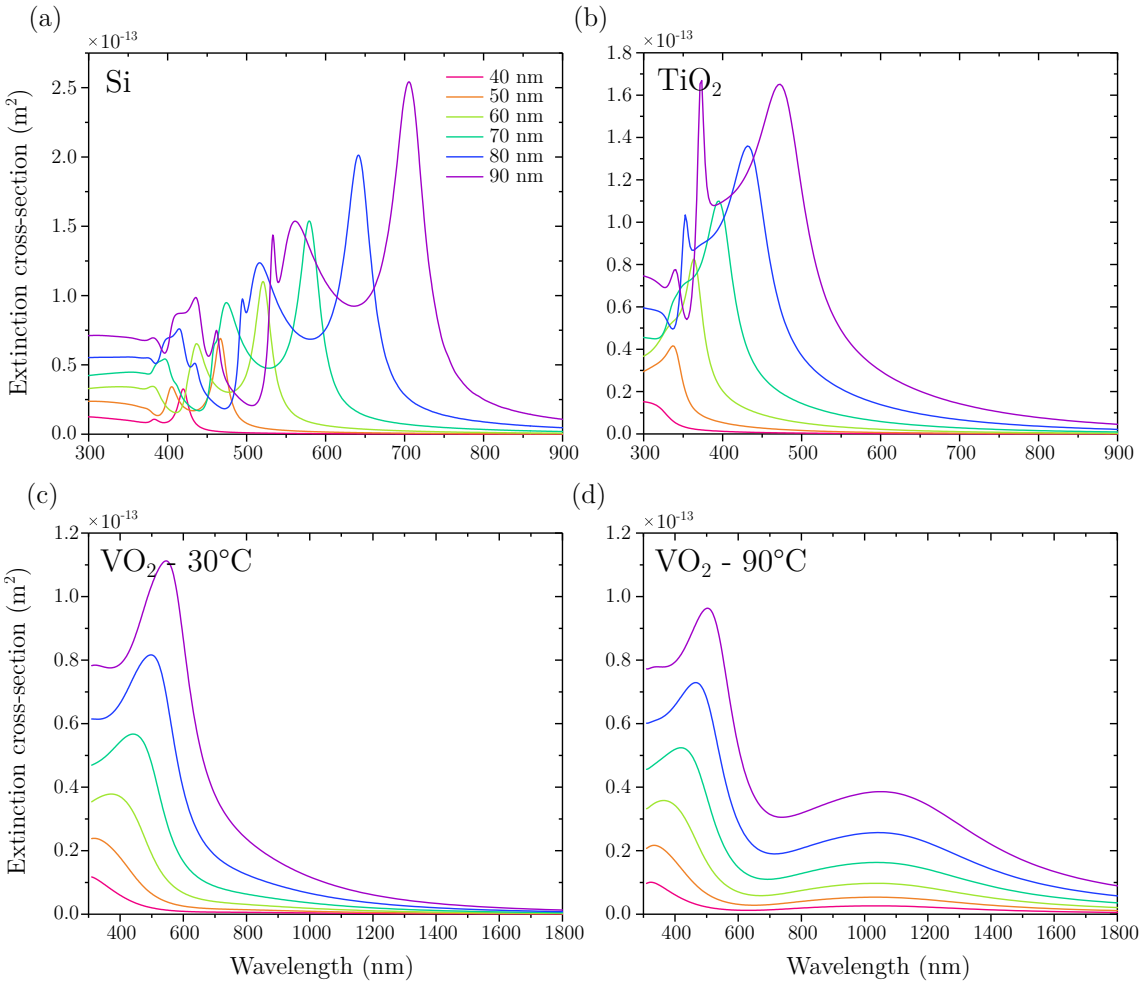

Fig. 1.14: Mie theory calculated extinction cross-sections corresponding to the spherical nanoparticles of various radii made of selected dielectrics relevant for nanophotonic applications: (a) silicon, (b) titanium dioxide, and vanadium dioxide in (c) the purely dielectric state at 30 °C, or (d) the metallic state at 90 °C, respectively, which are surrounded by air. The dielectric functions were taken from: Si [40, 41], TiO_2 [44], VO_2 [45], while the spectra were calculated using the modified miepython module [37]. Note the different wavelength scale for VO_2 which was selected to show an additional peak occurring in NIR after the VO_2 transition to a metallic state.

As mentioned previously, dielectric materials which exhibit Mie resonances can also be utilized in nanophotonics e.g. in metasurface development as a loss-less alternative to metals. The extinction cross-sections of dielectric NPs with different radii are shown in Fig. 1.14 for three materials that are often used: silicon, titanium dioxide and vanadium dioxide. The spectra, particularly for Si, show more features due to the presence of magnetic modes as well as electric ones. Additionally, the high index of refraction of Si ($\sim$ 4 at 550 nm [40]) allows the existence of more modes induced in the NPs than in the case of TiO_2 and VO_2 for the selected radii.

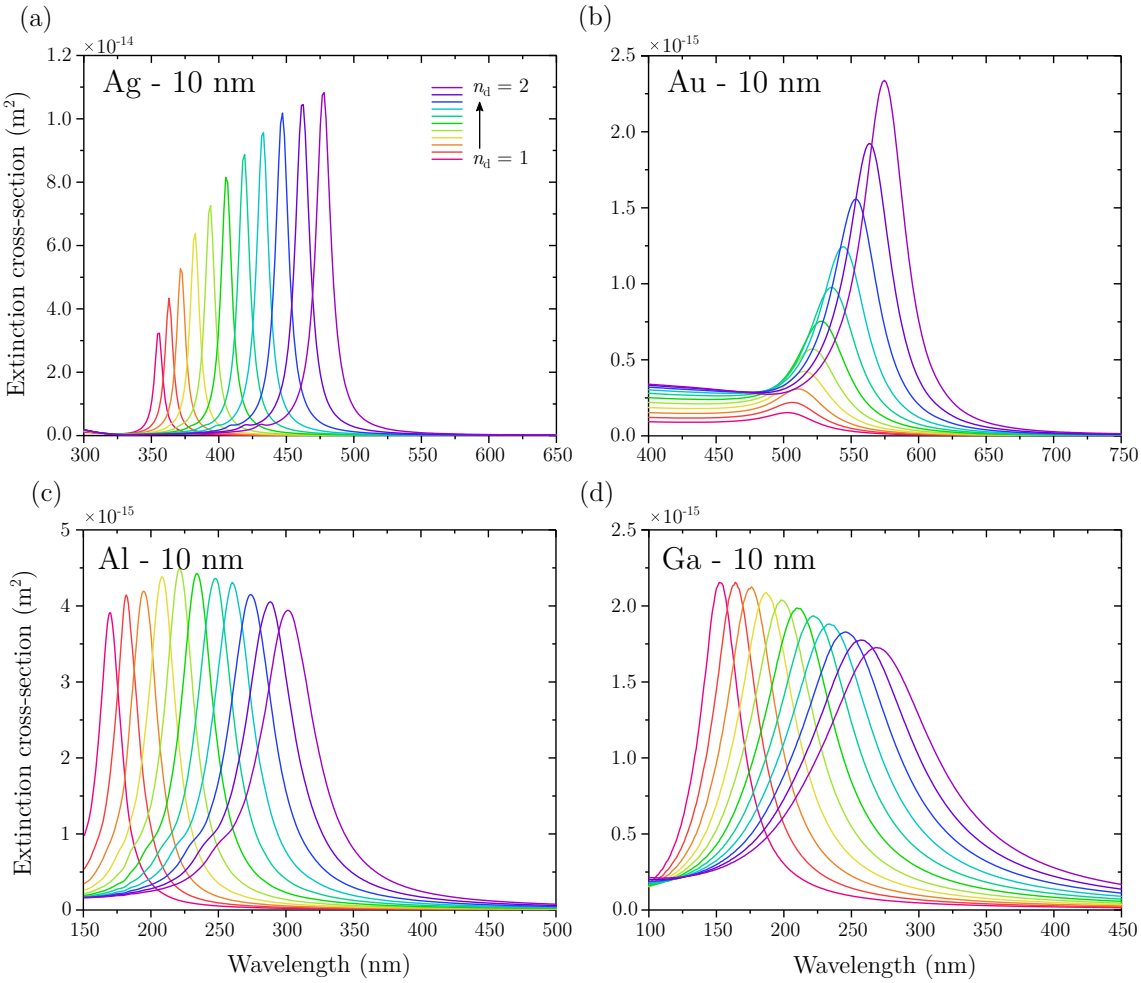

Fig. 1.15: Influence of the refractive index of surrounding media on plasmon resonance of metallic spherical nanoparticles of one selected radius (10 nm) calculated by the Mie theory: (a) silver, (b) gold, (c) aluminium, and (d) gallium. The refractive index varies from $n_d = 1$ to $n_d = 2$. The dielectric functions of Ag, Au, and Al were taken from [23], and Ga from [43] while the spectra were calculated using the modified miepython module [37].

Likewise, the redshift with the increasing NP radius is due to the same reason the most pronounced for Si than for TiO_2 and VO_2 NPs. Note that the extinction spectra of VO_2 NPs are shown in two windows, in the low-temperature dielectric state (at 30°C) and the high-temperature metal state (at 90°C) after it undergoes the insulator-to-metal transition. The wavelength scale for VO_2 is purposely larger so it shows the existence of an additional mode (plasmonic) in the NIR region for the metallic VO_2 giving it an additional functionality that can be turned on and off based on the sample temperature.

The environment surrounding the NPs plays a significant role in their optical properties [see Eq. (1.37) and (1.39)]. The dependence of the extinction cross-section on the refractive index of various surrounding environments is highlighted in Fig. 1.15

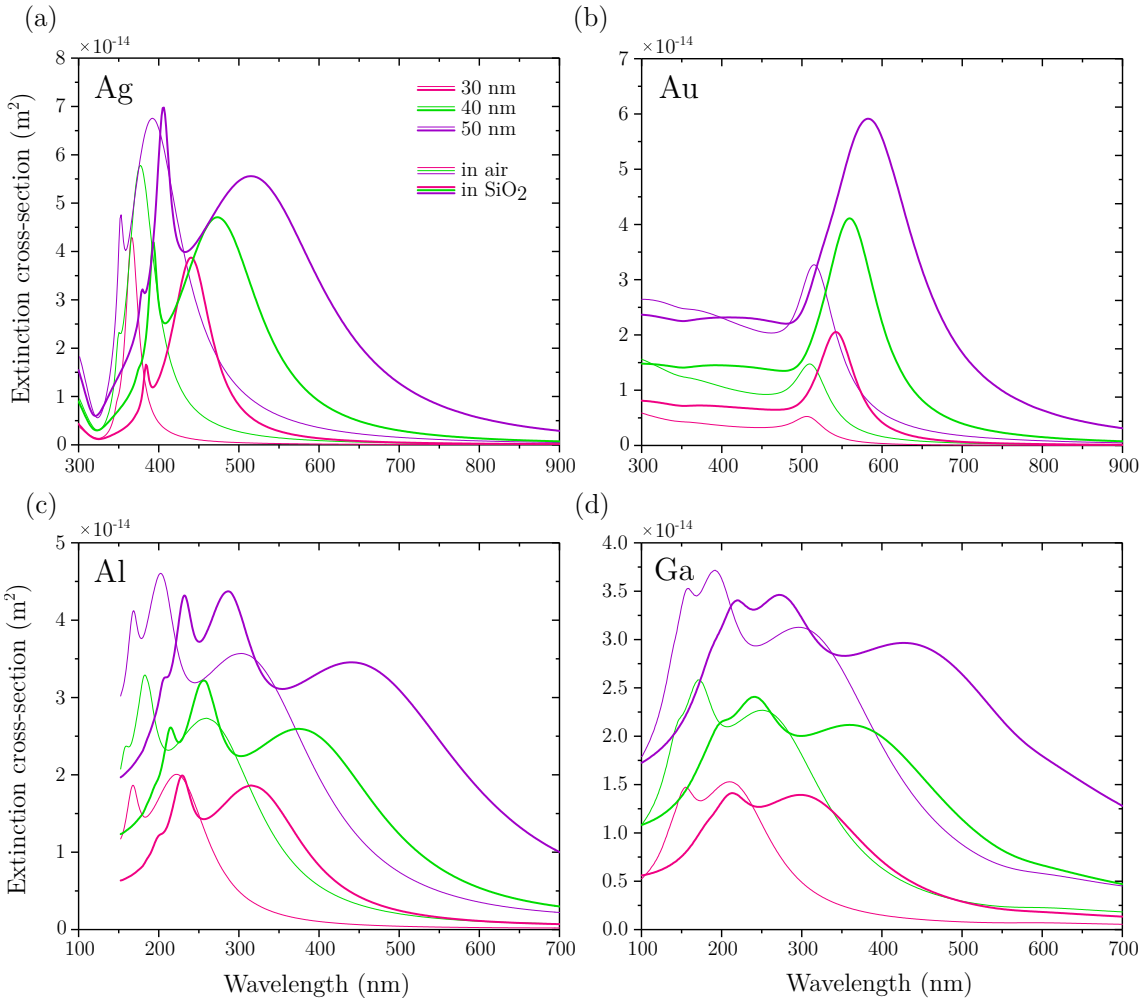

Fig. 1.16: Influence of a surrounding media on plasmon resonance of metallic spherical nanoparticles of three selected radii calculated by Mie theory: (a) silver, (b) gold, (c) aluminium, and (d) gallium. Thin lines correspond to nanoparticles surrounded by air with $n_{\mathrm{a}} = 1$ while thick lines represent nanoparticles surrounded by SiO_2 with $n_{SiO_2} = 1.46$ [46]. The dielectric functions of Ag, Au, and Al were taken from [23], and Ga from [43] while the spectra were calculated using the modified miepython module [37].

for one selected radius for each material. Rather small dimensions were chosen to show primarily the dipole mode and its shift with the increasing index of refraction. All the NPs exhibit significant red-shifts of the resonance wavelength as the n_{d} increases. Nevertheless, silver and gold also exhibit a dramatic increase in the extinction cross-section amplitude. This phenomenon can be understood by acknowledging their interband transition regions which still play a crucial role in their optical properties (around 350 nm in silver and 500 nm in gold), but the detrimental effects lessen as the resonance moves to longer wavelengths. In terms of the peak width, it is the smallest in the case of silver, followed by aluminium and gallium while gold

presents the largest peak width. It is also worth noting the increasing peak width for aluminium and gallium reflecting the growing losses in these materials at larger wavelengths.

An example of a more realistic situation is outlined in Fig. 1.16 where the metallic spheres of three selected radii are embedded into the SiO_2 surrounding. All the spectra exhibit significant red-shift which is observable even for the higher-order modes whose effect becomes more pronounced in optically denser media.

2 PLASMONIC NANOSTRUCTURES

The previous chapter has shown that localized surface plasmons inside a nanostructure interact strongly with impinging electromagnetic radiation, especially with wavelengths close to the plasmon resonance wavelength. At this condition one crucial property of metallic nanostructures, that is the unrivalled ability to concentrate light, occurs [47]. By squeezing the light into nanoscale volumes, the plasmonic elements allow the investigation of fundamental light-matter interactions in tiny dimensions otherwise inaccessible [48]. This is a fundamental property which makes plasmonics a tremendously versatile tool for all kinds of applications [47].

As shown in the previous chapter, the resonance wavelength as a characteristic aspect of plasmonic nanostructures can be rather easily tuned by varying their material, surroundings, size, and shape [49]. Thus control over the plasmonic nanostructures and their properties is crucial to utilize their potential and nanotechnology provides the tools to achieve that.

2.1 Fabrication of nanostructures

There are two main approaches to preparing plasmonic nanostructures depending on where the fabrication starts from. In top-down processes, the starting position is a bulk material from which much smaller nanostructures are fabricated, typically by lithographic methods. These can lead to large arrays of almost identical nanostructures with controlled orientation and precise distances between them but are rather time-consuming. In a bottom-up approach, the nanostructures are formed from much smaller components, such as atoms and molecules, and these can then be arranged to obtain the desired functionality. Typically, these methods encompass the chemical synthesis of nanoparticles and their self-assembly on a substrate. Such approaches are fast and produce high-quality nanostructures but their precise placement is rather challenging [50].

Top-down nanostructure fabrication is conventionally done by two basic lithographic methods: electron beam lithography (EBL) and focused ion beam (FIB) lithography [51], schematically shown in Fig. 2.1. A typical EBL procedure involves a high-resolution electron-sensitive polymer [such as poly(methyl methacrylate) – PMMA] which is spin-coated onto a substrate and its subsequent modification by focused electron beam [52]. The patterns are then chemically developed. Afterwards, a thin layer of metal is deposited covering the whole sample which is followed by a lift-off procedure which leaves metal only in the areas in direct contact with the substrate, i.e., the exposed regions. The spatial resolution can be below 5 nm [53] but is generally negatively affected by a polycrystallinity of deposited metal and often an adhesion layer is required which significantly worsens the plasmonic properties [54].

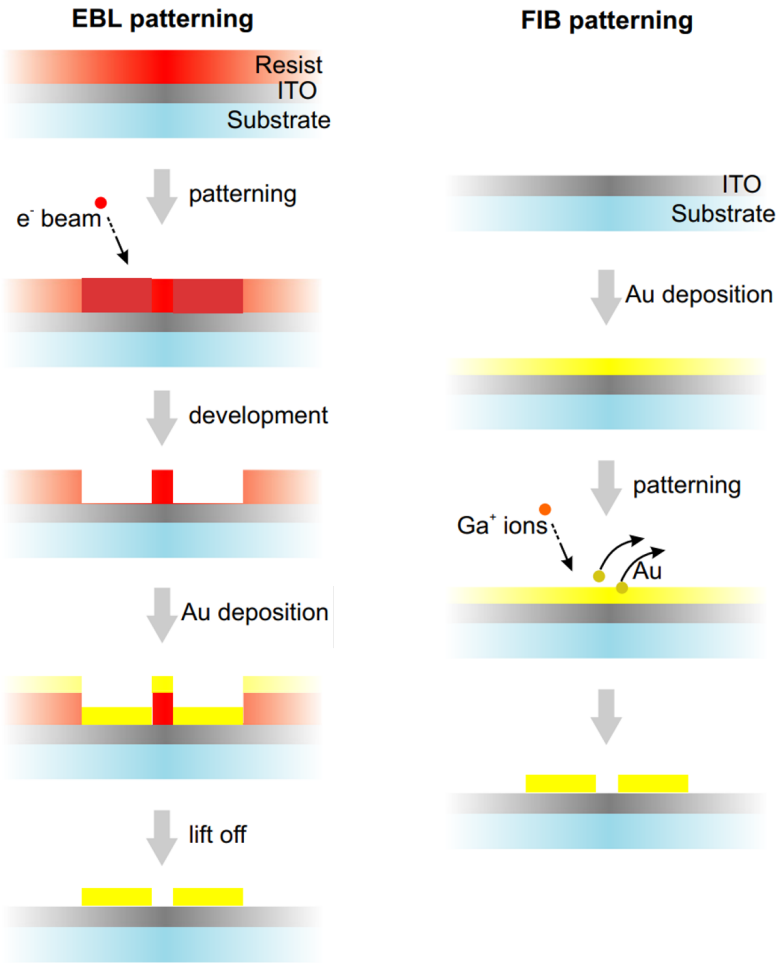

Fig. 2.1: Schematic of the two most common nanostructure preparation procedures. EBL on the left, FIB lithography on the right. Adapted from [50].

FIB lithography is a more straightforward method of fabrication which does not require any photoresist. A metallic layer is deposited first and it is directly sputtered away by a focused ion beam, usually Ga^+ ions, extracted from a liquid metal ion source [55]. Ions colliding with a sample create a collision cascade inside the layer knocking the atoms out of their equilibrium positions, thus eroding the layer. This approach does not require the adhesion layer and resulting nanostructures benefit from, e.g., very small gap sizes between them [56] and allow fabrication on curved surfaces [57].

Additional techniques involve UV [58] and nano-imprint [59] lithography, layer de-wetting [60] etc. [61]. Such fabricated nanostructures can be utilized in plenty of applications which are described below.

2.2 Metasurfaces

One of the leading applications of plasmonic structures are metasurfaces. The metasurface research aims to substitute the conventional optical components (lenses, polarizers, etc.) which are often quite bulky by planar structures [62, 63]. The bulkiness is caused by their working principle, where the desired effect like focusing and other beam shaping is attained by the change in phase of the light beam along the curved lens surface. This prevents the miniaturization of optical devices and their consequent use in modern photonic applications.

Conversely, plasmonic metasurfaces allow us to introduce abrupt changes in optical properties by a careful arrangement of sub-wavelength elements on a planar substrate surface [64, 65]. Such nanoantennas, with their ability to interact strongly with light, introduce more degrees of freedom to control the amplitude, phase, and polarization state of the outgoing light [66]. This enables the fabrication of ultrathin devices which can outperform traditional components and even introduce new functionalities.

There are several physical mechanisms which can be utilized to design a functional metasurface [67]. Firstly, multi-resonant metasurfaces that typically utilize V-shape nanostructures formed by two same-sized nanorods connected at different angles which determine their phase response [68]. Two modes, symmetric and antisymmetric, can be excited depending on the incident light polarization with respect to a nanostructure symmetry axis which can affect the polarization of the outgoing light [69]. These were one of the first proposed metasurfaces but their overall efficiency is rather low.

Secondly, gap-plasmon metasurfaces utilize a metal-insulator-metal architecture, where the metallic nanostructure arrays are separated from the underlying metallic mirror by an insulating layer, which allows strong coupling between the plasmon modes in the array and mirror dipoles in the metal layer [70]. The nanostructures can be, e.g., nanorods and the phase can be tuned by varying their size [71]. Such metasurfaces possess high efficiency but are limited to only reflective applications.

Thirdly, Pancharatnam-Berry-phase (or geometric-phase) metasurfaces rely on a set of identical nanostructures, e.g., nanorods, where the phase response is governed by their orientation [72]. When illuminated with circularly polarized light, the scattered light of the opposite handedness carries an additional phase difference corresponding to the double of the nanorod orientation angle [73]. These metasurfaces feature broadband activity and large fabrication tolerance but operate only with circularly polarized light.

Fourthly, Huygens' metasurfaces utilize the tailoring of electric and magnetic polarizabilities at the interface to achieve the desired effect on a transmitted light minimizing reflections [74]. Their design can incorporate nonperiodic or multilayered structures analogous to coils and capacitors to control the impedances locally [75]. Such metasurfaces based on plasmonic metals work well in microwave and IR regions

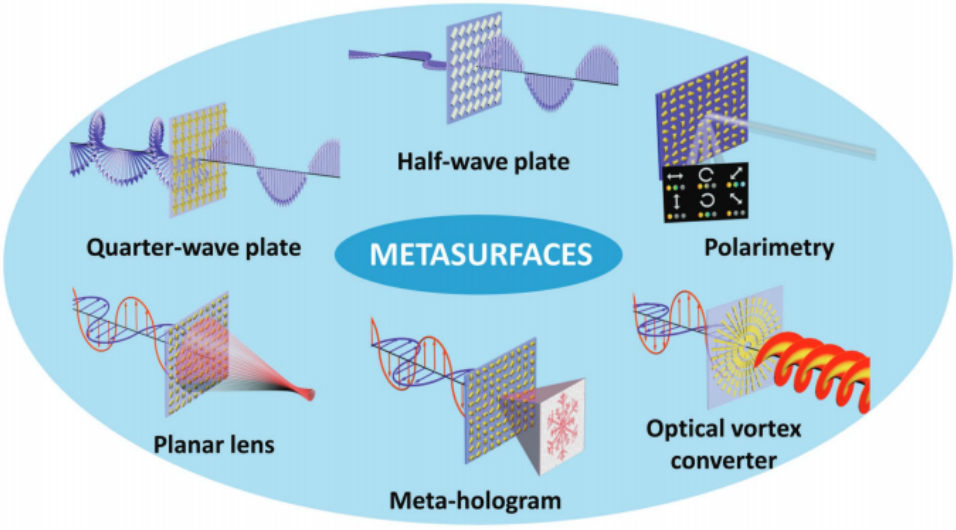

Fig. 2.2: An overview of typical applications of metasurfaces for changing the polarization state (quarter- and half-wave plates) and their spatial separation in polarimeters, for wave-front shaping in focusing, holography, and generation of vortex beams. Taken from [67].

but their performance in the optical region degrades significantly. Nevertheless, this can be overcome by utilizing only dielectric nanostructures [76, 77].

There is a plethora of metasurface applications (Fig. 2.2) in polarization control [78, 79] and its assessment [80], beam steering [81, 82], in light beam focusing [83, 84], holography [85, 86], and vortex beam shaping [87].

Conventional metasurfaces are generally single-purpose and thus lack any flexibility once fabricated and can be referred to as static. This can be overcome by implementing tunable elements into metasurfaces which allow them to change their properties dynamically [88, 89]. The degree of tunability can vary greatly as there are many physical phenomena which can be exploited [90]. The first class of metasurfaces whose optical properties can be switched between two different states are referred to as switchable which utilize phase-change materials like VO_2 and GeSbTe [91]. The second class of metasurfaces allows continuous tunability between two states which typically involves transparent conductive oxides like indium tin oxide (ITO) [92]. The third class represents fully reprogrammable metasurfaces, which are fully tunable and reconfigurable formed by individually addressable meta-atoms. This approach provides an ultimate flexibility but the fabrication is by far the most complicated and so far is limited mostly to GHz and THz [93], possibly IR regions [94].

2.3 Biodetection

The main principle of plasmonic biodetection resides in the fact that the frequency of plasmon resonance is affected by a refractive index increase in the proximity of a metallic surface (caused, e. g., by the presence of a biomolecule). This results in the screening of some of the surface charge induced by the electron oscillations, causing the resonance frequency to redshift [95]. The first detection schemes involved surface plasmon polaritons (surface plasmon resonance – SPR sensing) [96], where the light beam typically passes through a glass prism covered by a thin metallic layer where the light is reflected towards a detector. The resonance condition is unveiled by a sharp decrease in reflected light intensity as a function of the incident angle [97] or illumination wavelength [98]. The detection event is then related to the shift of the reflectance minimum [99, 100] or to the change in phase of the reflected light [101, 102].

In comparison to the relatively rigid SPR sensing in terms of resonance tunability, localized surface plasmons (localized surface plasmon resonance – LSPR sensing) [103] provide much broader spectral application range due to the resonance wavelength dependence on the size of the nanoparticle [104], material [105], shape [49] or whether it exists as a singular object or in assemblies [106, 107]. The sensing volume is localized to a very close proximity of the NP and the detection event is then recorded as a shift in the LSPR wavelength.

The refractive index sensing utilizing SPR and LSPR for label-free detection schemes has its limitations in being inherently nonspecific during the detection process. To detect only the desired biomolecules, the preliminary functionalization of the detection surface is necessary [108, 109].

A schematic comparing the principles of SPR and LSPR affinity biosensors based on the refractive index detection is depicted in Fig. 2.3. The metallic surfaces are functionalized by "capture"molecules that have an affinity towards the desired analyte and the changes in optical response upon detection are monitored [111]. Once the analyte is captured within the volume of enhanced electromagnetic field, which is much more localized with LSPR sensors [112], it manifests itself by a shift of resonance wavelength [113].

Similar systems were used for the detection of DNA molecules [114], cancer biomarkers [115], and viruses [116]. Even single biomolecule detection events have been recorded in the case of larger proteins [117, 118] but it requires a solution with very low concentrations preventing the use in real, much more complex media [119].

There are also nanoparticle-based detection approaches which do not require any spectroscopy setup for the analyte detection, e.g., colourimetry [120], where the binding event is accompanied by an evident change in colour observable by the naked eye due to the nanoparticle aggregation [121]. Another approach avoiding the need for a spectrometer is based on an array of nanoparticles with sharp resonances whose transmission contrast is recorded by a chip while changing the illumination wave-

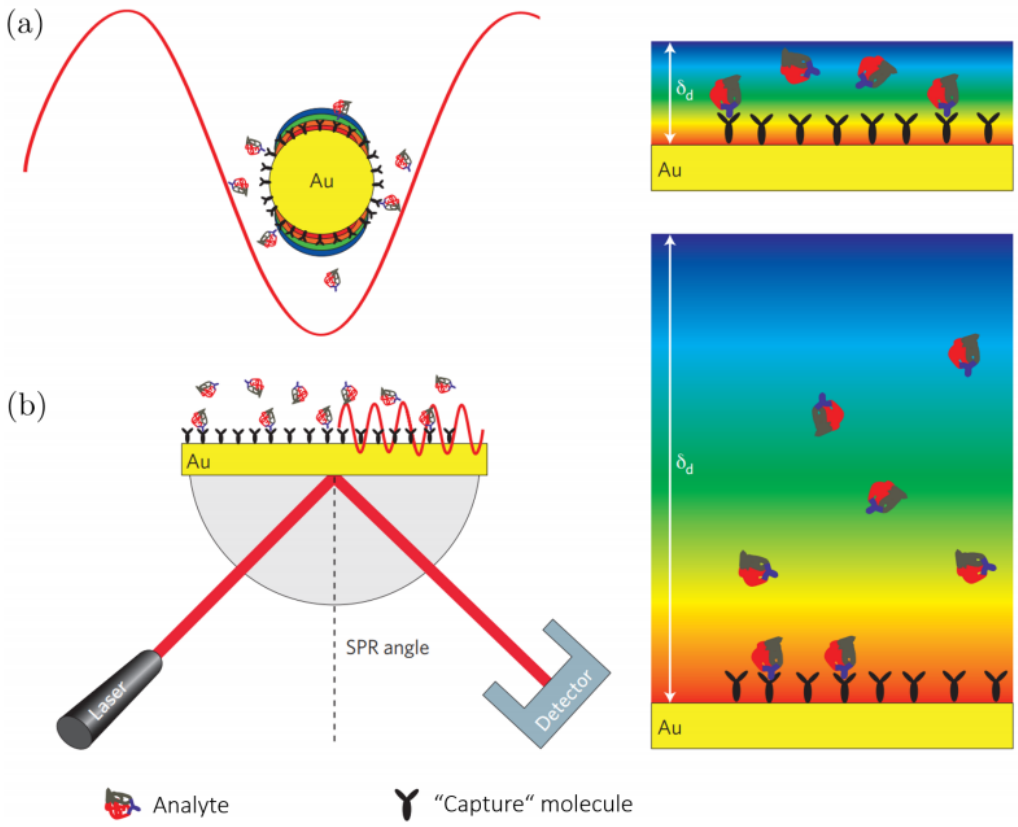

Fig. 2.3: A comparison of biosensors based on (a) LSPR and (b) SPR with characteristic decay length δ_d specifying the regions of the enhanced electromagnetic field. Modified from [110].

lengths [122], or even single wavelength [123]. These are the examples of biosensors based on metasurfaces which are currently intensively studied [124] and used for the detection of cancer markers [125], viruses [126], and microorganisms [127].

As opposed to the nonspecific refractive index sensing, where the biomolecule detection is usually resolved using extinction spectroscopy, the surface-enhanced Raman spectroscopy (SERS) provides highly specific fingerprint spectra of a detected biomolecule [128]. Plasmonic nanoparticles enhance the signal enormously, therefore increasing the detection sensitivity [129], while the analysis can be done even in vivo [130]. Similarly, characteristic IR absorption can be revealed by recording decreases in the reflected signal from IR multi-resonant arrays [131].

The scope of plasmonic biosensors can be broadened utilizing new classes of materials which can introduce real-time tunability using e.g. phase-change materials [132] or even 2D materials like graphene which can achieve tunability in the IR region via electrostatic gating [133, 134]. With constant innovations, the field is aiming to build compact detection systems capable of detecting multiple agents in complex samples advancing the point-of-care diagnostics [135].

2.4 Hot charge carriers

Upon excitation of LSP in metallic NPs, there are two ways for the plasmon to relax – either radiatively by a photon re-emission or non-radiatively by a generation of an electron–hole pair with the LSP energy [136]. These charges can have energies larger than those corresponding to the purely thermal Fermi-Dirac distribution and are often referred to as "hot"carriers [137].

In a noble metal NP, such as AuNP, there are two modes of hot carrier generation, either by an intraband (NP geometry related) or interband (NP material related) process [138, 139]. Lower energy excitations generally result in an intraband excitation of hot electrons above the Fermi level within the sp-band leaving behind a hot hole of about the same average energy below the Fermi level [140]. This behaviour is primarily a result of the so-called Landau damping where the energy transfer to the electron–hole pair is aided by the electron collisions with the surface of the nanoparticle [141]. These hot carriers are generated at the surface which makes their utilization more facile [142]. If the excitation energy is sufficient, the interband excitation can occur from the d-band to the sp-band of the metal leaving behind an energetic hot hole with a lower energy electron close to the Fermi level [143]. By carefully designing the experiment, either type of hot charge carrier can be utilized [144] even simultaneously [145]. Nevertheless, the hot holes generally have shorter lifetimes and mean free paths than hot electrons [146].

The dynamics of hot carrier generation and its relaxation with relevant timescales are summed up in Fig. 2.4(b–e). In the time of 1–100 fs following the Landau damping a highly non-thermal distribution of hot carriers is generated and decays either by photon re-emission or by carrier multiplication via an electron–electron interaction. In the time from 100 fs to 1 ps, hot carriers redistribute their energy by electron–electron scattering reaching the thermal-like (Fermi-Dirac) distribution. At larger timescales the electron–phonon scattering becomes dominant transferring the energy into heat which is then dissipated into the surroundings between 100 ps and 10 ns [147]. These typically undesired energy losses in the form of heat generation can then elevate the local temperature by tens to hundreds of °C [148, 149] which gave rise to a field of thermoplasmonics with a plethora of applications [150].

The energy distribution of the hot carriers is highly dependent on the NP material [151] and can recombine or decay very quickly unless some charge separation strategy is implemented [152, 153]. Two main charge separation strategies are schematically depicted in Fig. 2.5. One strategy is to utilize molecules whose vacant (occupied) energy levels overlap with the energy of hot electrons (holes) which can be transferred to the molecule and participate in its reduction (oxidation) [154]. The remaining charge can then participate in a different reaction or be collected by a sacrificial species to prevent charge buildup [155].

A second common approach is to attach the NP to a semiconductor where the so-called Schottky barrier can form [156]. Only a hot carrier with sufficient energy can

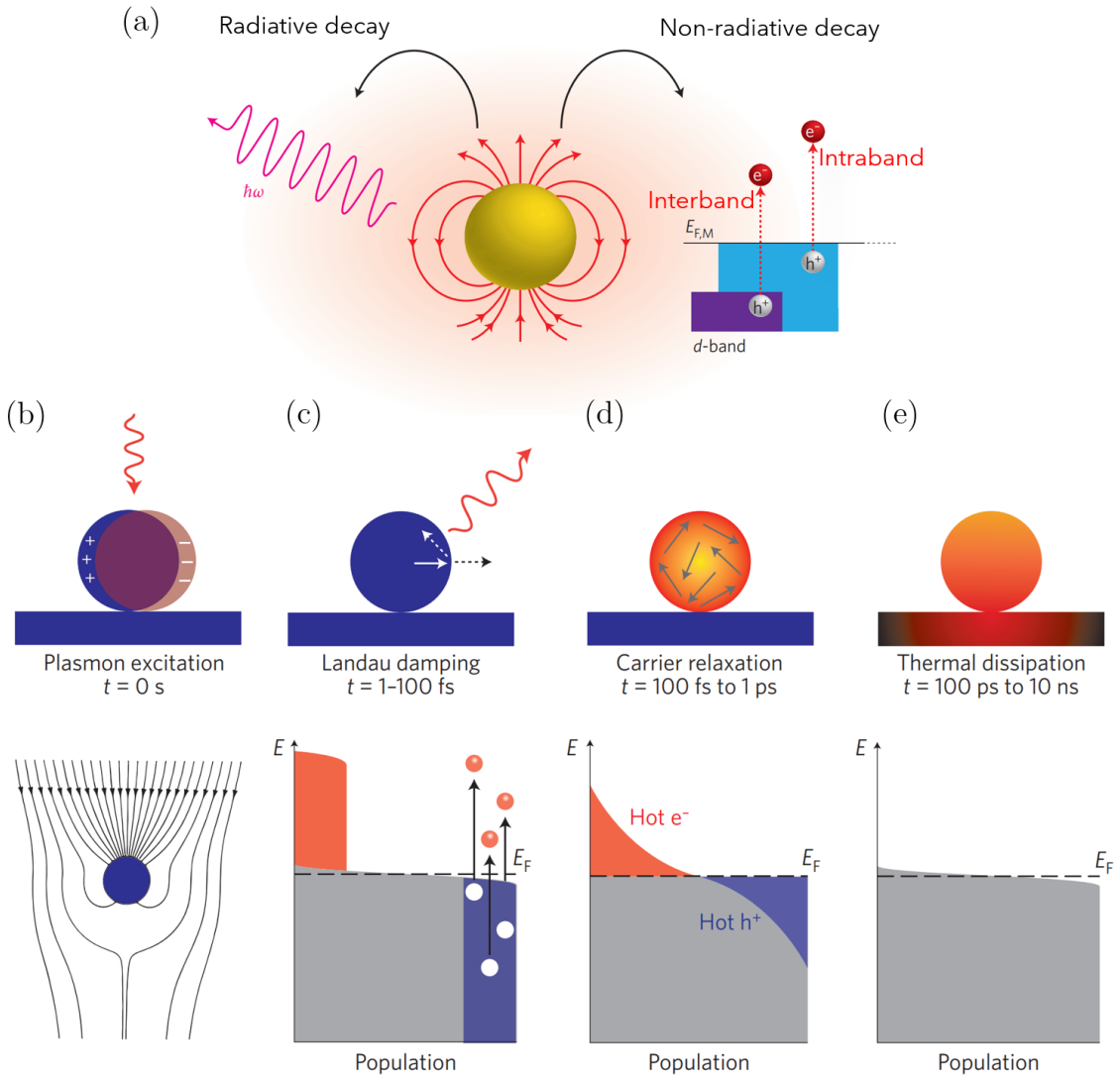

Fig. 2.4: (a) Two pathways of the LSP decay: radiative by a photon emission or non-radiative by an energetic "hot"charge carrier excitation. In noble nanoparticles, e.g., AuNP, energetic charge carriers can be excited above the Fermi level energy $E_{F,M}$ via two different processes - intraband within the conduction sp-band via the Landau damping or interband between the conduction d-band and sp-band. (b–e) LSP laser pulse excitation and relaxation in metallic NP with characteristic timescales. (b) LSP excitation concentrating the flow of light toward the NP. (c–e) Electronic state population shown in grey after the LSP excitation, with hot electrons shown as the red area above the E_F and hot holes in blue below E_F. (a) Modified from [143] (b–e) adapted from [147].

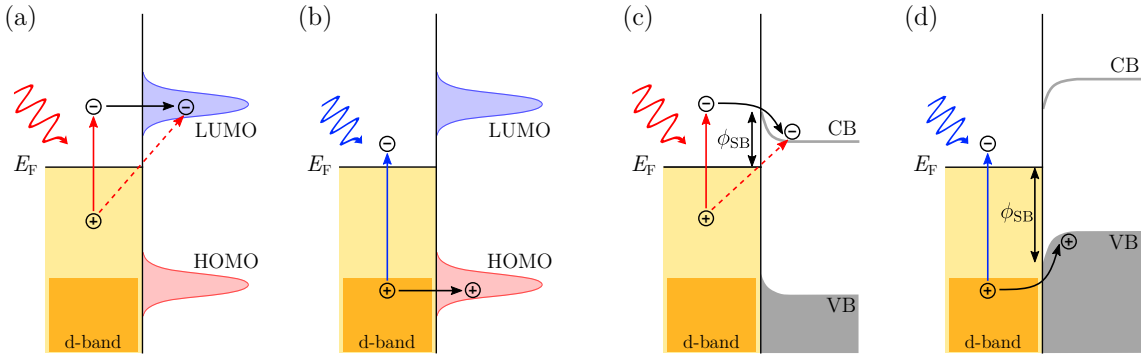

Fig. 2.5: The scheme of the main separation strategies of hot carriers generated in AuNP via (a,b) adsorbed molecules or (c,d) an adjacent semiconductor. (a) Red light (intraband) illumination with hot electron energies overlapping with the lowest unoccupied molecular orbital (LUMO) and (b) blue light (interband) illumination with hot holes overlapping with the highest occupied molecular orbital (HOMO). (c) Red light illumination with hot electrons of larger energy than the Schottky barrier ϕ_{SB} transferring to the vacant conduction band (CB) and (d) blue light illumination with hot holes of larger energy than the Schottky barrier ϕ_{SB} transferring to the occupied valence band (VB). E_F stands for the Fermi level energy. The dashed lines represent a possible direct excitation pathway of hot electrons. Based on [154].

overcome the barrier and move to the semiconductor leaving the other charge behind in the NP [157]. By careful selection of the semiconductor either hot a electron or a hot hole can be extracted [158] which dramatically improves the hot carrier utilization [159]. In these semiconductor–plasmonic NP systems there is an additional effect which can generate charges due to the plasmonic effects called plasmon-induced resonant energy transfer (PIRET) [160]. In this process, a large plasmonic dipole moment couples with the semiconductor and generates electron–hole pairs inside the semiconductor if the LSP energy is larger than the bandgap [161].

The overall photoactivity of the plasmonic nanoparticles and an adjacent semiconductor can be optimized in terms of size, shape, and material to achieve the desired application [162].

The hot charge carriers have been used in numerous applications in photovoltaic devices [163], photodetectors [164], energy storage [165], biosensors [166], and quite extensively in photocatalysis [167, 168, 169] for O_2 and H_2 dissociation [170], water splitting [157], CO_2 reduction, and other reactions [171].

Though the merits of plasmonic NPs in photocatalysis are unquestionable [172], there is lately a lot of debate about the actual contribution of the hot carriers [173, 174] as there are studies explaining the observed phenomena by pure thermal effects [175, 176]. Some studies tried to provide tools to distinguish the hot carrier and thermal effects [177] but more in-depth information about the energy spatial and temporal distribution is needed [178] to achieve competitive and reliable applications [179].

2.5 Other applications

There are plenty of other applications of plasmonics including **energy harvesting**, where metallic [180] and dielectric nanoparticles [181] help converting the solar energy into electron–hole pairs within a solar cell or into chemical energy of neighbouring molecules [182]; in **light generation** applications [183, 184] for enhancing the emission and directionality of light sources [185, 186], enhancing Raman signals [187], helping the generation of higher energy photons via nonlinear effects [188] e.g. in upconversion nanocrystals [189, 190], and also exploring many other quantum effects [191, 192] including the strong light–matter interaction [193]; in **medicine** for diagnostics [194], tumor therapy [195], and theranostics [196]; and in **opto-electronics** for a fabrication of nano-photonic counterparts to electronic circuits [197, 198], potentially revolutionizing the field of computer science [199].

3 PHASE IMAGING OF METASURFACES

The work on this project started during my master's studies, followed during the first two years of my Ph.D. studies and resulted in the publication [200]. The samples were fabricated by Ing. Jiří Babocký, and the phase measurements were done in collaboration with the people from the Experimental biophotonics group of Prof. Radim Chmelík who operated the Coherence-controlled holographic microscope (CCHM), and simulations were done by Dr. Martin Hrtoň. My part was mainly in the phase measurements and the following phase of image processing.

Metasurfaces' functionality stems from an ability to control a phase of transmitted or reflected electromagnetic waves. Thus, it is necessary to quantitatively assess its electric field phase distribution to assess the performance of the metasurface. Such procedures are commonly referred to as quantitative phase imaging methods and several experimental techniques can be utilized: 1) Elipsometry that provides information about the phase-altering properties of the materials [201] but not directly since it requires an inverse analysis. This can become a grave complication when dealing with samples of unknown composition. 2) Scattering-type scanning near-field optical microscopy that acquires the phase information with an exceptional lateral resolution [202] but as a scanning probe method, it is inherently slow. 3) Interferometric optical methods using either broadband continuous light sources [203] or ultra-short laser pulses [204] seem to be the most straightforward option to obtain the phase information. It is retrieved from the interference pattern of the sample and reference beams by employing the Fourier transformation between relevant domains. Nevertheless, the aforementioned interferometric methods suffer from problematic dispersion compensation and provide phase information only from a single spot on the sample surface which hinders their use in metasurface analysis.

We have used a quantitative phase-imaging technique which keeps all the benefits of interferometric methods, provides quantitative phase information from the whole field of view in one shot and thus alleviates the need for scanning. The method is referred to as coherence-controlled holographic microscopy which is based on the principles of off-axis holographic microscopy. It is a real-time technique, limited only by the speed of the CCD camera, providing wide-field phase information in situ, even in diffuse media [205]. The CCHM was developed at our institute by Prof. Chmelík and his group and is now commercially available (Tescan Q-Phase) [206]. The light coming from the source is split into object and reference arms as schematically depicted in Fig. 3.1(a). The light in the object arm interacts with the studied sample and interferes at an angle with the light passing through the reference sample in the identical reference arm. The resulting interference pattern is recorded by the CCD camera. Since the light interferes at an angle (off-axis setup), the consequent Fourier transform of the pattern results in a spatial separation of the phase-containing terms from the amplitude-only ones. This allows an independent extraction of these terms and numerically reconstruct the complex amplitude, i.e.,

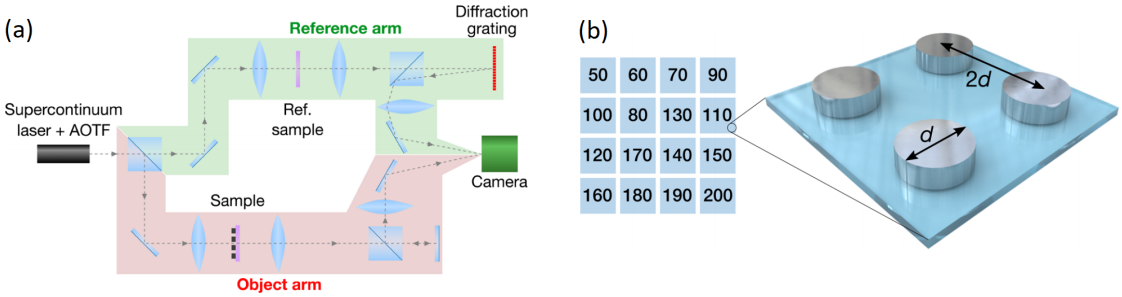

Fig. 3.1: (a) Schematic of the used optical setup consisting of the coherence-controlled holographic microscope (CCHM) coupled with a supercontinuum laser source and an acousto-optic tunable filter (AOTF). (b) The layout of the fabricated benchmark sample formed by the arrays (blue squares $10 \times 10\,\mu m^2$) of silver nanodisc antennas of various diameters from 50 to 200 nm with the height of 40 nm. The diameter d of nanodiscs (in nm) is denoted in each blue square; the pitch of all arrays was fixed to $2d$. Adapted from [200].

both amplitude and phase, of the light wave in every point of the sample [207]. These unique phase-imaging capabilities of CCHM were previously used exclusively in the fast characterization of the living cells based on the phase contrast arising from optical path differences [208]. We utilized the CCHM coupled with a tunable light source (supercontinuum laser Fianium WhiteLase + acousto-optic tunable filter) to perform a spectrally resolved phase imaging of plasmonic nanostructures.

To test the phase imaging capability of our setup on the plasmonic nanoantennas, we fabricated a benchmark sample [Fig. 3.1b] by EBL. The EBL was done using the PMMA resist (140 nm) and conductive polymer coating to reduce charging. After the resist development, 3 nm of a Ti adhesion layer and 40 nm of an Ag thin film were deposited by electron beam evaporation. Finally, the lift-off process was done in acetone. The sample consists of 16 $10 \times 10\,\mu m^2$ arrays, each formed by silver nanodisc antennas of different diameters d, ranging from 50 to 200 nm, with pitch fixed to $2d$ to have roughly the same antenna coverage ($\approx 20\%$) for each array. The nanodisc shape was chosen to obtain a polarization-independent dipole response.

The SEM analysis revealed that the real diameters of the nanodiscs were generally slightly larger (by about 4 nm) than the designed diameters. Additionally, the smallest nanodiscs of 50 and 60 nm were not fabricated successfully and were therefore excluded from the following analysis. Firstly, the optical properties of each array were tested employing extinction spectroscopy to verify their plasmonic activity. The extinction spectra were calculated as $1 - T/T_{\mathrm{REF}}$, where T represents the signal transmitted through the nanodisc array and T_{REF} the signal transmitted through the bare glass substrate. The resulting spectra in Fig. 3.2(a) show one strong peak corresponding to the dipole plasmon mode for each array. The position of the peak shifts to longer wavelengths with the increasing nanodisc diameter. The experimental spectra showed a reasonable agreement with the simulated spectra ob-

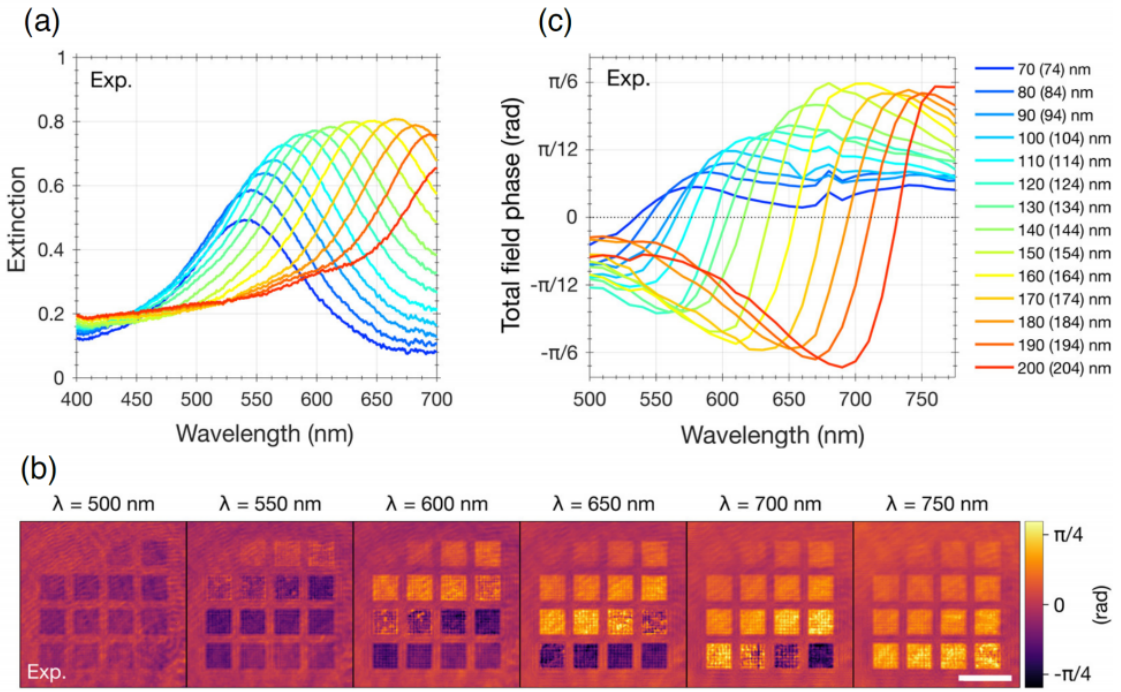

Fig. 3.2: (a) Extinction spectra of the fabricated silver nanodisc arrays on glass. The extinction has been calculated as $1 - T/T_{REF}$, where T and T_{REF} represent the signal transmitted through the nanodisc array and through the bare glass substrate, respectively. (b) Quantitative phase images of the same nanodisc arrays at a selected subset of illumination wavelengths acquired using CCHM. Scale bar corresponds to 20 µm. (c) Spectra of the total field phase at nanodisc arrays of various diameters extracted from the full set of measured CCHM images. Adapted from [200].

tained from a commercial finite-difference time-domain (FDTD) solver Lumerical FDTD Solutions (not shown here) done using periodic boundary conditions.

Next, we used the CCHM setup to record a series of the amplitude and phase images in the sample plane, while we changed the illumination wavelength in 10 nm steps throughout the whole accessible wavelength range of the CCHM (450–780 nm). The resulting phase distribution images are shown in Fig. 3.2(b) for a few selected illumination wavelengths. One can see that a rapid phase flip occurs and moves towards the arrays with larger nanodiscs, which have a resonance at longer wavelengths, as we illuminate the sample with longer wavelengths. To clarify and quantify the information from the phase-distribution images, we extracted the average phase value from every nanodisc array for each of the illumination wavelengths while we compensated for the small background by subtracting the phase outside the arrays [see Fig. 3.2(c)]. The phase extracted from CCHM exhibits an S-shaped flip from the negative phase for the wavelengths below the resonance to the positive phase for the wavelengths above the resonance with the zero-value crossing at the resonance wavelength. Additionally, the phase tends to approach a zero value in both regions far from resonance. Note, that we labelled the extracted phase information as the

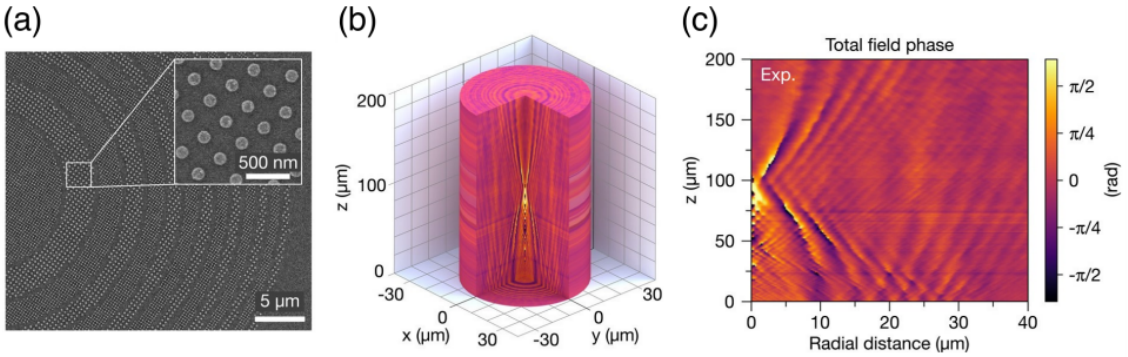

Fig. 3.3: (a) SEM micrograph of the fabricated focusing plasmonic metasurface where the individual zones are formed by silver nanodiscs (130 and 190 nm). (b) 3D visualization of the measured total phase distribution in the half-space above the plasmonic zone plate. (c) Measured phase maps in the xz-plane above the zone plate where the main ($z \approx 100\,\mu$m) and subsidiary ($z \approx 50\,\mu$m, $z \approx 25\,\mu$m) focal points are distinguishable close to the zero radial distance. Adapted from [200].

total field phase because it is given by the superposition of the scattered field from the nanodisc antennas and the driving field from the illumination. The information from the CCHM is therefore highly dependent on the respective amplitudes and phases of both fields. This assumption together with a theoretical description of CCHM image formation allowed us to complement the experimental data with the calculated ones with a very good agreement [200].

Since we were able to visualize the total phase from the plain nanodisc arrays we moved to the analysis of an actual metasurface. We designed a focusing metasurface based on a principle of zone plate [209]. The initial idea was developed by Soret [210] who realized the focusing zone plate by alternating transparent and opaque annuli. A more efficient variant was realized by Wood [211] who substituted the opaque annuli with a transparent material causing the π phase shift. We fabricated a zone plate with a focal point in $z = 100\,\mu$m for the 630 nm operational wavelength which is in the middle of our experimental range. The individual annuli in Fig. 3.3(a) were filled with nanodisc antennas whose phase response we obtained from our benchmark measurements. We chose those with diameters of 130 and 190 nm which maximized the phase difference at the operation wavelength reaching approximately $\pi/5$ [Fig. 3.2(c)]. Although the phase difference between the neighbouring annuli is significantly smaller than the prescribed π, the focusing capability of our metasurface is still satisfactory.

Using the precise sample positioning in the CCHM we were then able to record a 3D phase information behind the focusing metasurface by z-stacking phase images taken at different defocus levels. The quantitative phase images were recorded from the sample plane up to 200 µm with 1 µm step resulting in a 3D phase map of wavefronts propagating from the metasurface [Fig. 3.3(b)]. The cross-section in the xz-plane, shown in Fig. 3.3(c), displays the stripes of constant phase originating at

the sample plane converging into the main focal point at $z \approx 100\,\mu\text{m}$ according to the design. Nevertheless, the subsidiary focal points at $z \approx 50\,\mu\text{m}$ and $z \approx 25\,\mu\text{m}$ do not correspond to those of an ideal zone plate. For example, the secondary focal point should occur at one third not at one half of the zone plate focal length. This discrepancy can be explained by the differences between the design, where the phase change between zones is abrupt, and the actual sample, where the phase change is gradual which makes the zones effectively narrower. The xz-plane phase distribution was again very well reproduced by numerical simulations including the position of the subsidiary focal points.

In conclusion, we have demonstrated that CCHM represents a suitable option for optical characterization of plasmonic metasurfaces. It can provide spatially resolved quantitative phase information in the whole field of view at relatively short time scales and thus has the potential to become a versatile tool in metasurface research [212].

4 TUNABLE PLASMONIC NANOSTRUCTURES

As mentioned in chapter 2.2 , metasurfaces were originally based almost exclusively on nanostructures made of noble metals. However, the recent pursuit of metasurfaces with improved efficiency and reduced losses brought into focus alternative materials [213], typically the dielectrics [214]. Some of them also provide additional functionalities such as tunable optical properties [215, 216] which can help tackle the rigidity of static metasurface and thus open a new range of applications [217, 218]. One approach to introduce the tunability is utilization of phase-change materials represented primarily by germanium antimony telluride (GST) [219], antimony trisulphide (Sb_2S_3) [220], and vanadium dioxide (VO_2) [221], which can undergo substantial transformation of optical properties upon external stimuli.

The phase-change materials have found use in active metasurface components used for optical modulation [222], high absorption [223], beam steering [224], focusing [91], polarization selection [225], or for switching between modes in Mie resonators [226].

Tunable metasurfaces incorporating phase-change materials generally follow two lines of design – either a fabrication of nanoantennas on the layer of the phase-change material which then indirectly influences the optical response of the nanoantennas above [227, 228, 229], or via nanostructuring the phase-change material itself [230, 231, 232]. Creating a large-scale tunable metasurface remains a challenge since it generally requires the utilization of advanced nanofabrication methods.

In the rest of the chapter, we focus specifically on VO_2 as a means to achieve tunable plasmonic nanostructures for metasurfaces. A big part of this work was done during my research stay at The Hong Kong Polytechnic University in 2017 with collaborators from the Vanderbilt University and The University of Alabama (USA) and part of the work was published in [233].

4.1 Vanadium dioxide

Vanadium dioxide is a strongly correlated material from a large group of vanadium oxides, many of which undergo metal-insulator phase transition (MIT)[1]. The MIT is accompanied by abrupt changes in optical, electrical, thermal, and magnetic properties [234]. VO_2 is studied most extensively because the MIT occurs rather close to the room temperature with critical temperature $T_C \sim 340\,\mathrm{K}$ ($67\,^\circ\mathrm{C}$) [235] and can find applications in infrared detection [236], electronic devices [237], smart coatings [238], actuators [239] etc. [240].

At room temperature, VO_2 atoms are organized into the monoclinic crystal structure (M1 phase) and the crystal exhibits insulating properties. At temperatures above the T_C, where the MIT occurs, the crystal structure reorganizes into the

[1]The reversed process, i.e., the insulator-metal transition is abbreviated as IMT and both IMT and MIT are used interchangeably to refer to the phase transition process.

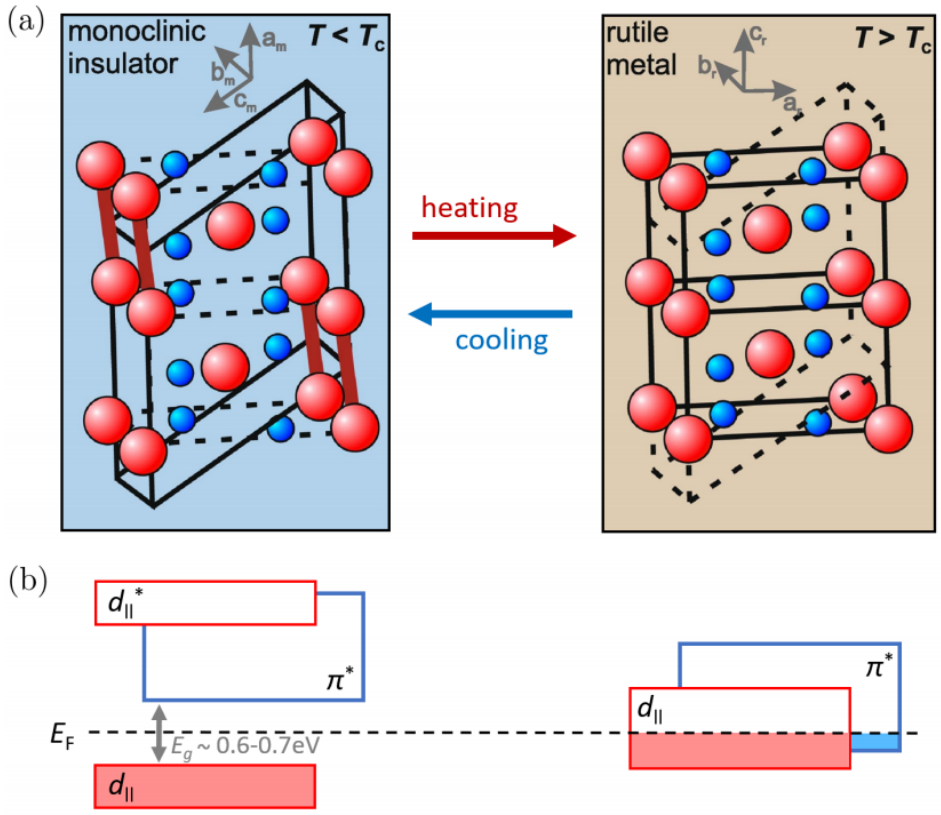

Fig. 4.1: (a) Comparison of VO_2 crystal structures corresponding to (left) the insulating monoclinic structure for temperatures below T_C and (right) the metallic rutile structure for temperatures above T_C. The red balls represent vanadium atoms, blue balls oxygen atoms and thick red lines highlight zigzag V-V dimers Modified from [242]. (b) Schematic representation of VO_2 electronic band structures near the Fermi level E_F for the respective crystallinities. Filled regions represent occupied states below the E_F. Simplified from [243, 244].

rutile (R phase) structure attaining metallic behaviour [241]. The crystal structures and electronic band structures of the two main phases are summed in Fig. 4.1.

The crystal structure of the high-temperature rutile phase VO_2(R) is defined by the unit cell parameters $a = b = 0.455\,\text{nm}$, and $c = 0.285\,\text{nm}$, where V^{4+} ions reside in the body centre and at vertex points and these are surrounded by 6 O^{2-} ions [245]. The low temperature monoclinic phase VO_2(M1) is characterized by $a = 0.575\,\text{nm}$, $b = 0.454\,\text{nm}$, $c = 0.538\,\text{nm}$, and $\beta = 122.6°$ [246]. Upon the MIT, V atoms deviate from the initial vertex positions and the highly symmetric rutile structure becomes a low-symmetry monoclinic structure with two different V–V bond lengths. The d-electrons in each V atom become localized due to the V–V dimer formation which in turn leads to the occurrence of insulating VO_2 properties [234].

The structural changes are accompanied by dramatic changes in the electron band structure. In the rutile phase, the Fermi level crosses the overlapping π^* and

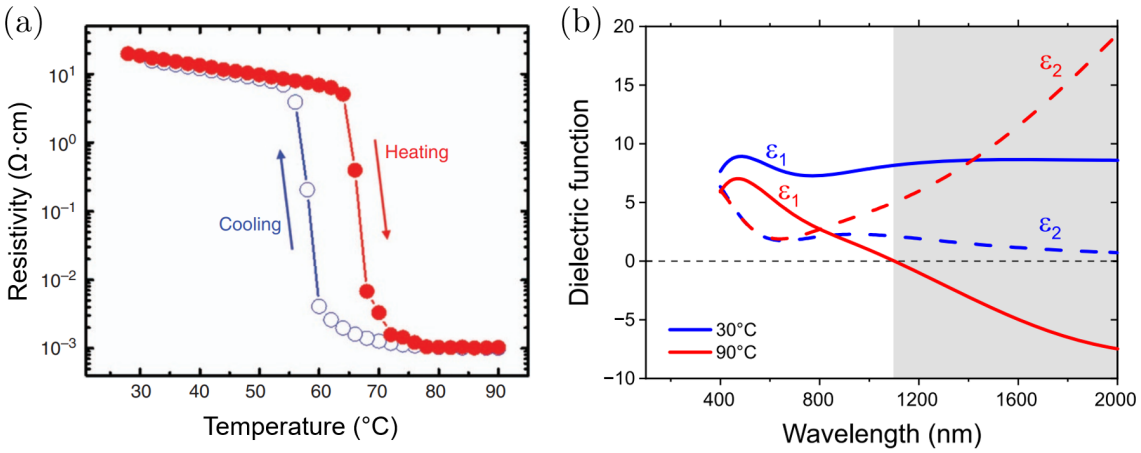

Fig. 4.2: (a) Typical VO_2 resistivity dependence on temperature during heating/-cooling cycle. Modified from [254]. (b) Dielectric functions of low temperature (insulating) and high temperature (metallic) VO_2 phases. The grey area highlights a wavelength region with a truly metallic character where $\varepsilon < 0$. Adapted from [45].

$d_{||}$ bands which is a signature of a metallic behaviour. In the monoclinic phase, the $d_{||}$-band splits in two – a lower-energy filled bonding $d_{||}$ band and higher-energy empty antibonding $d^*_{||}$. Concurrently, an empty antibonding band π^* shifts upwards resulting in a forbidden gap opening of about $0.6 - 0.7\,\mathrm{eV}$ [243].

The exact mechanism of the MIT has been debated for a long time but is still not completely resolved [247]. One possible mechanism is referred to as the Peierls MIT, where the MIT occurs based on structural changes in the lattice, i.e., by electron-phonon interaction. The lattice is deformed due to these changes and the V–V dimers form which results in the modification of ionic potentials in the material and consequently changes in the band structure [248]. The second mechanism, referred to as Mott-Hubbard MIT, explains the MIT in terms of electron correlation (electron–electron Coulomb interaction) between the conduction electrons possibly leading to their localization and an occurrence of insulating properties [249].

Additionally, other insulating phases (M2, M3, T) can exist under certain stress and temperature conditions [250, 251] which complicate the understanding of the nature of the MIT and changes in the respective electronic and structural properties [252]. Nevertheless, evidence was found for both the electron–electron interactions and electron–phonon interactions caused by lattice distortions, thus both mechanisms probably play a role [253].

As shown in Fig. 4.2, the actual MIT in VO_2 is accompanied by over four orders of magnitude change in resistivity which is reversible with characteristic hysteresis [254]. Regarding the optical properties, the difference between the two states is profound [45]. At room temperature, it behaves as a typical dielectric while above the T_C the metallic behaviour is indicated by the real part of the dielectric function becoming negative at wavelengths above about 1100 nm. This contrast predestines

VO_2 for a wide range of applications, especially in the IR region, where the contrast is the largest.

In terms of fabrication, VO_2 thin films can be prepared using a large number of methods including sputtering [255], evaporation [256], pulsed-laser deposition [257], chemical vapour deposition [258], sol-gel methods [259], and also other technologies like epitaxial growth providing nanowires and nanoparticles [260] or chemically [261], leading to monocrystals exhibiting improved properties [262].

Since some applications require different temperature ranges, the substitutional elemental doping with various elements was explored to adjust the critical temperature T_C. It can be lowered utilizing hexavalent/pentavalent metal ions like W, Mo, Nb, and Re [263], or increased by smaller trivalent ions like Al, Ga, and Cr [264]. Although the thermal transition is inherently slow [265], it can be substituted by significantly faster optical [266] and electronic excitations [267].

4.2 Dielectric metasurface based on VO_2

We developed a novel form of tunable plasmonic metasurface based on epitaxial vanadium dioxide (VO_2) nanobeams (prepared by Kannastassen Appavoo formerly from Vanderbilt University, now The University of Alabama). The main benefit of our approach is the preparation method which is based on self-limiting growth of VO_2 nanobeams using the pulsed-laser deposition. This single preparation step results in a large sample area covered by anisotropic nanostructures of VO_2, thus omitting the time-consuming lithographic procedures.

The anisotropy of our VO_2 is apparently induced by the mismatch in crystal lattice parameters of a substrate, i.e., a-cut sapphire $(11\bar{2}0)$, and VO_2 (100) which corresponds to around 35% along the x-axis and -5% along the y-axis in the RT phase of VO_2. Although 35% is a large mismatch between single unit cells, employing the domain matching epitaxy [268] integer multiples of the unit cells can be matched and result in a significantly smaller mismatch of about 3% which is smaller than -5% in the y-axis [269]. Such mismatches indicate an in-plane lattice strain that results in the preferential growth direction along the x-axis, i.e., [0001] of the sapphire.

The VO_2 film was prepared by a sputtering of a high-purity vanadium metal target using a pulsed excimer laser beam at a background oxygen pressure of 50 mTorr onto the a-cut face of a sapphire substrate which was held at 500 °C. The deposition procedure resulted in strongly anisotropic morphology of the thin VO_2 film which was evaluated using scanning electron microscopy (SEM, FEI Verios) and by atomic force microscopy (AFM, Bruker Dimension Icon – with the help of Martin Konečný).

The results of the structural analysis, depicted in Fig. 4.3, reveal a polycrystalline layer formed by monocrystalline nanobeams 100–200 nm wide, 1–2 μm long, and about 40 nm high. The AFM depth profile also highlights the closely packed nature of our nanobeams, suggesting self-limited growth. The crystal orientation of the nanobeams with respect to the sapphire substrate was identified by room-temperature

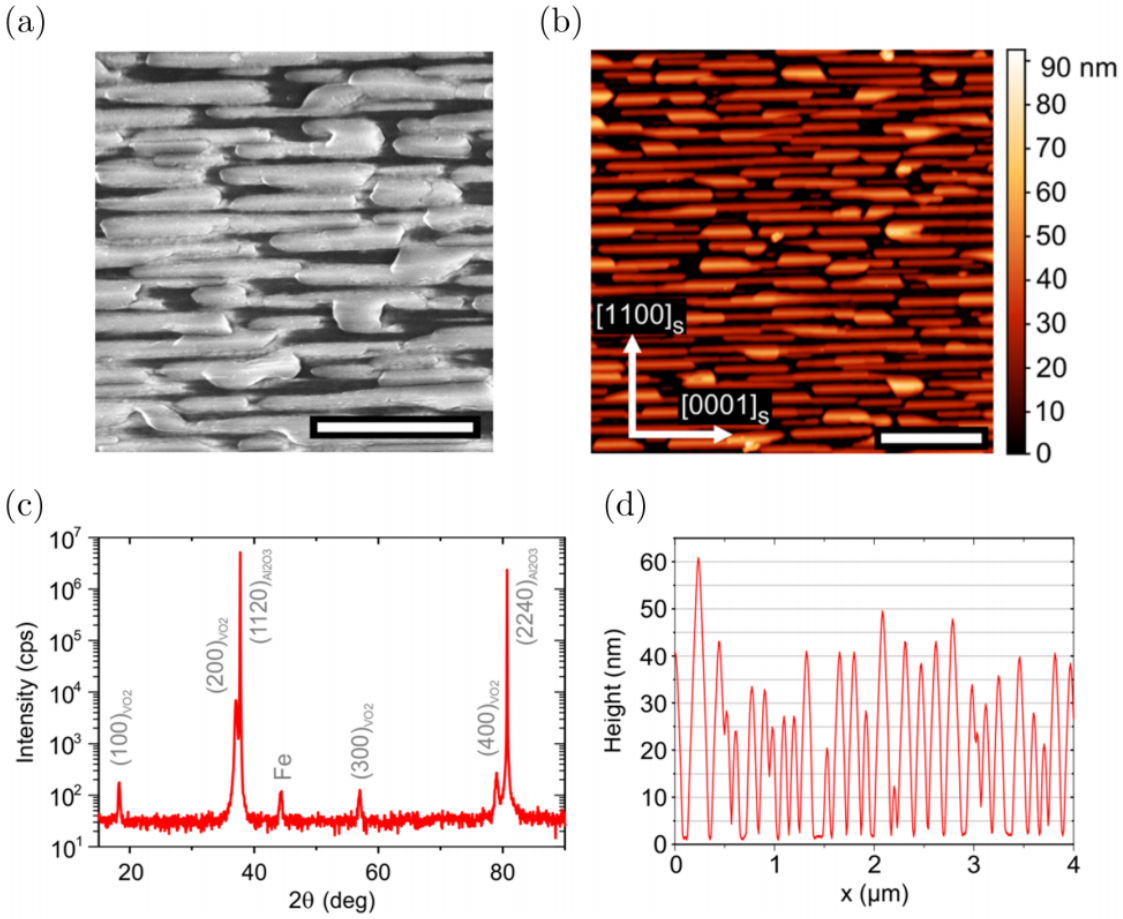

Fig. 4.3: (a) SEM and (b) AFM micrographs of the epitaxial VO_2 metasurface with a typical (d) AFM profile measured across the VO_2 nanobeams. The scale bars are 0.5 and 1 μm, respectively. (c) A room-temperature XRD spectrum of the VO_2 sample on a-cut sapphire substrate with diffraction peaks ascribed to the characteristic diffraction directions. Note that the iron peak comes from the sample stage. Adapted from [233].

X-ray diffraction (XRD, Rigaku Smartlab – with the help of Ondřej Caha).

The conventional $\theta - 2\theta$ scan, shown in the Fig. 4.3(c), proved that the preferred orientation of VO_2 on a-cut sapphire is (200). A small iron peak around 45 ° comes from the X-ray beam hitting the sample stage.

To specify the effect of the phase transition on the optical transmission through our anisotropic VO_2 sample, we utilized a halogen fiber-coupled light source for illumination and InGaAs for detection. The transmitted light signal was integrated over the NIR range to obtain a broadband unpolarized light transmission while sweeping the sample temperature. The results in Fig. 4.4(a) show that the epitaxial VO_2 layer (red curve) exhibits a sharp drop in transmittance around 65 °C with the hysteresis width only $\Delta T = 4\,°C$. In contrast, the reference hysteresis corresponding to a typical polycrystalline thin VO_2 film (grey curve) has a width of $\Delta T = 15\,°C$ which

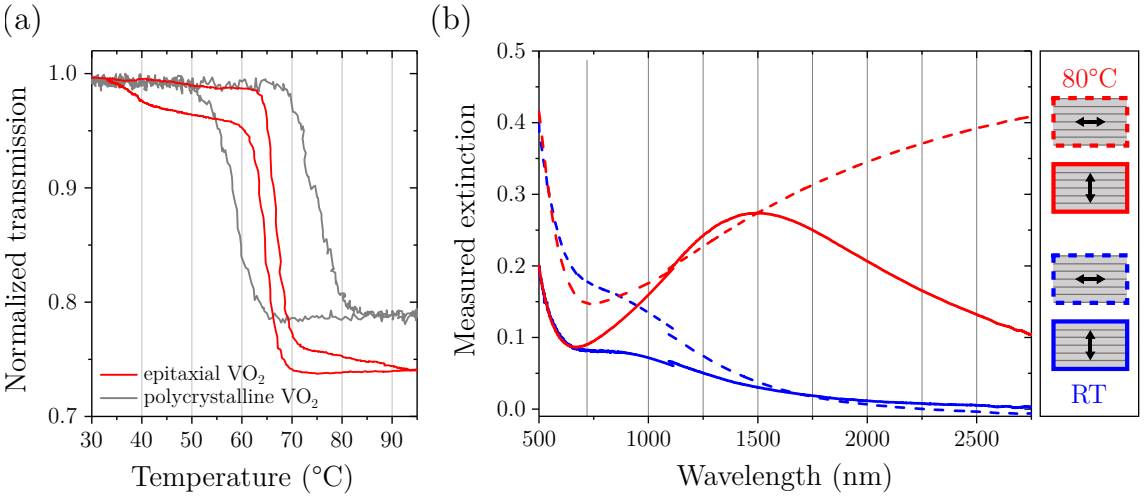

Fig. 4.4: (a) Measured broadband transmission hysteresis of an epitaxial (red) and a polycrystalline (grey) VO_2 film. The data are normalized to a maximum transmission (at room temperature). (b) Measured extinction spectra of the VO_2 metasurface sample at room (RT, blue) and elevated (80 °C, red) temperature which corresponds to insulating and metallic state, respectively. Spectra were acquired for two polarizations of incident light – along (dashed lines) and across (solid lines) the nanobeams. Note that the discontinuity around 1100 nm is due to the different measurement configurations used for the VIS/NIR and MIR regions. Adapted from [233].

evidently demonstrates the quality of epitaxial VO_2 and indicates the substantially reduced density of structural defects [270].

Spectrally-resolved optical properties of the fabricated VO_2 metasurface were evaluated by polarized Fourier-transform infrared spectroscopy (FTIR, Bruker Vertex 80V + Hyperion 3000). The extinction spectra in Fig. 4.4(b) were calculated as $1 - T/T_{\mathrm{REF}}$, where T is a transmission through the VO_2 nanobeams and T_{REF} is a transmission through the bare sapphire substrate. They are a result of stitching two spectra together which were obtained with different measurement configurations in the VIS/NIR (tungsten lamp, CaF_2 beamsplitter, silicon detector) and MIR (Globar light source, KBr beamsplitter, nitrogen-cooled MCT detector) regions. The measured extinction spectra are presented for both insulating (RT) and metallic (80 °C) VO_2 with incident light polarization parallel and perpendicular to the nanobeam long axis with unpolarized detection. At the RT, the dielectric nature of VO_2 assures high transmittance ($> 80\,\%$) throughout the whole infrared spectral region (from 700 mn to 3 µm) with observable effects of VO_2 nanobeams anisotropy mostly in the VIS/NIR spectral region.

At the elevated temperature, after the VO_2 undergoes insulator-to-metal transition (IMT), the spectra exhibit very different features for both polarizations. For the polarization parallel with the nanobeam's long axis the extinction in the infrared rises gradually, similarly to that observed for conventional isotropic thin films of metallic VO_2 [271]. Nevertheless, for the light polarized perpendicular to the na-

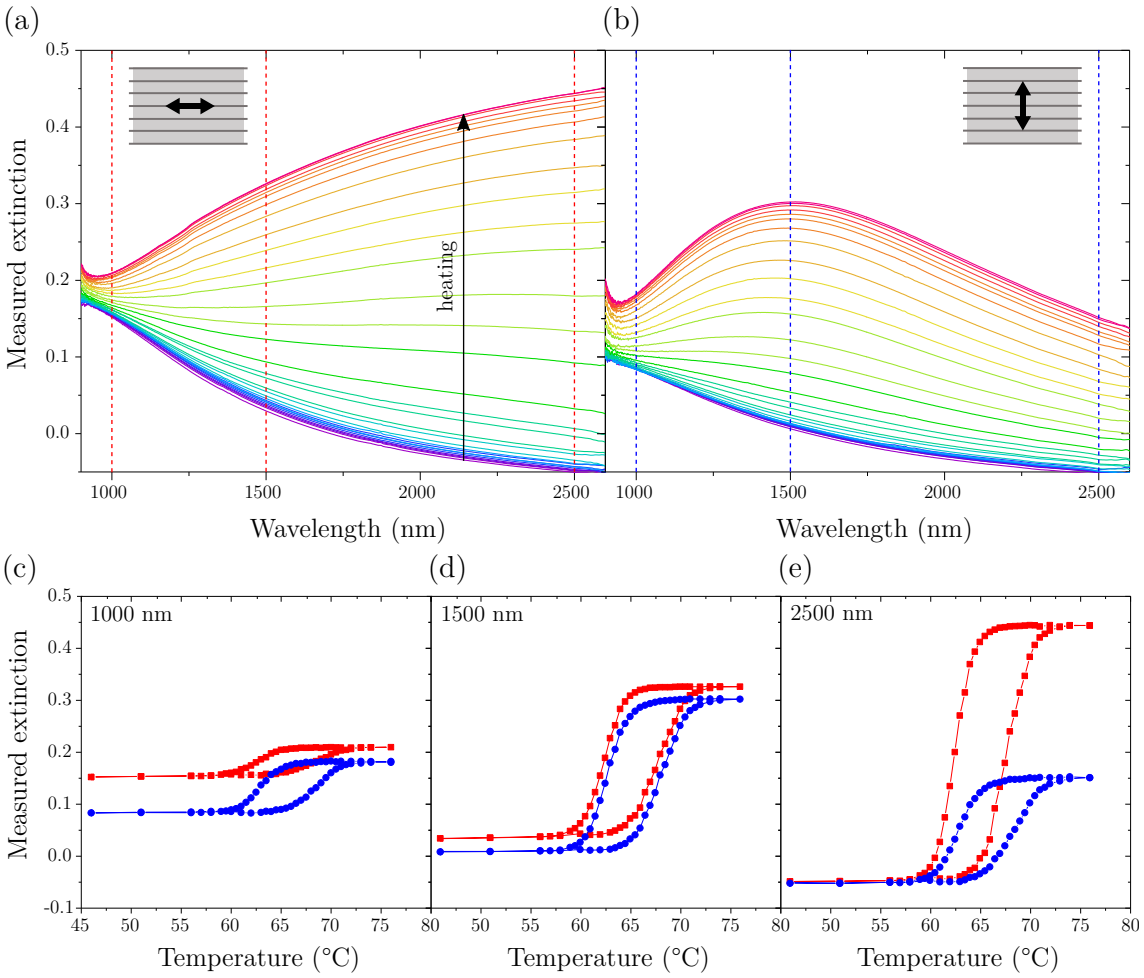

Fig. 4.5: Temperature dependent NIR/MIR extinction spectra of the VO_2 metasurface obtained with the incident light polarization (a) parallel and (b) perpendicular to the nanobeams during the heating from room temperature to 76 °C. The vertical dashed lines highlight the cross-sections through the spectra for selected wavelengths and their colour corresponds to the colour of the hysteresis curves below. The extinction variation with temperature during a full cycle going from RT to 76 °C and back to RT at specific wavelengths: (c) 1000 nm, (d) 1500 nm, and (e) 2500 nm recorded for a polarization parallel (red) and perpendicular (blue) to the nanobeams.

nobeams, we observe a distinctive peak centred around 1480 nm that we ascribe to the localized surface plasmon resonance. This is caused by the electron confinement inside the metallic nanostructures that were grown epitaxially in a self-limiting process without any lithographic steps. The lateral size of the nanobeams determines the wavelength of the extinction peak. This is also a region of maximum extinction contrast between the insulating and metallic phase of VO_2 which overlaps with the standard telecom wavelength bands (1260–1675 nm) [272]. This can be quantified by the reversible modulation depth [273] calculated from experimental data as $10\log(I_{80°C}/I_{RT})$, where $I_{80°C}$ and I_{RT} represent extinction measured at 80°C and at room temperature, respectively. The modulation depth is greater than 9 dB across the whole set of standard telecom wavelength bands. Even though our metasurface is structurally anisotropic, it exhibits only a weak polarization dependence in this spectral region and around 1.5 µm wavelength it is basically isotropic. Such a high extinction contrast and broad bandwidth are very desirable in light modulation devices, as they can provide high signal-transmission capacity, improved resistance to noise, and longer achievable distances [274].

Although the external heating is an inherently slow stimulus, there are reports about the phase transition in VO_2 being induced by an application of a strong electric field [275] or optical pulses on ultrafast timescales [276]. Additionally, the extinction anisotropy at wavelengths above 1.5 µm provides another light-modulating capability of our metasurface. While in the insulating state in this region, the layer acts almost completely isotropic, the extinction ratio of light polarized along (parallel) and across (perpendicular) the metallic VO_2 nanobeams gradually increases. This behavior can bring an extra degree of freedom, i.e., polarization of incident light which can serve as an additional modulation channel on top of the IMT-based switching.

A more detailed view of the infrared extinction dependence on the incident light polarization of our metasurface as it undergoes the IMT is shown in Fig. 4.5(a,b) as the temperature was increased step-wise from the RT to 76 °C. Changes in the extinction start to appear around 64 °C and stabilize around 73 °C. The cross-sections extracted from the spectra, shown in Fig. 4.5(c,d,e), highlight the extinction contrast through the IMT for both polarizations, with perpendicular being higher at 1000 nm, parallel at 2500 nm, while at 1500 nm the contrast is the same.

To verify the plasmonic nature of our sample's functionality and to get more insight into the relationship between metasurface morphology and its optical properties, we performed numerical simulations using Lumerical FDTD Solutions (done by Uddhab Tiwari from The University of Alabama). To reproduce the experimental extinction spectra, we created a model corresponding to the measured morphology. Namely, we arranged VO_2 nanobeams with the length of 1.3 µm, width 96 nm and height 28 nm into an array with a constant inter-rod spacing of 48 nm and random offset along the anisotropy axis with the dielectric function of VO_2 taken from Ref. [277]. Despite small discrepancies, the simulated extinction [Figure 4.6(a)] shows an

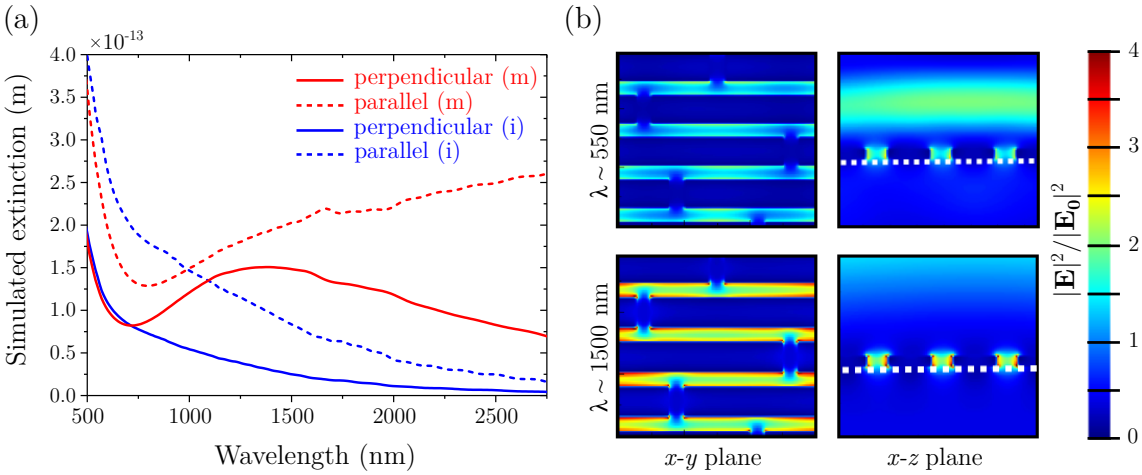

Fig. 4.6: (a) Calculated extinction spectra for VO_2 nanobeams with an insulating (i) and metallic (m) dielectric function for incident polarization parallel and perpendicular to their longitudinal anisotropy axis. Nanobeams were 96 nm wide, 28 nm high, 1.3 µm long, and were arranged into an array with a constant inter-rod spacing in both x- and y-directions (48 nm) and random offset along the anisotropy y-axis. (b) Calculated in-plane and out-of-plane distribution of electric field enhancement in VO_2 nanobeams for two representative illumination wavelengths. Adapted from [233].

excellent agreement with the experimentally obtained spectra. Figure 4.6(b) displays in-plane and out-of-plane maps of electric field enhancement within the simulated metallic VO_2 geometry for two representative illumination wavelengths. It signifies the plasmon dipole mode induced in the transverse direction of metallic nanobeams enhancing the electric field by about 4x. Consecutive simulations (not shown here) also confirmed that by varying the nanobeam width and height it is possible to move the position of the plasmon resonance peak to access new functionalities [233].

Similar to light transmission modulation via material absorption which is primarily related to the imaginary part of the dielectric function, modulation of the phase of transmitted light, governed by the real part of the dielectric function, is also possible. VO_2 nanobeams as sub-wavelength elements of our metasurface As the VO_2 undergoes a significant shift in both the real and imaginary part of the dielectric function upon the phase change, a similar modulation can be expected in both the amplitude and phase of the transmitted light [278]. To demonstrate this behaviour even in our metasurface, we fixed the angle of the incident light to 45° with respect to the nanobeams and the extinction was measured behind an additional polarizer, serving as an analyzer. Such a setup ensures equal light intensity for both principal polarizations – parallel and perpendicular to the VO_2 nanobeams. The anisotropy of the sample results in a different phase acquired for both polarizations, thus the initially linear polarization is transformed into an elliptical one. Since the testing wavelength of the light was chosen as 1500 nm, where the metasurface behaves basically isotropically in terms of the transmitted light amplitude

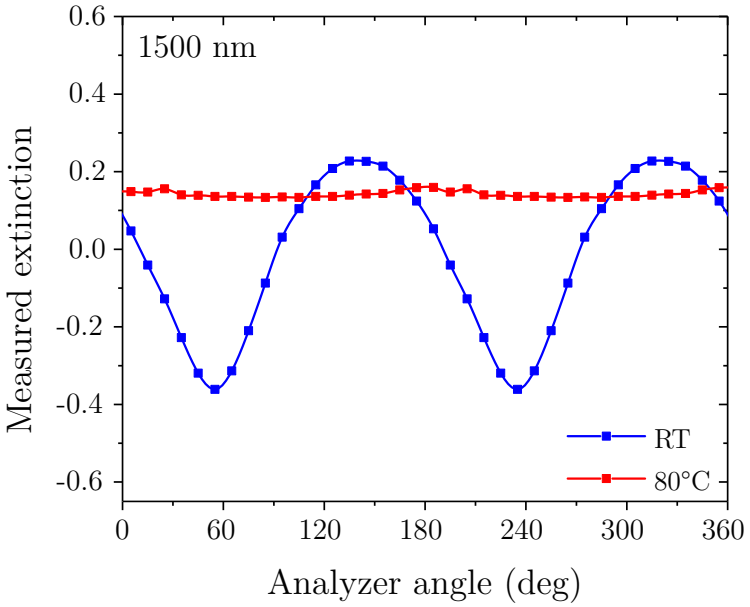

Fig. 4.7: Extinction of the epitaxial VO_2 metasurface for incident linearly polarized light with 45 ° angle with respect to the nanobeams measured as a function of analyser angle (0 ° is parallel to the nanobeams). The results are shown for the insulating (RT, in blue) and metallic (80 °C, in red) phase at 1500 nm. Note that the data from 180° to 360° are a copy of the data from 0 ° to 180 °. Additionally, the extinction, as defined in this work, can be negative or larger than one when measured with the combined polarizer and analyzer.

at both the RT and 80 °C [see Fig. 4.4(a)], the sole effect of the light phase shift is manifested. The dependence of the extinction on the analyzer angle for insulating and metallic state is shown in Fig. 4.7.

The resulting curve corresponding to the VO_2 metasurface at RT exhibits a strong oscillation in extinction with changing the analyzer angle. In this regime, the metasurface behaves as a simple attenuator with intensity oscillations according to Malus's law. Nevertheless, after the transition to the metallic state, the behaviour changes dramatically. The transmitted intensity is basically independent on the analyzer angle indicating the circular polarization after going through the sample. The metasurface at 80 °C behaves like a quarter-wave plate, turning the linear polarization into a circular one.

Alongside the intensity modulation mentioned previously, phase modulation can serve as an additional degree of freedom in optical applications. Our sample can thus serve as a multifunctional optical device controlling the transmitted light in both the amplitude and the phase.

4.3 VO_2 as a tunable substrate for gold antennas

The previous section showed VO_2 as a material which can be used to construct purely dielectric metasurfaces, utilizing the plasmonic properties in the infrared region [279] and, possibly, in the visible region thanks to Mie resonances [45]. Another approach dwells in using the VO_2 as a base substrate for either conventional metallic nanostructures [280] or dielectric ones too [281]. In the majority of cases, the underlying VO_2 substrate is formed by randomly oriented crystals in a polycrystalline layer [282] which can be considered isotropic. Nevertheless, as opposed to single domain VO_2 where the transition can occur instantaneously [283], the presence of multiple grains causes the phase transition to occur gradually with some regions already metallic while other still dielectric as revealed by scattering near-field infrared spectroscopy [284]. Plasmonic properties of antennas on top of such mixed phases strongly reflect the underlying phases in the polycrystalline layers [285, 286]. Thus, the nanorod orientation with respect to the substrate does not play any role in its properties.

Here, instead of a layer with randomly oriented grains, we have used the anisotropic VO_2 metasurface, formed by aligned epitaxial VO_2 nanobeams, described previously. The goal of this project was to observe the effect of the VO_2 substrate anisotropy on the plasmon resonance of the overlaying gold nanorods (AuNR). EBL was used to fabricate plasmonic AuNR antenna arrays onto the anisotropic VO_2. The length of the AuNR was set to 220 nm, the width to 55 nm, and their thickness was 20 nm. The AuNRs were arranged into 100 µm square arrays with a pitch of 600 nm in both directions which were surrounded by 100 µm of bare VO_2 in every direction.

Two arrays of AuNRs with two principal orientations with respect to the long axis of the VO_2 nanobeams were fabricated with details shown in Fig. 4.8(a). The first array contains AuNRs with the long side oriented parallel to the VO_2 nanobeams, where the AuNR crosses none or one boundary between the nanobeams. The second array was oriented perpendicular to the nanobeams, which resulted in crossing one to three boundaries between the nanobeams. On average, the AuNRs oriented perpendicular to the VO_2 nanobeams should cross more boundaries between the nanobeams than AuNRs oriented parallel. This could translate into differences in the optical response of AuNRs on such an anisotropic substrate.

The plasmon response of both AuNR arrays was examined by Bruker Vertex 80V FTIR combined with the Hyperion 2000 microscope. The illumination path included a broadband linear polarizer to separate the excitation of longitudinal or transverse modes and was done in a transmission setup. A single spectrum transmitted through the array of AuNR on VO_2 was recorded together with four spectra through bare VO_2 at four different positions near the array at room temperature (VO_2 is dielectric) and at 80 °C (VO_2 is metallic). The resulting extinction spectra were calculated as $1 - T/T_{\mathrm{REF}}$, where T is the transmission through the AuNR on VO_2 nanobeams and

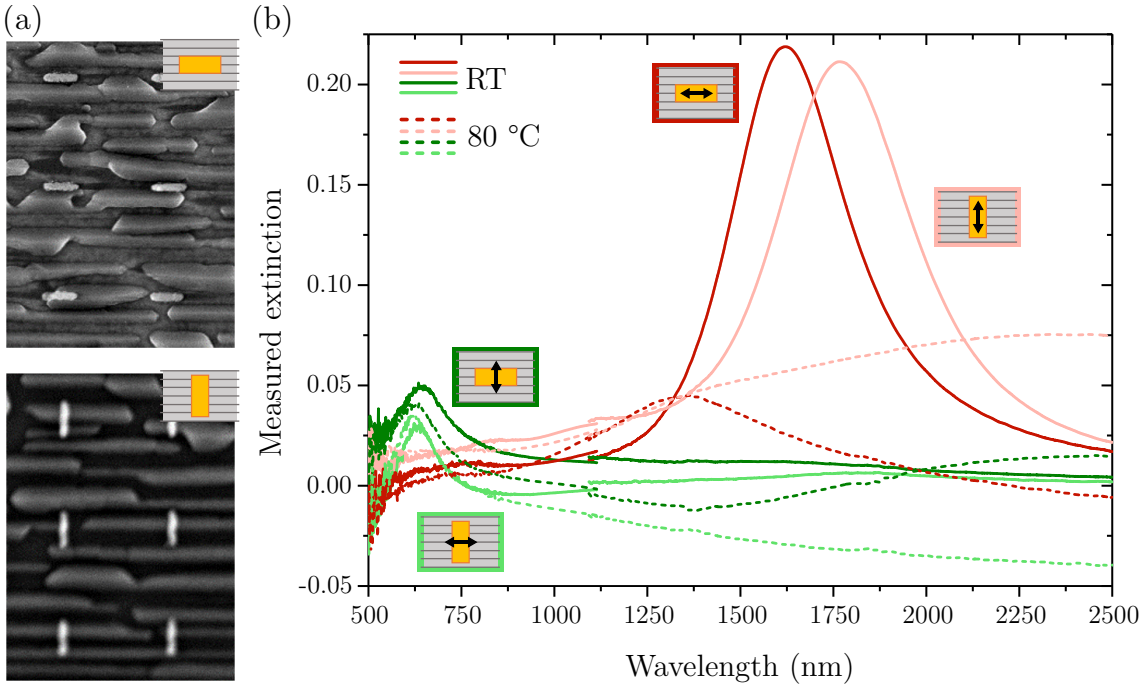

Fig. 4.8: (a) SEM images of the two fabricated AuNRs orientations with respect to the anisotropic VO_2 substrate. (b) Polarization-resolved extinction of the AuNR antennas, where the full lines represent the spectra obtained at RT (dielectric VO_2 substrate) and the dashed lines represent the spectra obtained at 80 °C (metallic VO_2 substrate). The respective orientations of the nanorod long axis and VO_2 nanobeams are shown as insets together with the incident light polarization.

T_{REF} is an average transmission through the bare VO_2 surrounding the array.

Fig. 4.8(b) shows the resulting spectra of both plasmon modes, i.e., transverse mode in the VIS region and longitudinal mode in the IR region. Comparing the spectra at RT (full lines), one can see a notable red-shift in extinction peaks when the plasmon mode oscillates perpendicularly to the VO_2 nanobeams. It is the case for both plasmon modes, clearly visible in the case of the longitudinal mode in the arrays with AuNR perpendicular to the nanobeams and noticeable even in the transverse mode in the arrays with AuNRs parallel to the nanobeams. Based on the respective orientation of the plasmon mode oscillation and underlying VO_2 nanobeams it can be argued that the plasmon oscillations sense the nanobeam boundaries present in the substrate. The larger average number of grain boundaries which the respective plasmon mode crosses results in a noticeable shift of the plasmon resonance to longer wavelengths.

At elevated temperatures (80 °C, dashed lines), the amplitudes corresponding to the longitudinal plasmons are dramatically reduced due to the metallic nature of high-temperature VO_2 involved in plasmon damping. The damping in AuNRs perpendicular to the nanobeams is more significant, where the peak around 1350 nm is almost disappearing completely in the background. Regarding the peak positi-

ons, they shift dramatically towards shorter wavelengths due to a decrease in the real part of the dielectric function of VO_2 in agreement with previous reports [227]. The transverse plasmon modes, on the other hand, exhibit lesser blue shifts and the damping seems negligible. This is a reflection of the smaller effect of the phase transition in the visible region, where the true metallic character of the high temperature VO_2 is not developed as the real part of the dielectric function goes negative only above 1100 nm wavelengths [45]. In further experiments, we focused mostly on the longitudinal AuNR plasmon modes because of much more pronounced changes in the plasmon response with temperature.

One can notice that the high-temperature spectra feature the negative extinction in the NIR region, suggesting smaller light transmission through bare VO_2 than that with AuNRs on top. The explanation might come from some defects or a speck of dirt on the surrounding bare VO_2 partially blocking light transmission and thus shifting the whole extinction spectrum down, or related to the improper polarization axis alignment. Nevertheless, the shape of the negative extinction curves strongly resembles the shape of the extinction recorded for the bare VO_2 [Fig. 4.4(b)], just reversed. There might be some additional effect stemming from the interaction between AuNRs and plasmons in underlying VO_2 but it requires further investigation, e.g., by simulations.

To obtain quantitative information about the plasmon peaks, the spectra were fitted with two harmonic oscillators. The mathematical description of a harmonic oscillator and extracted parameters, i.e., the amplitude, centre energy, and FWHM are summed in Fig. 4.9(a,b). Note that only the imaginary part of the harmonic oscillator was utilized for the peak fitting.

Since the spectra always contained some background as an imprint of the optical response of the bare VO_2 nanobeams, it was not possible to do the fit with a single oscillator. One oscillator was thus utilized to specify the background and the second one was used to fit the remaining AuNR LSP peak [see Fig. 4.9(c)]. This approach was semi-automatic and was done in the VWASE software, which is used for fitting ellipsometric data through the least square method, starting from the RT spectra, where the AuNR peak is clearly visible. The initial fit parameters were set manually for the main peak to get the closest possible fit to the peak and the second oscillator was utilized for the background shoulder next to the peak. A fit of both oscillator parameters was then run and all the parameters were extracted. These parameters were then used as the starting parameters for a fit of the spectrum recorded at the higher temperature till the highest temperature was fitted.

After characterization at the RT and 80 °C as the limiting cases with either purely dielectric or purely metallic VO_2, we wanted to observe gradual changes upon the temperature increase. The longitudinal plasmon spectra for both AuNR orientations are displayed in Fig. 4.10(a,b) for the temperatures going from RT to 76 °C showing a gradual blue-shift of the plasmon peak as the phase transition starts to occur. The extracted fit parameters corresponding to the AuNR longitudinal plasmon spectra

(a)

$$\varepsilon_n = \frac{A_n B r_n E_n}{E_n^2 - E^2 + 1/4 B r_n^2 - \mathrm{i} B r_n E}$$

A_n - amplitude (dimensionless)

(b)

$$\mathrm{Im}\{\varepsilon_n\} = \frac{A_n B r_n^2 E_n E}{(E_n^2 - E^2 + 1/4 B r_n^2)^2 + (B r_n E)^2}$$

Br_n - FWHM (eV)

E_n - center energy (eV)

(c)

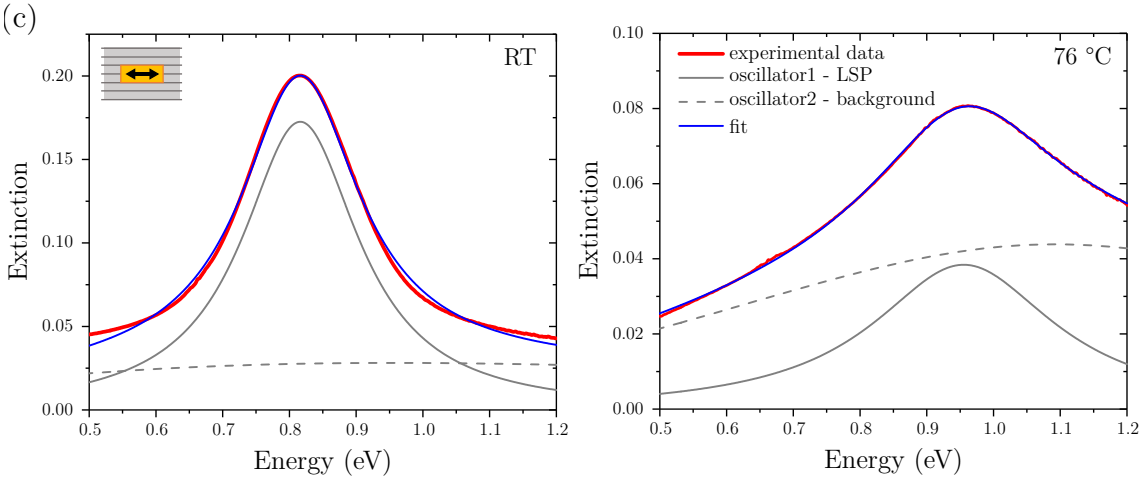

Fig. 4.9: (a) Mathematical description of the harmonic oscillator with its (b) imaginary part used to fit the experimental extinction data and the main parameters extracted from the procedure. (c) Examples of the experimental data corresponding to the longitudinal LSP mode measured on AuNRs parallel to the VO_2 nanobeams at RT and at 76 °C which were fitted by two harmonic oscillators – one used to capture the AuNR LSP peak characteristics and the other to account for a nontrivial background.

are summed up below the spectra. The peak position, i.e., the resonance wavelength and corresponding energy in Fig. 4.10(c) demonstrates a blue-shift of the AuNR resonance with increasing temperature. The tuning range of resonance wavelengths is significantly larger for the AuNRs laying perpendicular to the VO_2 grains which can be related to the different extinction contrast of underlying VO_2. Nevertheless, the temperature-induced extinction contrast of bare VO_2 in Fig. 4.5(a) below the parallel AuNR at its RT resonance wavelength of 1.52 µm is slightly larger than contrast in VO_2 in Fig. 4.5(b) below the perpendicular AuNR at its RT resonance wavelength of 1.65 µm. The extracted peak amplitudes in Fig. 4.10(d) were tunable across a similar range only slightly larger in the case of parallel AuNRs and perpendicular AuNRs resulted in almost vanishing peaks at the elevated temperatures.

As opposed to the previous parameters which exhibited gradual, smooth, and rather predictable changes with temperature, in terms of FWHM in Fig. 4.10(e), the response was dramatically different. With increasing temperature, the FWHM of both AuNR arrays rises similarly and gradually. But after reaching the temperature of about 70 °C the FWHM decreases rather sharply for both AuNR orientations. This is a rather intriguing effect and the temperature dependence resembles the effects observed in bare VO_2 when recording the real part of the dielectric function at

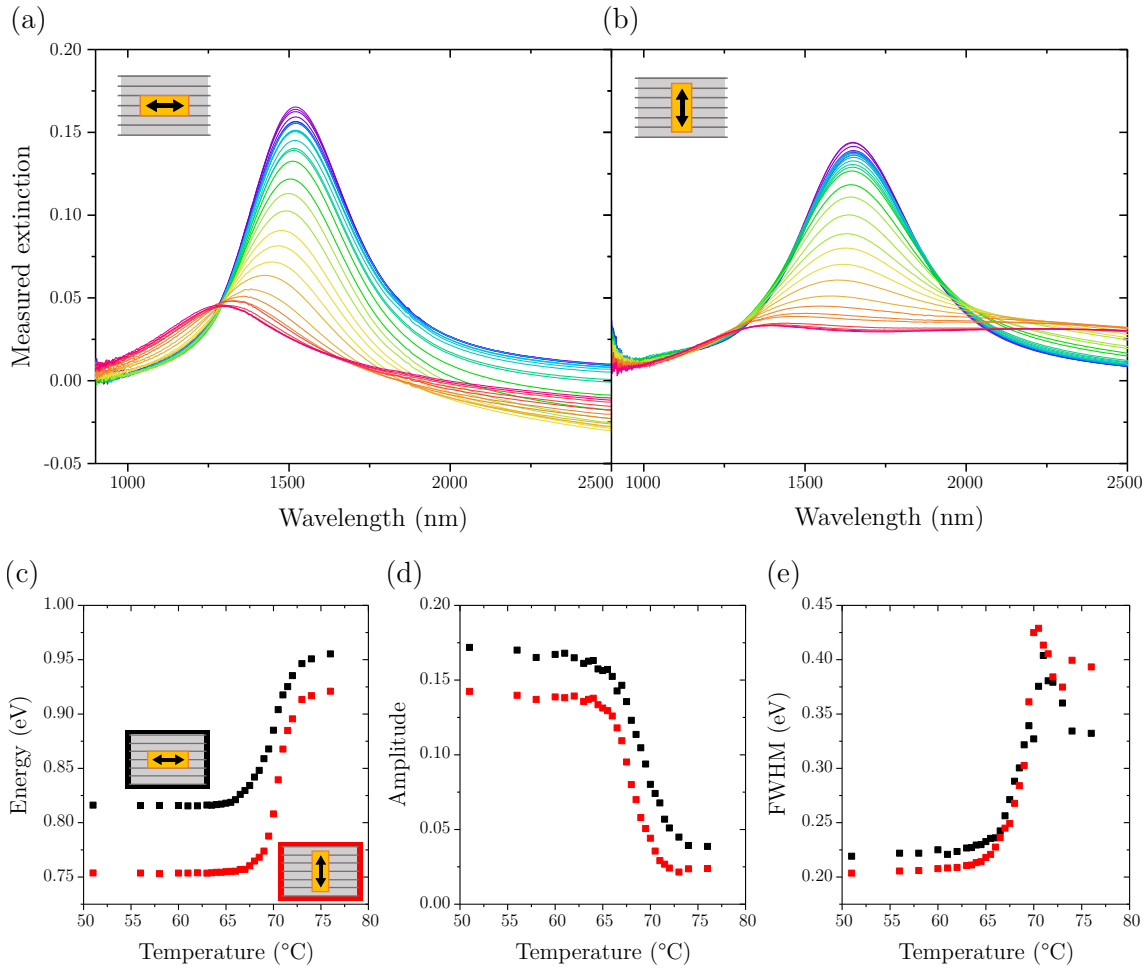

Fig. 4.10: Temperature development (from RT to 76 °C) of the polarization-resolved extinction of the longitudinal mode in AuNR antennas fabricated on top of the epitaxial VO_2 substrate with AuNR (a) parallel and (b) perpendicular to the VO_2 nanobeams. Extracted fit parameters: (c) the peak position in terms of energy, (d) peak amplitude, and (e) peak FWHM for both AuNR orientations. The colour of the inset frames corresponds to the colour of extracted parameters.

the low-frequency limit by Basov [271]. This suggests the possibility of probing the phase-transition phenomenon by plasmon resonance [287] and some of the parameters have shown a similar shape [288] as we have observed in Fig. 4.10(e). One can see that the observed changes in FWHM differ between the two AuNR orientations with perpendicular AuNRs showing a larger span of values though in parallel AuNRs the spike in FWHM is sharper and values stabilize at lower values for the high temperature limit.

This intriguing effect is worth further investigation in terms of simulations as well as new sample fabrication. Anisotropic VO_2 with AuNR antennas of different dimensions with resonances even out of the range of transverse VO_2 plasmon resonance would confirm the observed effects beyond doubt. Here, with only one AuNR size, there is still some uncertainty, especially regarding the fitting procedure which requires a second oscillator to account for the non-trivial background present in the spectra. Its parameters are at first set up manually and the starting values can then provide slightly different results of the final two oscillator fit. Although the fitting with different starting values resulted in rather similar values, additional AuNR dimensions would give our results firmer ground.

4.4 Conclusions

In this chapter, the use of the phase-change material VO_2 for tunable plasmon resonances. In the beginning, the fundamental properties of the VO_2 were summarized together with our current understanding of the underlying phase transition. We then demonstrated its use via two different approaches. In the first approach, the VO_2 itself was nanostructured by a self-limiting epitaxial growth of VO_2 nanobeams and exhibited plasmonic properties above the phase transition temperature. Accompanying simulations manifested a possibility of moving the resonance wavelength when changing the nanobeams' dimensions. The metasurface formed by such VO_2 nanobeams behaved as an attenuator at RT while at 80 °C it behaved as a quarter-wave plate.

The use of the aforementioned VO_2 metasurface as an active substrate for AuNR antennas was demonstrated as well. The tunability of AuNR plasmon resonance wavelengths of AuNRs was proved as a function of temperature. Most importantly, the AuNR arrays oriented parallel or perpendicular to the VO_2 nanobeams exhibited different responses already at RT, but also with increasing temperatures suggesting the strong effect of the VO_2 anisotropy on the AuNR plasmon resonance. Additionally, the observed AuNR resonances featured an interesting spike in extracted FWHM of both AuNR orientations probably as a result of a strong correlation in VO_2 during the phase transition. Nevertheless, further investigation is necessary to confirm the nature of the observed behaviour, ideally by fabricating AuNRs of different sizes. We would thus obtain AuNRs with resonance wavelengths that do not overlap that much with the transverse resonance in VO_2 nanobeams themselves,

which would make the fitting of the resulting peaks more reliable. Some further insight could also be produced by employing further simulations of the AuNRs on the VO_2 nanobeams.

Overall the VO_2 was shown as a promising platform to introduce tunability into metasurfaces. It also suggested that when used as a substrate, its anisotropy can affect the plasmon resonances of the overlying AuNRs.

5 EFFECT OF CRYSTALLINITY IN PLASMONIC NANOSTRUCTURES

The information outlined within the following chapter is based on the following publication [289].

Plasmonic nanoantennas are conventionally prepared by two basic lithographic methods: electron beam lithography (EBL) which utilizes a resist mask, or more straightforwardly using a direct milling by focused ion beam (FIB) lithography [51]. The energy of the LSP resonance of the resulting nanoantenna is highly dependent on the choice of a nanoantenna material and its quality, the size and shape of the nanoantenna, as well as on the surrounding environment [49].

Typical plasmonic nanoantennas are fabricated from thin films of noble metals like gold and silver deposited by evaporation of sputtering techniques. These preparation methods predetermine the polycrystalline nature of nanoantennas with randomly oriented grains of varying sizes [290, 291]. The inhomogeneity then negatively affects the fabrication resolution thus making each nanoantenna of a slightly different shape [292] which may be detrimental, e.g., for the performance of metasurfaces as they introduce random noise into their phase response.

This is not such a troublesome issue with antenna array studies by optical methods, where the differences slightly broaden the plasmon resonance peaks. In single antenna studies, however, the response of each antenna is recorded and might exhibit a different behaviour which makes them harder to directly compare.

Although the optimization of deposition parameters can increase the grain size [293], the presence of grain boundaries within the nanoantennas is related to decreasing the plasmon resonance quality factors as well as increasing the relaxation rates [294]. Some improvement of these detrimental effects can be achieved, e.g., by subsequent annealing, [295, 296]. In combination with some advanced deposition procedures such as template stripping, the layer quality can be improved even more [23], and the larger grains permit a nanoantenna fabricated from a single grain. This can be achieved readily via the chemical synthesis of nanoparticles which can be formed by a single crystal grain with a rich shape variability [297], nevertheless, their precise placement onto a substrate remains somewhat challenging. Ideally, a whole nanoantenna array is fabricated from a single large grain of material, e.g., a large 2D monocrystal [298, 299] which is placed on a supporting substrate, alleviating the shape and size inconsistency of the nanoantennas after the follow-up lithographic process.

Gold, as a quintessential plasmonic metal, can be prepared by several pathways of chemical reduction of typically $HAuCl_4$ into a form of large monocrystalline microplates (AuMPs) in reactions based on aniline [300], two-component ionic liquids [301], ethylene glycol [302, 303, 304], or tetraoctylammonium bromide (TOABr) [305, 306, 307] where the latter two methods are the most prevalent.

Although the improvement in optical properties of monocrystalline versus po-

lycrystalline gold is not that radical in bulk [308], it has been shown as a useful platform with an improved propagation length of surface plasmons [309] even in complex devices [310, 311, 312, 313, 314]. Additionally, this grain-less gold allows an advanced fabrication of far more complex structures with a higher resolution, better-defined shape, and consequently, better optical performance [315, 316].

Nevertheless, a detailed study comparing the monocrystalline and polycrystalline nanoantennas in terms of their material properties and shape correlation with induced plasmon modes at very high spatial and energy resolution has been largely missing in the literature.

5.1 Au microplate preparation

We set out to directly compare the gold plasmonic nanorods (AuNRs) fabricated either from monocrystalline or polycrystalline gold substrates using FIB lithography. We selected a nanorod shape due to well-isolated modes and the existence of an analytical description [317]. We characterize the material properties of the input substrates as well as the resulting nanorods, correlate the nanorod shape with its plasmonic properties, and visualize the supported plasmonic modes by scanning transmission electron microscopy (STEM) in combination with electron energy loss spectroscopy (EELS) with the nanometer spatial resolution not achievable employing other methods.

The main driver of this work was the ability to prepare large gold monocrystalline microplates. The preparation of gold monocrystalline microplates was achieved via the two most prevalent procedures reported by Hecht's group [303] and Kulkarni's group [306]. The method by Hecht, which generally yielded smaller and thinner AuMPs, resulted in best results when grown on glass substrates, while ITO substrates contained fewer and smaller AuMPs. The Kulkarni method produced generally larger and thicker AuMPs, resulting in large AuMPs on ITO, glass, and Si substrates.

For the utilization of STEM with EELS, the microplates needed to be prepared on a thin membrane. We chose 30 nm-thin SiN_x TEM membranes with a 250 µm thinned window. Using the Hecht procedure we were not able to grow the microplates directly on the membrane surface, so the Kulkarni method was selected because of the promising preliminary experiments.

The preparation process of the selected procedure is summed up in Fig. 5.1 and is based on [306]. Briefly, 1.6 ml of 25 mM $HAuCl_4$ is mixed with 4 ml of 50 mM TOABr in toluene under vigorous stirring. During the stirring, the $(AuCl_4)^-$ ions are transferred from the water phase to the toluene phase where they create an $(AuCl_4)^-$–TOABr complex. This process is accompanied by a dramatic change in colour from the initially colourless toluene phase to a ruby red. Due to the immiscibility of the two phases the $(AuCl_4)^-$–TOABr complex in toluene separates from the water phase and thus can be easily extracted for the follow-up AuMP growth.

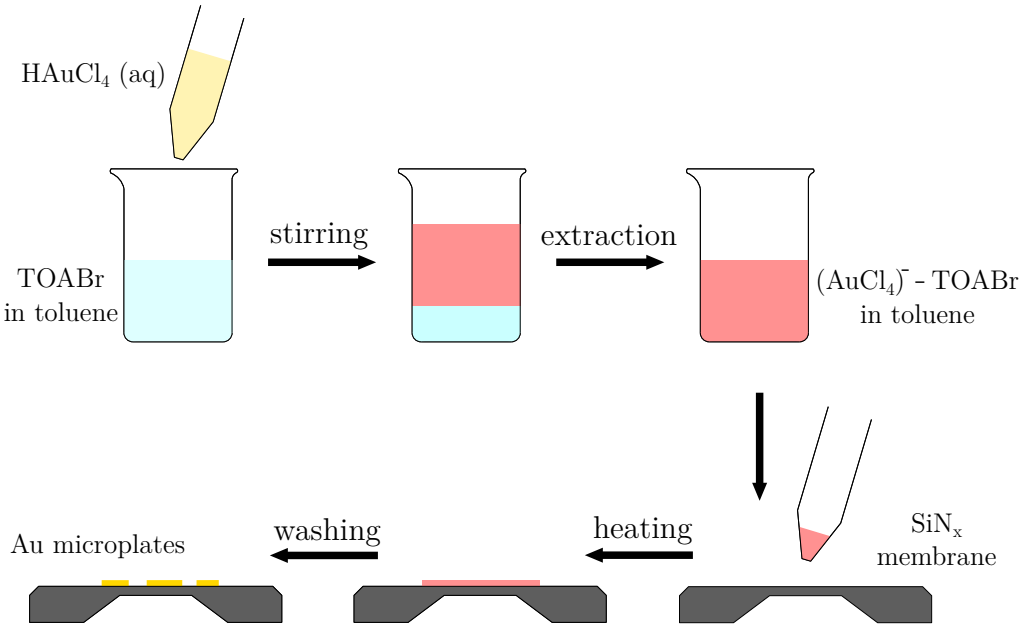

Fig. 5.1: Monocrystalline gold microplate preparation procedure: aqueous solution of 25 mM $HAuCl_4$ is mixed with 50 mM TOABr in toluene under vigorous stirring while $(AuCl_4)^-$ ions undergo a transfer into the toluene phase which separates from the aqueous solution due to their immiscibility. The extracted $(AuCl_4)^-$–TOABr complex in toluene is then applied on a SiN_x membrane and heated to a desired temperature ($140 - -150°$ C) for 24 to 48 hours followed by washing procedure. The procedure is based on [306].

The brittle SiN_x membrane was stuck to the Si substrate by a double-sided Kapton tape to ease the manipulation with the sample and put on a hot plate which was set to 75 °C. The extracted solution was then applied to the preheated membrane and after the toluene evaporates the temperature is set to the growth temperature. We have varied the amount of the applied solution (1–5 µl), growth temperature (130–200 °C), growth time (12–48 h) and the procedures generally resulted in monocrystalline AuMPs of various lateral sizes (tens of micrometres) and thicknesses (tens to hundreds of nanometers). Afterwards, the remaining precursor residues were carefully washed away in toluene, ethanol, and deionized water baths, respectively.

AuMPs started to appear from a temperature of 140 °C upwards, and though more AuMPs were grown with a larger lateral size at higher temperatures the thickness increased too. The aim was to grow Au MPs with a thickness below 70 nm to avoid additional thinning of the AuMPs for the following FIB fabrication. To quickly assess the thickness of the synthesized AuMPs, we utilized bright field optical microscopy. As shown in Fig. 5.2, AuMPs with a thickness above 100 nm completely reflected the incoming light which gave them the typical golden colour. The thinner ones, though, transmitted a portion of light through which resulted in a slight shade of pink colour. The darker the shade of pink, the thinner the respective

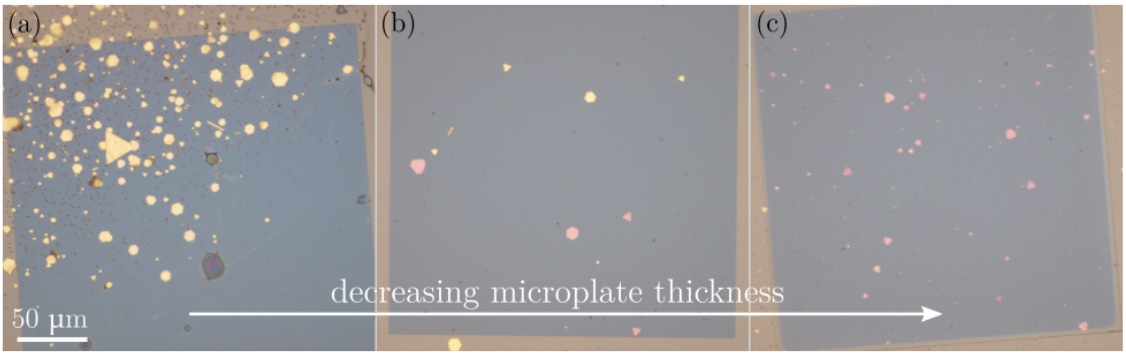

Fig. 5.2: Bright field optical images of gold microplates grown on 30 nm SiN_x TEM membrane (darker region - square 250 × 250 µm^2) highlighting the possibility of discerning the microplates' thickness from the contrast in optical images. Membrane with (a) microplates of 100 nm thickness and more which are completely opaque for the incident light, (b) a combination of thicker microplates as well as the thinner ones exhibiting the slightly pinky shade, and (c) thin microplates with thicknesses well below 100 nm where the darker the shade of pink, the thinner the microplate. Adapted from [289].

AuMP. Such thin microplates then proceeded to a lithography procedure.

The optimized growth process using 1–2 µl of the growth solution, at a growth temperature of 140–145 °C grown for 35–48 h resulted in most thin AuMPs.

5.2 AuNR fabrication and their properties

To obtain the polycrystalline substrate counterpart, we deposited about 30 nm of gold on another TEM membrane by magnetron sputtering (Leica coater EM ACE600) without any adhesion layer which would prevent a direct comparison to the monocrystalline gold.

As highlighted in Fig. 5.3, both substrates then underwent the FIB lithography procedure to obtain monocrystalline and polycrystalline plasmonic AuNRs. The FIB lithography was performed using the dual-beam FIB/SEM microscope FEI Helios using Ga^+ ions with an energy of 30 keV and ion beam current of 1.3 pA. The nanorods were designed as rectangles 240 nm long and 80 nm wide and were situated inside a 1.5×1 µm^2 window where the metal was removed to prevent its interaction with the nanorod. The energy-resolved X-ray spectroscopy (EDS) has shown a small amount of Ga implanted into the membrane (see Ref. [289]) but its effect on plasmon resonance is negligible [51].

For the sample characterization, we mainly used analytical transmission electron microscopy including STEM-EELS which was performed using TEM FEI Titan equipped with the Super-X spectrometer for EDS and GIF Quantum spectrometer for EELS operated at a primary electron energy of 300 keV. Before STEM-EELS

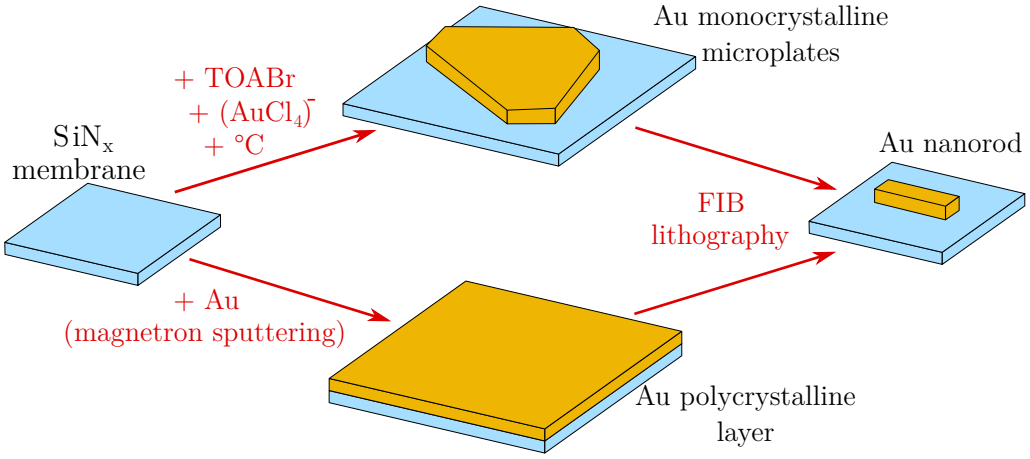

Fig. 5.3: Nanorod preparation routes for two Au crystallinities done directly on the 30 nm SiN_x membrane surface. (Top route) represents the chemical synthesis of monocrystalline gold microplates and (bottom route) the preparation of conventional polycrystalline gold layer deposited by magnetron sputtering used for the following FIB lithography to fabricate AuNRs. Adapted from [289].

experiments, all the samples were cleaned in oxygen/argon plasma for 10 seconds to prevent carbon contamination [51]. The beam current was set around 0.2 nA, the full-width at half-maximum (FWHM) of the zero-loss peak (ZLP) was in the range from 0.1 eV to 0.15 eV, and the beam diameter was approximately 1 nm. For further information about the experimental conditions, see Ref. [289].

It is also worth noting that the mechanical stability of the membranes undergoing the chemical synthesis was dramatically decreased. The probable cause dwelt in the membrane heating, loading it with the growth solution, and subsequent washing procedure in various liquid solvents. The brittleness resulted in many membranes being ruptured during the manipulation, FIB fabrication, and the actual analysis. The membrane with the polycrystalline layer didn't suffer any equivalent issues.

The monocrystalline microplates and polycrystalline films were analyzed by selected-area electron diffraction (SAED) in TEM and by AFM. Fig.5.4(a) shows a monocrystalline microplate with the fabricated nanorods and corresponding electron diffraction pattern recorded at an area away from the nanorods. The diffraction pattern exhibits a 6-fold rotational symmetry and corresponds to the face-centred cubic (FCC) Au crystal lattice viewed along the [111] direction. A point-like symmetric character of the pattern indicates the single-crystalline nature of the synthesized Au microplates lying flat on the membrane with the (111)-oriented basal plane [318, 319]. Similarly, Fig. 5.4(b) shows the SAED pattern related to the polycrystalline gold film. For the selected scale, the individual grains of the polycrystal is not well visible [see Fig. 5.5(b) for zoomed-in images]. Nevertheless, a circular diffraction pattern clearly corresponds to a polycrystalline sample with a random orientation of individual grains. One can still resolve individual spots forming most of the di-

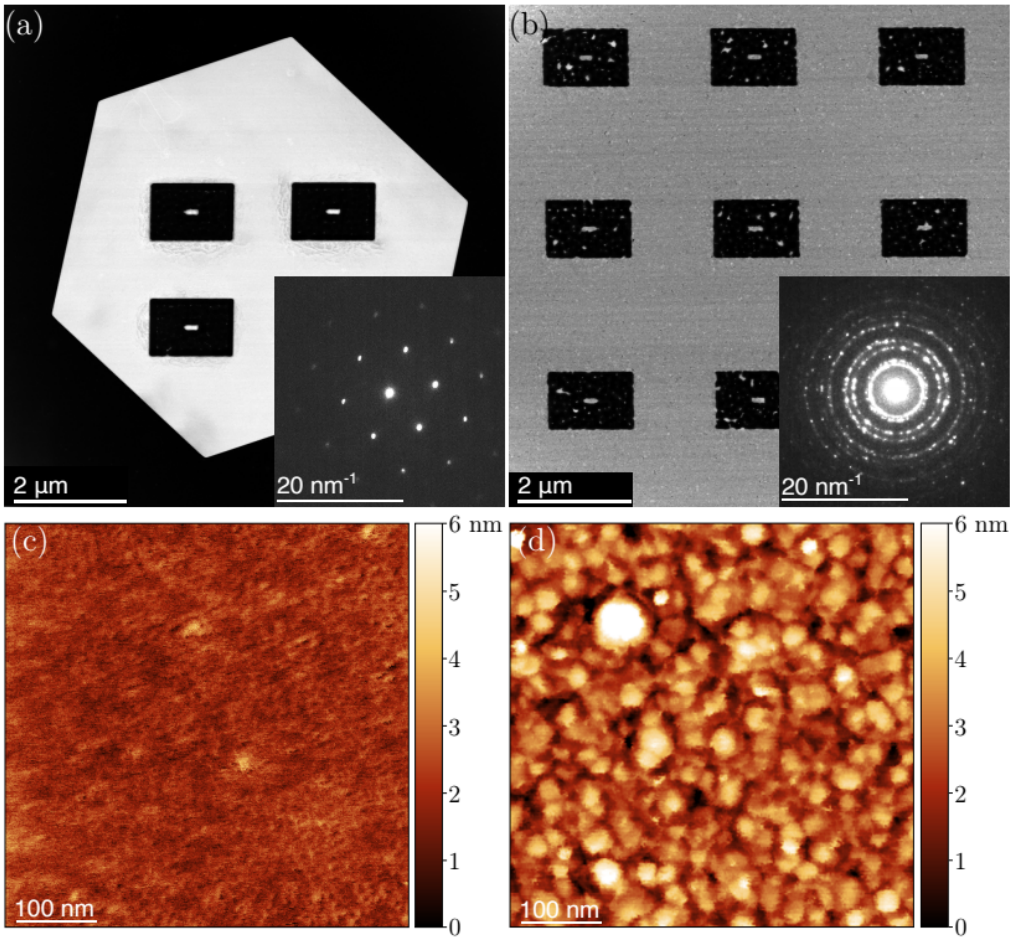

Fig. 5.4: Structural and morphological information about the two substrates. (a,b) STEM ADF images of (a) monocrystalline and (b) polycrystalline substrates after fabrication of AuNRs. The insets show the electron diffraction patterns recorded on both substrates before nanorod fabrication. (c,d) AFM images of the roughness of a typical (c) monocrystalline and (d) polycrystalline substrate with the same height scale. Adapted from [289].

ffraction circles, but in the inner-most circles the spots are merged, thus we were not able to infer the number of grains participating in the diffraction pattern. Together with the information about the electron beam spot size in the sample plane, the number of grains within the spot could give us an estimate of the average grain size.

Also, note that the areas around the nanorods seem to be completely clean of gold residues in monocrystalline gold as opposed to polycrystalline gold with a lot of gold residues around due to a different milling efficiency of randomly oriented gold grains [320].

AFM analysis (Bruker Dimension Icon in tapping ScanAssyst mode) has been performed on a different set of samples prepared at the same growth conditions as the samples with nanorods. It revealed rather flat surfaces of both the monocrys-

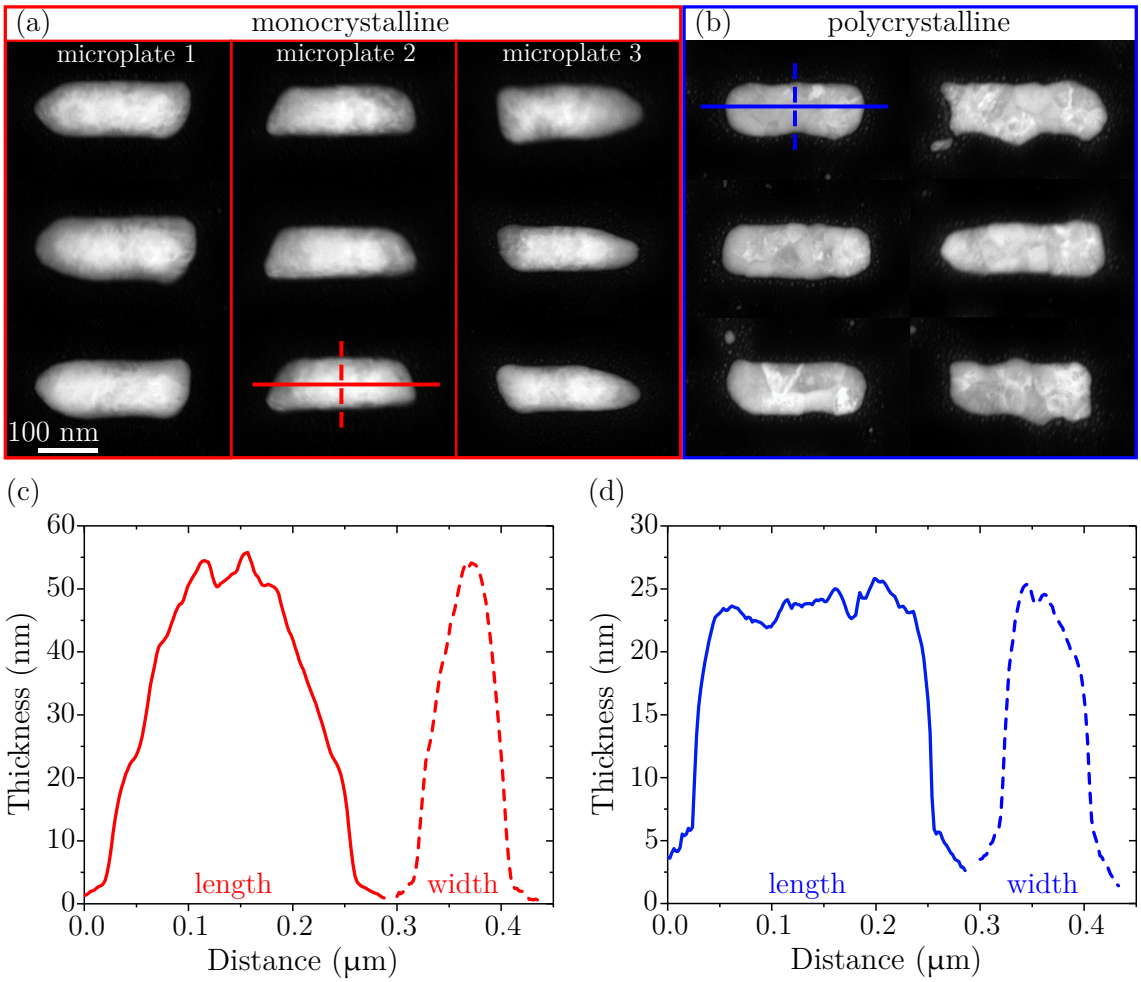

Fig. 5.5: (a,b) STEM ADF detail images of the gold nanorods fabricated from (a) the monocrystalline and (b) polycrystalline substrate. Note the nanorods arranged in the same columns in (a) are fabricated from the same microplate. (c,d) Thickness profiles along the long and short axis of the selected (c) monocrystalline and (d) polycrystalline nanorod determined by EELS. The thickness profiles correspond to the nanorods with cross-sections highlighted in (a,b). Adapted from [289]

talline [Fig. 5.4(c)] gold with an average root mean square (RMS) of 0.6 nm and polycrystalline one [Fig. 5.4(d)] with an average RMS of 1.2 nm. Higher RMS of the polycrystalline gold film is related to varying sizes of individual grains.

A closer inspection of the individual nanorods, which were then analyzed by EELS, in Fig. 5.5(a) shows a rather regular shape with smooth edges in the case of monocrystalline nanorods. However, the tips of the nanorods are faceted and deviate from the desired rectangular shape. The shapes across all the nanorods differ quite significantly, nevertheless, nanorods fabricated from the same microplate are almost identical with tips faceted in the same manner. Additionally, these nanorod facets seem to bear an imprint of their "mother"microplate side facets which indicates that the fabrication results might be improved by a proper alignment of the monocrystal

Tab. 5.1: Summary of average dimensions and plasmon resonance parameters of polycrystalline and monocrystalline gold nanorods characterized by EELS. The parameters below are averaged over the nanorods fabricated from the same gold monocrystalline microplate. Note that the numbers in parentheses in the left column indicate the number of analyzed nanorods. Theoretical calculations were done in MNPBEM and the values of calculated Q factors include the convolution with a Gaussian function (FWHM 0.3 eV) accounting for the instrumental broadening.

	Length (nm)	**Width (nm)**	**LD Energy (eV)**	**LD Q factor**	**LQ Energy (eV)**	**LQ Q factor**
Poly. – all (7)	238 ± 14	84 ± 3	1.01 ± 0.05	3.2 ± 0.4	1.67 ± 0.08	4.5 ± 0.6
Mono. – all (9)	232 ± 9	82 ± 7	1.14 ± 0.03	3.4 ± 0.3	1.78 ± 0.03	5.1 ± 0.4
– AuMP 1 (3)	243 ± 3	90 ± 5	1.12 ± 0.03	3.1 ± 0.2	1.81 ± 0.01	4.9 ± 0.4
– AuMP 2 (3)	231 ± 2	80 ± 2	1.13 ± 0.01	3.4 ± 0.1	1.75 ± 0.02	5.0 ± 0.4
– AuMP 3 (3)	223 ± 2	76 ± 5	1.17 ± 0.02	3.7 ± 0.2	1.77 ± 0.01	5.3 ± 0.4
Theory poly.	240 ± 24	80 ± 8	1.08 ± 0.07	2.8 ± 0.2	1.88 ± 0.08	5.5 ± 0.1
Theory mono.	240 ± 24	80 ± 8	1.06 ± 0.08	2.9 ± 0.2	1.62 ± 0.07	4.4 ± 0.5

side facet with the FIB milling direction. The polycrystalline nanorods in Fig. 5.5(b) generally exhibit larger irregularities in shape and have rougher edges due to their grainy structure. Some nanorods, though, reproduce the desired rectangular shape quite well [e.g. 1st and 2nd nanorod in Fig. 5.5(b)].

The thickness profiles over the nanorods [see Fig. 5.5(c,d)] were obtained from EELS using a calculated relative thickness multiplied by inelastic mean free path in the material, a method described in Ref. [321, 322]. The thickness profiles of a representative monocrystalline nanorod revealed that their boundaries are not upright but rather notably inclined. It can be attributed to the microplate's anisotropy and possible gold redeposition [320] but their impact could be lessened by further FIB milling optimization. In contrast, polycrystalline nanorods feature fairly upright boundaries with a small inclination related to the diameter of the ion beam with nominal FWHM around 3 nm.

The dimensions of the monocrystalline nanorods were $L = (232 \pm 9)$ nm, $W = (82 \pm 7)$ nm, and $H = (52 \pm 5)$ nm, while the dimensions of the polycrystalline nanorods were $L = (238 \pm 14)$ nm, $W = (84 \pm 3)$ nm, and $H = (30 \pm 3)$ nm (see Tab. 5.1 for a complete summary). The targeted lateral dimensions were reproduced very well but the thickness differed. The thickness of monocrystalline gold was not quantitatively controlled, as opposed to a rather well-thickness-controlled polycrystalline layer, but the actual thickness was evaluated only after the nanorod fabrication together with EELS characterization of plasmon modes in TEM. We therefore didn't adjust the thickness of the polycrystalline layer to the thickness of the gold microplates because we wanted to ensure that the FIB fabrication was done with the same parameter setup and alignment in the microscope. Additionally, the inclined boundaries in monocrystalline nanorods resulted in plasmon modes at basically the same energies as the polycrystalline ones allowing the direct comparison.

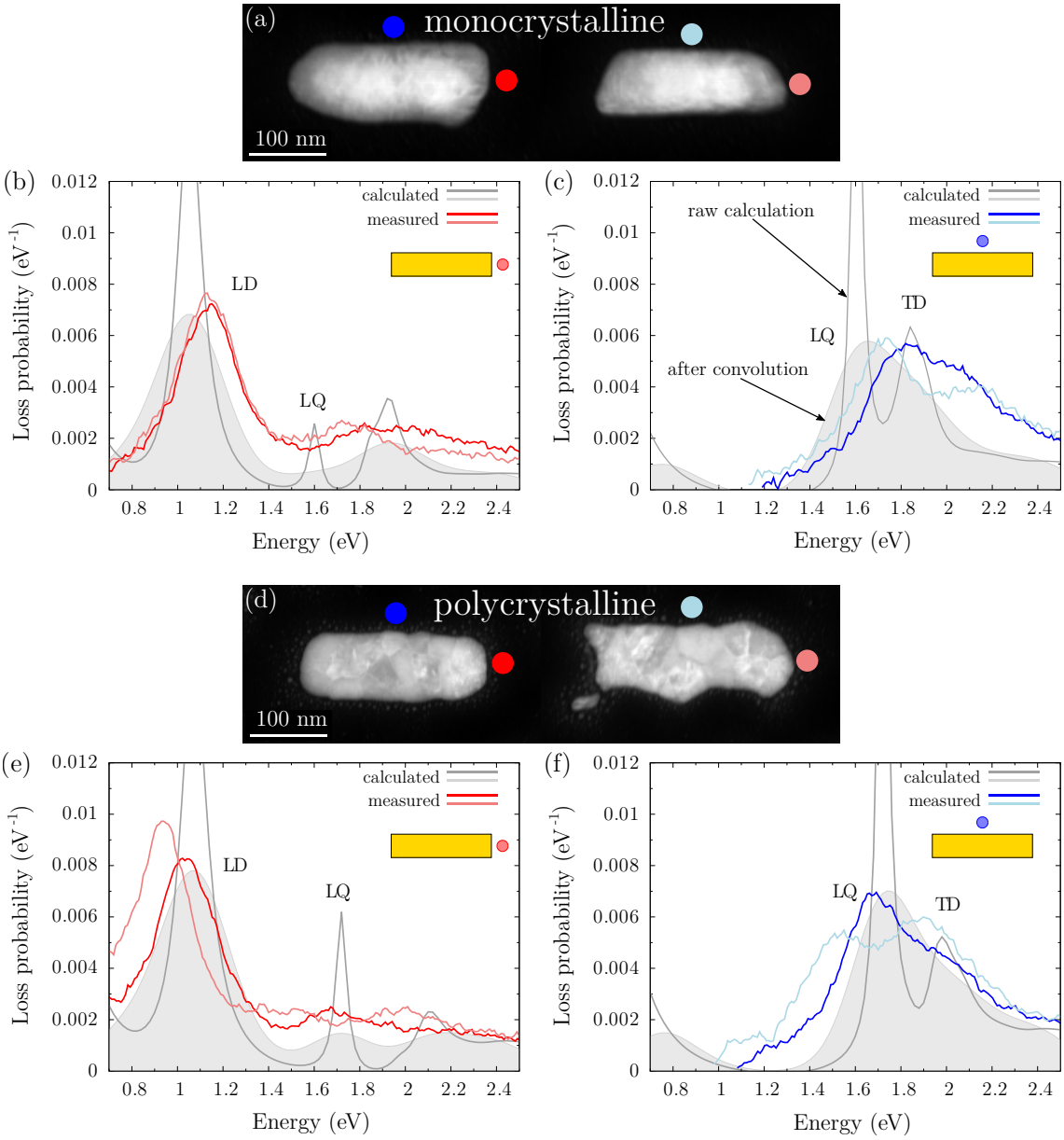

Fig. 5.6: (a,d) STEM ADF images of the two selected (a) monocrystalline and (d) polycrystalline gold nanorods with the coloured dots indicating the electron beam positions during the spectra acquisition with colours corresponding to the loss probability spectra that are outlined in (b,c) for the monocrystalline and (e,f) polycrystalline gold nanorods. Loss probability spectra were recorded with the electron beam located at the centre of (b,e) the short and (c,f) long edges of the selected nanorods. Experimental spectra are displayed by red or blue lines. The calculated spectra are displayed by grey lines, and the calculated spectra convoluted with a 0.3 eV FWHM Gaussian function to reproduce the experimental broadening are displayed by grey shaded areas. The main electric LSP modes are labelled in the spectra as LD (longitudinal dipole), LQ (longitudinal quadrupole), and TD (transverse dipole) mode. Adapted from [289].

Fig. 5.6 presents a typical experimental loss probability spectra of two representative monocrystalline and polycrystalline nanorods whose morphologies are shown in Fig. 5.6(a) and (d). The lowest-energy LSP mode around 1.1 eV can be unequivocally ascribed to a longitudinal dipole (LD) mode regarding the energy-filtered maps at that peak energy shown in Fig. 5.7(a) and (c). The higher energy peak around 1.8 eV is attributed to two spectrally overlapping LSP modes, the longitudinal quadrupole (LQ) and transverse dipole (TD) mode. It is difficult to resolve the LQ and TD modes in the experiment, as well as the higher-order modes. However, the inspection of the energy-filtered maps for the peak energy in Fig. 5.7(e) and (g) shows a pattern suggesting the domination of the longitudinal quadrupole mode at this energy.

Both main peaks corresponding to the monocrystalline nanorods are slightly blue-shifted when compared to polycrystalline ones. Since the overall difference in dielectric functions of the two crystallinities was previously found to be insignificant [308], we attribute the blue shift to the discrepancies in shape and thickness of the nanorods.

The experimental spectra are accompanied by calculations carried out using the boundary element method (BEM) [323] with a software package MNPBEM [324]. The calculations take into account the actual shape of the fabricated nanorods – 30 nm thick nanorods with upright boundaries and 50 nm thick nanorods with inclined boundaries corresponding to polycrystalline and monocrystalline nanorods, respectively. Supplemental calculations revealed that the increased thickness moves the LSP modes to higher energies while the inclination of the boundaries shifts the modes to lower energies (SI of Ref.[289]). To bring the theoretical spectra closer to the actual experiment, the calculated spectra were convoluted with a Gaussian function (FWHM 0.3 eV) accounting for the instrumental broadening. After the convolution, the calculated spectra are in good agreement with the experimental ones.

The quantitative parameters of the LSP modes were retrieved by fitting the spectral profiles by a Gaussian function. The energy of the mode E and the Q factor, defined as the LSP mode energy divided by FWHM, were extracted for both main modes and summarized in Tab 5.1. The mean energies in the experiment averaged to (1.14 ± 0.03) eV (LD mode) and (1.78 ± 0.03) eV (LQ mode) in case of the monocrystalline nanorods, and (1.02 ± 0.05) eV (LD mode) and (1.67 ± 0.08) eV (LQ mode) in case of the polycrystalline nanorods, respectively. The mean energies were slightly higher in monocrystalline nanorods but after taking into account the experimental energy resolution of our EELS setup, estimated as 0.1 eV, the differences in energies can be considered as insignificant. Similarly, the Q factors were slightly higher in monocrystalline nanorods but still within the uncertainty of the experimental technique. The calculation accounting for the differences in length and width of nanorods by a 10 % deviation from the designed dimensions, yielded (1.06 ± 0.08) eV (LD mode) and (1.62 ± 0.07) eV (LQ mode) for monocrystalline

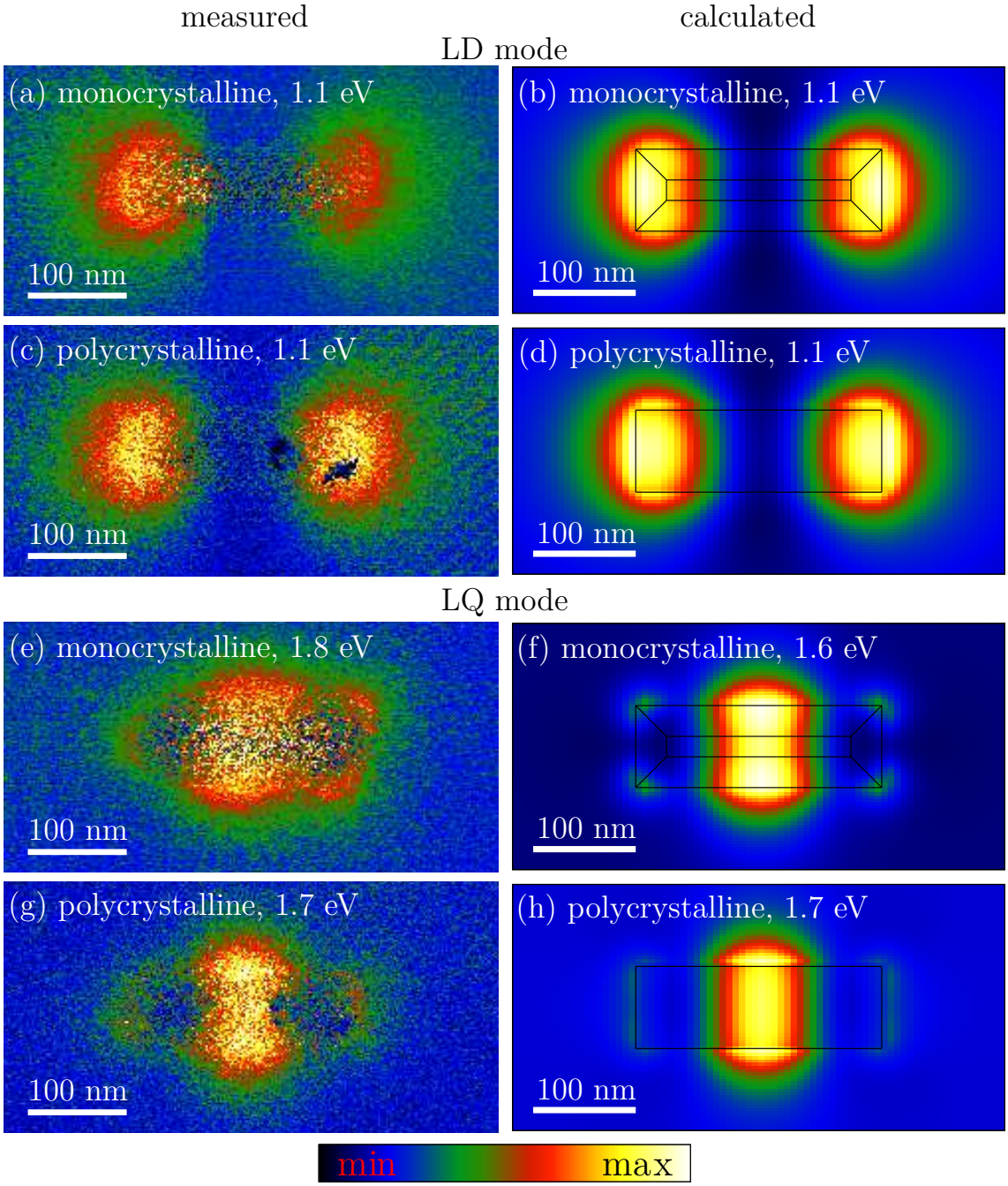

Fig. 5.7: Spatial distribution of the loss probability at the energy of (a-d) the LD mode and (e-h) LQ mode with the energy window width of ±0.1 eV. The panels on the left correspond to the measured loss probability maps recorded for the nanorod on the left side in Fig 5.6(a) and (d). The panels on the right correspond to the calculated loss probability maps with the contours of the nanorods highlighted by black lines. The energy of the respective mode is indicated at the top of each panel. Adapted from [289].

and (1.08 ± 0.07) eV (LD mode) and (1.88 ± 0.08) eV for polycrystalline nanorods showing a good agreement with the experimental data.

To confirm the nature of the LSP modes induced inside the nanorods, maps of the loss probability at the peak energies were generated. Fig.5.7(a) and (c) depict the energy-filtered maps at the energy of 1.1 eV for monocrystalline and polycrystalline gold nanorods with a pattern evidently corresponding to the LD mode. Likewise, Fig. 5.7(e) and (g) present the energy-filtered maps at the higher energy peak at 1.8 eV for monocrystalline and at 1.7 eV for polycrystalline nanorods, respectively. These patterns imply that the LQ mode is more prevalent than the TD mode. The energy-filtered maps show only minimal differences between the two crystallinities, although the polycrystalline modes are slightly easier to discern. The experimental energy-filtered maps are accompanied by the simulated ones performed for the morphologies according to the experiments and they show a very good agreement in LD and LQ modes for both crystallinities.

Tab. 5.1 sums the major parameters extracted from all the analyzed nanorods during the structural and optical characterization. In total, we have analyzed 7 polycrystalline and 9 monocrystalline nanorods which were fabricated from three monocrystalline microplates in total. In terms of nanorods dimensions, the average length of polycrystalline nanorods is closer to the desired length (240 nm) though with larger deviations, the average width of monocrystalline nanorods was closer to the design (80 nm) also with larger deviations. The average energy of the LD mode is slightly higher and with smaller deviations in the case of monocrystalline nanorods and for the LQ mode it is even more pronounced. Similarly, the extracted Q factors are slightly larger in the case of monocrystalline nanorods for both modes.

Overall, the average parameters of the plasmon resonances for monocrystalline and polycrystalline nanorods are quite similar. However when we focus on the nanorods fabricated from the same gold microplate, the dispersion of measured parameters is significantly reduced, especially in terms of LD and LQ mode energy.

5.3 Conclusions

In conclusion, we have prepared monocrystalline and polycrystalline gold nanorods and compared their structural and optical properties. In terms of shape, the most significant differences were the inclined boundaries in monocrystalline and upright boundaries in polycrystalline nanorods. Monocrystalline nanorods are better than polycrystalline ones in slightly reduced size and shape fluctuations, especially when fabricated from the same AuMP. Their fabrication also resulted in no gold residues around the monocrystal nanorods while plenty of gold crystallites were found in the vicinity of polycrystalline nanorods due to the incomplete gold removal. Nevertheless, monocrystalline nanorods systematically deviate from the desired shape due to the crystal orientation of the gold microplates as their facets are imprinted onto the

nanorod shape. Moreover, the membranes with monocrystalline gold suffered from increased brittleness.

In terms of optical properties, we have not found any significant differences between the two crystallinities. LSP mode energies, Q factors, and magnitudes of the loss probability spectra acquired by EELS are very similar with differences within the experimental accuracy. Our findings suggest that the plasmon response of gold nanorods does not deteriorate when polycrystalline gold is used instead of monocrystalline in the studied region of energies. Therefore, using polycrystalline gold as a convenient substitute for monocrystalline gold does not necessarily bring along a compromise to the optical response of the resulting nanostructures.

6 ELECTROCHEMISTRY AND PLASMONICS

In previous chapters, fundamental aspects of plasmonic nanostructures were studied in detail, driving innovation in novel research areas, like metasurfaces. Plasmonics can also bring new functionalities into already well-established research areas like electrochemistry and photocatalysis which can benefit from electromagnetic energy concentration and hot carrier generation effects. We have set out to study these aspects in two systems – WS_2 nanotubes and TiO_2 layers where plasmonic nanostructures were introduced. This project has been worked on together with my colleague Dr. Filip Ligmajer under the oversight of Assoc. Prof. Miroslav Kolíbal and with the electrochemistry insight of Dr. Aleš Daňhel from the Biophysical institute of Czech Academy of Sciences.

6.1 Introduction to electrochemistry

At the base of the electrochemistry is an interplay between electrical and chemical phenomena. The main focus is the study of chemical changes occurring under the passage of an electric current and the generation of electrical energy by chemical reactions. The relevance of this field is demonstrated by a large set of applications [325] like electroplating of metals, aluminium production, in devices such as sensors, batteries, and fuel cells, as well as its crucial role in other relevant effects like electrophoresis and corrosion [326].

Analytical use of electrochemistry is driven by an interest in chemical transformations, obtaining relevant, e.g., thermodynamic information about it, generation of unstable species and a study of their decay, or the presence of metallic or organic species in a solution.

Chemical reactions which involve electron transfer are generally referred to as redox (oxidation-reduction) reactions. These redox reactions are a result of simultaneously proceeding half-reactions, i.e., oxidation and reduction. During these reactions, the oxidation state of the reactants changes. The reactant which gains electrons (its oxidation number decreases) undergoes reduction and the reactant which loses electrons (its oxidation number increases) undergoes oxidation.[1] The redox reaction equation of n-electron process is highlighted in Eq. 6.1:

$$\mathrm{O} + n\mathrm{e}^- \underset{\text{oxidation}}{\overset{\text{reduction}}{\rightleftharpoons}} \mathrm{R}^{n-}, \tag{6.1}$$

where O stands for the oxidized and R for the reduced form of the redox couple which is typically dissolved in a liquid medium containing an ionic conductor (electrolyte). A study of the electron transfer between two phases, e.g., an electric conductor

[1] To remember the direction of the electron flow easier, it is useful to use the "OIL RIG" mnemonic, standing for Oxidation Is Loosing (electrons) and Reduction Is Gaining (electrons).

(electrode) and an ionic conductor (electrolyte) is at the centre of all the electrochemical systems. When the potential is applied to the electrode, an electric current flows as a result of events occurring at the interface.

In the electrode material, the charge is transferred via the movement of electrons and holes. The electrode can be metallic, either solid (Pt, Au) or liquid (Hg, amalgams), semiconducting (indium tin oxide, boron-doped nanocrystalline diamond) or from other materials (graphite). In the electrolyte phase, however, the charge is carried by a movement of ions. It is mostly liquid, aqueous or non-aqueous, and contains ions like Na^+, Cl^-, K^+, H^+. In case of a potential difference between the electrode and the electrolyte phase, sufficient conductivity of the electrolyte ensures that the potential change is localized almost entirely to the interface. It implies a very strong electric field at the interface which dramatically affects the behaviour of nearby charged redox species and drives their changes [326].

An electron behaviour inside a metal electrode can be descried considering its Fermi level E_F, which represents the energy of the highest occupied electron level [see Fig. 6.1(a-c)]. This level is not fixed and can be adjusted, e.g., by an application of an electric potential on the electrode with respect to the equilibrium conditions. An application of positive bias shifts the electrode's E_F to lower energies which allows electrons to flow from the reduced species into the empty electron levels of the same energy inside the metal, generating the anodic current. Conversely, a negative bias moves the E_F to a higher energy, thus the electrons can flow from the electrode into the vacant levels of the same energy related to the oxidized species, generating the cathodic current. Without the driving potential bias, the charges are exchanged between the two phases till the equilibrium conditions are reached as the common Fermi level is established [327].

Fig. 6.1(d-f) displays an analogous situation in the case of n-type semiconductor electrode. The obvious difference when compared to the metallic electrode dwells in the presence of bandgap in the semiconductor electrode band diagram which is framed by conduction and valence bands with respective energies E_C and E_V. Additionally, two kinds of mobile carriers can be distinguished here, negative electrons in the conduction band and positive holes in the valence band. The overall conductivity of a semiconductor electrode is much lower than a metal one. The equilibrium conditions established after the contact of the electrode with the electrolyte are generally accompanied by a formation of the space-charge region with a bending of both bands near the surface of the semiconductor. This affects the movement of the carriers from the bulk to the surface of a semiconductor. A positive bias applied to the electrode increases the band bending in the space-charge region even further and electrons can flow either over the barrier or tunnel through from the reduced molecules to the conduction band of the electrode. Upon a negative bias, the band-bending can be even reversed, making it easier for the electrons in the conduction band to occupy the vacant levels in oxidized redox molecules. Generally, the holes in the valence band can also participate in a charge transfer if there is

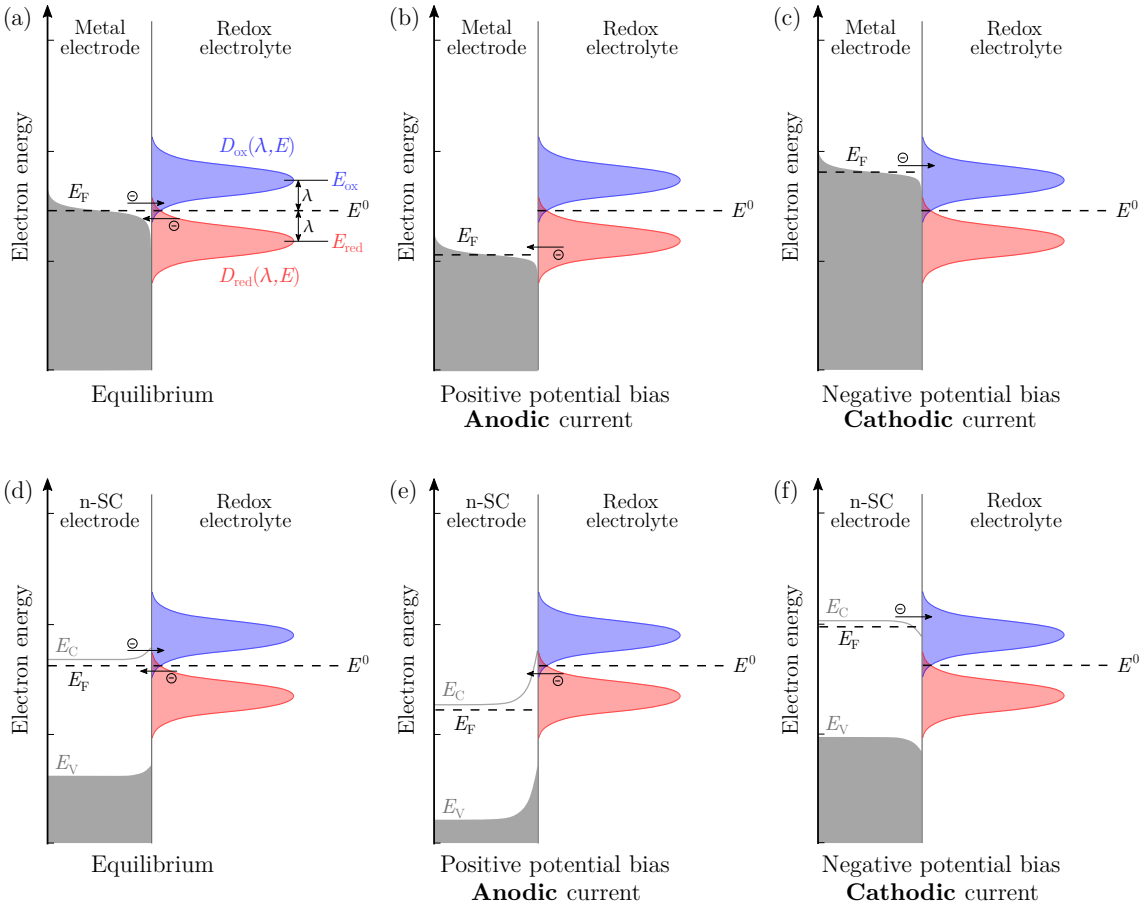

Fig. 6.1: Band diagrams of (a-c) a metallic (specified by the Fermi level E_F) and (d-f) an n-type semiconductor (specified by conduction E_C and valence E_V bands, and E_F) electrodes in contact with a solution containing the redox species characterized by a standard potential E^0. D_{ox} and D_{red} stand for a concentration density of the oxidized and reduced molecules with E_{ox} and E_{red} as the energies related to their peaks, λ is the reorganization energy. Electron energy levels are shown for three situations (a,d) equilibrium, (b,e) positive, and (c,f) negative applied potential bias in a metallic and semiconductor electrode.

an overlap between the electrode's valence band states and filled states in reduced redox molecules [328].

The band diagrams of the interfaces between the electrode and the electrolyte with redox species correspond to the classical Gerischer model [329, 330]. The standard electrochemical potential E^0 is analogous to the Fermi level of redox species. The density of states of the redox molecules is represented by the Gaussian distribution D_{red} for the reduced species (occupied electron levels) and D_{ox} for the oxidized species (unoccupied electron levels) with peak energies E_{red} and E_{ox}. Due to the ionic nature of the redox species, the solvent molecules (dipoles) are oriented around them according to the ion charge. Upon the oxidation of the reduced species, the electron is transferred very quickly to the electrode, while the reorganization process of the

solvent dipoles takes much longer. After the oxidation, the ion is less negative but the surrounding solvent dipoles are still oriented the same as before the transfer. The equilibrium is reached after the solvent dipoles relax and the corresponding energy difference corresponds to the so-called reorganization energy λ. Similarly, upon gaining an electron, it takes much longer to reorganize the solvent dipoles around the ion to reach the equilibrium again related to the energy λ. Note, that there is only one electronic state of the redox couple. D_{red} and D_{ox} are then only related to the probabilities of finding the empty or occupied state at the energy E. The energy difference thus comes only from the interaction of the redox ion with the solvent molecules [331].

The key equation of equilibrium electrochemistry is the Nernst equation (see Eq. 6.2) which can be written for the model redox couple with the concentrations [Ox] and [Red] of the oxidized and reduced species as:

$$E = E^0 + \frac{RT}{nF} \ln \frac{[\mathrm{Ox}]}{[\mathrm{Red}]}, \tag{6.2}$$

where E is the electrochemical cell potential, E^0 the standard potential of the redox system, R the universal gas constant, F the Faraday's constant, n the number of electrons transferred in the reaction, and T the thermodynamic temperature [332].

The Nernst equation sets the relation between the electrode potential and the concentrations of the respective components of the redox couple. It allows the prediction of how the system responds to the change either in the concentrations of the species in solution or to the potential applied to the electrode.

Since the potential related to the equilibrium conditions established between the electrode and the electrolyte is highly dependent on the electrode material and the electrolyte composition, it is necessary to have some fixed potential to refer to. One point of reference can be the vacuum level which represents the energy of a stationary electron outside of any material. If set to zero energy, the electron levels inside a material or molecule have a negative energy when compared to the vacuum level, since energy is required to free them from the material.

In electrochemistry, redox systems with stable and well-known electrochemical potentials are utilized as a reference. The normal hydrogen electrode (NHE) and standard hydrogen electrode (SHE) are the idealized reference electrodes (RE) defined by the redox potential of the hydrogen redox couple H^+/H_2 which is set to 0 V potential regardless of the solution conditions. More practical is the reversible hydrogen electrode (RHE) which takes into account solution pH and hydrogen pressure. Most common REs are based on Ag/AgCl (0.197 V vs. NHE) and saturated calomel electrode (SCE) based on Hg/Hg_2Cl_2 (0.241 V vs. NHE). Their respective potential scales are presented in Fig. 6.2. These systems are generally enclosed in a tube filled with electrolyte, typically KCl. The separation from the outer electrolyte is provided by a ceramic frit which allows only a minuscule current of ions to flow through without a significant mixing of the two electrolytes.

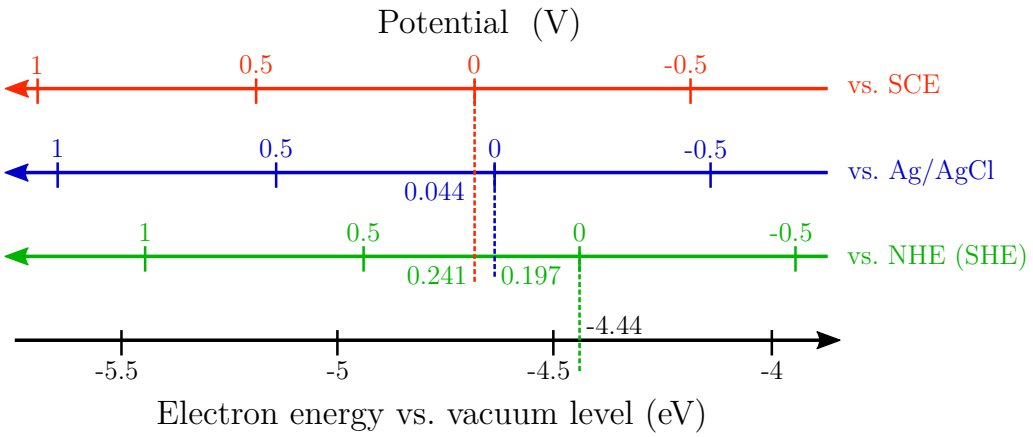

Fig. 6.2: Scales of the electric potential commonly used in electrochemistry, their respective potential offsets (for saturated KCl filling), and how are they related to the electron vacuum level energy which is an energy scale commonly used in physics. SCE stands for the saturated calomel electrode, NHE and SHE for the normal or standard hydrogen electrode. Based on [326].

The electrochemical reactions of interest occur on the electrode which is referred to as the working electrode (WE). The potential is applied (with respect to RE) and it drives the reactions near its surface resulting in changes in the current through the WE. The third electrode in this system, the so-called counter or auxiliary electrode (CE), completes the electric circuit with a vast majority of the current flowing between WE and CE. If oxidation of redox species takes place at the WE, then CE is subject to the reduction of the redox species and vice versa. The electrochemical setup utilizing all three electrodes, i.e., WE, CE, and RE, is operating in a three-electrode configuration. All three electrodes are submerged into a container with a supporting electrolyte, forming an electrochemical cell. Ideally, the RE should be very close to the WE to minimize the potential drop due to the electrolyte resistance. Note that a two-electrode system can also be used where CE and RE are formed by a single electrode. However, when larger currents flow through the CE/RE electrode, its reference potential might not be stable thus making the results more difficult to interpret.

The control over the potential applied to the working electrode and its stability is ensured by connecting the electrodes to the potentiostat. In simple terms, this device sets and maintains a potential difference between WE and RE while it can measure the current passing between WE and CE.

Fig. 6.3 shows a more detailed scheme of a typical potentiostat. At its centre, there is the electrochemical cell with the three electrodes and other electronic components including two operation amplifiers (op-amps), one with a high gain, and the other with a low gain. The voltage at the potentiostatic set point is set by the user as V_i and it is connected to the inverting input ε_- of the high gain op-amp. The output V_o provides magnified inverted voltage which is applied to the CE and

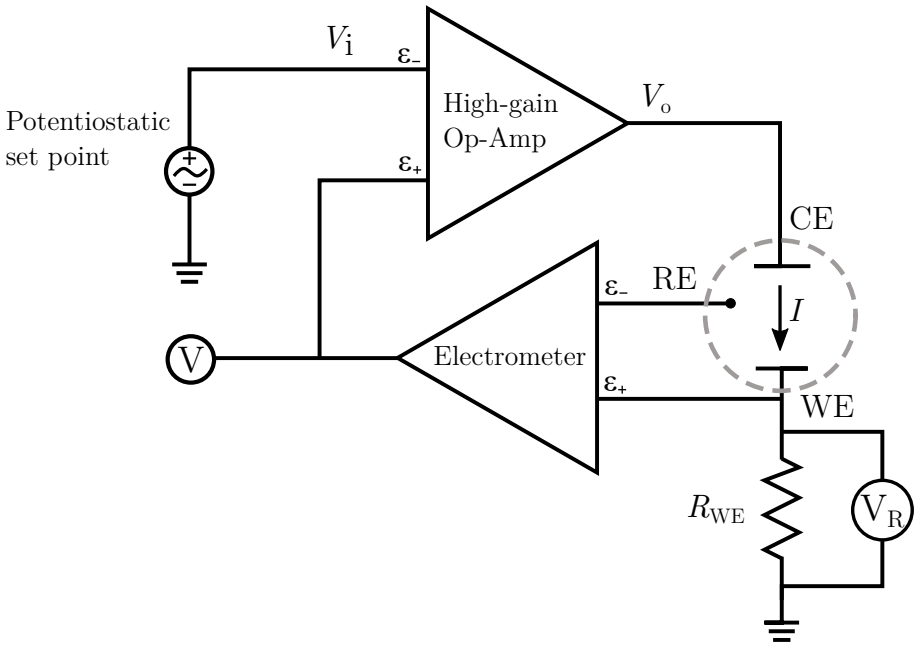

Fig. 6.3: A circuit diagram of a typical potentiostat used in electrochemistry. The dashed circle represents the electrochemical cell. Adapted from [333].

drives the current between CE and WE. This in turn results in a potential change on the WE with respect to the RE. RE and WE are connected to the inverting ε_- and non-inverting ε_+ inputs of the low-gain op-amp called electrometer (voltage follower). The output voltage of the electrometer represents the voltage difference between its inputs, i.e., between the RE and WE, and its value is then measured by the voltmeter V. This output is also fed back to the ε_+ input of the high-gain op-amp completing the feedback loop for the high-gain op-amp. Thus the current is driven between CE and WE until the potential difference between the WE and RE reaches the value set by the user.

The current I flows to the WE and through the resistor R_WE of known resistivity to the ground. The actual current value is then calculated from the voltage V_R measured on a resistor $R_\mathbf{WE}$ with a known resistance. Note that the current can not flow through the electrometer's inputs due to its inherently high input impedance [334]. In the following text, we will use the simplified notion of the potentiostat function, where a potential is applied to the WE and the current flowing between WE and CE is measured.

With the instrumentation described, we can move to the electrochemical methods. The examples of the most fundamental methods used in electrochemistry are outlined in Fig. 6.4. In general, some form of an electric potential stimuli is applied to the WE and the corresponding current response is recorded. In chronoamperometry, the current is recorded as a function of time upon a single or double potential step. The current decays exponentially with time obeying the Cottrell equation in relation to the decreasing concentration of a reactant near the electrode surface

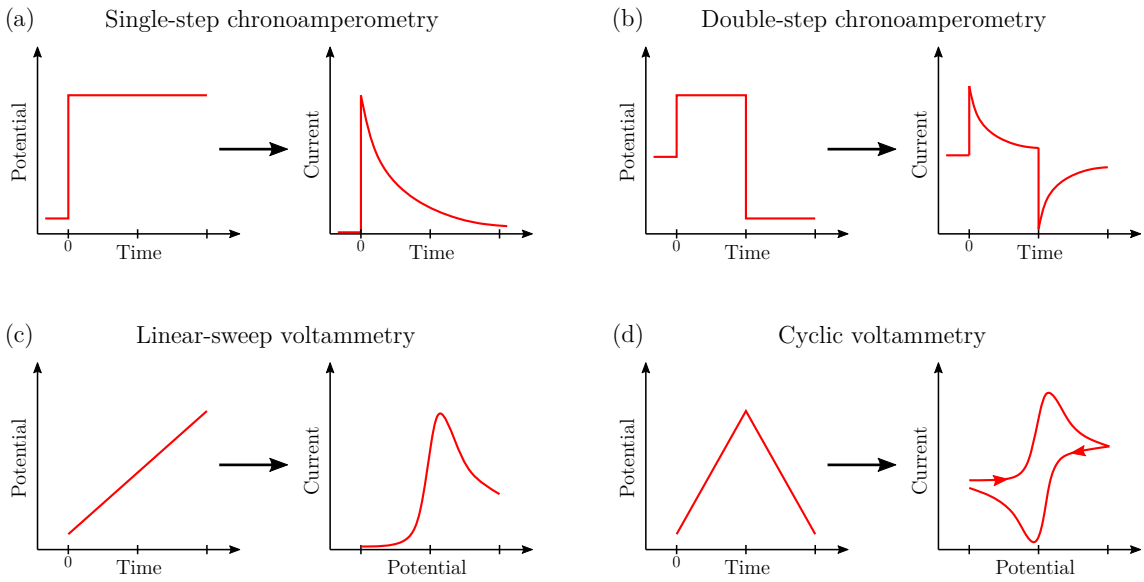

Fig. 6.4: Overview of basic electrochemical methods where a change in the electric potential is a driver for current response recorded with a potentiostat: (a,b) Amperometric methods – current response on a stepwise potential change, (c,d) voltammetric methods – current as a function of a continuous change of the applied potential.

[335]. Voltammetric methods, on the other hand, record the current as a function of a continually changing electric potential between two limiting values. The rate of the potential change, the so-called scan rate, is a crucial parameter of cyclic voltammetry. The resulting voltammogram shows a typical wave-shape in current as the potential is swept in one direction in the case of linear-sweep voltammetry and also the reversed current wave as it is swept back in the case of cyclic voltammetry. The advantage of these methods lies in characterizing the analyzed species in a wide range of potentials within a single experiment [336].

A more detailed understanding of the cyclic voltammetry can be drawn from Fig. 6.5. It shows a typical voltammogram recorded for the ferricyanide $[Fe(CN)_6]^{3-}$ (here abbreviated as Fe^{3-}) which can be reduced to ferrocyanide $[Fe(CN)_6]^{4-}$ (abbrev. Fe^{4-}). This redox couple, $[Fe(CN)_6]^{3-/4-}$ (abbrev. $Fe^{3-/4-}$), is one of the standard ones used very frequently to study the properties of working electrodes. The graphs surrounding the voltammogram display the concentration–distance profiles of both components – Fe^{3-} in blue, and Fe^{4-} in green colour, which change during the potential sweep according to the Nernst equation (see Eq. 6.2).

The potential is referenced with respect to the equilibrium potential $E_{1/2}$ [2] that is located between the peak potentials (points F and C) which is dependent on the experimental conditions but generally close to the standard redox potential E_0 of the redox couple. Typically, the starting potential is such that it doesn't drive any

[2] If potential $E_{1/2}$ is set to the WE, the Fe^{3-} will be reduced to Fe^{4-} until the concentrations $[Fe^{3-}] = [Fe^{4-}]$, and equilibrium is reached.

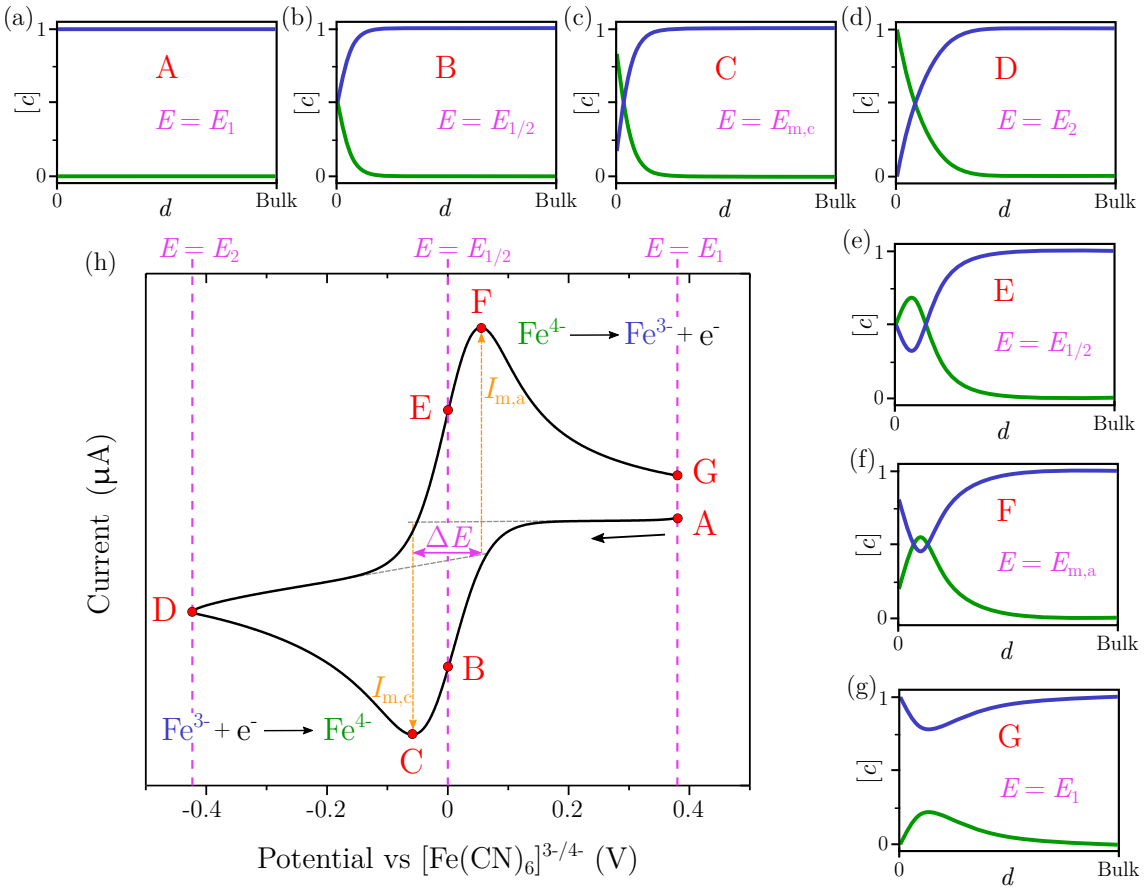

Fig. 6.5: (a-g) Normalized concentration profiles for $[Fe(CN)_6]^{3-}$ (Fe^{3-}, blue) and $[Fe(CN)_6]^{4-}$ (Fe^{4-}, green) as a function of the distance corresponding to various phases of the cyclic voltammogram highlighted by red dots. Note that the respective distance scale displayed is on the order of units to tens of micrometres. (h) Model voltammogram representing the Fe^{3-} reduction to Fe^{4-} with the maximum cathodic current $I_{\mathbf{m,c}}$ and back to Fe^{3-} with the maximum anodic current $I_{\mathbf{m,a}}$ with the potential separation ΔE. The voltammogram was recorded with a bare ITO electrode in 0.5 mM Fe^{3-} in the 0.1 M KCl electrolyte with the 100 mV/s scan rate. Inspired by [337].

change in the redox molecules, i.e., the current doesn't flow through the system. Here the potential sweep starts at the positive potential E_1 (point A) and goes to more negative potentials (cathodic scan) until it reaches E_2 (point D) from where it is swept in the opposite direction back to E_1 (point G). When the potential is swept to more negative values, Fe^{3-} is reduced to Fe^{4-} at the electrode, which is manifested by the flow of cathodic current and local depletion of Fe^{3-} close the electrode surface. At point C, where the maximum cathodic current ($I_{m,c}$) is reached, the current is limited by the diffusion of the fresh Fe^{3-} from the bulk solution to the depleted region near the electrode. Throughout the cathodic scan, the region near the electrode containing the reduced Fe^{4-} (diffusion layer) is growing. As the layer thickness increases, the mass transport of the Fe^{3-} to the electrode is slowed down, i.e., the diffusion rate is decreasing, which results in a decrease in the current magnitude as the scan continues from point C to D.

Upon reaching the E_2, the potential sweeping is reversed to the positive potential direction (anodic scan). While the Fe^{3-} was depleted near the electrode, the concentration of Fe^{4-} increased significantly. The Fe^{4-} can thus be oxidized back to Fe^{3-} resulting in a positive (anodic) current through the electrode as the potential becomes more positive. At the points B and E, i.e., at the potential $E_{1/2}$, the concentrations of Fe^{3-} and Fe^{4-} are equal at the electrode surface. The maximum anodic current ($I_{m,a}$) occurs at point F. Going to the higher potentials leads to further depletion of Fe^{4-} and to the current magnitude dropping to the starting potential E_1 (G) [337].

The potential separation between the two current peaks is caused by the diffusion of the redox molecules to and away from the electrode. For a fully-reversible single-electron diffusion-limited process, the peak separation ΔE should be around 57 mV. The maximum current can be determined from the Randles–Ševčík equation and its magnitude is a linear function of the square root of the scan rate [338].

Electrochemical analytical methods deliver precise information about the presence and amount of an analyte and allow fast in situ tracking of chemical pathways close to the electrode surface, while the instrumentation is kept relatively cheap and straightforward [339]. Recently, similarly to other established fields of research, electrochemistry has benefited from advances in nanotechnology. Examples include the utilization of metallic nanoparticles for a specific pathogen DNA detection [340], the use of carbon nanotubes to enhance the overall electrochemical signal [341] or single nanobjects serving as nanoelectrodes [342].

6.2 A study of WS_2 nanotubes with Au nanoparticles

A very promising class of materials are transition metal dichalcogenides (TMDs) which represent a class of 2D materials of the MX_2 type, where a layer of transition metal atoms M (e.g., Mo or W) is sandwiched between two layers of chalcogen atoms X (e.g., S, Se or Te) [343]. The metal atom layer is strongly bound to the

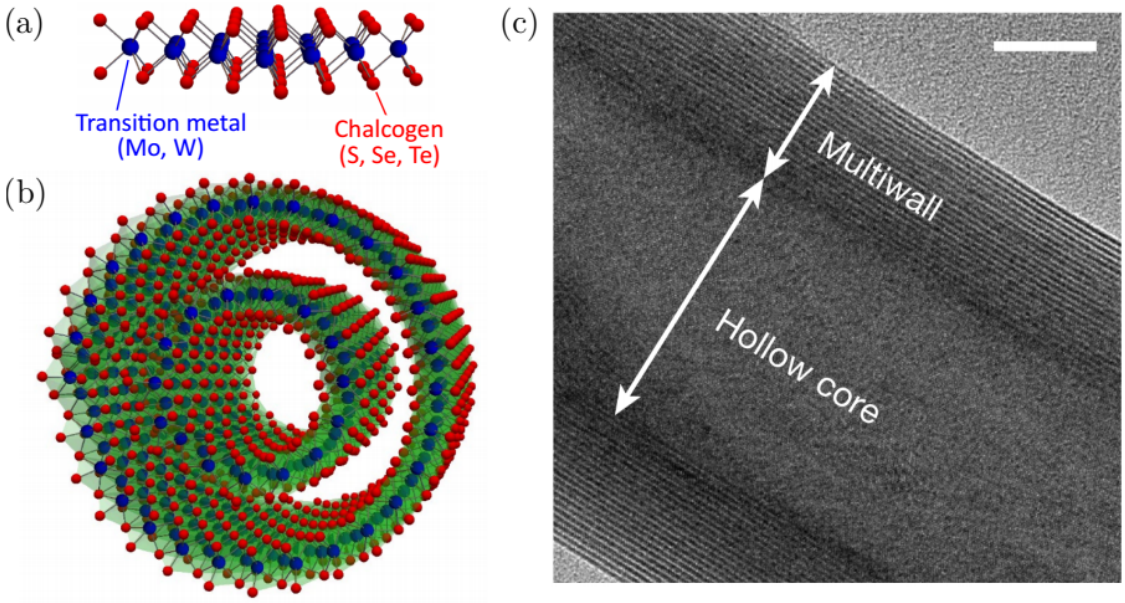

Fig. 6.6: (a) Monolayer atomic structure of a general transition metal dichalcogenide in the planar configuration, (b) TMD in the form of a multilayer nanotube, where blue and red dots represent transition metal atoms (e.g., Mo, W) and chalcogen atoms (e.g., S, Se, Te), respectively. c) TEM image of a typical hollow-core multilayer WS_2 nanotube. The scale bar corresponds to 10 nm. Adapted from [349].

two chalcogen atom layers by covalent bonds while the interlayer bonds between MX_2 slabs are generally of a weak van den Waals type, which enables exfoliation of TMDs down to a single layer [344]. Choosing the appropriate combinations of M and X atoms allows the formation of materials with profoundly different properties [345].

Also the structural phase of TMDs, most common being 1T, 2H, and 3R polymorphs, can play a big role in its properties. Here, the numeric value specifies the number of layers in the crystallographic unit cell and the letter represents the type of symmetry where T stands for tetragonal, H for hexagonal and R for rhombohedral symmetry. A monolayer TMD can have an octahedral phase 1T that is generally unstable and exhibits metallic behaviour or trigonal prismatic 1H which is more stable and has a semiconducting nature. 1H layers can be stacked in two ways depending on the stacking sequence as either 2H or 3R polymorphs [346]. A transition between the outlined structural phases can be achieved [347] and additional exotic metastable phases can be synthesized [348].

As was seen previously with graphene, dramatic changes in properties were observed going from bulk graphite to a monolayer graphene [350] which then exhibits extraordinary electrical [351] and optical properties [352]. Unlike graphene which is a semi-metal with a zero bandgap [353], TMDs have mainly a semiconducting character with a non-zero bandgap.

Their common characteristics are extraordinary mechanical, electrical, and optical properties, especially in a monolayer form where it becomes a direct bandgap semiconductor [354]. Due to their properties, TMDs are used, e.g., in tribology [355], for the fabrication of electronic devices [356, 357], and as single-photon emitters [358]. 2D TMDs also exhibit a promising electrochemical activity [359] with edges more active than the basal planes [360], which was utilized for hydrogen evolution [361], supercapacitors [362], biodetection [363], and photocatalysis [364].

Recently, rapid progress in understanding 2D TMD morphologies has sparked interest in new research opportunities, moving beyond 2D layers, e.g., to quantum dots, nanoribbons, and nanotubes [365].

Most studied representatives of TMDs, MoS_2 and WS_2, have already been synthesized in the form of nanotubes (NTs) [366, 367]. These NTs exhibit a plethora of interesting properties like superconductivity [368], thickness-dependent bandgap [369, 370], robust cathodoluminescence [371], nonlinear response [372], even strong light–matter interaction [373, 374], and can be utilized in energy research as well [375].

Additionally, WS_2NTs also exhibited compelling photo-induced currents observed upon illumination [376, 349] hinting at a promising future in photoelectrochemistry and photocatalysis.

We set out to explore the inherent electrochemistry of WS_2NTs followed by an observation of their response upon illumination. Besides the study of WS_2NTs in their natural form, we explored a hybrid complex of WS_2NTs decorated with AuNPs which may introduce additional functionalities, e.g., in generating hot charge carriers (see Section 2.4).

6.2.1 WS_2NT electrode preparation

To study the electrochemical properties of electrodes as well as their response upon illumination, a conventional three-electrode electrochemical cell design [Fig. 6.7(a)] which is usually quite bulky and does not allow light transmission, was modified. We have developed a closed-volume electrochemical cell [Fig. 6.7(b)] that is smaller, transparent, integrable into an optical microscope and has a liquid inlet and outlet for a facile liquid exchange. At the same time, our design provides the electrical connections needed to perform electrochemical experiments in a three-electrode setup. Such a design could be easily integrated into an optical microscope to possibly conduct simultaneous optical and electrochemical experiments. Nevertheless, the vast majority of the actual experiments were conducted out of the microscope, therefore, we used a conventional open electrochemical cell which allowed an easier electrolyte and working electrode exchange. The design was slightly modified to become optically transparent, thus allowing an introduction of light to the bottom side of the cell when needed.

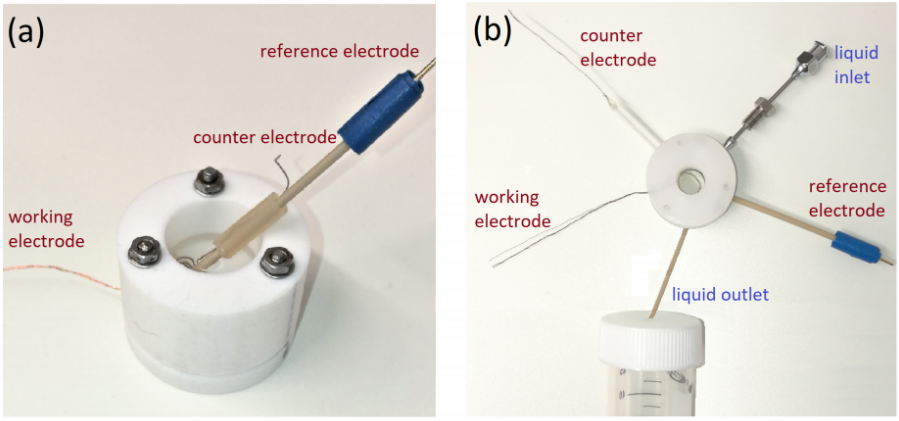

Fig. 6.7: (a) Conventional and (b) closed-volume electrochemical cell: Ag/AgCl reference electrode, coiled Pt wire as counter electrode and transparent ITO-covered glass with a copper contact cable attached as the working electrode. Note that (b) allows simultaneous electrochemical and optical measurements with the solution easily exchangeable using the liquid inlet/outlet.

We used a platinum wire loop (Alfa Aesar) as a counter electrode, leakless miniature Ag/AgCl reference electrode (Edaq Co.) and indium tin oxide (ITO)-covered glass ($\sim$ 180 nm, Delta Technologies) as a conductive and transparent working electrode. In further experiments, the ITO-covered glass was modified by electrochemically and plasmonically active substances. The electrical control over the electrodes was attained using a PalmSens potentiostat (later substituted by CHI 706E potentiostat).

For the WE functionalization, we had chosen WS_2 multiwall nanotubes [Fig. 6.6(c)] to study their inherent electrochemical properties. WS_2NTs, typically 50–200 nm in diameter and 1–10 µm long, were provided by Prof. Reshef Tenne's group from the Weizmann Institute of Science [377].

A dry powder of these NTs was dispersed in various solvents using an ultrasonic bath and simply drop-cast onto an ITO substrate to achieve the best possible homogeneity as well as the coverage of the substrate while maintaining proper contact between the NTs and the substrate. We tested solvents of various polarities ranging from nonpolar cyclohexane over the sulphur-containing thiophene to polar solvents like water and acetone [378]. The resulting dispersions were then applied onto ITO substrates, cleaned previously in ultrasonic baths of acetone, isopropylalcohol (IPA), and deionized water, and left to dry. Fig. 6.8 shows the results for seven solvents for which the solubility of WS_2NTs differed dramatically. Generally, the solubility of WS_2NTs in polar solvents was much higher and the resulting dispersions were more stable, especially the IPA and acetone. The outcome of the the drop-casting deposition, examined in a dark-field optical microscope, revealed that with polar dispersions the coverage was higher with far better homogeneity. Arguably the best results were obtained with acetone but related analysis by a surface-sensitive low-

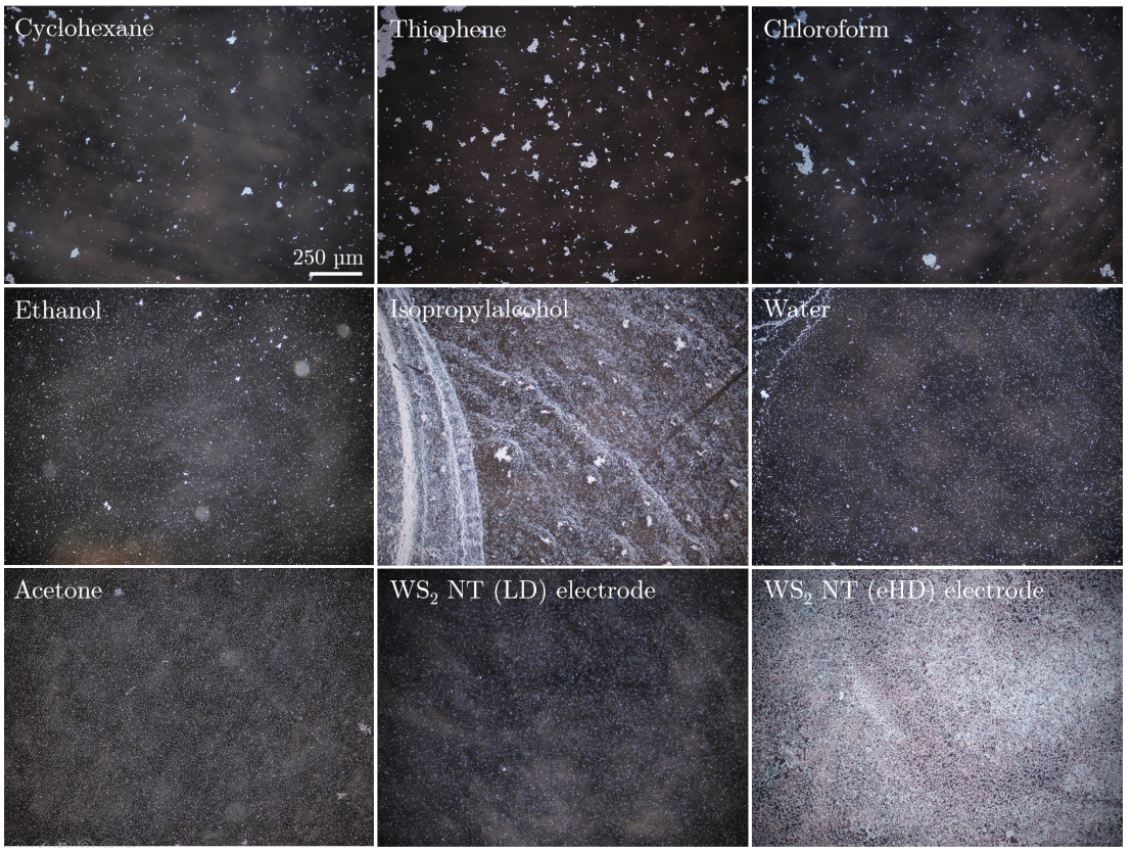

Fig. 6.8: Optical images of WS_2NTs (white spots) on ITO substrate (dark background) via a dispersion of WS_2NT powder in various solvents noted in the images. The solvents are ordered by their dipole moment as a measure of polarity from the lowest one (cyclohexane, nonpolar) to the highest one (acetone, polar). The inhomogeneity of the sample deposited from IPA shown here is due to a higher concentration of WS_2NTs in solution, but at lower concentrations, it is a viable solvent. WS_2NT (LD) and WS_2NT (eHD) are actual electrodes prepared by spincoating of the IPA dispersion and by immersion through liquid–liquid interface, respectively.

energy ion scattering technique showed organic residues left on the sample after the acetone solvent evaporation, therefore, acetone was not used eventually.

For the sake of homogeneity, we had chosen to use a spin-coating technique instead of the drop-casting mentioned above. For this purpose, IPA was used as a solvent due to its high volatility which was found to be crucial for the spin-coating deposition. Additionally, the deposition results could be further improved by increasing the ITO hydrophilicity via oxygen plasma treatment [379] (80 % O_2, 20 % Ar) but the resulting electrochemical performance of such substrates was notably worsened and it will be addressed further in the text.

Two concentrations of WS_2NTs dispersions (approximately 4 and 1 mM) were prepared and 40 µl of the respective dispersions were subsequently applied onto a spinning ITO at 500 rpm to spread the solution and 4000 rpm to remove the residues

building up close to the edges of the ITO. Thus, two series of samples with different concentrations were prepared by spincoating – high (HD) and low density (LD) WS_2NTs were prepared for further electrochemical studies. Additionally, extra high density (eHD) NT samples were prepared via the separation of WS_2NTs on a liquid-liquid interface of two immiscible liquids [380]. WS_2NTs were dispersed in deionized water, mixed with a half volume of cyclohexane and sonicated for about 10 min. The immiscible phases separate quickly afterwards and at the interface, a thin layer with a high concentration of NTs is formed. Submerging the ITO below the interface and slowly pulling it out, results in a very dense WS_2NT coverage of the ITO (see Fig. 6.8). We have also prepared electrodes containing 20 nm colloidal AuNPs (BBI solutions, citrate-stabilized) for comparison as an example of metallic nanomaterial functionalization. These samples were prepared by a 2 h-long self-assembly on ITO in a colloid solution modified by HF acid (2.5 mM final concentration).

Note that we have also tested additional approaches to the WS_2NT deposition exploiting a small negative charge of the NTs in neutral solvents [381], e.g., in self-assembly on the ITO surface submerged in the water-based NT dispersion. When the solution pH was decreased, the coverage of the WS_2NTs on the ITO increased noticeably, nevertheless, the coverage was still relatively low. A few tests were also done utilizing the electrophoretic deposition of WS_2NTs on the ITO surface. A positive potential was applied (5/10 V) on the ITO with respect to a metal plate counter electrode for various conductivities of water (deionized, or with KCl), while the lower the conductivity, the higher the coverage and less damage visible. The resulting coverage was very high but there was an uncertainty about the damage induced by the high voltage application, so none of these approaches were used for electrode preparation.

6.2.2 WS_2NT electrochemistry

At first, we needed to determine the suitability of bare ITO itself as an electrode in the electrochemical experiments. It was assessed by performing a cyclic voltammetry with the aqueous 0.1 M KCl electrolyte obtaining a so-called potential window which determines the potential range where the ITO does not undergo any irreversible changes [382]. That means finding the potential limits defined by ITO stability together with the hydrogen reduction limit at negative potentials and water oxidation limit at positive potentials [383]. The resulting curve (orange curve in Fig. 6.9) highlights the potential window with no significant current increase, only at the maximum and minimum potentials, respectively. Therefore, the ITO is stable at potentials ranging from -0.5 V[3] to 1.5 V in the 0.1 M KCl electrolyte. With WS_2NTs and AuNPs, the potential window decreases to about 0.8 V at positive potentials,

[3]The current starting at -0.4 V is a result of reduction of O_2 present in the aqueous electrolyte, which could be removed, e.g., by nitrogen purging [384], and thus further increase the bottom limit in negative potential region.

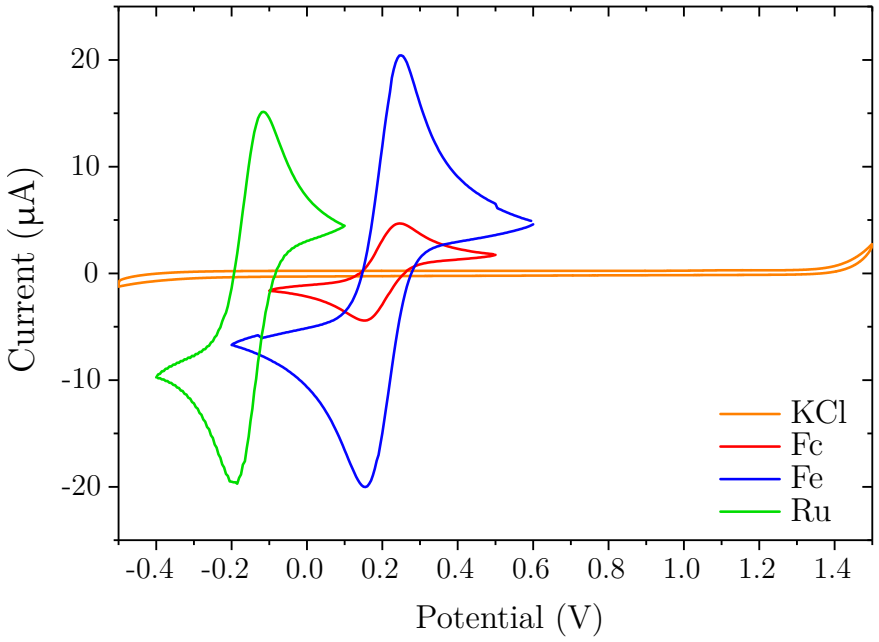

Fig. 6.9: Cyclic voltammograms recorded with the bare ITO electrode: in the standard 0.1 M KCl electrolyte (orange) to define the potential window of bare ITO, in the 0.1 mM methylferrocenemethanol redox probe (denoted as Fc – red), in 0.5 mM hexacyanoferrate (Fe – blue) and in 0.5 mM hexaaminruthenium redox couple (Ru – green). All redox couples are dissolved in the aqueous 0.1 M KCl electrolyte.

where both materials start to oxidize. Note that the widest potential windows can be found in a boron-doped nanocrystalline diamond electrode [385].

In order to study the unknown electrochemical properties of our electrodes, we have chosen three standard redox couples to probe our system. These organometallic compounds, which consist of a metallic atom centre surrounded by organic groups, can be easily oxidized (by losing an electron) or reduced (by accepting an electron) in a reversible manner [386]. Thus, it can be used to study various electrochemical aspects of our electrodes. They can differ by an overall charge which affects the electrostatic attraction towards the electrode, by the standard redox potentials, or by electron transfer mechanisms. In terms of the electron transfer mechanism, redox molecules can be organized into two main categories: inner-sphere and outer-sphere redox molecules [387]. The outer-sphere redox molecules do not require adsorption to the electrode surface to exchange electrons and thus are not sensitive to the electrode surface impurities or surface defects but rather to the electron density of states. The inner-sphere redox molecules, on the other hand, need to adsorb on the surface and thus are sensitive to the moieties present at the electrode surface [388].

As a representative inner-sphere redox couple, negatively-charged hexacyanoferrate $[Fe(CN)_6]^{\mathbf{3-}/4-}$ (in further text denoted as Fe) was chosen. From an outer-sphere redox couples, neutral methylferrocenemethanol $[MeFcMeOH]^{\mathbf{0}/+}$ (denoted as Fc) and positively-charged hexaammineruthenium $[Ru(NH_3)_6]^{\mathbf{3}+/2+}$ (denoted as

Tab. 6.1: A summary of used redox couples with their characteristic properties. The charge of the molecule written in bold corresponds to the original state of the used redox couple.

	$[MeFcMeOH]^{\mathbf{0}/+}$	$[Fe(CN)_6]^{\mathbf{3}-/4-}$	$[Ru(NH_3)_6]^{\mathbf{3}+/2+}$
Name:	Methylferrocene-methanol	Hexacyanoferrate	Hexaamine-ruthenium
Abbreviation:	Fc	Fe	Ru
Concentration:	0.1 mM	0.5 mM	0.5 mM
Charge transfer:	outer-sphere	inner-sphere	outer-sphere
E_0 (vs Ag/AgCl):	195 mV [389]	230 mV [390]	-150 mV [391]

Ru) were chosen. All these redox probes were dissolved in aqueous 0.1 M KCl to make sure the resulting solutions are conductive and their properties are summed in Tab. 6.1. Fig. 6.9 shows their respective cyclic voltammograms recorded with the bare ITO working electrode.

Measuring the cyclic voltammograms at various scan rates (5–1000 mV/s) provides information about an electrode charge transfer kinetics which can be assessed regarding two experimental parameters: maximum current magnitude I_m and electric potential difference ΔE between the cathodic and anodic current maxima [see Fig.6.5(h)].

I_m should be proportional to the electrode active surface area and ΔE reflects the rate of the charge transfer. In a fully reversible system, where the current is limited by diffusion processes and not by the charge transfer kinetics, I_m depends linearly on the square root of the scan rate fulfilling the Randles-Ševčík equation. ΔE in a fully reversible single-electron transfer system should be around 57 mV regardless of the scan rate while larger values suggest a slower charge transfer or its irreversibility.

In our experiments, cyclic voltammograms were recorded for all the scan rates with one redox species, then a fresh working electrode was used for another redox species to have the same starting conditions. The results of CV analysis (Fig. 6.10) show that the additional material present at the electrode surface improves the maximum current I_m compared to bare ITO with Fc and Fe redox molecules. Additionally, the WS_2NT (HD) and AuNP electrodes exhibit almost ideal linear dependence of the I_m on the square root of the scan rate. This can be explained by the increased electrode surface area by the additional semiconductor or metallic nanomaterial present at the ITO surface. Nevertheless, as the WS_2NTs (LD) and (HD) show an increasing current with the coverage, (eHD) electrodes show a significant decrease again. This might be due to imperfect contact between NTs and the ITO as they are often laying on top of each other having either partial or no direct contact with the ITO which hinders the charge transfer towards it. Another possible cause of the worsened charge transfer capabilities could come from plasma treatment of bare ITO before WS_2NTs (eHD) preparation (see Fig. 6.11).

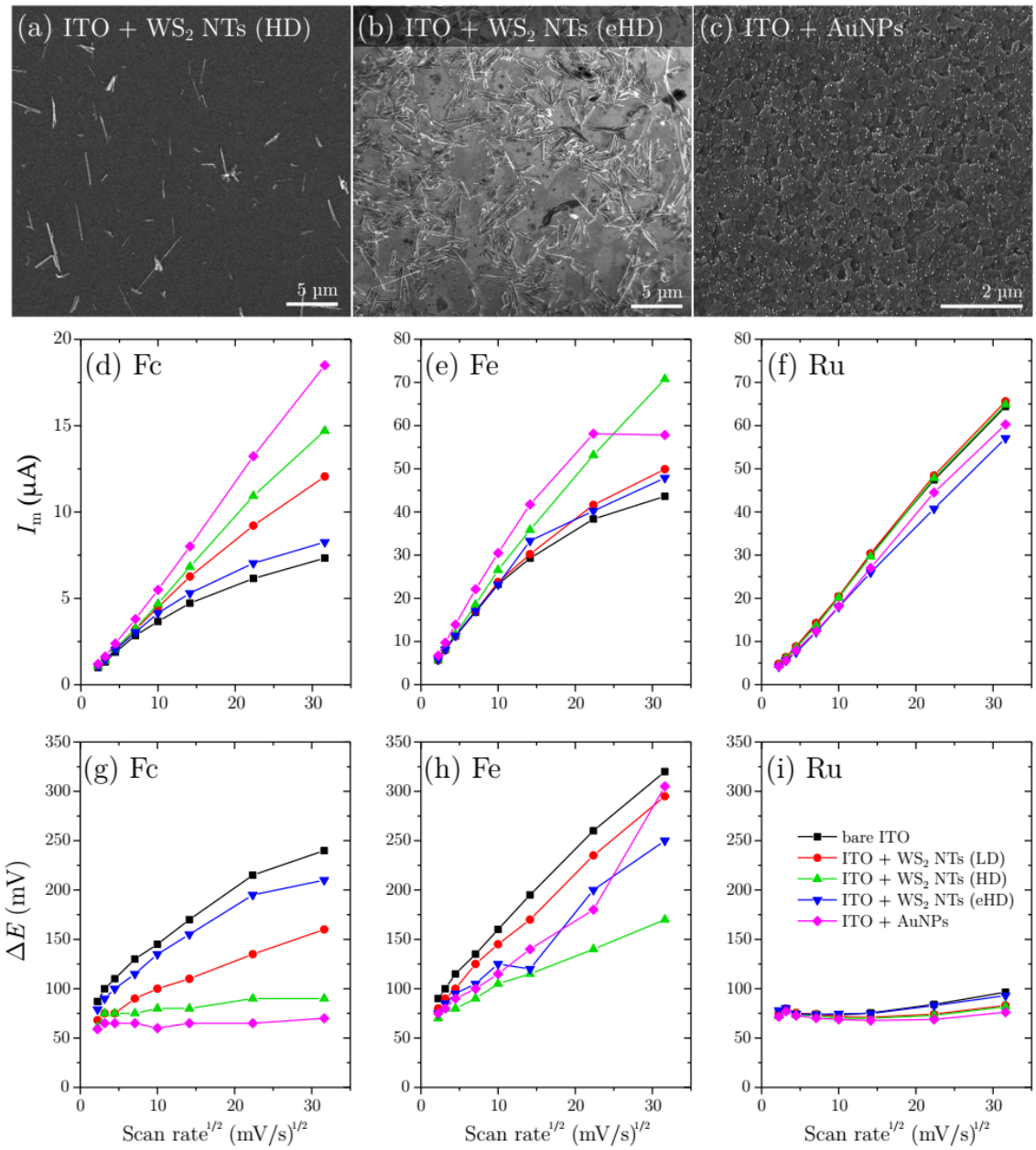

Fig. 6.10: (a,b,c) SEM images of used electrodes, (d,e,f) maximum of anodic current (I_m) and (g,h,i) potential separation between anodic and cathodic current peaks (ΔE) extracted from cyclic voltammetry performed with ITO electrodes functionalized by WS_2 NTs of various coverages - low (LD), higher (HD), and extra high (eHD) density, and with 20 nm AuNPs.

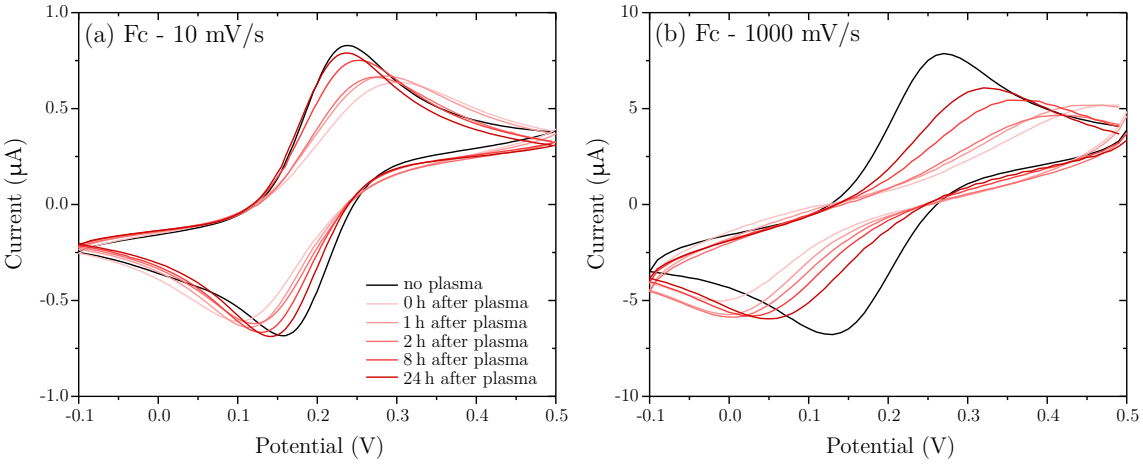

Fig. 6.11: The effect of plasma treatment prior to the cyclic voltammetry with voltammograms recorded at (a) slow scan rate of 10 mV/s and (b) fast scan rate of 1000 mV/s using the 0.1 mM Fc redox couple in 0.1 M KCl. The black curves represent the bare ITO electrode without plasma treatment while the curves with different shades of red color correspond to the ITO which underwent a 5 min plasma treatment with different delays between the procedure and cyclic voltammetry recording.

In the case of Ru, all electrodes exhibit ideal linear dependence of I_{m} and the observed differences among electrodes are rather small thanks to the inherent insensitivity of Ru to the electrode surface. Although a similar behaviour of I_{m} should be observed in the case of Fc due to its outer-sphere nature, eventually, it turned out to be rather sensitive to the electrode surface. Nevertheless, there are still some disputes about the exact charge transfer mechanism and some form of an adsorption process might play a role [392].

In terms of ΔE, a significant decrease when compared to the bare ITO can be seen in the presence of WS_2NTs (especially HD) and AuNPs, which is related to the improvement of charge transfer kinetics with Fc and Fe redox molecules. With the Fc redox molecules, WS_2NTs (HD) and AuNPs approach the ideal 57 mV value while with Ru all electrodes are close to that value.

Although our electrodes with the redox probes did not result in a fully reversible electrochemical system, the overall performance of the electrodes was vastly improved by the presence of WS_2NTs, thus confirming their benefit to the charge transfer kinetics. Further improvement might be achieved by an optimization of the WS_2NT amount present on the ITO surface.

Only later, we had observed some negative effects of ITO plasma treatment on the electrochemical performance of bare ITO electrodes. Plasma treatment is often used to remove organic contamination and to increase the polarity of the surface [379]. Fig. 6.11 shows a comparison of cyclic voltammograms recorded in the 0.1 mM Fc solution with 0.1 M KCl for a regular untreated bare ITO electrode and those which undergone a 5 min plasma treatment by O_2/Ar (80/20 %) plasma (Low-pressure

plasma resist stripper Diener Nano, 300 W). At a low scan rate of 10 mV/s, the voltammogram recorded right after plasma treatment showed a slight decrease in the peak current and an increased potential separation between the peaks, suggesting slightly worsened charge transfer properties. After about 24 h from the treatment, the detrimental effects basically disappeared. At faster scan rates, the negative effects of plasma treatment are much more pronounced and at 1000 mV/s the anodic peak almost disappears showing a substantial decrease in the maximum current and a dramatic increase of the potential separation between the peaks hinting at significantly worsened charge transfer capabilities of the electrodes. The detrimental effects tend to be rectified with an increased time delay between the treatment and CV recording.

These effects might be related to the nature of conductivity of ITO, which is a highly-doped degenerate n-type semiconductor due to the Sn doping and oxygen vacancies present [393]. Oxygen plasma significantly increases the oxygen amount at the surface thus depleting the vacancies and also slightly decreases the Sn content which could result in worsened charge transfer capability of the ITO surface [394]. Nevertheless, given enough time, the properties of plasma-treated ITO might return to those of untreated ITO, and not be detrimental at least for the slow charge transfer processes. Unless it is mentioned explicitly, we didn't use plasma treatment on our electrodes.

6.2.3 AuNP-WS_2NT photoelectrochemistry

After the analysis of the electrochemical properties of WS_2NTs as an electrode material, we moved to the observations of photo-induced effects in bare WS_2NTs and in combination with plasmonic nanoparticles. To introduce the plasmonic element into our system, we decorated the WS_2NTs with AuNPs according to the chemical procedure described in Ref. [395]. Briefly, 2.6 mg of powdered WS_2NTs were dispersed in 2 ml of IPA using an ultrasonic bath for about 5 min with mechanical shaking after every minute. The WS_2NT dispersion was then added into 14 ml of boiling aqueous solution of $HAuCl_4$ with varying concentrations. The resulting WS_2 concentration in 16 ml of the total solution volume was about 0.65 mM which was kept the same between experiments while the concentration of $HAuCl_4$ was adjusted to achieve a specific $HAuCl_4/WS_2$ molar ratio. The solution was stirred vigorously and, after the WS_2 addition, boiled for three more minutes before cooling down to room temperature. Such a procedure resulted in WS_2NTs decorated with AuNPs (AuNP-WS_2NT complex) whose mean size could be adjusted in a range from approximately 15 nm to 5 nm by varying the $HAuCl_4/WS_2$ molar ratio correspondingly in the range from 1:5 to 1:20 (Fig. 6.12). We generally utilized the 1:7 or 1:10 ratios resulting in AuNPs of about 10 nm diameter, and 10 µl of this aqueous solution was then drop-cast onto a cleaned ITO substrate and left to dry undisturbed in a closed gel pack.

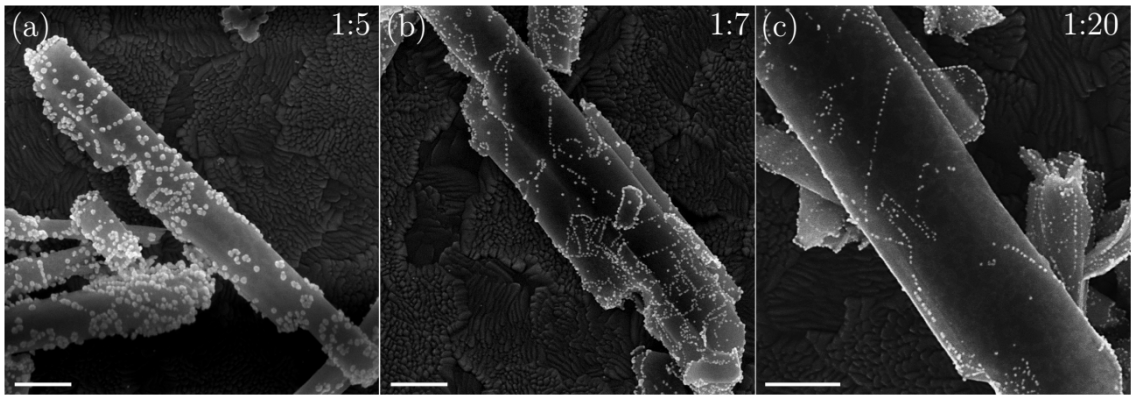

Fig. 6.12: WS_2NTs after the decoration by chemically synthesized AuNPs. The variation of AuNP sizes was achieved by mixing a fixed amount of WS_2NTs with different concentrations of $HAuCl_4$ leading to $HAuCl_4/WS_2$ ratios of (a) 1:5, (b) 1:7, and (c) 1:20. The scale bars correspond to 200 nm.

With this AuNP-WS_2NT heterostructure, as well as the individual components, we performed electrochemical experiments while the electrodes were illuminated from the bottom side by laser light with three different wavelengths: blue (450 nm, 2.76 eV), green (532 nm, 2.33 eV), and red (650 nm, 1.91 eV). Generally, the power was set to 60 mW for all lasers, unless specified otherwise. Cyclic voltammograms didn't provide significant differences when recorded with or without illumination as the photo-induced current was minuscule when compared to the current magnitudes observed in cyclic voltammetry. Thus other electrochemical methods were utilized: chronoamperometry (CA, see Section 6.4) and measuring the open circuit potential (OCP).

As opposed to CV, where the electrical potential at the working electrode is swept continuously, in chronoamperometry the working electrode potential is fixed and the electric current is measured in time. The (background) current caused by applying the potential step on the electrode and forcing the system out of equilibrium decreases with time as the reactant gets continually depleted near the electrode surface. As the background current decreases, introducing alternating illumination and darkness time intervals, it is much easier to observe the photo-induced current due to laser illumination. The open circuit potential corresponds to the equilibrium electric potential which is reached for a given electrode/redox molecule system when no current flows between the CE and WE. The response upon alternating illumination is a photo-induced voltage (photovoltage) at the electrode which represents the electrode's ability to accumulate the charge despite the charge recombination [396]. This results in shifting the electron Fermi level energy which is sensed by the electrode and can be recorded as a function of time. Change of the OCP to a more negative (positive) potential generally corresponds to electron (hole) accumulation in the electrode which translates into the shift of its Fermi level to higher (lower) energies.

In all the OCP experiments, after adding the electrolyte, the system was let to settle in the dark conditions for at least 6 min before the light was introduced in 10 s intervals alternating with 10 s of the dark conditions. We started with the 650 nm laser and after a desired number of repetitions, the solution was stirred to return to the initial conditions while the same procedure was repeated with the 532 nm and 450 nm light respectively. First, the control OCP experiments were performed to try to separate the contributions of individual components to the overall response of AuNP-WS_2NT complex system. Fig. 6.13 sums the changes in OCP upon illumination in pure KCl and with Fc molecules. Additionally, the respective band structures are outlined together with energy levels related to the Fc redox molecules and the levels available in pure water. Three main redox reactions can occur in water: HER represents the hydrogen evolution reaction (reduction, $2H^+ + 2e^- \rightarrow H_2$), ORR stands for oxygen reduction reaction (reduction, $O_2 + e^- \rightarrow O_2^-$), and OER for oxygen evolution reaction (oxidation, $2H_2O \rightarrow O_2 + 4H^+ + 4e^-$).

In the charts showing the OCP response, the curve colour represents the respective laser light introduced. The absolute OCP values observed with respect to the Ag/AgCl electrode were generally in the range from 0.15 to 0.25 V. The background OCP was subtracted to see only the changes due to the illumination.

In the case of bare ITO [Fig. 6.13(a–c)], there is a decrease of OCP upon illumination, suggesting an electron accumulation in the conduction band of ITO which is in line with ITO being an n-type semiconductor in nature. Although the energy of the used light is lower than the bandgap (4 eV), due to doping there are mid-gap defect/surface states present from which the electrons can be excited to the conduction band. The positive holes left behind could then participate in the oxygen evolution reaction.

With pure KCl, the decrease of OCP is gradual and it seems to reflect the laser light energy inducing a larger negative change in OCP with higher energy of the incoming photons. Possibly, the higher the photon energy, the larger the number of defect states from which the electrons can be excited to the conduction band. More electrons are accumulated in the conduction band while holes can participate in some oxidation reactions, such as an oxygen evolution reaction. Consequently, this results in a negative change in the OCP. In the case of the 650 nm light, the OCP drop stabilizes after about 5 s, while for the 532 nm and 450 nm light a stable value is not reached within the 10 s interval, suggesting rather slow charge transfer processes. After switching off the illumination, the OCP rises back to approximately the initial position. In the presence of the Fc redox molecules, the OCP response is negative while its magnitude is typically reduced, probably due to additional electron levels available in the electrolyte. The excited electrons can thus participate in Fc^+ reduction making the overall electrode charging less pronounced for red and blue lasers.

The OCP response of AuNP-covered ITO [Fig. 6.13(d–f)] upon illumination with red and green light was rather similar to the bare ITO across all solutions. The

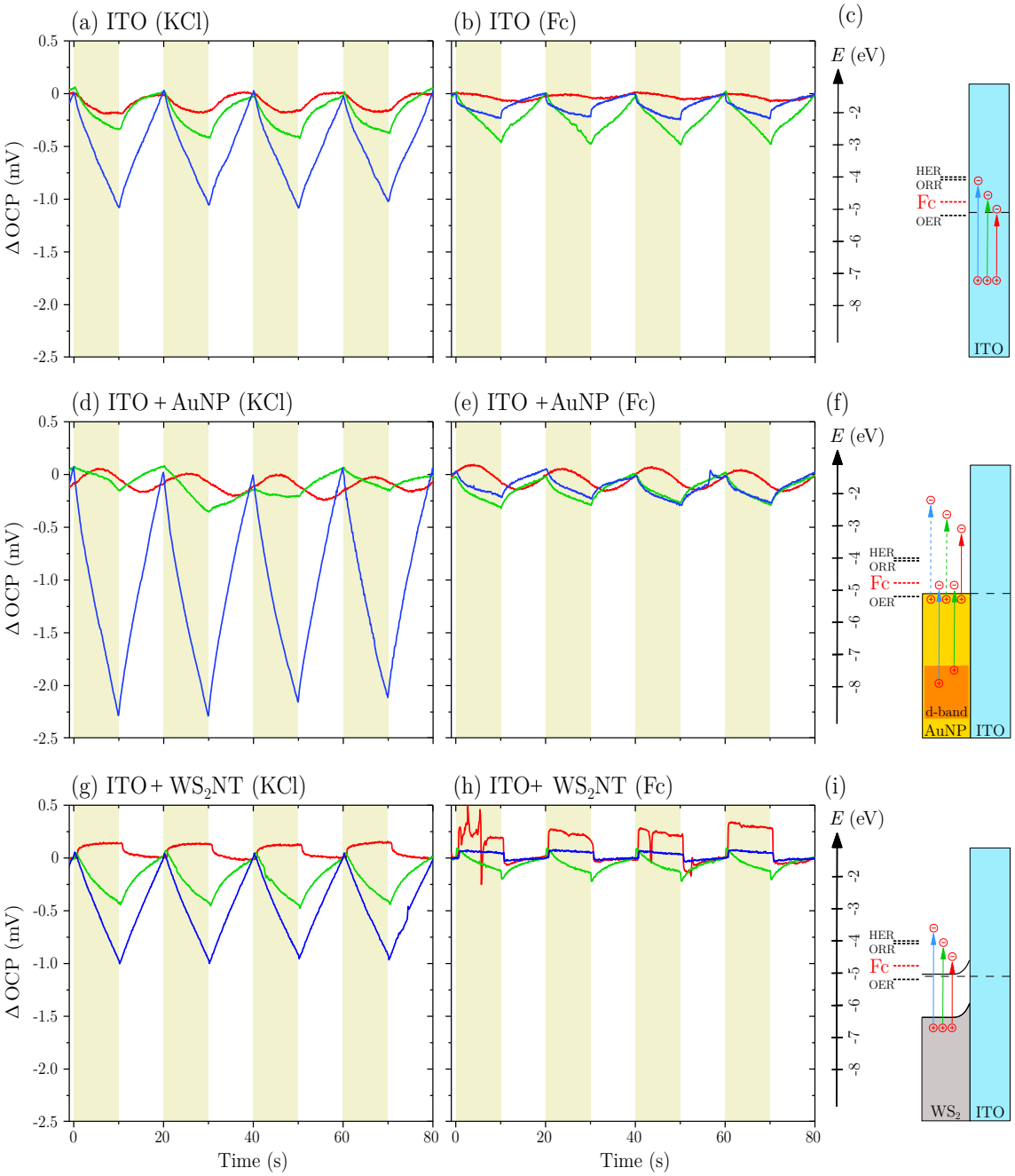

Fig. 6.13: Open circuit potential response upon alternating 10 s-illumination intervals provided by 60 mW lasers recorded in 0.1 M KCl base electrolyte (left panels) and in the presence of 0.1 mM Fc redox molecules (right panels) for various electrodes: (a,b) bare ITO, (d,e) ITO covered with 20 nm AuNPs, and (g,h) ITO covered by bare WS_2NTs with (c,f,i) respective band structures based on Ref. [397, 398, 399, 400]. The colour of the curves corresponds to the laser light colour used for the illumination and yellow regions highlight the intervals of illumination.

Ohmic contact between the AuNP and ITO prevents any charge separation in the AuNP and the photogenerated charges in AuNP thus recombine before they can participate in any redox reaction. In the case of the blue illumination, there is a significant change in the OCP magnitude of about twofold when compared to bare ITO. This additional negative charging might be a result of citrate oxidation by energetic hot holes generated in the AuNP d-band with light of wavelengths shorter than 514 nm [401] or even 525 nm [402][4]. Citrate is present on the AuNP surface to prevent their aggregation in colloid solutions. An energetic hole can accept an electron from the citrate, making the electrode even more negative. In the case of Fc, the OCP response to blue light is significantly reduced again due to the presence of additional electron levels in the solution which can drain the excess electrons gathering in either the Au or the ITO. Thermal effects may also play a role and it may be a cause of a delayed OCP response on red light illumination suggesting some slower process occurring, e.g., thermal due to local heating of the AuNPs.

Bare WS_2NTs [Fig. 6.13(g–i)] exhibit a rather different response as there is a notable positive OCP change right after the illumination for all the lasers. In KCl, the response to a red light is purely positive. In the case of green and blue, there is an immediate change of OCP in the positive direction too but then it starts dropping in the negative direction, similarly to bare ITO. Due to a rather significant response of ITO to a green and blue light, it eventually overshadows the WS_2NT contribution. Is is important to note that the light from all the lasers has higher energy than the WS_2 bandgap of 1.3-1.4 eV [397], i.e., it can generate excitons (electron–hole pairs) in WS_2. The immediate positive OCP change can be related to the formation of a small Schottky barrier of about 0.6 eV at the WS_2NT/ITO interface. This is forming an energy barrier which the photoexcited electrons have to overcome to get to the ITO or vice versa.

In the case of the red light, the photoexcited electrons can have at most about the same energy as the barrier so it might not be enough to get to the ITO. Additionally, the bending of the WS_2NT conduction band draws the electrons from the WS_2NTs/ITO interface. Due to the barrier and conduction band bending the electrons accumulate in WS_2NTs while the holes from the WS_2NTs valence band can be transferred to the ITO, making it a bit more positively charged. Nevertheless, the electron cumulation causes a lowering of WS_2NTs band bending which in turn stops the holes from going further into the ITO. A relatively small response of the ITO itself towards the red light lets the positive OCP response of the WS_2NTs be the dominant contribution. With green and blue the electron accumulation in WS_2NTs and the hole transfer to ITO occurs in a similar way and with a similar magnitude as in the case of red. However, the underlying strong negative OCP response of ITO itself upon illumination with green and blue light quickly overshadows the initial positive OCP change and becomes the dominant contribution. However,

[4]This suggests that even our 532 nm laser might result in a partial d-band hole excitation but no clear sign of it was observed.

some electrons generated in WS_2NTs could have sufficient energy to overcome the Schottky barrier and reach ITO.

In the presence of Fc molecules, the electrons do not cumulate too much in neither WS_2NTs nor the ITO as they can readily participate in, e.g., Fc^+ reduction. Upon illumination, it generally results in more positive OCP than in the case of bare KCl. The WS_2NTs seem to add an immediate positive OCP change to counter the negative response of the bare ITO with Fc molecules. It is worth mentioning that the response on red and blue lights reaches a stable potential almost immediately while the response on green light takes longer time for the OCP to stabilize.

Similar experiments were performed on the AuNP-WS_2NT hybrid system. Fig. 6.14 shows the OCP changes induced by laser illumination when in pure 0.1 M KCl electrolyte and electrolytes containing Fc, Fe, and Ru redox molecules. The effects observed here are again tightly connected to the band structure of the hybrid system. In this case, there is an additional Schottky barrier present between AuNPs and WS_2NTs. Both the WS_2NTs and AuNPs can generate electric charges – excitons in the semiconductor and hot carriers in AuNPs. In a standalone AuNP, the energetic charges which are a result of LSP non-radiative damping recombine very fast and thus can hardly participate in outside redox processes. When a semiconductor is attached to the NP, the Schottky barrier formed between them allows an extraction of electrons from the NP and therefore both the extracted electron and leftover hole can participate in the outside redox processes.

As opposed to the OCP response of the individual components, where it was mostly dominated by the negative response of the underlying ITO except for the small positive response of bare WS_2NTs, the hybrid system exhibited an OCP change exclusively in the positive direction for all the solutions and illumination wavelengths. There was generally a fast response, resulting in an almost immediate increase of the OCP upon illumination and then some slower equilibration process which takes much longer to settle. In the pure KCl electrolyte, the initial response is the highest for the red laser while the blue and green ones show a smaller response, similar to each other. In the case of the red laser, the photovoltage increase continues after the fast phase and represents the dominant process as it reaches more than double the value of that obtained with green and blue light.

The immediate positive OCP change resembles the response of the bare WS_2NT on ITO though its magnitude is now larger. In such a case, the positive OCP contribution of WS_2NTs is larger than that of the underlying ITO. In addition, there is another Schottky barrier formed between AuNPs and WS_2NTs of about 0.6 eV [403] which can help to separate hot carriers generated in AuNPs. Hot electrons excited by red light have sufficient energy to go over the Schottky barrier into the WS_2NT conduction band leaving the AuNP positively charged by the remaining low energy holes. In this case, the holes generated in AuNP can not move further and only the holes from WS_2NT can get into the ITO unless some dramatic shift of the AuNP Fermi level due to charging occurs. Conversely, the illumination with green and blue

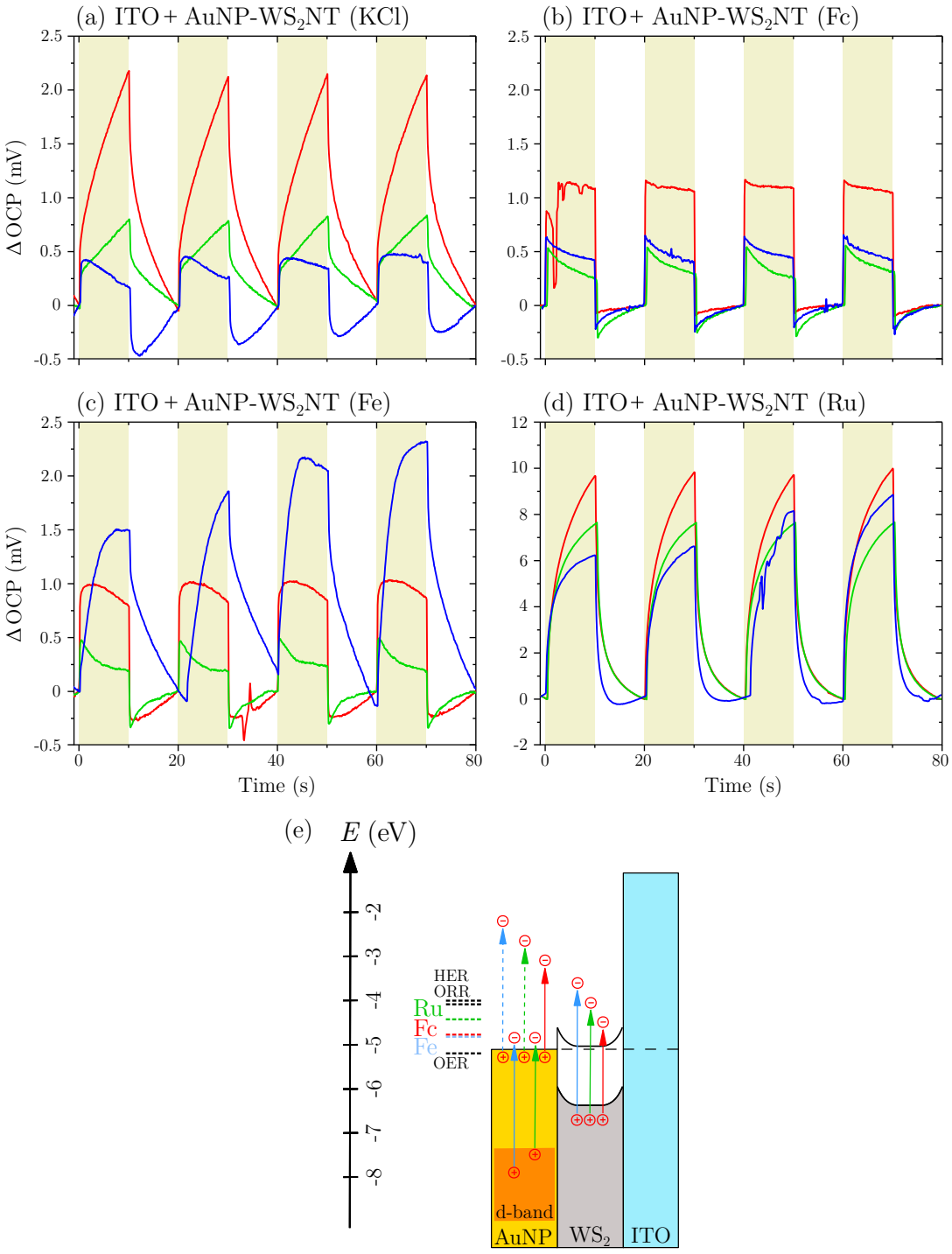

Fig. 6.14: AuNP-WS_2NT OCP response upon alternating 10 s-illumination intervals with 60 mW lasers recorded in (a) pure 0.1 M KCl base electrolyte and in the presence of (b) 0.1 mM Fc, (c) 0.5 mM Fe, (d) 0.5 mM Ru, and (e) the respective band structure based on Ref. [397, 398, 399, 400]. The colour of the curves corresponds to the laser light colour used for the illumination and yellow regions highlight the intervals of illumination.

should result in hot holes generated in AuNPs which could move into WS_2NTs and further into ITO. The response upon green and blue light should thus be stronger than on red but our results show that it is not the case and the reason for it is not completely clear.

In the presence of Fc molecules, the whole photovoltage change is immediate with the slower equilibration processes less noticeable, especially for the red light which also results in the largest OCP change. The explanation could come from the fact that hot carriers generated by red light consist of energetic electrons and low-energy holes near the Fermi level. The electron has sufficient energy to overcome the Schottky barrier and is separated from the hole, and subsequently in the WS_2NT can participate in the reduction of Fc^+ (together with electrons excited within WS_2NT) resulting in an overall positive charge accumulating in the ITO. Blue and possibly green illumination result mostly in hot electrons near the Fermi level, which might not have enough energy to overcome the Schottky barrier, and in energetic hot holes which might be transferred to WS_2NT and the ITO or participate in an oxidation of Fc. With Fe in the solution, the response for green and red colour is quite similar to the results obtained with Fc. However, the blue illumination resulted in a significant increase in photovoltage. The cause might dwell in Fe^{3-} having an absorption peak around 420 nm overlapping the 450 nm laser wavelength [404]. This might add some additional change to the system and increase the measured photovoltage further on top of the immediate response.

In the case of the solution with Ru, the response to all stimuli of laser lights was rather similar and dominated mostly by slow processes. Nevertheless, the magnitude of the photovoltage is significantly larger than in the case of other redox molecules or the pure electrolyte. The exact explanation for the large increase is still not completely clear. There are probably some other aspects at play which are beyond our control - different sensitivities of the redox molecules towards the electrode surface, as well as discrepancies between the outlined band positions and the reality and role of surface states present in the WS_2NTs affecting the photo-generated charge path.

It is even possible, that the role of AuNP is diminished by their relative scarcity over the NT surface [see Fig. 6.12(b)] or that hot carriers inside AuNPs recombine before they can be utilized and thus effectively do not participate in the observed processes. The increase in the magnitude of the positive OCP could then possibly be explained by the higher coverage of ITO with AuNP-WS_2NT than with bare WS_2NTs previously (different deposition methods).

To get additional information about the processes occurring on our electrodes, we then moved to study the photo-induced current (photocurrent) via the chronoamperometric method. As opposed to the OCP measurement where the whole system was in equilibrium conditions, in chronoamperometry the system is driven out of equilibrium by an application of electric potential to the WE while observing the current flowing between CE and WE. The background (dark) current, stemming from the

Cottrell equation and caused by applying a potential on the electrode, decreases exponentially as the oxidation and reduction rates equalize. After some settling time in the dark to reduce the background current, the electrode was repeatedly illuminated for 10 s by the 20 mW 532 nm laser with in-between 10 s intervals of darkness. The experiment was performed for potentials ranging from −500 mV to +1000 mV for all redox couples. In the subsequent analysis, the remaining background current was subtracted to show only the photo-induced current.

A typical example of the resulting photocurrent response of AuNP-WS_2NT electrode for 200 mV potential is shown in Fig. 6.15(a). When we compare the stabilized photocurrent at the 10-th second of illumination with the dark baseline current (the difference is referred to as the photocurrent step), the response for each redox couple is rather different. While the response observed for the Fe redox couple is positive, for Ru it is around zero and for Fc it is negative. The only common feature of the photoresponse is a sharp current spike in the negative (positive) direction when the illumination starts (stops), most probably caused by the charging and discharging of surface states in the WS_2NTs [405, 406]. We extracted the photocurrent step magnitudes for various applied potentials corresponding to all three redox couples [shown in Fig. 6.15(b)]. At negative potentials, the negative photocurrent polarity is probably related to the increased supply of electrons which get scavenged by oxygen within the oxygen reduction reaction. The positive photocurrent steps above 500 mV can already be related to oxygen evolution reaction and corresponding WS_2 oxidation which is aided by the photo-induced phenomena. But overall, the photocurrent for each redox couple is a nontrivial function of the applied potential attaining both positive and negative photocurrent polarities. On top of that, the observed response changed yet again when a different illumination wavelength was used (not shown here). It is interesting to notice that the most significant differences in photocurrent response among the redox couples occur around the Fermi level of the respective redox couples (highlighted by dashed lines). This effect was repeatable and only the height of photocurrent step peaks differed between the experiments. It might be related to the lower overall dark current near these regions so a rather minute photocurrent is not drowned in the background flow of charge. The reversed photocurrent step polarity near the respective Fermi levels between the positive Fe and Ru, and negative Fc could not be adequately explained.

To make a definitive statement about the actual processes occurring at the electrodes during the illumination, more experiments are necessary. We have tested other techniques like electrochemical impedance spectroscopy combined with laser illumination. These experiments were done for all the redox molecules with the AuNP-WS_2NT-decorated electrodes and all the control samples, but the results were inconclusive.

One of the main aspects hindering our study was the suboptimal control over the electrode morphology and its reproducibility. Some uncertainties might stem from a rather complex geometry of the AuNP-WS_2NT hybrid system where all

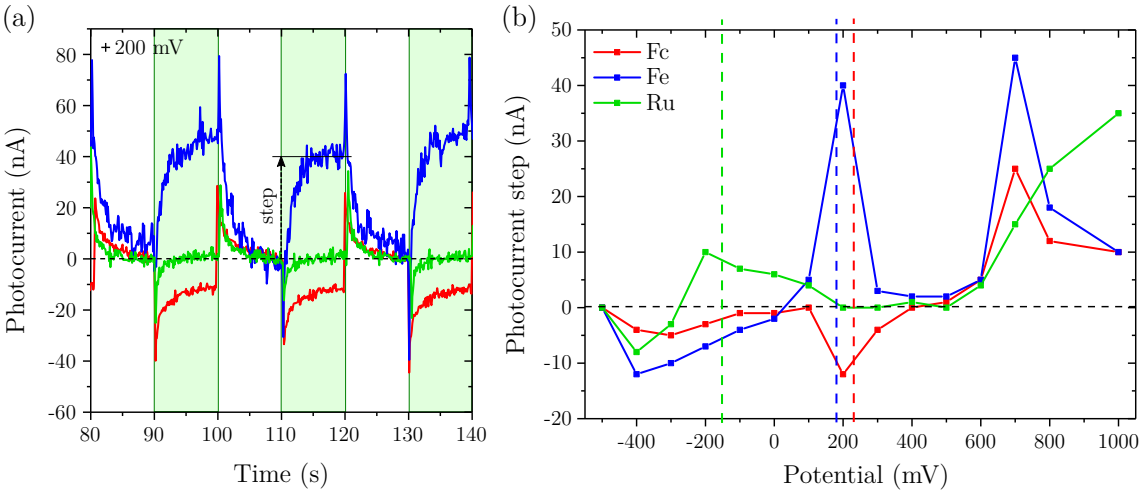

Fig. 6.15: (a) Example of the photocurrent response of AuNP-WS_2NT upon intermittent 10 s-illumination intervals provided by the 532 nm laser (20 mW) for different redox couples at the 200 mV applied potential. Green-shaded regions correspond to the intervals of illumination. (b) Extracted photocurrent step magnitude at respective potentials for each redox couple, where the dashed lines correspond to the Fermi levels E^0 of the respective redox couples.

the components are in direct contact with the electrolyte and can react with it. Additionally, the electric contact to the ITO might not be very robust, either through WS_2NT or the AuNPs decorating it which can create competing charge pathways further complicating its response. Also, the coverage of the ITO by either AuNPs and WS_2NTs or the hybrid system differs and it is thus harder to directly compare. There might also be a significant effect of the local electrolyte heating induced by plasmonic nanoparticles as there is still an ongoing debate whether the effects occurring in the systems utilizing plasmonic nanoparticles come from the excitation of hot carriers or from the NP heating which is a final step in a non-radiative plasmon damping. Additionally, due to the small bandgap of the WS_2NTs and its spectral overlap with plasmon resonance, direct exciton generation can not be separated from the generation of hot carriers. As a result of the above, using three kinds of redox molecules produced very different responses both in terms of photovoltage and photocurrent without a satisfactory explanation achieved.

To get a deeper understanding of how the various redox molecules react to photo-induced effects in a metal-semiconductor photoelectrochemical system, we moved to a much simpler and better-defined system consisting of a large-bandgap semiconductor layer with plasmonic NPs on top of it.

6.3 A study of TiO_2 with Au nanoislands

We have chosen the prototypical Au-TiO_2 complex to get a deeper insight into the photoelectrochemistry of metal–semiconductor systems. The TiO_2 is one of the most

frequently used materials for photocatalysis due to its chemical stability, low cost, and nontoxicity [407]. Its unique photocatalitic properties can be used in hydrogen production [408], removing water pollution [409], CO_2 reduction [410], etc. [411, 412].

The most common polymorphs of TiO_2 are anatase, rutile, and brookite [413]. It can be prepared by several methods – sputtering and evaporation of Ti and subsequent annealing in an oxygen atmosphere, by atomic layer deposition, by electrochemical oxidation of Ti, by sol-gel methods, or by hydrothermal chemical synthesis [414]. It has a fairly large bandgap of 3.20 eV for anatase and 3.02 eV for rutile [415], which results in sensitivity only towards the UV light, with band level energies depending on the surrounding media [416]. This large bandgap results in a rather poor response to solar radiation as only about 5% of the light has higher energy than the TiO_2 bandgap which complicates its use in photocatalysis [417].

Nevertheless, there are a few approaches to increase the TiO_2 responsiveness in the visible region: metal or non-metal doping, combination with sensitization molecules, combination with VIS active species, e.g., semiconductors with a smaller bandgap or utilizing the metallic nanoparticles [418]. Incorporation of plasmonic nanoparticles to the TiO_2 can significantly enhance its performance in the visible region through the excitation of LSP. The benefit of plasmonic nanoparticles is twofold: it increases the local electromagnetic field, which might improve the efficiency of exciton generation, and plasmon non-radiative decay can result in the generation of hot carriers [419].

The combination of gold plasmonic nanoparticles and TiO_2 results in the Schottky barrier formation [420] of about 1 eV [421] which allows a spatial charge separation and thus slower recombination rates for charges excited both in the semiconductor and nanoparticle. The combination of materials defines which charges will be transferred to the semiconductor – with an n-type semiconductor (TiO_2) the hot electrons can overcome the barrier and the holes stay in Au, while with a p-type semiconductor (GaN) hot holes can go over the barrier [422].

In the Au-TiO_2 system, the lower energy excitations result in intraband transitions and a generation of energetic hot electrons which can get over the barrier to the TiO_2 while the low energy holes are left behind in Au. The higher energy excitation results in dominant interband transitions [151] generating a low energy electron and energetic hot hole but neither have sufficient energy to be extracted by TiO_2, thus a very high recombination rate and a rather small overall benefit can be expected.

6.3.1 Preparation of the TiO_2 electrodes with Au nanoislands

We have prepared the TiO_2 using an atomic layer deposition method (ALD, Ultratech/CambridgeNanoTech Fiji 200) with tetrakis(dimethylamido)titanium and oxygen plasma as precursors at a temperature of 150°C. Approximately 30 nm of TiO_2 by performing 580 deposition cycles was grown on the transparent ITO electrodes leaving one corner covered for later contact directly to ITO. Prior to the TiO_2

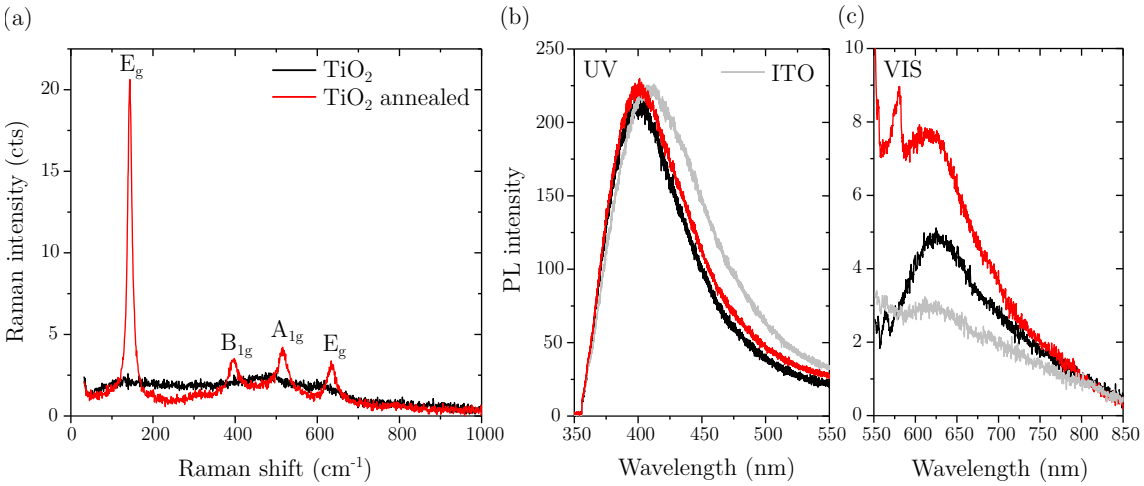

Fig. 6.16: Characterization of a 30 nm ALD-grown TiO_2 layer: (a) Raman spectrum provided by a 532 nm laser on the as-grown and annealed (1 h / 325°C) TiO_2 film with the highlighted peaks characteristic for the anatase phase TiO_2. Photoluminescence spectra excited by a (b) 355 nm UV laser and (c) 532 nm VIS laser before and after annealing complemented with a bare ITO spectra.

deposition, the ITO substrates were cleaned by sonication in acetone, IPA, and water baths. Some TiO_2 samples were also annealed for 1 h at 325°C on air to have information about the changes in TiO_2 after thermal treatment which it undergoes during the follow-up Au nanoisland (AuNI) formation.

The TiO_2 layers were characterized in a confocal Witec Alpha R300 system to assess their optical properties. The photoluminescence of the TiO_2 layer was acquired upon the UV laser excitation (355 nm) at a power of about 4 mW delivered through a 40X UV-optimized objective or upon the VIS laser excitation (532 nm) at a power of about 10 mW delivered through a 100X objective. The latter configuration was also used for the micro-Raman spectroscopy.

The Raman analysis in Fig. 6.16(a) shows spectra of the as-grown and annealed samples. The spectra are distinctly different as the annealed sample exhibits sharp Raman peaks which can be assigned to the anatase phase of TiO_2 [423] while the as-grown sample exhibits only a rather broad background signal without sharp Raman peaks. This suggests that the as-grown TiO_2 is amorphous [424] and after the annealing, the anatase phase is formed in agreement with the literature [425].

The PL spectra of the TiO_2 in Fig. 6.16(b) feature a single dominant peak centred around 400 nm (3.1 eV) for both the as-grown and annealed TiO_2 which is close to the anatase TiO_2 bandgap [426]. Nevertheless, even the bare ITO showed strong PL in this region, so the recorded PL spectra on TiO_2 might come from the underlying ITO. Some weaker PL signal [see Fig. 6.16(c)] was also observed in response to the 532 nm illumination, the largest one in the annealed TiO_2, and it is related to the presence of defects in TiO_2 [427], such as oxygen vacancies and Ti^{3+} species [428].

To introduce the plasmonic elements to the electrodes, gold layers were deposited

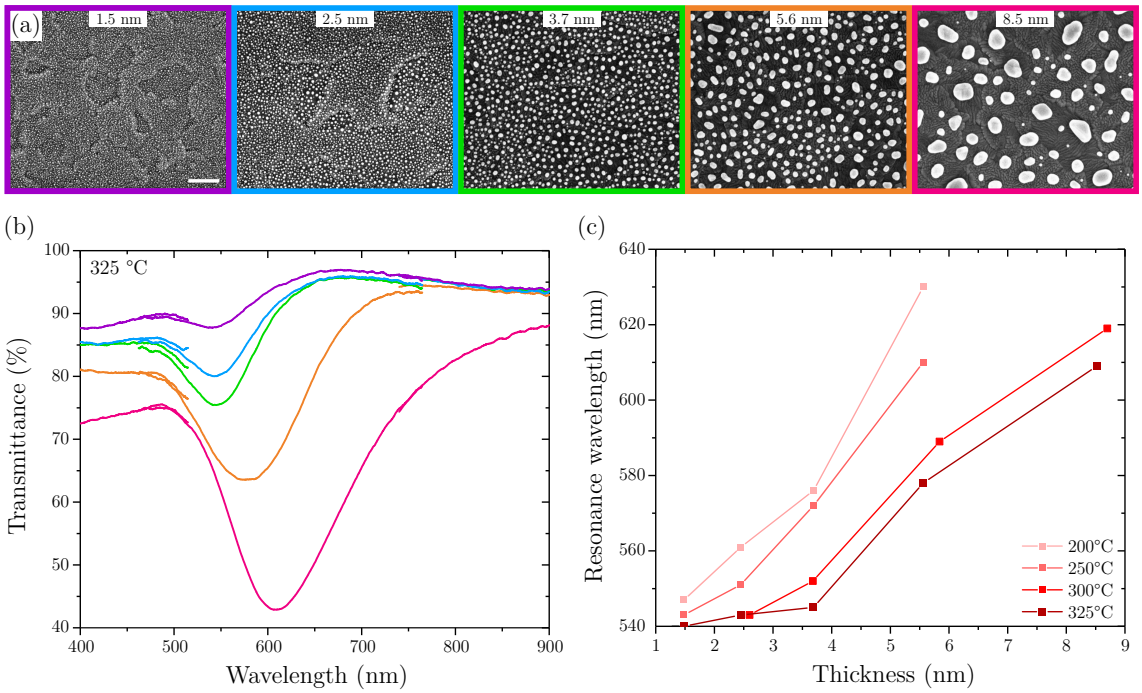

Fig. 6.17: (a) SEM morphology images of AuNIs formed after 1 h-long annealing of gold layers at 325°C with varying nominal thickness highlighted in the images and deposited on the ITO substrate (scale bar corresponds to 200 nm). (b) Transmittance spectra of AuNIs utilizing the bare ITO as a reference with colours corresponding to the colours of the frames surrounding the SEM images in (a). The discontinuities in the spectra around 500 and 750 nm are a result of stitching together three spectra recorded in different wavelength ranges. (c) Resonance wavelengths extracted from the transmittance spectra as a function of the layer thickness and annealing temperature sum up all the optimization experiments.

by a magnetron sputtering (Leica Microsystems EM ACE 600) on top of TiO_2 and subsequently annealed in air to form gold nanoislands (AuNIs). This system is rather well-defined in terms of geometry and contact between the metal, semiconductor, and conducting ITO base. Similarly, the Au layer was deposited to the bare ITO electrode and annealed to have a reference sample without the semiconductor component. The ITO-AuNI samples were first used for the AuNI growth optimization varying the Au layer thickness and annealing temperatures to obtain the LSP resonance close to the red 650 nm laser. In this way, the effect of dipole LSP on the hot charge generation can be maximized [429] and is spectrally separated from the interband transitions which can occur with green and blue lasers.

Fig 6.17(a) shows the morphology of AuNIs prepared from Au layers of varying thickness by their 1 h-long annealing in air at 325°C which was the highest used temperature for the AuNI optimization. It demonstrates that the thicker the Au layer, the larger the resulting AuNIs formed during the annealing at a fixed temperature. The optical response of the respective AuNIs was recorded by UV-VIS fibre

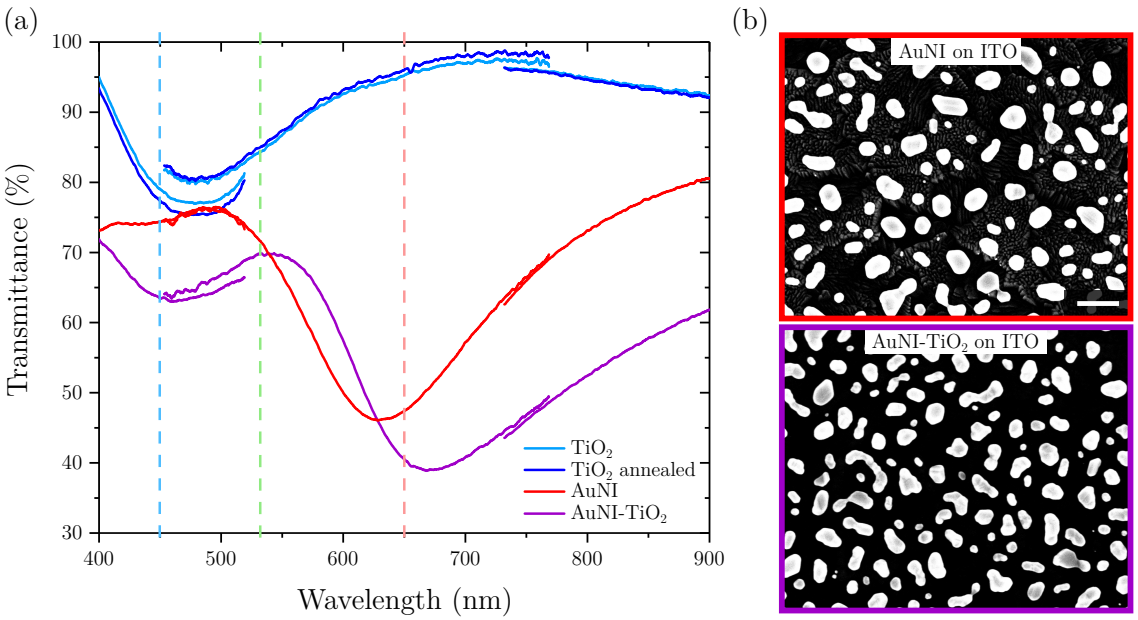

Fig. 6.18: Comparison of bare TiO_2 electrodes with AuNIs and AuNI-TiO_2 formed from the 8.4 nm Au layer on ITO: (a) Transmittance spectra of bare TiO_2, AuNIs, and AuNI-TiO_2 with bare ITO as a reference with dashed lines representing the laser excitation wavelengths used in the following photoelectrochemical experiments, (b) SEM morphology images of AuNIs and AuNI-TiO_2 on ITO with the frame colour corresponding to spectra in (a) (scale bar corresponds to 200 nm).

spectrometer Ocean optics Jaz as a transmittance spectrum with the bare ITO being a reference as shown in Fig 6.17(b). The position of the minimum in the transmittance spectrum corresponds to the resonance wavelength of the respective AuNIs and its shift to longer wavelengths reflects the increasing dimensions of AuNIs with increasing Au layer thickness. The resonance wavelengths extracted from spectra obtained after annealing at different temperatures as a function of the Au layer thickness are shown in Fig 6.17(c). Increasing the annealing temperature at a fixed Au thickness results in smaller AuNIs which in turn results in shorter resonance wavelengths. At lower annealing temperatures with the thickest layers the AuNIs are not yet completely formed and no well-defined plasmon mode was observed.

Based on the obtained spectra, we have chosen the highest available annealing temperature which resulted in the most pronounced and sharpest dips in the transmittance spectra. For the selected annealing temperature, the larger thickness of the Au layer resulted in resonance at longer wavelengths closer to the desired 650 nm. Thus the largest tested thickness of about 8.4 nm was selected for the final AuNI-TiO_2 and AuNI sample fabrication with an expected red-shift of the AuNI-TiO_2 spectra due to a higher refractive index of TiO_2 when compared to ITO.

The resulting AuNIs and AuNI-TiO_2 morphologies and transmittance spectra are summed in Fig. 6.18. The plasmon resonance of AuNI-TiO_2 is shifted to longer wavelengths when compared to AuNIs directly on ITO as expected. This effect is

dominant even as the SEM analysis revealed slightly larger AuNIs formed on ITO than on TiO_2 which would result in the wavelength shift in the opposite direction. The plasmon peak of the AuNI-TiO_2 is positioned almost exactly at the 650 nm wavelength which was desired. The transmittance through bare TiO_2 shows a dip centred around 480 nm which is also noticeable in the AuNI-TiO_2 spectrum. Its origin is probably associated with a defective nature of our TiO_2 layer, mainly the oxygen vacancies [430].

6.3.2 AuNI-TiO_2 photoelectrochemistry

The OCP response of the individual components of the AuNI-TiO_2 to illumination was tested for AuNI on ITO and bare TiO_2 on ITO before and after annealing. The measurement procedure was the same as in the case of WS_2NT system. The resulting responses to three 60 mW lasers with 450 nm, 532 nm, and 650 nm wavelengths are summarized in Fig. 6.19 for pure KCl and Fc in KCl solutions, Fe and Ru are not shown. Additionally, the related band structures of the electrodes together with the electron levels in the solution are outlined. Note that one sample was used for all four solutions which were exchanged between the experiments.

AuNIs on ITO electrodes [Fig. 6.19(a,b)] show only a minute response upon every illumination colour corresponding to the majority of hot carriers to recombine before participating in any redox process. When compared to 6.13 in the case of bare ITO and with colloidal AuNPs the response is very similar, where the main contribution can be assigned to the ITO itself and its electron accumulation upon illumination. In the presence of Fc molecules, the OCP background is much more stable as there is a well-defined reversible redox system in the solution which allows reaching the equilibrium between the Fermi levels of the electrode and the solution. The additional levels are available for the photo-generated charges in the solution so the charging is less pronounced.

In the case of TiO_2 [Fig. 6.19(d,e)], the response on various lasers is different. For a perfect TiO_2 crystal, none of the lasers could generate electron–hole pairs as its energy does not overcome the bandgap. Nevertheless, plenty of defect (trap) or surface states can exist within the bandgap [431] so even the visible light can result in change generation. The OCP change upon red laser illumination is minuscule but in the positive direction by about 1.5 mV. A barely noticeable indication of this initial OCP change in positive direction can also be recognized upon green illumination, where the increase is quickly overshadowed by a more profound change in negative direction throughout the whole illumination period. A purely negative response can be observed for the blue illumination. This could be related to the presence of a Schottky barrier between ITO and TiO_2 and the bent conduction band makes it more difficult for the electrons in the TiO_2 conduction band to be extracted to ITO. The red light can excite charges from the defect states but they do not have enough energy to overcome the potential barrier of TiO_2, but holes could move to the ITO

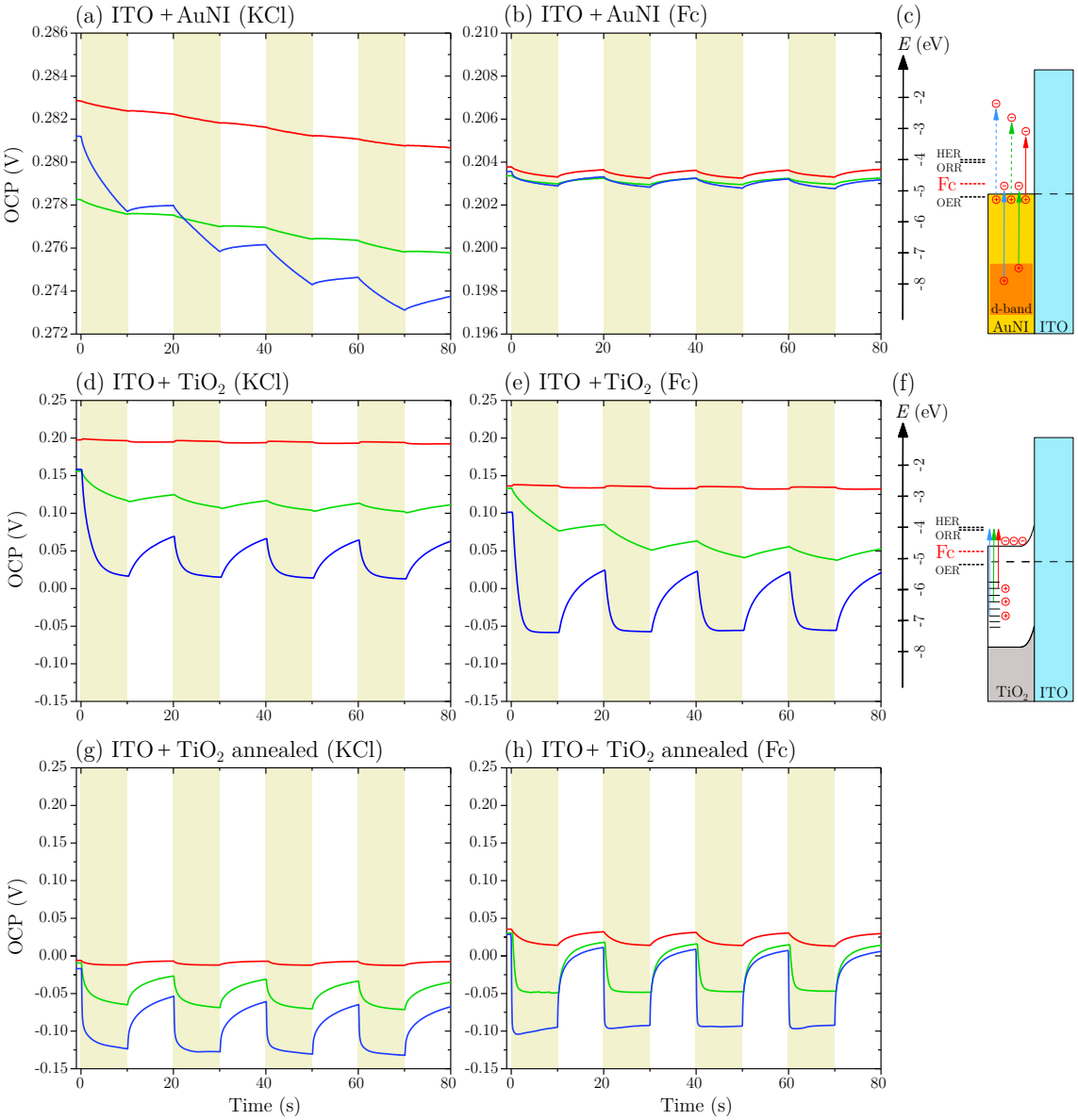

Fig. 6.19: OCP response upon alternating 10 s intervals of 60 mW laser illumination recorded at 0.1 M KCl base electrolyte (left panels) and in the presence of 0.1 mM Fc redox molecules (right panels) with different electrodes: (a,b) ITO with AuNI from 8.4 nm thick gold layer, (d,e) ITO covered with TiO_2 before, and (g,h) after annealing at 325°C with (c,f) respective bandstructures based on Ref. [156, 398, 399, 400]. The colour of the curves corresponds to the laser colour used for the illumination and yellow regions highlight the intervals of illumination.

due to the upward bending of the valence band, thus generating positive OCP. In the case of the green and blue light, a similar effect occurs but more electrons from deeper levels or with greater energy are excited increasing the conduction band energy thus flattening the band bending or possibly even reversing the curvature. In this way, the electrons could flow to the ITO while holes need to overcome the energy barrier or participate in oxidation reactions. Note that the rate of change is relatively slow and once the illumination stops, it does not come back to the initial OCP value suggesting that the charge movement and occurring reactions are rather slow. In pure KCl, it is likely only the oxygen evolution reaction whose kinetics is slow. With Fc in the solution, there is only a small difference so it does not affect the movement of charges significantly. This could be related to the overall worse charge transfer rates between the TiO_2 and the electrolyte.

Illumination of annealed TiO_2 [Fig. 6.19(g,h)] resulted in a rather similar OCP response with a faster rate of charging. Nevertheless, upon red illumination, there is an OCP change in the negative direction, which could be related to a slight change in band positions after annealing to higher energies (more negative electric potential) which results in a smaller band bending with little or even no barrier for electrons, so they can flow to the ITO easier. This change in the band bending is also supported by the negative offset of the OCP curves for annealed TiO_2 versus the pristine TiO_2. Another possibility is the improved charge transfer rate due to the increased presence of anatase phase after annealing and/or due to lowering the concentration of defects in TiO_2 [396].

The same experiments were performed with the remaining redox molecules (Fe and Ru) and the obtained results were similar to the corresponding responses shown in Fig. 6.19 overall. Notably, the results with Fe resembled those with Fc while those with Ru resembled those with KCl. Overall the response in the case of TiO_2 is much greater than that observed in the case of WS_2 NTs probably mainly due to a much larger amount of semiconductor material in the case of TiO_2.

The OCP response of the AuNI-TiO_2 complex for all redox molecules and pure KCl is summarized in Fig. 6.20. In KCl solution, the change in OCP upon repeating illumination with all the colours is about the same, though the response upon initial illumination is greater for green and even larger for blue. When compared to annealed TiO_2, the response on all the lasers is increased, most dramatically on the red laser which implies the enhanced photo-response in longer wavelengths due to the presence of AuNIs and their hot electron generation and transfer to the TiO_2 conduction band. Holes close to the AuNI Fermi level do not have enough energy to be utilized by OER unless they accumulate. Concerning the d-band excitations (high energy hole and low energy electron) with green and mainly with blue light, the charges are likely to recombine quickly because the electrons do not have sufficient energy to overcome the Schottky barrier.

In the presence of Fc molecules, the response changes dramatically as it features very sharp changes in OCP upon illumination. As opposed to the pure KCl solution,

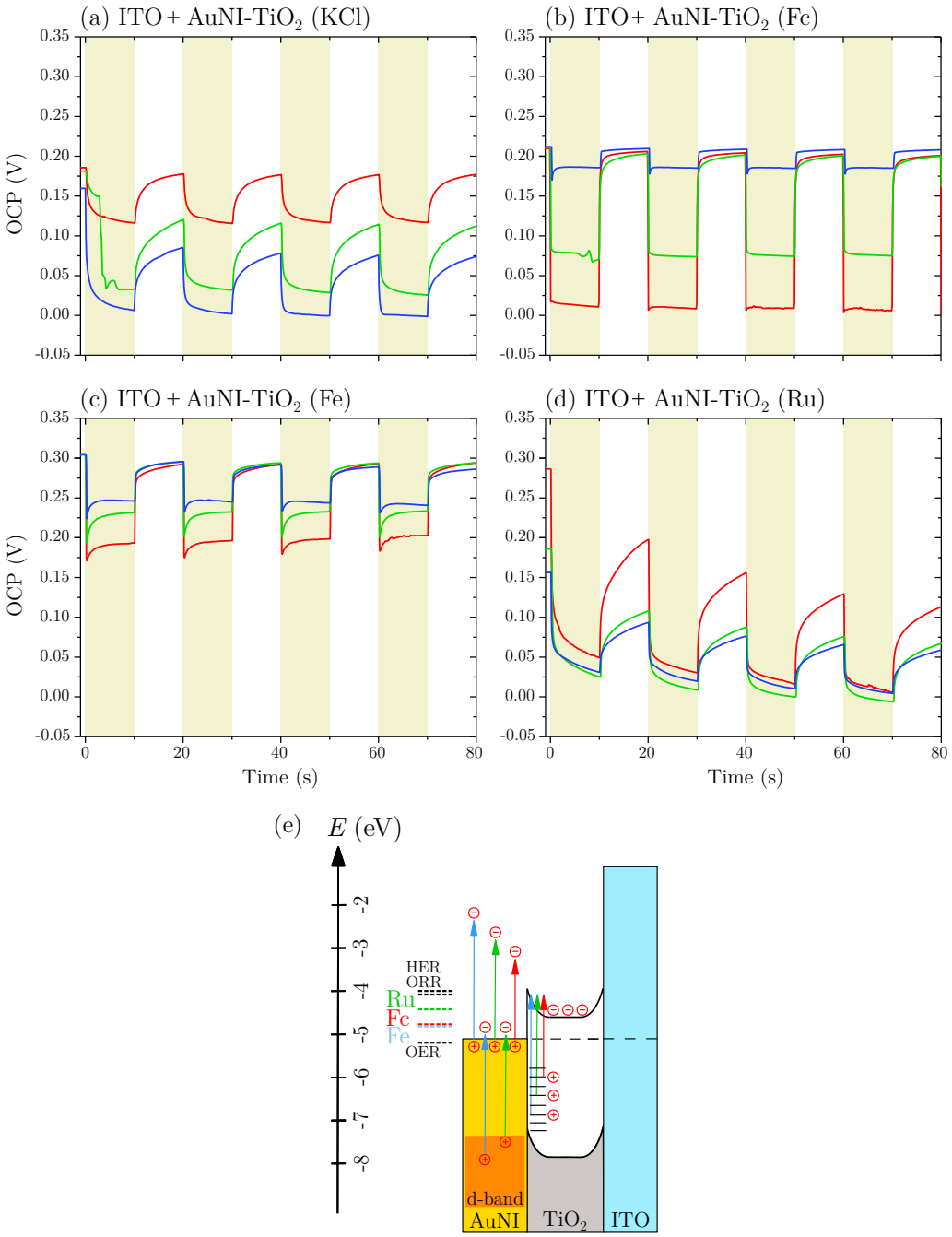

Fig. 6.20: OCP response of AuNI-TiO_2 obtained from 8.4 nm of Au upon alternating illumination with 60 mW lasers recorded at (a) pure 0.1 M KCl base electrolyte and in the presence of (b) 0.1 mM Fc, (c) 0.1 mM Fe, and (d) 0.1 mM Ru. The colour of the curves corresponds to the laser colour used for the illumination and yellow regions highlight the intervals of illumination. (e) Band structure of the AuNI-TiO_2 complex with band positions based on Refs. [156, 398, 399, 400].

the response upon red light is the largest one suggesting a synergy between the hot electrons generated by AuNI which are transferred to TiO_2 and further to the ITO. The holes left behind below the Fermi level in AuNI can collect electrons from Fc, i.e., oxidize Fc^0 to Fc^+ molecules, thus reaching a stable potential rather quickly. Blue light, though, induced a rather small change in OCP which would hint at two processes competing against each other or an increased charge recombination rate, e.g., in the defect sites. The shape of the response upon illumination suggests the competing processes too because after the quick transient decrease in OCP, it returns up where it stabilizes. The exact mechanism of the charge transfer in this case is still elusive and it may involve electron spilling from TiO_2 to the AuNI [432] where there can participate in Fc^+ reduction, if present, but further study is required. Alternatively, the energetic d-band holes could move through the TiO_2 defect states into the ITO thus decreasing its negative charging.

Note that a similar response (not shown here) was observed with slightly smaller AuNIs on TiO_2 from a 7.8 nm thick Au layer which still exhibited a plasmon resonance near the 650 nm wavelength. AuNIs from thinner or thicker Au layers on TiO_2 did not exhibit such a different response upon used illumination wavelengths. The response thus strongly depends on the size of AuNI [433] and on the LSP wavelength, respectively.

In the case of Fe molecules, the OCP response was still largest for red light followed by green and blue. In all cases here, the OCP goes down sharply, then rises up and stabilizes, similar to the blue light response in Fc. It would also suggest some competing processes which could be related to electron extraction from the electrode by Fe^{3-} reduction to Fe^{4-} which prevents their further accumulation.

With Ru molecules in the solution, the OCP changes upon illumination are also largest in the case of red light followed by green, and blue. In the case of red light, the OCP change could be explained by the electrons from AuNI accumulating in the TiO_2 and holes participating in slow oxygen evolution. Since the standard electrochemical potential of Ru is at -0.15 V the electrons in the electrode do not have sufficient energy to reduce the surrounding Ru^{3+} to Ru^{2+}. Thus the OCP response is qualitatively similar to the response of KCl alone at least in the case of green and blue. The reason for the increased response upon red light is still unclear as the Ru molecules do not utilize the holes left behind in AuNI.

Overall the OCP analysis showed generally higher starting OCP with AuNI-TiO_2 samples, than with bare TiO_2, suggesting that its Fermi level is at higher energies. It also demonstrated a dramatically enhanced response upon red light which is clearly connected to the presence of plasmonic AuNIs and thus most probably an injection of hot electrons to the TiO_2. Additionally, the rate of charging was significantly higher with AuNI-TiO_2 electrodes with redox molecules present. The proposed band diagram of the AuNI-TiO_2 system is shown in Fig. 6.20(e) with possible charge generation scenarios.

After the OCP measurements, where we observed the equilibrium potentials in

which no current could flow through between WE and CE, we proceeded to chronoamperometry, where the system is driven out of equilibrium by applying a potential on the WE. For these experiments, a different set of electrodes were prepared from 8.5 nm Au layer annealed at the same conditions as those used for OCP experiments. After setting the potential, starting at -0.4 V, the current in the dark was recorded for 100 s before the light was introduced for 10 s followed by 10 s of darkness repeatedly for 260 s in total. The solution was then mixed by a micropipette and a higher potential was set going up to 0.6 V. A photocurrent step, which was defined as a stable current at the end of illumination interval minus the current in the dark, induced by light of different wavelengths for AuNI, bare TiO_2, and AuNI-TiO_2 electrodes is depicted in Fig. 6.21 for Fc solution. Note that with TiO_2 and AuNI-TiO_2 the actual photocurrent response was generally more complex and featured a transient photocurrent reaching to higher values than the extracted photocurrent step representing the stabilized current flow. This transient photocurrent might be related to the charging and discharging of the surface defect levels followed by charge recombination through them [434] and/or depletion of the reactant close to the electrode [435].

The AuNI electrode features large negative photocurrent steps in negative potentials which can be related to the formation of O_2^- via oxygen reduction reaction. It is the dominant process at these potentials which was also seen in cyclic voltammograms in the dark as a huge cathodic peak (not shown here) overshadowing the Fc redox processes, and then a lot of peaks related to Au oxidation and reduction. AuNI facilitate the reaction as they can provide hot electrons to the O_2 dissolved in the solution [436] which is aided by increasing the Fermi level energy at applied negative voltages or can help the reaction by thermal effects. Small photocurrents at positive potentials represent the effect of more energetic carriers in AuNI which help with Fc oxidation, or possibly Au oxidation. The photocurrent response on all colours of light is very similar.

Bare TiO_2 which was not annealed showed virtually no response upon red, a rather small one on green and the strongest on blue light. This behaviour was expected according to the OCP study [Fig. 6.19(d)] which also showed the largest photovoltage under blue light illumination. Here, the CVs showed the oxygen reduction reaction to be significantly suppressed or moved to even lower potentials, thus it does not play such a big role with these electrodes and Fc oxidation is dominant, possibly oxygen evolution reaction.

The AuNI-TiO_2 complex electrode exhibited significantly enhanced step photocurrents for all three laser colours when compared to the bare TiO_2. The largest qualitative difference is in the case of red light going from zero to about 150 nA which demonstrates the significant improvement in the photocatalytic activity at longer wavelengths and stresses the crucial role of the plasmonic AuNIs. The CVs in the dark also showed only a small role in oxygen reduction reaction, though larger than in the case of bare TiO_2. The positive photocurrent steps are related to Fc oxi-

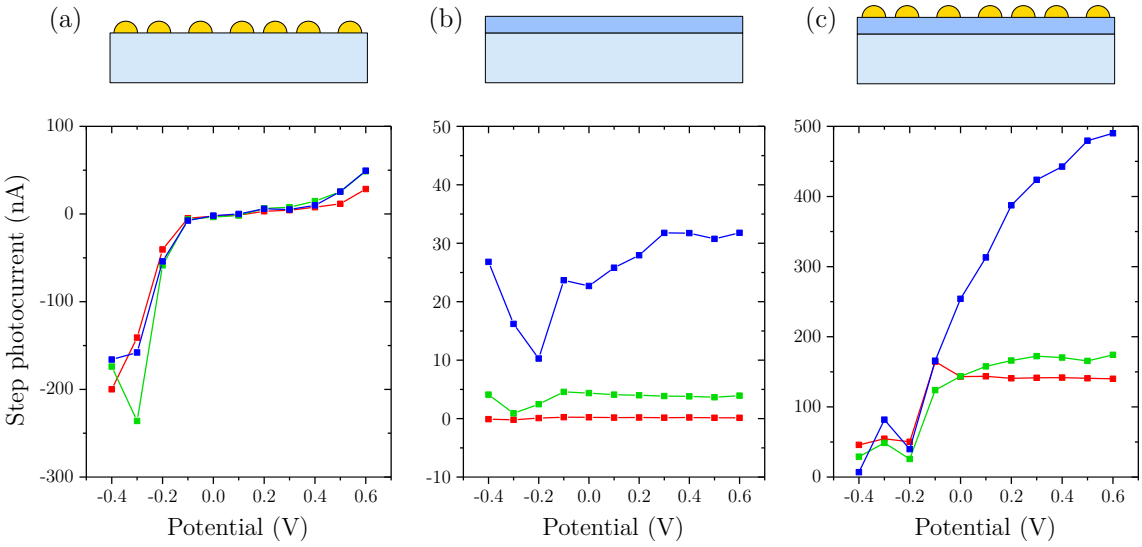

Fig. 6.21: Photocurrent step extracted from chronoamperometric curves recorded in Fc solution under 10 s intervals of alternating illumination with 650 nm, 532 nm, and 450 nm lasers after 100 s of settling time for various electrodes: (a) AuNI on ITO, (b) bare TiO_2 on ITO, (c) AuNI-TiO_2 complex on ITO.

dation or oxygen evolution reaction. At negative potentials, the photocurrent steps are smaller (≤ -0.2 V) which is a region where the small oxygen reduction peak appeared in CV. At these potentials, some of the generated electrons can be scavenged by O_2. This corresponds with the observation of the largest transient photocurrents in these regions going down rather quickly. At higher potentials, this pathway is becoming much less significant and the electrons are collected by the electrode. For red light the photocurrent step height seems to saturate which can be related to the fact that holes left in AuNI do not benefit from lowering the Fermi level energy, as they are already available for the Fc oxidation due to their fast accumulation at lower potentials while the vast majority of the hot electrons are collected by the TiO_2 and then ITO regardless of the potential. Upon blue light, the photocurrent step continually increases from -0.2 V up. This might be related to the fact that the electrons generated in TiO_2 conduction band are less likely to drift to the AuNI and participate in a reduction reaction and more likely to be collected by the ITO and holes more accessible to some oxidation reaction. These results also show, that the largest measured OCP response upon illumination (red in Fig. 6.20) does not have to correspond to the highest photocurrent generation capability.

All other redox molecules were examined as well, but the obtained results were similar to those shown in Fig. 6.21 and the small differences were not yet completely understood. Though, with pure KCl smaller overall photocurrent steps were observed.

The positive effect of AuNI presence on the TiO_2 is undeniable, especially upon red light illumination. Whether their role is always an active one, providing additi-

onal charges via hot carrier generation, or a passive one, where the AuNI provides a place for the charges generated inside Ti_2, where they can be more easily accessed by the redox molecules, is still unclear.

6.4 Conclusions

At the beginning of the chapter, the basic concepts of electrochemistry were outlined with a focus on the interface between the electrode (metallic or semiconductor) and an electrolyte. Basic electrochemical methods were introduced with a focus on voltammetric and amperometric methods together with the instrumentation necessary to perform them.

The experimental section started with the study of WS_2NTs and their inherent electrochemistry. The optimization process of WS_2NT deposition on ITO electrodes is presented achieving a rather dense and homogeneous coverage. The CV experiments with carefully selected redox molecules showed the positive effect of WS_2NTs present on the ITO electrodes both in terms of redox process reversibility and electroactive area. Though the highest coverage of WS_2 (eHD) showed significantly worsened properties, it could be attributed to a different preparation method which involved plasma treatment of ITO to improve the coverage. A dramatic detrimental effect of plasma treatment on the electrochemistry of ITO was later clearly demonstrated. Plasmonic NPs were introduced to the WS_2NTs by a chemical synthesis and we were able to tune their average diameter rather reliably. Photovoltage and photocurrent experiments with three redox molecules and bare electrolyte, three laser wavelengths, and all the individual components of the complex AuNP-WS_2NT system were performed to shed light on its photochemical properties. Although we have observed plenty of effects pointing to the hot carriers' participation in the photo-induced electrode processes, the effects were relatively small, and the geometry complexity of the AuNP-WS_2NT on the ITO led to some ambiguous and unclear results. Additionally, due to a small bandgap of WS_2, charges are also directly excited in the semiconductor, not only in an AuNP. These complications prevented us from stating definitive photo-induced charge carrier pathways and their role in redox processes.

For these reasons, we then focused on a better-defined system of a TiO_2 layer with plasmonic AuNIs on top which provides much more straightforward geometry. The AuNI size was well-controlled, optimized, and tuned to one of the excitation lasers, while the TiO_2 bandgap is larger than all used laser energies so electron–hole pairs should not be generated inside. Nevertheless, using photovoltage and photocurrent measurements we have shown notable charging in the bare TiO_2 itself due to its defects, which again brings two charge carrier generation pathways together. The significant enhancement in measured photocurrents in the presence of plasmonic AuNI on the TiO_2 points to a huge benefit of plasmon-induced hot charge carrier effects, especially with red light, where bare TiO_2 exhibited minuscule response.

Overall, the effects observed in TiO_2-based systems were much stronger than those based on WS_2.

Yet, there is still a lot of information hidden and not all the results were satisfactorily explained. Further experiments limiting the effects of electron scavenging O_2 or utilizing irreversible redox processes to separate the effects utilizing only one charge polarity should be carried out. Additional information about the interfaces, more precise electron energy levels, defects states, work functions, and Schottky barrier heights could be accessed, e.g., by electrochemical impedance spectroscopy, Kelvin probe force microscopy, and ultraviolet photoemission spectroscopy.

CONCLUSIONS AND FUTURE OUTLOOK

The dissertation began by outlining the fundamental aspects of light interacting with matter. Its coupling with electrons inside metallic layers forming a surface plasmon polariton was explained and the governing equations were derived. The main focus was on the localized surface plasmons as they are more versatile in tuning their response towards light which was demonstrated by calculating extinction cross-section spectra. The LSP dependence on the nanoparticle's material, size, and surrounding environment was demonstrated. The summary of applications utilizing the unrivalled ability of plasmonic nanoparticles to concentrate light was put forth. Three main topics were outlined and discussed in more detail: metasurfaces, biodetection, and hot charge carrier generation.

The following parts of the dissertation were devoted to the practical research done during the Ph.D. studies. The first topic was related to plasmonic metasurfaces, how their components influence the incoming light, and a novel approach to evaluate the related changes in the phase of light. We have demonstrated that it is possible to utilize the coherence-controlled holographic microscope to visualize and quantify the changes in the phase of light induced by plasmonic nanostructures. By adding a tunable light source, we first obtained a spectrally resolved phase of light transmitted through gold nanodisc arrays of different nanodisc dimensions. Based on the acquired information, we selected two nanodisc dimensions with the largest phase difference and utilized them in the construction of a simple focusing metasurface. By collecting quantitative phase images with different defocus we obtained a 3D phase map of converging wavefronts propagating from the metasurface. This wide-field method of 3D quantitative phase imaging with a rather fast acquisition time has the potential to become a useful and versatile tool in metasurface research. Its use can even be expanded towards the observation of the geometric phase by adding optical components (polarizers, half-wave plates...) that introduce and control the circular polarization of light.

The second topic tackles the rigidity of conventional static metasurfaces by introducing an element of tunability allowing dynamic changes in their properties. This can be achieved, e.g., by utilizing phase-change materials which can undergo metal-insulator phase transition. Vanadium dioxide, as a most prevalent member of phase-change materials, exhibits abrupt changes in optical, electrical, thermal, and magnetic properties upon the phase transition. These abrupt changes of properties were exploited in two different ways to achieve tunable plasmon resonances: nanostructuring the VO_2 itself or serving as an active substrate for conventional metallic nanostructures on top. The first approach was demonstrated on the nanostructured VO_2 formed by a self-limiting epitaxial growth on a-cut sapphire. Such VO_2 nanobeams exhibited plasmonic properties in the infrared region above the phase transition temperature while behaving as a dielectric at room temperature. This behaviour then collectively translated into a metasurface with two different modes of

operation acting as an attenuator at room temperature and as a quarter-wave plate at the elevated temperature. Further steps could move beyond the sole utilization of plasmonic properties of metallic VO_2 at elevated temperatures, to exploring the Mie resonances in dielectric VO_2 at room temperature. By careful design, two different functionalities could thus be achieved, one via Mie resonances below the phase transition and the other via plasmon resonances above the phase transition temperature. The second approach dwelt in using the aforementioned VO_2 nanobeams as an active substrate for gold nanorod antennas. The tunability of AuNR resonance wavelengths was shown as a function of temperature. We have also observed an effect of VO_2 anisotropy on the AuNR plasmon resonance as their response differed when oriented parallel and perpendicular to the VO_2 nanobeams. Additionally, the observed AuNR resonances featured an interesting spike in the extracted FWHM of both AuNR orientations probably as a result of a strong correlation in VO_2 during the phase transition. Nevertheless, further investigation is necessary to confirm the nature of the observed behaviour, ideally by fabricating additional AuNRs of different sizes on such a substrate.

Third topic is related to the effects of the crystallinity of plasmonic nanostructures on their plasmonic properties. The section started with a summary of the literature related to the detrimental effects of grain boundaries in plasmonic nanostructures and a description of methods to achieve monocrystalline gold without the presence of grains. We prepared and compared monocrystalline and polycrystalline gold nanorods, focusing on their structural and optical differences. In terms of morphology, the monocrystalline AuNRs featured slightly reduced size and shape fluctuations when fabricated from the same AuMP, though between different AuMPs the deviation increased. Additionally, there were no gold residues around after the fabrication. Nevertheless, polycrystalline AuNRs exhibited sharp upright boundaries while monocrystalline AuNRs featured inclined boundaries, and the membranes with monocrystalline gold suffered from increased brittleness due to the AuMP fabrication process. In terms of optical properties, we found no significant differences. LSP mode energies, Q factors, and loss probability spectra were very similar. This suggests that in our case using polycrystalline gold instead of monocrystalline gold didn't compromise the optical response of the resulting nanostructures. However, some optimization of the monocrystalline AuNR fabrication could improve their optical response.

The last topic is related to the combination of electrochemistry and plasmonics. This chapter began by introducing fundamental electrochemical concepts, particularly focusing on the electrode-electrolyte interface. Basic voltammetric and amperometric electrochemical methods were discussed along with the necessary instrumentation. The experimental section centred on studying WS_2NTs and their inherent electrochemistry. It covered the optimization of WS_2NT deposition on ITO electrodes, highlighting the positive impact of WS_2NTs on redox process reversibility and available electroactive area. Plasmonic AuNPs were incorporated onto

WS_2NTs through chemical synthesis, and their average diameter could be controlled. Photovoltage and photocurrent experiments were conducted to investigate the photochemical properties of the AuNP-WS_2NT system. There was a positive effect of the introduced materials to the electrode photoelectrochemistry but its origin is still unclear. While there were indications of hot carrier involvement in photoinduced electrode processes, the complex geometry of our system led to unclear results. Subsequently, the focus shifted to a better-defined system involving a TiO_2 layer with plasmonic gold nanoislands on top. This system provided better control over geometry and contact between individual components, the possibility to tune AuNI size and thus the resonance wavelength, and supposedly only plasmon-related effects should be observed. Photovoltage and photocurrent measurements revealed significant response even upon sub-bandgap excitations leading to considerable charging in bare TiO_2 probably due to its defects. With plasmonic AuNIs on top of the TiO_2, notably faster charging rates and enhanced photocurrents were observed, especially striking upon red light illumination. Overall, the TiO_2-based system exhibited much stronger effects compared to WS_2. However, further experiments are still needed to fully explain these results, including limiting electron scavenging effects and exploring additional characterization techniques like electrochemical impedance spectroscopy, Kelvin probe force microscopy, and ultraviolet photoemission spectroscopy to gain more insights into interface properties, energy levels, and defect states.

BIBLIOGRAPHY

[1] Maxwell, J. C. A dynamical theory of the electromagnetic field. *Philosophical transactions of the Royal Society of London*, **1865**. 155, pp. 459–512. ISSN 0261-0523. doi: 10.1098/rstl.1865.0008.

[2] Heaviside, O. *Electromagnetic theory*. The Electrician Printing and Publishing Company Limited, **1894**.

[3] Fujiwara, H. *Spectroscopic ellipsometry: principles and applications*. John Wiley & Sons, **2007**. ISBN 978-0-470-01608-4.

[4] Lorentz, H. A. *The Theory of Electrons and Its Applications to the Phenomena of Light and Radiant Heart: A Course of Lectures Delivered in Columbia University, New York in March and April, 1906*, vol. 29. Teubner, **1916**.

[5] Drude, P. Zur elektronentheorie der metalle. *Annalen der Physik*, **1900**. 306 (3), pp. 566–613. doi: 10.1002/andp.19003060312.

[6] Fox, M. *Optical Properties of Solids*. Oxford Master Series in Physics. OUP Oxford, **2010**. ISBN 9780199573363.

[7] Cai, W. and Shalaev, V. M. *Optical metamaterials – Fundamentals and Applications*, vol. 10. Springer, **2010**. ISBN 978-1-4419-1151-3. doi: 10.1007/978-1-4419-1151-3.

[8] van Exter, M. and Grischkowsky, D. Carrier dynamics of electrons and holes in moderately doped silicon. *Phys. Rev. B*, **1990**. 41, pp. 12140–12149. doi: 10.1103/PhysRevB.41.12140.

[9] Johnson, P. B. and Christy, R. W. Optical constants of the noble metals. *Physical Review B*, **1972**. 6, pp. 4370–4379. doi: 10.1103/PhysRevB.6.4370.

[10] Grady, N., Halas, N., and Nordlander, P. Influence of dielectric function properties on the optical response of plasmon resonant metallic nanoparticles. *Chemical Physics Letters*, **2004**. 399 (1), pp. 167 – 171. ISSN 0009-2614. doi: https://doi.org/10.1016/j.cplett.2004.09.154.

[11] Hao, F. and Nordlander, P. Efficient dielectric function for fdtd simulation of the optical properties of silver and gold nanoparticles. *Chemical Physics Letters*, **2007**. 446 (1), pp. 115 – 118. ISSN 0009-2614. doi: 10.1016/j.cplett.2007.08.027.

[12] Rakić, A. D., Djurišić, A. B., Elazar, J. M., and Majewski, M. L. Optical properties of metallic films for vertical-cavity optoelectronic devices. *Appl. Opt.*, **1998**. 37 (22), pp. 5271–5283. doi: 10.1364/AO.37.005271.

[13] Shahbazyan, T. V. and Stockman, M. I. *Plasmonics: theory and applications*. Springer, **2013**. ISBN 978-94-007-7804-7.

[14] Zayats, A. V., Smolyaninov, I. I., and Maradudin, A. A. Nano-optics of surface plasmon polaritons. *Physics Reports*, **2005**. 408 (3), pp. 131 – 314. ISSN 0370-1573. doi: https://doi.org/10.1016/j.physrep.2004.11.001.

[15] Dastmalchi, B., Tassin, P., Koschny, T., and Soukoulis, C. M. A new perspective on plasmonics: confinement and propagation length of surface plasmons for different materials and geometries. *Advanced Optical Materials*, **2016**. 4 (1), pp. 177–184. doi: 10.1002/adom.201500446.

[16] Barnes, W. L., Dereux, A., and Ebbesen, T. W. Surface plasmon subwavelength optics. *Nature*, **2003**. 424 (6950), pp. 824–830. doi: 10.1038/nature01937.

[17] Maier, S. A. *Plasmonics: Fundamentals and applications*. Springer US, **2007**. ISBN 0387331506. doi: 10.1007/0-387-37825-1.

[18] Richardson, N. V. and Holloway, S. *Modern Plasmonics*. Elsevier, **2014**. doi: 10.1016/b978-0-444-59526-3.00016-1.

[19] Hopfield, J. J. Theory of the contribution of excitons to the complex dielectric constant of crystals. *Phys. Rev.*, **1958**. 112, pp. 1555–1567. doi: 10.1103/PhysRev.112.1555.

[20] Ru, E. *Principles of surface-enhanced Raman spectroscopy : and related plasmonic effects*. Elsevier, Amsterdam Boston, **2009**. ISBN 9780444527790.

[21] Klimov, V. V. *Nanoplasmonics*. CRC Press, Boca Raton, **2013**. ISBN 978-981-4267-42-7.

[22] Kim, K. *Plasmonics - Principles and Applications*. IntechOpen, Erscheinungsort nicht ermittelbar, **2012**. ISBN 978-953-51-4269-0.

[23] McPeak, K. M., *et al.* Plasmonic films can easily be better: Rules and recipes. *ACS Photonics*, **2015**. 2 (3), pp. 326–333. ISSN 23304022. doi: 10.1021/ph5004237.

[24] Bozhevolnyi, S. *Plasmonic nanoguides and circuits*. Distributed by World Scientific Pub, Singapore Hackensack, NJ, **2009**. ISBN 978-9814241328.

[25] Kretschmann, E. and Raether, H. Notizen: Radiative decay of non radiative surface plasmons excited by light. *Zeitschrift fÄLr Naturforschung A*, **1968**. 23 (12), pp. 2135–2136. doi: doi:10.1515/zna-1968-1247.

[26] Otto, A. Excitation of nonradiative surface plasma waves in silver by the method of frustrated total reflection. *Zeitschrift für Physik A Hadrons and nuclei*, **1968**. 216 (4), pp. 398–410. ISSN 0939-7922. doi: 10.1007/BF01391532.

[27] Devaux, E., Ebbesen, T. W., Weeber, J.-C., and Dereux, A. Launching and decoupling surface plasmons via micro-gratings. *Applied Physics Letters*, **2003**. 83 (24), pp. 4936–4938. doi: 10.1063/1.1634379.

[28] Bouhelier, A. and Wiederrecht, G. P. Surface plasmon rainbow jets. *Opt. Lett.*, **2005**. 30 (8), pp. 884–886. doi: 10.1364/OL.30.000884.

[29] Hecht, B., Bielefeldt, H., Novotny, L., Inouye, Y., and Pohl, D. W. Local excitation, scattering, and interference of surface plasmons. *Phys. Rev. Lett.*, **1996**. 77, pp. 1889–1892. doi: 10.1103/PhysRevLett.77.1889.

[30] Xu, H. *Nanophotonics : manipulating light with plasmons*. Pan Stanford Publishing, Singapore, **2018**. ISBN 9789814774147.

[31] Mie, G. Beiträge zur optik trüber medien, speziell kolloidaler metallösungen. *Annalen der Physik*, **1908**. 330 (3), pp. 377–445. doi: https://doi.org/10.1002/andp.19083300302.

[32] Jackson, J. *Classical electrodynamics*. Wiley, New York, **1999**. ISBN 978-0-471-30932-1.

[33] Hohenester, U. *Nano and quantum optics : an introduction to basic principles and theory*. Springer, Cham, Switzerland, **2020**. ISBN 978-3-030-30504-8.

[34] Sio, L. *Active plasmonic nanomaterials*. Pan Stanford Publishing, Singapore, **2016**. ISBN 9789814613002.

[35] Bohren, C. F. and Huffman, D. R. *Absorption and Scattering of Light by Small Particles*. Wiley, **1998**. ISBN 0-471-05772-X. doi: 10.1002/9783527618156.

[36] Mayer, K. M. and Hafner, J. H. Localized surface plasmon resonance sensors. *Chemical Reviews*, **2011**. 111 (6), pp. 3828–3857. ISSN 0009-2665. doi: 10.1021/cr100313v.

[37] Miepython module. `https://github.com/scottprahl/miepython`.

[38] Pendry, J., Holden, A., Robbins, D., and Stewart, W. Magnetism from conductors and enhanced nonlinear phenomena. *IEEE Transactions on Microwave Theory and Techniques*, **1999**. 47 (11), pp. 2075–2084. doi: 10.1109/22.798002.

[39] Luk'yanchuk, B., *et al.* The Fano resonance in plasmonic nanostructures and metamaterials. *Nature Materials*, **2010**. 9 (9), pp. 707–715. ISSN 1476-1122. doi: 10.1038/nmat2810.

[40] Jellison, G. Optical functions of silicon determined by two-channel polarization modulation ellipsometry. *Optical Materials*, **1992**. 1 (1), pp. 41–47. ISSN 0925-3467. doi: https://doi.org/10.1016/0925-3467(92)90015-F.

[41] Adachi, S. *Optical Constants of Crystalline and Amorphous Semiconductors: Numerical Data and Graphical Information*. 1 edn. Springer US, **1999**. ISBN 978-0-7923-8567-7,978-1-4615-5247-5.

[42] Knight, M. W., *et al.* Gallium plasmonics: Deep subwavelength spectroscopic imaging of single and interacting gallium nanoparticles. *ACS Nano*, **2015**. 9 (2), pp. 2049–2060. ISSN 1936-0851. doi: 10.1021/nn5072254.

[43] McMahon, J. M., Schatz, G. C., and Gray, S. K. Plasmonics in the ultraviolet with the poor metals al, ga, in, sn, tl, pb, and bi. *Phys. Chem. Chem. Phys.*, **2013**. 15, pp. 5415–5423. doi: 10.1039/C3CP43856B.

[44] Siefke, T., *et al.* Materials pushing the application limits of wire grid polarizers further into the deep ultraviolet spectral range. *Advanced Optical Materials*, **2016**. 4 (11), pp. 1780–1786. doi: https://doi.org/10.1002/adom.201600250.

[45] Kepič, P., *et al.* Optically tunable mie resonance vo2 nanoantennas for metasurfaces in the visible. *ACS Photonics*, **2021**. 8 (4), pp. 1048–1057. doi: 10.1021/acsphotonics.1c00222.

[46] RefractiveIndex.info refractive index database. `https://refractiveindex.info/?shelf=main&book=SiO2&page=Malitson`. Accessed: 2021-11-04.

[47] Fernández-Domínguez, A. I., García-Vidal, F. J., and Martín-Moreno, L. Unrelenting plasmons. *Nature Photonics*, **2017**. 11 (1), pp. 8–10. ISSN 1749-4893. doi: 10.1038/nphoton.2016.258.

[48] Schuller, J. A., *et al.* Plasmonics for extreme light concentration and manipulation. *Nature Materials*, **2010**. 9 (3), pp. 193–204. ISSN 14764660. doi: 10.1038/nmat2630.

[49] Kelly, K. L., Coronado, E., Zhao, L. L., and Schatz, G. C. The optical properties of metal nanoparticles: the influence of size, shape, and dielectric environment. *The Journal of Physical Chemistry B*, **2003**. 107 (3), pp. 668–677. ISSN 1520-6106. doi: 10.1021/jp026731y.

[50] Biagioni, P., Huang, J.-S., and Hecht, B. Nanoantennas for visible and infrared radiation. *Reports on Progress in Physics*, **2012**. 75 (2), p. 024402. doi: 10.1088/0034-4885/75/2/024402.

[51] Horák, M., *et al.* Comparative study of plasmonic antennas fabricated by electron beam and focused ion beam lithography. *Scientific Reports*, **2018**. 8 (1), p. 9640. ISSN 2045-2322. doi: 10.1038/s41598-018-28037-1.

[52] Rai-Choudhury, P. *Handbook of Microlithography, Micromachining, and Microfabrication, Volume 1*. Press Monographs. SPIE Press, Bellingham, WA, **1997**.

[53] Grigorescu, A. E. and Hagen, C. W. Resists for sub-20-nm electron beam lithography with a focus on HSQ: state of the art. *Nanotechnology*, **2009**. 20 (29), p. 292001. doi: 10.1088/0957-4484/20/29/292001.

[54] Jiao, X., Goeckeritz, J., Blair, S., and Oldham, M. Localization of near-field resonances in bowtie antennae: Influence of adhesion layers. *Plasmonics*, **2009**. 4 (1), pp. 37–50. ISSN 1557-1963. doi: 10.1007/s11468-008-9075-x.

[55] Melngailis, J. Focused ion beam technology and applications. *Journal of Vacuum Science & Technology B: Microelectronics Processing and Phenomena*, **1987**. 5 (2), pp. 469–495. doi: 10.1116/1.583937.

[56] Huang, J.-S., *et al.* Mode imaging and selection in strongly coupled nanoantennas. *Nano Letters*, **2010**. 10 (6), pp. 2105–2110. ISSN 1530-6984. doi: 10.1021/nl100614p.

[57] Farahani, J. N., Pohl, D. W., Eisler, H.-J., and Hecht, B. Single quantum dot coupled to a scanning optical antenna: A tunable superemitter. *Phys. Rev. Lett.*, **2005**. 95, p. 017402. doi: 10.1103/PhysRevLett.95.017402.

[58] Chen, N. F. Y. L. X. M. Z. Euv lithography: State-of-the-art review. *Journal of Microelectronic Manufacturing*, **2019**. 2, p. 19020202. doi: 10.33079/jomm.19020202.

[59] Traub, M. C., Longsine, W., and Truskett, V. N. Advances in nanoimprint lithography. *Annual Review of Chemical and Biomolecular Engineering*, **2016**. 7 (1), pp. 583–604. doi: 10.1146/annurev-chembioeng-080615-034635. PMID: 27070763.

[60] Bonvicini, S. N., Fu, B., Fulton, A. J., Jia, Z., and Shi, Y. Formation of au, pt, and bimetallic au–pt nanostructures from thermal dewetting of single-layer or bilayer thin films. *Nanotechnology*, **2022**. 33 (23), p. 235604. doi: 10.1088/1361-6528/ac5a83.

[61] Qiu, T., *et al.* Nanosphere lithography: A versatile approach to develop transparent conductive films for optoelectronic applications. *Advanced Materials*, **2022**. 34 (19), p. 2103842. doi: https://doi.org/10.1002/adma.202103842.

[62] Zhao, Y., Belkin, M. A., and Alù, A. Twisted optical metamaterials for planarized ultrathin broadband circular polarizers. *Nature Communications*, **2012**. 3 (May). ISSN 20411723. doi: 10.1038/ncomms1877.

[63] Chen, X., *et al.* Dual-polarity plasmonic metalens for visible light. *Nature Communications*, **2012**. 3 (1), p. 1198. ISSN 2041-1723. doi: 10.1038/ncomms2207.

[64] Kildishev, A. V., Boltasseva, A., and Shalaev, V. M. Planar Photonics with Metasurfaces. *Science*, **2013**. 339 (6125), p. 1232009. ISSN 0036-8075. doi: 10.1126/science.1232009.

[65] Yu, N. and Capasso, F. Flat optics with designer metasurfaces. *Nature Materials*, **2014**. 13 (2), pp. 139–150. ISSN 14764660. doi: 10.1038/nmat3839.

[66] Su, V.-C., Chu, C. H., Sun, G., and Tsai, D. P. Advances in optical metasurfaces: fabrication and applications

invited

. *Opt. Express*, **2018**. 26 (10), pp. 13148–13182. doi: 10.1364/OE.26.013148.

[67] Hsiao, H.-H., Chu, C. H., and Tsai, D. P. Fundamentals and Applications of Metasurfaces. *Small Methods*, **2017**. 1 (4), p. 1600064. ISSN 23669608. doi: 10.1002/smtd.201600064.

[68] Yu, N., *et al.* Light propagation with phase discontinuities: Generalized laws of reflection and refraction. *Science*, **2011**. 334 (6054), pp. 333–337. doi: 10.1126/science.1210713.

[69] Yu, N., *et al.* A broadband, background-free quarter-wave plate based on plasmonic metasurfaces. *Nano Letters*, **2012**. 12 (12), pp. 6328–6333. ISSN 1530-6984. doi: 10.1021/nl303445u.

[70] Ding, F., Yang, Y., Deshpande, R. A., and Bozhevolnyi, S. I. A review of gap-surface plasmon metasurfaces: fundamentals and applications. *Nanophotonics*, **2018**. 7 (6), pp. 1129–1156. doi: doi:10.1515/nanoph-2017-0125.

[71] Sun, S., *et al.* High-efficiency broadband anomalous reflection by gradient meta-surfaces. *Nano Letters*, **2012**. 12 (12), pp. 6223–6229. ISSN 1530-6984. doi: 10.1021/nl3032668.

[72] Jing, X., *et al.* Manipulation of terahertz wave based on three-layer transmissive pancharatnam-berry phase metasurface. *IEEE Access*, **2020**. 8, pp. 164795–164806. doi: 10.1109/ACCESS.2020.3022373.

[73] Zhuo, Wang, Sun, Shulin, He, Qiong, and Zhou, Lei. A review of high-efficiency pancharatnam-berry metasurfaces. *TST*, **2020**. 13 (3), pp. 73–89. doi: 10.1051/tst/2020133073.

[74] Chen, M., Kim, M., Wong, A. M., and Eleftheriades, G. V. Huygensm̀etasurfaces from microwaves to optics: a review. *Nanophotonics*, **2018**. 7 (6), pp. 1207–1231. doi: doi:10.1515/nanoph-2017-0117.

[75] Monticone, F., Estakhri, N. M., and Alù, A. Full control of nanoscale optical transmission with a composite metascreen. *Phys. Rev. Lett.*, **2013**. 110, p. 203903. doi: 10.1103/PhysRevLett.110.203903.

[76] Jahani, S. and Jacob, Z. All-dielectric metamaterials. *Nature Nanotechnology*, **2016**. 11 (1), pp. 23–36. ISSN 1748-3395. doi: 10.1038/nnano.2015.304.

[77] Kruk, S., *et al.* Invited article: Broadband highly efficient dielectric metadevices for polarization control. *APL Photonics*, **2016**. 1 (3), p. 030801. doi: 10.1063/1.4949007.

[78] Zhao, Y. and Alù, A. Tailoring the dispersion of plasmonic nanorods to realize broadband optical meta-waveplates. *Nano Letters*, **2013**. 13 (3), pp. 1086–1091. doi: 10.1021/nl304392b.

[79] Duempelmann, L., Luu-Dinh, A., Gallinet, B., and Novotny, L. Four-fold color filter based on plasmonic phase retarder. *ACS Photonics*, **2016**. 3 (2), pp. 190–196. doi: 10.1021/acsphotonics.5b00604.

[80] Arbabi, E., Kamali, S. M., Arbabi, A., and Faraon, A. Full-stokes imaging polarimetry using dielectric metasurfaces. *ACS Photonics*, **2018**. 5 (8), pp. 3132–3140. doi: 10.1021/acsphotonics.8b00362.

[81] Ding, F., Deshpande, R., and Bozhevolnyi, S. I. Bifunctional gap-plasmon metasurfaces for visible light: polarization-controlled unidirectional surface plasmon excitation and beam steering at normal incidence. *Light: Science & Applications*, **2018**. 7 (4), pp. 17178–17178. ISSN 2047-7538. doi: 10.1038/lsa.2017.178.

[82] Meng, C., Tang, S., Ding, F., and Bozhevolnyi, S. I. Optical gap-surface plasmon metasurfaces for spin-controlled surface plasmon excitation and anomalous beam steering. *ACS Photonics*, **2020**. 7 (7), pp. 1849–1856. doi: 10.1021/acsphotonics.0c00681.

[83] Khorasaninejad, M., Chen, W. T., Oh, J., and Capasso, F. Super-dispersive off-axis meta-lenses for compact high resolution spectroscopy. *Nano Letters*, **2016**. 16 (6), pp. 3732–3737. doi: 10.1021/acs.nanolett.6b01097. PMID: 27119987.

[84] Zhang, J., *et al.* Plasmonic metasurfaces with 42.3% transmission efficiency in the visible. *Light: Science & Applications*, **2019**. 8 (1), p. 53. ISSN 2047-7538. doi: 10.1038/s41377-019-0164-8.

[85] Zheng, G., *et al.* Metasurface holograms reaching 80% efficiency. *Nature Nanotechnology*, **2015**. 10 (4), pp. 308–312. ISSN 1748-3395. doi: 10.1038/nnano.2015.2.

[86] Huang, L., Zhang, S., and Zentgraf, T. Metasurface holography: from fundamentals to applications. *Nanophotonics*, **2018**. 7 (6), pp. 1169–1190. doi: doi:10.1515/nanoph-2017-0118.

[87] Huang, L., *et al.* Volumetric generation of optical vortices with metasurfaces. *ACS Photonics*, **2017**. 4 (2), pp. 338–346. doi: 10.1021/acsphotonics.6b00808.

[88] Che, Y., Wang, X., Song, Q., Zhu, Y., and Xiao, S. Tunable optical metasurfaces enabled by multiple modulation mechanisms. *Nanophotonics*, **2020**. 9 (15), pp. 4407–4431. doi: doi:10.1515/nanoph-2020-0311.

[89] Nemati, A., Wang, Q., Hong, M., and Teng, J. Tunable and reconfigurable metasurfaces and metadevices. *Opto-Electron Adv*, **2018**. 1 (5), pp. 180009–1–180009–25. ISSN 2096-4579. doi: 10.29026/oea.2018.180009.

[90] Badloe, T., Lee, J., Seong, J., and Rho, J. Tunable metasurfaces: The path to fully active nanophotonics. *Advanced Photonics Research*, **2021**. 2 (9), p. 2000205. doi: https://doi.org/10.1002/adpr.202000205.

[91] Wang, Q., *et al.* Optically reconfigurable metasurfaces and photonic devices based on phase change materials. *Nature Photonics*, **2016**. 10 (1), pp. 60–65. ISSN 1749-4893. doi: 10.1038/nphoton.2015.247.

[92] Forouzmand, A., *et al.* Tunable all-dielectric metasurface for phase modulation of the reflected and transmitted light via permittivity tuning of indium tin oxide. *Nanophotonics*, **2019**. 8 (3), pp. 415–427. doi: doi:10.1515/nanoph-2018-0176.

[93] Chen, K., *et al.* Active anisotropic coding metasurface with independent real-time reconfigurability for dual polarized waves. *Advanced Materials Technologies*, **2020**. 5 (2), p. 1900930. doi: https://doi.org/10.1002/admt.201900930.

[94] Thureja, P., *et al.* Array-level inverse design of beam steering active metasurfaces. *ACS Nano*, **2020**. 14 (11), pp. 15042–15055. ISSN 1936-0851. doi: 10.1021/acsnano.0c05026.

[95] Miller, M. M. and Lazarides, A. A. Sensitivity of metal nanoparticle surface plasmon resonance to the dielectric environment. *The Journal of Physical Chemistry B*, **2005**. 109 (46), pp. 21556–21565. doi: 10.1021/jp054227y.

[96] Liedberg, B., Nylander, C., and LunstrÄ¶m, I. Surface plasmon resonance for gas detection and biosensing. *Sensors and Actuators*, **1983**. 4, pp. 299–304. ISSN 0250-6874. doi: https://doi.org/10.1016/0250-6874(83)85036-7.

[97] Liu, Y. and Cheng, Q. Detection of membrane-binding proteins by surface plasmon resonance with an all-aqueous amplification scheme. *Analytical Chemistry*, **2012**. 84 (7), pp. 3179–3186. doi: 10.1021/ac203142n.

[98] Wang, Y., Luo, Z., Liu, K., Wang, J., and Duan, Y. In situ targeting TEM8 via immune response and polypeptide recognition by wavelength-modulated surface plasmon resonance biosensor. *Scientific Reports*, **2016**. 6 (1). doi: 10.1038/srep20006.

[99] Eletxigerra, U., *et al.* Surface plasmon resonance immunosensor for ErbB2 breast cancer biomarker determination in human serum and raw cancer cell lysates. *Analytica Chimica Acta*, **2016**. 905, pp. 156–162. doi: 10.1016/j.aca.2015.12.020.

[100] Knez, K., *et al.* Spherical nucleic acid enhanced FO-SPR DNA melting for detection of mutations in legionella pneumophila. *Analytical Chemistry*, **2013**. 85 (3), pp. 1734–1742. doi: 10.1021/ac303008f.

[101] Kochergin, V. E., Beloglazov, A. A., Valeiko, M. V., and Nikitin, P. I. Phase properties of a surface-plasmon resonance from the viewpoint of sensor applications. *Quantum Electronics*, **1998**. 28 (5), pp. 444–448. doi: 10.1070/qe1998v028n05abeh001245.

[102] Zhang, C., Wang, R., Min, C., Zhu, S., and Yuan, X.-C. Experimental approach to the microscopic phase-sensitive surface plasmon resonance biosensor. *Applied Physics Letters*, **2013**. 102 (1), p. 011114. doi: 10.1063/1.4773997.

[103] Tabish, T. A., *et al.* Smart gold nanostructures for light mediated cancer theranostics: Combining optical diagnostics with photothermal therapy. *Advanced Science*, **2020**. 7 (15), p. 1903441. ISSN 2198-3844. doi: 10.1002/advs.201903441.

[104] Link, S. and El-Sayed, M. A. Spectral properties and relaxation dynamics of surface plasmon electronic oscillations in gold and silver nanodots and nanorods. *The Journal of Physical Chemistry B*, **1999**. 103 (40), pp. 8410–8426. doi: 10.1021/jp9917648.

[105] Zorić, I., Zäch, M., Kasemo, B., and Langhammer, C. Gold, platinum, and aluminum nanodisk plasmons: Material independence, subradiance, and damping mechanisms. *ACS Nano*, **2011**. 5 (4), pp. 2535–2546. doi: 10.1021/nn102166t.

[106] Muskens, O. L., Giannini, V., Sánchez-Gil, J. A., and Rivas, J. G. Optical scattering resonances of single and coupled dimer plasmonic nanoantennas. *Optics Express*, **2007**. 15 (26), p. 17736. doi: 10.1364/oe.15.017736.

[107] Fan, J. A., *et al.* Self-assembled plasmonic nanoparticle clusters. *Science*, **2010**. 328 (5982), pp. 1135–1138. doi: 10.1126/science.1187949.

[108] Dahlin, A. B., Wittenberg, N. J., Höök, F., and Oh, S. H. Promises and challenges of nanoplasmonic devices for refractometric biosensing. *Nanophotonics*, **2013**. 2 (2), pp. 83–101. ISSN 21928606. doi: 10.1515/nanoph-2012-0026.

[109] Oliverio, M., Perotto, S., Messina, G. C., Lovato, L., and Angelis, F. D. Chemical functionalization of plasmonic surface biosensors: A tutorial review on issues, strategies, and costs. *ACS Applied Materials & Interfaces*, **2017**. 9 (35), pp. 29394–29411. doi: 10.1021/acsami.7b01583.

[110] Brolo, A. G. Plasmonics for future biosensors. *Nature Photonics*, **2012**. 6 (11), pp. 709–713. ISSN 1749-4893. doi: 10.1038/nphoton.2012.266.

[111] Anker, J. N., *et al.* Biosensing with plasmonic nanosensors. *Nature Materials*, **2008**. 7 (6), pp. 442–453. doi: 10.1038/nmat2162.

[112] Brolo, A. G. Plasmonics for future biosensors. *Nature Photonics*, **2012**. 6 (11), pp. 709–713. doi: 10.1038/nphoton.2012.266.

[113] Jackman, J. A., Ferhan, A. R., and Cho, N.-J. Nanoplasmonic sensors for biointerfacial science. *Chemical Society Reviews*, **2017**. 46 (12), pp. 3615–3660. doi: 10.1039/c6cs00494f.

[114] Zhao, Y., *et al.* Shell-engineered chiroplasmonic assemblies of nanoparticles for zeptomolar DNA detection. *Nano Letters*, **2014**. 14 (7), pp. 3908–3913. doi: 10.1021/nl501166m.

[115] Aćimović, S. S., *et al.* LSPR chip for parallel, rapid, and sensitive detection of cancer markers in serum. *Nano Letters*, **2014**. 14 (5), pp. 2636–2641. doi: 10.1021/nl500574n.

[116] Yanik, A. A., *et al.* An optofluidic nanoplasmonic biosensor for direct detection of live viruses from biological media. *Nano Letters*, **2010**. 10 (12), pp. 4962–4969. doi: 10.1021/nl103025u.

[117] Ament, I., Prasad, J., Henkel, A., Schmachtel, S., and Sönnichsen, C. Single unlabeled protein detection on individual plasmonic nanoparticles. *Nano Letters*, **2012**. ISSN 15306984. doi: 10.1021/nl204496g.

[118] Zijlstra, P., Paulo, P. M. R., and Orrit, M. Optical detection of single non-absorbing molecules using the surface plasmon resonance of a gold nanorod. *Nature Nanotechnology*, **2012**. 7 (6), pp. 379–382. doi: 10.1038/nnano.2012.51.

[119] Špringer, T., Bocková, M., and Homola, J. Label-free biosensing in complex media: A referencing approach. *Analytical Chemistry*, **2013**. 85 (12), pp. 5637–5640. doi: 10.1021/ac401062m.

[120] Mirkin, C. A., Letsinger, R. L., Mucic, R. C., and Storhoff, J. J. A DNA-based method for rationally assembling nanoparticles into macroscopic materials. *Nature*, **1996**. 382 (6592), pp. 607–609. doi: 10.1038/382607a0.

[121] Chen, S., Svedendahl, M., Duyne, R. P. V., and Käll, M. Plasmon-enhanced colorimetric ELISA with single molecule sensitivity. *Nano Letters*, **2011**. 11 (4), pp. 1826–1830. doi: 10.1021/nl2006092.

[122] Yesilkoy, F., *et al.* Ultrasensitive hyperspectral imaging and biodetection enabled by dielectric metasurfaces. *Nature Photonics*, **2019**. 13 (6), pp. 390–396. ISSN 1749-4893. doi: 10.1038/s41566-019-0394-6.

[123] Jahani, Y., *et al.* Imaging-based spectrometer-less optofluidic biosensors based on dielectric metasurfaces for detecting extracellular vesicles. *Nature Communications*, **2021**. 12 (1), p. 3246. ISSN 2041-1723. doi: 10.1038/s41467-021-23257-y.

[124] Zhang, S., *et al.* Metasurfaces for biomedical applications: imaging and sensing from a nanophotonics perspective. *Nanophotonics*, **2021**. 10 (1), pp. 259–293. doi: doi:10.1515/nanoph-2020-0373.

[125] Leitis, A., *et al.* Angle-multiplexed all-dielectric metasurfaces for broadband molecular fingerprint retrieval. *Science Advances*, **2019**. 5 (5), p. eaaw2871. doi: 10.1126/sciadv.aaw2871.

[126] Ahmed, R., *et al.* Tunable fano-resonant metasurfaces on a disposable plastic-template for multimodal and multiplex biosensing. *Advanced Materials*, **2020**. 32 (19), p. 1907160. doi: https://doi.org/10.1002/adma.201907160.

[127] Park, S. J., *et al.* Detection of microorganisms using terahertz metamaterials. *Scientific Reports*, **2014**. 4 (1), p. 4988. ISSN 2045-2322. doi: 10.1038/srep04988.

[128] Mosier-Boss, P. Review of SERS substrates for chemical sensing. *Nanomaterials*, **2017**. 7 (6), p. 142. doi: 10.3390/nano7060142.

[129] Sharma, B., Frontiera, R. R., Henry, A.-I., Ringe, E., and Duyne, R. P. V. SERS: Materials, applications, and the future. *Materials Today*, **2012**. 15 (1-2), pp. 16–25. doi: 10.1016/s1369-7021(12)70017-2.

[130] Laing, S., Jamieson, L. E., Faulds, K., and Graham, D. Surface-enhanced raman spectroscopy for in vivo biosensing. *Nature Reviews Chemistry*, **2017**. 1 (8). doi: 10.1038/s41570-017-0060.

[131] Tittl, A., *et al.* Imaging-based molecular barcoding with pixelated dielectric metasurfaces. *Science*, **2018**. 360 (6393), pp. 1105–1109. doi: 10.1126/science.aas9768.

[132] Wuttig, M., Bhaskaran, H., and Taubner, T. Phase-change materials for non-volatile photonic applications. *Nature Photonics*, **2017**. 11 (8), pp. 465–476. doi: 10.1038/nphoton.2017.126.

[133] Grigorenko, A. N., Polini, M., and Novoselov, K. S. Graphene plasmonics. *Nature Photonics*, **2012**. 6 (11), pp. 749–758. ISSN 17494885. doi: 10.1038/nphoton.2012.262.

[134] Li, Z., *et al.* Hybrid metasurface-based mid-infrared biosensor for simultaneous quantification and identification of monolayer protein. *ACS Photonics*, **2019**. 6 (2), pp. 501–509. doi: 10.1021/acsphotonics.8b01470.

[135] Oh, S.-H. and Altug, H. Performance metrics and enabling technologies for nanoplasmonic biosensors. *Nature Communications*, **2018**. 9 (1), p. 5263. ISSN 2041-1723. doi: 10.1038/s41467-018-06419-3.

[136] Sönnichsen, C., *et al.* Drastic reduction of plasmon damping in gold nanorods. *Phys. Rev. Lett.*, **2002**. 88, p. 077402. doi: 10.1103/PhysRevLett.88.077402.

[137] Khurgin, J. B. How to deal with the loss in plasmonics and metamaterials. *Nature Nanotechnology*, **2015**. 10 (1), pp. 2–6. ISSN 1748-3395. doi: 10.1038/nnano.2014.310.

[138] Zheng, B. Y., *et al.* Distinguishing between plasmon-induced and photoexcited carriers in a device geometry. *Nature Communications*, **2015**. 6 (1), p. 7797. ISSN 2041-1723. doi: 10.1038/ncomms8797.

[139] Tagliabue, G., *et al.* Quantifying the role of surface plasmon excitation and hot carrier transport in plasmonic devices. *Nature Communications*, **2018**. 9 (1), p. 3394. ISSN 2041-1723. doi: 10.1038/s41467-018-05968-x.

[140] Khurgin, J. B. Fundamental limits of hot carrier injection from metal in nanoplasmonics. *Nanophotonics*, **2020**. 9 (2), pp. 453–471. doi: doi:10.1515/nanoph-2019-0396.

[141] Shahbazyan, T. V. Landau damping of surface plasmons in metal nanostructures. *Phys. Rev. B*, **2016**. 94, p. 235431. doi: 10.1103/PhysRevB.94.235431.

[142] Khurgin, J. B. Hot carriers generated by plasmons: where are they generated and where do they go from there? *Faraday Discuss.*, **2019**. 214, pp. 35–58. doi: 10.1039/C8FD00200B.

[143] Clavero, C. Plasmon-induced hot-electron generation at nanoparticle/metal-oxide interfaces for photovoltaic and photocatalytic devices. *Nature Photonics*, **2014**. 8 (2), pp. 95–103. ISSN 1749-4893. doi: 10.1038/nphoton.2013.238.

[144] Sun, Q., Zhang, C., Shao, W., and Li, X. Photodetection by hot electrons or hot holes: A comparable study on physics and performances. *ACS Omega*, **2019**. 4 (3), pp. 6020–6027. doi: 10.1021/acsomega.9b00267.

[145] Kontoleta, E., *et al.* Using hot electrons and hot holes for simultaneous co-catalyst deposition on plasmonic nanostructures. *ACS Applied Materials & Interfaces*, **2020**. 12 (32), pp. 35986–35994. ISSN 1944-8244. doi: 10.1021/acsami.0c04941.

[146] Bernardi, M., Mustafa, J., Neaton, J. B., and Louie, S. G. Theory and computation of hot carriers generated by surface plasmon polaritons in noble metals. *Nature Communications*, **2015**. 6 (1), p. 7044. ISSN 2041-1723. doi: 10.1038/ncomms8044.

[147] Brongersma, M. L., Halas, N. J., and Nordlander, P. Plasmon-induced hot carrier science and technology. *Nature Nanotechnology*, **2015**. 10 (1), pp. 25–34. doi: 10.1038/nnano.2014.311.

[148] Chen, Z., *et al.* Imaging local heating and thermal diffusion of nanomaterials with plasmonic thermal microscopy. *ACS Nano*, **2015**. 9 (12), pp. 11574–11581. ISSN 1936-0851. doi: 10.1021/acsnano.5b05306.

[149] Baffou, G., Polleux, J., Rigneault, H., and Monneret, S. Super-heating and micro-bubble generation around plasmonic nanoparticles under cw illumination. *The Journal of Physical Chemistry C*, **2014**. 118 (9), pp. 4890–4898. ISSN 1932-7447. doi: 10.1021/jp411519k.

[150] Baffou, G., Cichos, F., and Quidant, R. Applications and challenges of thermoplasmonics. *Nature Materials*, **2020**. 19 (9), pp. 946–958. ISSN 1476-4660. doi: 10.1038/s41563-020-0740-6.

[151] Brown, A. M., Sundararaman, R., Narang, P., Goddard, W. A., and Atwater, H. A. Nonradiative plasmon decay and hot carrier dynamics: Effects of phonons, surfaces, and geometry. *ACS Nano*, **2016**. 10 (1), pp. 957–966. ISSN 1936-0851. doi: 10.1021/acsnano.5b06199.

[152] Boerigter, C., Aslam, U., and Linic, S. Mechanism of charge transfer from plasmonic nanostructures to chemically attached materials. *ACS Nano*, **2016**. 10 (6), pp. 6108–6115. ISSN 1936-0851. doi: 10.1021/acsnano.6b01846.

[153] Tatsuma, T., Nishi, H., and Ishida, T. Plasmon-induced charge separation: chemistry and wide applications. *Chem. Sci.*, **2017**. 8, pp. 3325–3337. doi: 10.1039/C7SC00031F.

[154] Zhang, C., Jia, F., Li, Z., Huang, X., and Lu, G. Plasmon-generated hot holes for chemical reactions. *Nano Research*, **2020**. 13 (12), pp. 3183–3197. ISSN 1998-0000. doi: 10.1007/s12274-020-3031-2.

[155] Kim, Y., Smith, J. G., and Jain, P. K. Harvesting multiple electron–hole pairs generated through plasmonic excitation of au nanoparticles. *Nature Chemistry*, **2018**. 10 (7), pp. 763–769. ISSN 1755-4349. doi: 10.1038/s41557-018-0054-3.

[156] Zhang, X., Chen, Y. L., Liu, R.-S., and Tsai, D. P. Plasmonic photocatalysis. *Reports on Progress in Physics*, **2013**. 76 (4), p. 046401. doi: 10.1088/0034-4885/76/4/046401.

[157] Mubeen, S., *et al.* An autonomous photosynthetic device in which all charge carriers derive from surface plasmons. *Nature Nanotechnology*, **2013**. 8 (4), pp. 247–251. ISSN 1748-3395. doi: 10.1038/nnano.2013.18.

[158] DuChene, J. S., Tagliabue, G., Welch, A. J., Cheng, W.-H., and Atwater, H. A. Hot hole collection and photoelectrochemical co2 reduction with plasmonic au/p-gan photocathodes. *Nano Letters*, **2018**. 18 (4), pp. 2545–2550. ISSN 1530-6984. doi: 10.1021/acs.nanolett.8b00241.

[159] Suzuki, K., Li, X., Wang, Y., Nagasawa, F., and Murakoshi, K. Active intermediates in plasmon-induced water oxidation at au nanodimer structures on a single crystal of tio2. *ACS Energy Letters*, **2020**. 5 (4), pp. 1252–1259. doi: 10.1021/acsenergylett.0c00478.

[160] Li, J., *et al.* Plasmon-induced resonance energy transfer for solar energy conversion. *Nature Photonics*, **2015**. 9 (9), pp. 601–607. ISSN 1749-4893. doi: 10.1038/nphoton.2015.142.

[161] Mascaretti, L., *et al.* Plasmon-enhanced photoelectrochemical water splitting for efficient renewable energy storage. *Advanced Materials*, **2019**. 31 (31), p. 1805513. doi: https://doi.org/10.1002/adma.201805513.

[162] da Silva, A. G. M., Rodrigues, T. S., Wang, J., and Camargo, P. H. C. Plasmonic catalysis with designer nanoparticles. *Chem. Commun.*, **2022**. 58, pp. 2055–2074. doi: 10.1039/D1CC03779J.

[163] Reineck, P., Brick, D., Mulvaney, P., and Bach, U. Plasmonic hot electron solar cells: The effect of nanoparticle size on quantum efficiency. *The Journal of Physical Chemistry Letters*, **2016**. 7 (20), pp. 4137–4141. doi: 10.1021/acs.jpclett.6b01884.

[164] Zhu, Y., Xu, H., Yu, P., and Wang, Z. Engineering plasmonic hot carrier dynamics toward efficient photodetection. *Applied Physics Reviews*, **2021**. 8 (2), p. 021305. doi: 10.1063/5.0029050.

[165] Zhu, Z., *et al.* Surface plasmon mediates the visible light–responsive lithium–oxygen battery with au nanoparticles on defective carbon nitride. *Proceedings of the National Academy of Sciences*, **2021**. 118 (17), p. e2024619118. doi: 10.1073/pnas.2024619118.

[166] Qiao, Y., *et al.* A label-free photoelectrochemical aptasensor for bisphenol a based on surface plasmon resonance of gold nanoparticle-sensitized zno nanopencils. *Biosensors and Bioelectronics*, **2016**. 86, pp. 315–320. ISSN 0956-5663. doi: https://doi.org/10.1016/j.bios.2016.06.062.

[167] Zhang, Y., *et al.* Surface-plasmon-driven hot electron photochemistry. *Chemical Reviews*, **2018**. 118 (6), pp. 2927–2954. ISSN 0009-2665. doi: 10.1021/acs.chemrev.7b00430.

[168] Ahlawat, M., Mittal, D., and Govind Rao, V. Plasmon-induced hot-hole generation and extraction at nano-heterointerfaces for photocatalysis. *Communications Materials*, **2021**. 2 (1), p. 114. ISSN 2662-4443. doi: 10.1038/s43246-021-00220-4.

[169] Thangamuthu, M., Raziman, T., Martin, O. J. F., and Tang, J. Review—origin and promotional effects of plasmonics in photocatalysis. *Journal of The Electrochemical Society*, **2022**. 169 (3), p. 036512. doi: 10.1149/1945-7111/ac5c97.

[170] Mukherjee, S., *et al.* Hot electrons do the impossible: Plasmon-induced dissociation of h2 on au. *Nano Letters*, **2013**. 13 (1), pp. 240–247. ISSN 1530-6984. doi: 10.1021/nl303940z.

[171] Wang, Y., *et al.* Plasmon-directed polymerization: Regulating polymer growth with light. *Nano Research*, **2018**. 11 (12), pp. 6384–6390. ISSN 1998-0000. doi: 10.1007/s12274-018-2163-0.

[172] Tang, H., *et al.* Plasmonic hot electrons for sensing, photodetection, and solar energy applications: A perspective. *The Journal of Chemical Physics*, **2020**. 152 (22), p. 220901. doi: 10.1063/5.0005334.

[173] Aizpurua, J., *et al.* Theory of hot electrons: general discussion. *Faraday Discuss.*, **2019**. 214, pp. 245–281. doi: 10.1039/C9FD90012H.

[174] Baumberg, J. J. Hot electron science in plasmonics and catalysis: what we argue about. *Faraday Discuss.*, **2019**. 214, pp. 501–511. doi: 10.1039/C9FD00027E.

[175] Dubi, Y. and Sivan, Y. „"Hot"“ electrons in metallic nanostructures—non-thermal carriers or heating? *Light: Science & Applications*, **2019**. 8 (1), p. 89. ISSN 2047-7538. doi: 10.1038/s41377-019-0199-x.

[176] Yonatan Dubi, Y. S. „"Hot"“ electrons in metallic nanostructuresâ€”nonthermal carriers or heating? *Light: Advanced Manufacturing*, **2019**. 8 (xjzz-2019-8-828), p. 828. ISSN 2689-9620. doi: 10.1038/s41377-019-0199-x.

[177] Baffou, G., Bordacchini, I., Baldi, A., and Quidant, R. Simple experimental procedures to distinguish photothermal from hot-carrier processes in plasmonics. *Light: Science & Applications*, **2020**. 9 (1), p. 108. ISSN 2047-7538. doi: 10.1038/s41377-020-00345-0.

[178] Linic, S., Chavez, S., and Elias, R. Flow and extraction of energy and charge carriers in hybrid plasmonic nanostructures. *Nature Materials*, **2021**. 20 (7), pp. 916–924. ISSN 1476-4660. doi: 10.1038/s41563-020-00858-4.

[179] Cortés, E., *et al.* Challenges in plasmonic catalysis. *ACS Nano*, **2020**. 14 (12), pp. 16202–16219. ISSN 1936-0851. doi: 10.1021/acsnano.0c08773.

[180] Atwater, H. A. and Polman, A. Plasmonics for improved photovoltaic devices. *Nature Materials*, **2010**. 9 (3), pp. 205–213. ISSN 1476-4660. doi: 10.1038/nmat2629.

[181] Brongersma, M. L., Cui, Y., and Fan, S. Light management for photovoltaics using high-index nanostructures. *Nature Materials*, **2014**. 13 (5), pp. 451–460. ISSN 1476-4660. doi: 10.1038/nmat3921.

[182] Linic, S., Christopher, P., and Ingram, D. B. Plasmonic-metal nanostructures for efficient conversion of solar to chemical energy. *Nature Materials*, **2011**. 10 (12), pp. 911–921. ISSN 14764660. doi: 10.1038/nmat3151.

[183] Noginov, M. A., *et al.* Demonstration of a spaser-based nanolaser. *Nature*, **2009**. 460 (7259), pp. 1110–1112. ISSN 1476-4687. doi: 10.1038/nature08318.

[184] Yang, A., *et al.* Real-time tunable lasing from plasmonic nanocavity arrays. *Nature Communications*, **2015**. 6 (1), p. 6939. ISSN 2041-1723. doi: 10.1038/ncomms7939.

[185] Lozano, G., *et al.* Plasmonics for solid-state lighting: enhanced excitation and directional emission of highly efficient light sources. *Light: Science & Applications*, **2013**. 2 (5), pp. e66–e66. ISSN 2047-7538. doi: 10.1038/lsa.2013.22.

[186] Lozano, G., Rodriguez, S. R., Verschuuren, M. A., and Gómez Rivas, J. Metallic nanostructures for efficient led lighting. *Light: Science & Applications*, **2016**. 5 (6), pp. e16080–e16080. ISSN 2047-7538. doi: 10.1038/lsa.2016.80.

[187] Su, H.-S., Feng, H.-S., Wu, X., Sun, J.-J., and Ren, B. Recent advances in plasmon-enhanced raman spectroscopy for catalytic reactions on bifunctional metallic nanostructures. *Nanoscale*, **2021**. 13, pp. 13962–13975. doi: 10.1039/D1NR04009J.

[188] Kauranen, M. and Zayats, A. V. Nonlinear plasmonics. *Nature Photonics*, **2012**. 6 (11), pp. 737–748. ISSN 1749-4893. doi: 10.1038/nphoton.2012.244.

[189] Wu, D. M., García-Etxarri, A., Salleo, A., and Dionne, J. A. Plasmon-enhanced upconversion. *The Journal of Physical Chemistry Letters*, **2014**. 5 (22), pp. 4020–4031. doi: 10.1021/jz5019042.

[190] Wu, Y., *et al.* Upconversion superburst with sub-2 μs lifetime. *Nature Nanotechnology*, **2019**. 14 (12), pp. 1110–1115. ISSN 1748-3395. doi: 10.1038/s41565-019-0560-5.

[191] Tame, M. S., *et al.* Quantum plasmonics. *Nature Physics*, **2013**. 9 (6), pp. 329–340. ISSN 1745-2481. doi: 10.1038/nphys2615.

[192] Zhou, Z.-K., *et al.* Quantum plasmonics get applied. *Progress in Quantum Electronics*, **2019**. 65, pp. 1–20. ISSN 0079-6727. doi: https://doi.org/10.1016/j.pquantelec.2019.04.002.

[193] Yu, H., Peng, Y., Yang, Y., and Li, Z.-Y. Plasmon-enhanced light–matter interactions and applications. *npj Computational Materials*, **2019**. 5 (1), p. 45. ISSN 2057-3960. doi: 10.1038/s41524-019-0184-1.

[194] Howes, P. D., Rana, S., and Stevens, M. M. Plasmonic nanomaterials for biodiagnostics. *Chem. Soc. Rev.*, **2014**. 43 (11), pp. 3835–3853. doi: 10.1039/c3cs60346f.

[195] Dreaden, E. C., Mackey, M. A., Huang, X., Kang, B., and El-Sayed, M. A. Beating cancer in multiple ways using nanogold. *Chemical Society Reviews*, **2011**. 40 (7), p. 3391. doi: 10.1039/c0cs00180e.

[196] Menon, J. U., *et al.* Nanomaterials for photo-based diagnostic and therapeutic applications. *Theranostics*, **2013**. 3 (3), pp. 152–166. doi: 10.7150/thno.5327.

[197] Ozbay, E. Plasmonics: Merging photonics and electronics at nanoscale dimensions. *Science*, **2006**. 311 (5758), pp. 189–193. doi: 10.1126/science.1114849.

[198] Harter, T., *et al.* Silicon–plasmonic integrated circuits for terahertz signal generation and coherent detection. *Nature Photonics*, **2018**. 12 (10), pp. 625–633. ISSN 1749-4893. doi: 10.1038/s41566-018-0237-x.

[199] Harris, N. C., *et al.* Quantum transport simulations in a programmable nanophotonic processor. *Nature Photonics*, **2017**. 11 (7), pp. 447–452. ISSN 1749-4893. doi: 10.1038/nphoton.2017.95.

[200] Babocký, J., *et al.* Quantitative 3D Phase Imaging of Plasmonic Metasurfaces. *ACS Photonics*, **2017**. 4 (6). ISSN 23304022. doi: 10.1021/acsphotonics.7b00022.

[201] Chen, W.-Y., Lin, C.-H., and Chen, W.-T. Plasmonic phase transition and phase retardation: essential optical characteristics of localized surface plasmon resonance. *Nanoscale*, **2013**. 5, pp. 9950–9956. doi: 10.1039/C3NR02603E.

[202] Neuman, T., *et al.* Mapping the near fields of plasmonic nanoantennas by scattering-type scanning near-field optical microscopy. *Laser & Photonics Reviews*, **2015**. 9 (6), pp. 637–649. doi: 10.1002/lpor.201500031.

[203] Pshenay-Severin, E., Falkner, M., Helgert, C., and Pertsch, T. Ultra broadband phase measurements on nanostructured metasurfaces. *Applied Physics Letters*, **2014**. 104 (22), p. 221906. doi: 10.1063/1.4881332.

[204] Dolling, G., Enkrich, C., Wegener, M., Soukoulis, C. M., and Linden, S. Simultaneous negative phase and group velocity of light in a metamaterial. *Science*, **2006**. 312 (5775), pp. 892–894. ISSN 0036-8075. doi: 10.1126/science.1126021.

[205] Lošt'ák, M., Chmelík, R., Slabá, M., and Slabý, T. Coherence-controlled holographic microscopy in diffuse media. *Opt. Express*, **2014**. 22 (4), pp. 4180–4195. doi: 10.1364/OE.22.004180.

[206] Kolman, P. and Chmelík, R. Coherence-controlled holographic microscope. *Opt. Express*, **2010**. 18 (21), pp. 21990–22004. doi: 10.1364/OE.18.021990.

[207] Kreis, T. Digital holographic interference-phase measurement using the fourier-transform method. *J. Opt. Soc. Am. A*, **1986**. 3 (6), pp. 847–855. doi: 10.1364/JOSAA.3.000847.

[208] Slabý, T., *et al.* Off-axis setup taking full advantage of incoherent illumination in coherence-controlled holographic microscope. *Opt. Express*, **2013**. 21 (12), pp. 14747–14762. doi: 10.1364/OE.21.014747.

[209] Hristov, H. and Hristov, H. *Fresnel Zones in Wireless Links, Zone Plate Lenses and Antennas*. Antennas and Propagation Library. Artech House, **2000**. ISBN 9780890068496.

[210] Soret, J. L. Ueber die durch kreisgitter erzeugten diffractionsphänomene. *Annalen der Physik*, **1875**. 232 (9), pp. 99–113. doi: https://doi.org/10.1002/andp.18752320906.

[211] Wood, R. W. Liii. phase-reversal zone-plates, and diffraction-telescopes. *The London, Edinburgh, and Dublin Philosophical Magazine and Journal of Science*, **1898**. 45 (277), pp. 511–522. doi: 10.1080/14786449808621159.

[212] Faßbender, A., Babocký, J., Dvořák, P., Křápek, V., and Linden, S. Invited Article: Direct phase mapping of broadband Laguerre-Gaussian metasurfaces. *APL Photonics*, **2018**. 3 (11), p. 110803. ISSN 23780967. doi: 10.1063/1.5049368.

[213] Boltasseva, A. and Atwater, H. A. Low-Loss Plasmonic Metamaterials. *Science*, **2011**. 331 (6015), pp. 290–291. ISSN 0036-8075. doi: 10.1126/science.1198258.

[214] Kuznetsov, A. I., Miroshnichenko, A. E., Brongersma, M. L., Kivshar, Y. S., and Luk'yanchuk, B. Optically resonant dielectric nanostructures. *Science*, **2016**. 354 (6314). ISSN 0036-8075. doi: 10.1126/science.aag2472.

[215] Shaltout, A. M., Kildishev, A. V., and Shalaev, V. M. Evolution of photonic metasurfaces: from static to dynamic. *J. Opt. Soc. Am. B*, **2016**. 33 (3), pp. 501–510. doi: 10.1364/JOSAB.33.000501.

[216] Choudhury, S. M., *et al.* Material platforms for optical metasurfaces. *Nanophotonics*, **2018**. 7 (6), pp. 959–987. doi: doi:10.1515/nanoph-2017-0130.

[217] Che, Y., Wang, X., Song, Q., Zhu, Y., and Xiao, S. Tunable optical metasurfaces enabled by multiple modulation mechanisms. *Nanophotonics*, **2020**. 9 (15), pp. 4407–4431. doi: doi:10.1515/nanoph-2020-0311.

[218] Gutierrez, Y., Brown, A. S., Moreno, F., and Losurdo, M. Plasmonics beyond noble metals: Exploiting phase and compositional changes for manipulating plasmonic performance. *Journal of Applied Physics*, **2020**. 128 (8), p. 080901. doi: 10.1063/5.0020752.

[219] Ding, F., Yang, Y., and Bozhevolnyi, S. I. Dynamic metasurfaces using phase-change chalcogenides. *Advanced Optical Materials*, **2019**. 7 (14), p. 1801709. doi: https://doi.org/10.1002/adom.201801709.

[220] Qin, S., *et al.* Near-infrared thermally modulated varifocal metalens based on the phase change material sb2s3. *Opt. Express*, **2021**. 29 (5), pp. 7925–7934. doi: 10.1364/OE.420014.

[221] Ko, B., Badloe, T., and Rho, J. Vanadium dioxide for dynamically tunable photonics. *ChemNanoMat*, **2021**. 7 (7), pp. 713–727. doi: https://doi.org/10.1002/cnma.202100060.

[222] Karvounis, A., Gholipour, B., MacDonald, K. F., and Zheludev, N. I. All-dielectric phase-change reconfigurable metasurface. *Applied Physics Letters*, **2016**. 109 (5), p. 051103. doi: 10.1063/1.4959272.

[223] Mou, N., *et al.* Large-scale, low-cost, broadband and tunable perfect optical absorber based on phase-change material. *Nanoscale*, **2020**. 12, pp. 5374–5379. doi: 10.1039/C9NR07602F.

[224] Yin, X., *et al.* Beam switching and bifocal zoom lensing using active plasmonic metasurfaces. *Light: Science & Applications*, **2017**. 6 (7), pp. e17016–e17016. ISSN 2047-7538. doi: 10.1038/lsa.2017.16.

[225] Earl, S. K., *et al.* Switchable polarization rotation of visible light using a plasmonic metasurface. *APL Photonics*, **2017**. 2 (1), p. 016103. doi: 10.1063/1.4968840.

[226] Tian, J., *et al.* Active control of anapole states by structuring the phase-change alloy ge 2 sb 2 te 5. *Nature Communications*, **2019**. 10 (1), p. 396. ISSN 2041-1723. doi: 10.1038/s41467-018-08057-1.

[227] Lei, D. Y., *et al.* Optically-triggered nanoscale memory effect in a hybrid plasmonic-phase changing nanostructure. *ACS Photonics*, **2015**. 2 (9), pp. 1306–1313. doi: 10.1021/acsphotonics.5b00249.

[228] de Galarreta, C. R., *et al.* Nonvolatile reconfigurable phase-change metadevices for beam steering in the near infrared. *Advanced Functional Materials*, **2018**. 28 (10), p. 1704993. doi: https://doi.org/10.1002/adfm.201704993.

[229] Qu, Y., *et al.* Dynamic thermal emission control based on ultrathin plasmonic metamaterials including phase-changing material gst. *Laser & Photonics Reviews*, **2017**. 11 (5), p. 1700091. doi: https://doi.org/10.1002/lpor.201700091.

[230] Chu, C. H., *et al.* Active dielectric metasurface based on phase-change medium. *Laser and Photonics Reviews*, **2016**. 10 (6), pp. 986–994. ISSN 18638899. doi: 10.1002/lpor.201600106.

[231] Ke, Y., *et al.* Controllable fabrication of two-dimensional patterned vo2 nanoparticle, nanodome, and nanonet arrays with tunable temperature-dependent localized surface plasmon resonance. *ACS Nano*, **2017**. 11 (7), pp. 7542–7551. ISSN 1936-0851. doi: 10.1021/acsnano.7b02232.

[232] Zhu, Z., Evans, P. G., Haglund, R. F., and Valentine, J. G. Dynamically reconfigurable metadevice employing nanostructured phase-change materials. *Nano Letters*, **2017**. 17 (8), pp. 4881–4885. ISSN 1530-6984. doi: 10.1021/acs.nanolett.7b01767.

[233] Ligmajer, F., *et al.* Epitaxial VO2 nanostructures: A route to large-scale, switchable dielectric metasurfaces. *ACS Photonics*, **2018**. 5 (7), pp. 2561–2567. doi: 10.1021/acsphotonics.7b01384.

[234] Shao, Z., Cao, X., Luo, H., and Jin, P. Recent progress in the phase-transition mechanism and modulation of vanadium dioxide materials. *NPG Asia Materials*, **2018**. 10 (7), pp. 581–605. ISSN 1884-4057. doi: 10.1038/s41427-018-0061-2.

[235] SchwingenschlÄ¶gl, U. and Eyert, V. The vanadium magnÄ©li phases vno2n-1. *Annalen der Physik*, **2004**. 516 (9), pp. 475–510. doi: https://doi.org/10.1002/andp.20045160901.

[236] Gurvitch, M., Luryi, S., Polyakov, A., and Shabalov, A. Nonhysteretic behavior inside the hysteresis loop of vo2 and its possible application in infrared imaging. *Journal of Applied Physics*, **2009**. 106 (10), p. 104504. doi: 10.1063/1.3243286.

[237] Zhou, Y. and Ramanathan, S. Mott memory and neuromorphic devices. *Proceedings of the IEEE*, **2015**. 103 (8), pp. 1289–1310. doi: 10.1109/JPROC.2015.2431914.

[238] Zheng, J., Bao, S., and Jin, P. Tio2(r)/vo2(m)/tio2(a) multilayer film as smart window: Combination of energy-saving, antifogging and self-cleaning functions. *Nano Energy*, **2015**. 11, pp. 136–145. ISSN 2211-2855. doi: https://doi.org/10.1016/j.nanoen.2014.09.023.

[239] Ma, H., *et al.* Flexible, all-inorganic actuators based on vanadium dioxide and carbon nanotube bimorphs. *Nano Letters*, **2017**. 17 (1), pp. 421–428. ISSN 1530-6984. doi: 10.1021/acs.nanolett.6b04393.

[240] Liu, K., Lee, S., Yang, S., Delaire, O., and Wu, J. Recent progresses on physics and applications of vanadium dioxide. *Materials Today*, **2018**. 21 (8), pp. 875–896. ISSN 1369-7021. doi: https://doi.org/10.1016/j.mattod.2018.03.029.

[241] Ke, Y., *et al.* Vanadium dioxide: The multistimuli responsive material and its applications. *Small*, **2018**. 14 (39), p. 1802025. doi: https://doi.org/10.1002/smll.201802025.

[242] Wegkamp, D. and StÄ¤hler, J. Ultrafast dynamics during the photoinduced phase transition in vo2. *Progress in Surface Science*, **2015**. 90 (4), pp. 464–502. ISSN 0079-6816. doi: https://doi.org/10.1016/j.progsurf.2015.10.001.

[243] Yang, Z., Ko, C., and Ramanathan, S. Oxide electronics utilizing ultrafast metal-insulator transitions. *Annual Review of Materials Research*, **2011**. 41 (1), pp. 337–367. doi: 10.1146/annurev-matsci-062910-100347.

[244] Aetukuri, N. B., *et al.* Control of the metal–insulator transition in vanadium dioxide by modifying orbital occupancy. *Nature Physics*, **2013**. 9 (10), pp. 661–666. ISSN 1745-2481. doi: 10.1038/nphys2733.

[245] McWhan, D. B., Marezio, M., Remeika, J. P., and Dernier, P. D. X-ray diffraction study of metallic vo_2. *Phys. Rev. B*, **1974**. 10, pp. 490–495. doi: 10.1103/PhysRevB.10.490.

[246] Longo, J. M., *et al.* A refinement of the structure of vo2. *Acta Chemica Scandinavica*, **1970**. 24, pp. 420–426.

[247] Wentzcovitch, R. M., Schulz, W. W., and Allen, P. B. vo_2: Peierls or mott-hubbard? a view from band theory. *Phys. Rev. Lett.*, **1994**. 72, pp. 3389–3392. doi: 10.1103/PhysRevLett.72.3389.

[248] Cavalleri, A., Dekorsy, T., Chong, H. H. W., Kieffer, J. C., and Schoenlein, R. W. Evidence for a structurally-driven insulator-to-metal transition in vo_2:

A view from the ultrafast timescale. *Phys. Rev. B*, **2004**. 70, p. 161102. doi: 10.1103/PhysRevB.70.161102.

[249] Kim, H.-T., *et al.* Monoclinic and correlated metal phase in vo_2 as evidence of the mott transition: Coherent phonon analysis. *Phys. Rev. Lett.*, **2006**. 97, p. 266401. doi: 10.1103/PhysRevLett.97.266401.

[250] Tselev, A., *et al.* Symmetry relationship and strain-induced transitions between insulating m1 and m2 and metallic r phases of vanadium dioxide. *Nano Letters*, **2010**. 10 (11), pp. 4409–4416. ISSN 1530-6984. doi: 10.1021/nl1020443.

[251] Atkin, J. M., *et al.* Strain and temperature dependence of the insulating phases of vo_2 near the metal-insulator transition. *Phys. Rev. B*, **2012**. 85, p. 020101. doi: 10.1103/PhysRevB.85.020101.

[252] Lu, H., Clark, S., Guo, Y., and Robertson, J. The metalâ€“insulator phase change in vanadium dioxide and its applications. *Journal of Applied Physics*, **2021**. 129 (24), p. 240902. doi: 10.1063/5.0027674.

[253] Yao, T., *et al.* Understanding the nature of the kinetic process in a vo_2 metal-insulator transition. *Phys. Rev. Lett.*, **2010**. 105, p. 226405. doi: 10.1103/PhysRevLett.105.226405.

[254] Zhang, H.-T., *et al.* Wafer-scale growth of vo2 thin films using a combinatorial approach. *Nature Communications*, **2015**. 6 (1), p. 8475. ISSN 2041-1723. doi: 10.1038/ncomms9475.

[255] Shigesato, Y., Enomoto, M., and Odaka, H. Thermochromic VO_2 films deposited by RF magnetron sputtering using V_2O_3 or V_2O_5 targets. *Japanese Journal of Applied Physics*, **2000**. 39 (Part 1, No. 10), pp. 6016–6024. doi: 10.1143/jjap.39.6016.

[256] Babulanam, S., Eriksson, T., Niklasson, G., and Granqvist, C. Thermochromic vo2 films for energy-efficient windows. *Solar Energy Materials*, **1987**. 16 (5), pp. 347–363. ISSN 0165-1633. doi: https://doi.org/10.1016/0165-1633(87)90029-3.

[257] Dumas-Bouchiat, F., Champeaux, C., Catherinot, A., Crunteanu, A., and Blondy, P. rf-microwave switches based on reversible semiconductor-metal transition of vo2 thin films synthesized by pulsed-laser deposition. *Applied Physics Letters*, **2007**. 91 (22), p. 223505. doi: 10.1063/1.2815927.

[258] Manning, T. D., Parkin, I. P., Pemble, M. E., Sheel, D., and Vernardou, D. Intelligent window coatings: atmospheric pressure chemical vapor deposition of tungsten-doped vanadium dioxide. *Chemistry of Materials*, **2004**. 16 (4), pp. 744–749. ISSN 0897-4756. doi: 10.1021/cm034905y.

[259] Yin, D., Xu, N., Zhang, J., and Zheng, X. High quality vanadium dioxide films prepared by an inorganic sol-gel method. *Materials Research Bulletin*, **1996**. 31 (3), pp. 335–340. ISSN 0025-5408. doi: https://doi.org/10.1016/0025-5408(95)00191-3.

[260] Sohn, J. I., *et al.* Direct observation of the structural component of the metal-insulator phase transition and growth habits of epitaxially grown VO_2 nanowires. *Nano Letters*, **2007**. 7 (6), pp. 1570–1574. ISSN 1530-6984. doi: 10.1021/nl070439q.

[261] Dai, L., Cao, C., Gao, Y., and Luo, H. Synthesis and phase transition behavior of undoped vo2 with a strong nano-size effect. *Solar Energy Materials and Solar Cells*, **2011**. 95 (2), pp. 712–715. ISSN 0927-0248. doi: https://doi.org/10.1016/j.solmat.2010.10.008.

[262] Shi, R., *et al.* Recent advances in fabrication strategies, phase transition modulation, and advanced applications of vanadium dioxide. *Applied Physics Reviews*, **2019**. 6 (1), p. 011312. doi: 10.1063/1.5087864.

[263] Shibuya, K., Kawasaki, M., and Tokura, Y. Metal-insulator transition in epitaxial $V_{1-x}W_xO_2(0 \leq x \leq 0.33)$ thin films. *Applied Physics Letters*, **2010**. 96 (2), p. 022102. doi: 10.1063/1.3291053.

[264] Strelcov, E., *et al.* Doping-based stabilization of the m2 phase in free-standing VO_2 nanostructures at room temperature. *Nano Letters*, **2012**. 12 (12), pp. 6198–6205. ISSN 1530-6984. doi: 10.1021/nl303065h.

[265] Earl, S. K., *et al.* Switchable polarization rotation of visible light using a plasmonic metasurface. *APL Photonics*, **2017**. 2 (1), p. 016103. doi: 10.1063/1.4968840.

[266] Muskens, O. L., *et al.* Antenna-assisted picosecond control of nanoscale phase transition in vanadium dioxide. *Light: Science & Applications*, **2016**. 5 (10), pp. e16173–e16173. ISSN 2047-7538. doi: 10.1038/lsa.2016.173.

[267] Kim, Y., *et al.* Phase modulation with electrically tunable vanadium dioxide phase-change metasurfaces. *Nano Letters*, **2019**. 19 (6), pp. 3961–3968. ISSN 1530-6984. doi: 10.1021/acs.nanolett.9b01246.

[268] Narayan, J. and Larson, B. C. Domain epitaxy: A unified paradigm for thin film growth. *Journal of Applied Physics*, **2003**. 93 (1), pp. 278–285. doi: 10.1063/1.1528301.

[269] Brady, N. F., *et al.* Heterogeneous nucleation and growth dynamics in the light-induced phase transition in vanadium dioxide. *Journal of Physics: Condensed Matter*, **2016**. 28 (12), p. 125603. doi: 10.1088/0953-8984/28/12/125603.

[270] Marvel, R. E., Harl, R. R., Craciun, V., Rogers, B. R., and Haglund, R. F. Influence of deposition process and substrate on the phase transition of vanadium dioxide thin films. *Acta Materialia*, **2015**. 91, pp. 217–226. ISSN 1359-6454. doi: https://doi.org/10.1016/j.actamat.2015.03.009.

[271] Qazilbash, M. M., *et al.* Mott transition in VO2 revealed by infrared spectroscopy and nano-imaging. *Science*, **2007**. 318 (5857), pp. 1750–1753. doi: 10.1126/science.1150124.

[272] Paschotta, R. Rp photonics encyclopedia. `https://www.rp-photonics.com/optical_fiber_communications.html`. Accessed: 2021-03-22.

[273] Lei, D. Y., *et al.* Optically-Triggered Nanoscale Memory Effect in a Hybrid Plasmonic-Phase Changing Nanostructure. *ACS Photonics*, **2015**. 2 (9), pp. 1306–1313. ISSN 23304022. doi: 10.1021/acsphotonics.5b00249.

[274] Reed, G. T., Mashanovich, G., Gardes, F. Y., and Thomson, D. J. Silicon optical modulators. *Nature Photonics*, **2010**. 4 (8), pp. 518–526. ISSN 1749-4893. doi: 10.1038/nphoton.2010.179.

[275] Gopalakrishnan, G., Ruzmetov, D., and Ramanathan, S. On the triggering mechanism for the metal–insulator transition in thin film vo2 devices: electric field versus thermal effects. *Journal of Materials Science*, **2009**. 44 (19), pp. 5345–5353. ISSN 1573-4803. doi: 10.1007/s10853-009-3442-7.

[276] Rini, M., *et al.* Optical switching in vo2 films by below-gap excitation. *Applied Physics Letters*, **2008**. 92 (18), p. 181904. doi: 10.1063/1.2921784.

[277] Verleur, H. W., Barker, A. S., and Berglund, C. N. Optical properties of vo_2 between 0.25 and 5 ev. *Phys. Rev.*, **1968**. 172, pp. 788–798. doi: 10.1103/PhysRev.172.788.

[278] Kana Kana, J., Ndjaka, J., Vignaud, G., Gibaud, A., and Maaza, M. Thermally tunable optical constants of vanadium dioxide thin films measured by spectroscopic ellipsometry. *Optics Communications*, **2011**. 284 (3), pp. 807–812. ISSN 0030-4018. doi: https://doi.org/10.1016/j.optcom.2010.10.009.

[279] Howes, A., *et al.* Optical limiting based on huygens' metasurfaces. *Nano Letters*, **2020**. 20 (6), pp. 4638–4644. ISSN 1530-6984. doi: 10.1021/acs.nanolett.0c01574.

[280] Shu, F.-Z., *et al.* Electrically driven tunable broadband polarization states via active metasurfaces based on joule-heat-induced phase transition of vanadium dioxide. *Laser & Photonics Reviews*, **2021**. 15 (10), p. 2100155. doi: https://doi.org/10.1002/lpor.202100155.

[281] Tripathi, A., *et al.* Tunable mie-resonant dielectric metasurfaces based on vo2 phase-transition materials. *ACS Photonics*, **2021**. 8 (4), pp. 1206–1213. doi: 10.1021/acsphotonics.1c00124.

[282] Driscoll, T., *et al.* Dynamic tuning of an infrared hybrid-metamaterial resonance using vanadium dioxide. *Applied Physics Letters*, **2008**. 93 (2), p. 024101. doi: 10.1063/1.2956675.

[283] Cao, J., *et al.* Strain engineering and one-dimensional organization of metal–insulator domains in single-crystal vanadium dioxide beams. *Nature Nanotechnology*, **2009**. 4 (11), pp. 732–737. ISSN 1748-3395. doi: 10.1038/nnano.2009.266.

[284] Qazilbash, M. M., *et al.* Infrared spectroscopy and nano-imaging of the insulator-to-metal transition in vanadium dioxide. *Phys. Rev. B*, **2009**. 79, p. 075107. doi: 10.1103/PhysRevB.79.075107.

[285] Abate, Y., *et al.* Control of plasmonic nanoantennas by reversible metal-insulator transition. *Scientific Reports*, **2015**. 5 (1), p. 13997. ISSN 2045-2322. doi: 10.1038/srep13997.

[286] McGahan, C., *et al.* Geometric constraints on phase coexistence in vanadium dioxide single crystals. *Nanotechnology*, **2017**. 28 (8), p. 085701. doi: 10.1088/1361-6528/aa5652.

[287] Lopez, R., Feldman, L. C., and Haglund, R. F. Size-dependent optical properties of vo_2 nanoparticle arrays. *Phys. Rev. Lett.*, **2004**. 93, p. 177403. doi: 10.1103/PhysRevLett.93.177403.

[288] Lei, D. Y., Appavoo, K., Sonnefraud, Y., Richard F. Haglund, J., and Maier, S. A. Single-particle plasmon resonance spectroscopy of phase transition in vanadium dioxide. *Opt. Lett.*, **2010**. 35 (23), pp. 3988–3990. doi: 10.1364/OL.35.003988.

[289] Kejík, L., Horák, M., Šikola, T., and Křápek, V. Structural and optical properties of monocrystalline and polycrystalline gold plasmonic nanorods. *Opt. Express*, **2020**. 28 (23), pp. 34960–34972. doi: 10.1364/OE.409428.

[290] Kobayashi, S., Takagi, H., and Watanabe, T. Grain boundary character distribution and texture evolution during surface energy-driven grain growth in nanocrystalline gold thin films. *Philosophical Magazine*, **2013**. 93 (10-12), pp. 1425–1442. doi: 10.1080/14786435.2012.756991.

[291] Parajuli, P., Mendoza-Cruz, R., Santiago, U., Ponce, A., and Yacamán, M. J. The Evolution of Growth, Crystal Orientation, and Grain Boundaries Disorientation Distribution in Gold Thin Films. *Crystal Research and Technology*, **2018**. 53 (8), p. 1800038. ISSN 02321300. doi: 10.1002/crat.201800038.

[292] Huang, J. S., *et al.* Atomically flat single-crystalline gold nanostructures for plasmonic nanocircuitry. *Nature Communications*, **2010**. 1 (9), p. 150. ISSN 20411723. doi: 10.1038/ncomms1143.

[293] Mahmoodi, N., *et al.* Room temperature thermally evaporated thin Au film on Si suitable for application of thiol self-assembled monolayers in MEMS/NEMS sensors. *Journal of Vacuum Science & Technology A*, **2017**. 35, p. 041514. doi: 10.1116/1.4990026.

[294] Huang, W., Qian, W., El-Sayed, M. A., Ding, Y., and Wang, Z. L. Effect of the lattice crystallinity on the electron-phonon relaxation rates in gold nanoparticles. *Journal of Physical Chemistry C*, **2007**. 111 (29), pp. 10751–10757. ISSN 19327447. doi: 10.1021/jp0738917.

[295] Chen, K. P., Drachev, V. P., Borneman, J. D., Kildishev, A. V., and Shalaev, V. M. Drude relaxation rate in grained gold nanoantennas. *Nano Letters*, **2010**. 10 (3), pp. 916–922. ISSN 15306984. doi: 10.1021/nl9037246.

[296] Bosman, M., *et al.* Encapsulated annealing: Enhancing the plasmon quality factor in lithographically-defined nanostructures. *Scientific Rep.*, **2014**. 4 (1), pp. 1–6. ISSN 20452322. doi: 10.1038/srep05537.

[297] Langille, M. R., Personick, M. L., Zhang, J., and Mirkin, C. A. Defining rules for the shape evolution of gold nanoparticles. *Journal of the American Chemical Society*, **2012**. 134 (35), pp. 14542–14554. ISSN 00027863. doi: 10.1021/ja305245g.

[298] Hu, H., Zhou, J., Kong, Q., and Li, C. Two-Dimensional Au Nanocrystals: Shape/Size Controlling Synthesis, Morphologies, and Applications. *Particle & Particle Systems Characterization*, **2015**. 32 (8), pp. 796–808. ISSN 09340866. doi: 10.1002/ppsc.201500035.

[299] Chen, Y., *et al.* Two-dimensional metal nanomaterials: synthesis, properties, and applications. *Chemical reviews*, **2018**. 118 (13), pp. 6409–6455.

[300] Guo, Z., *et al.* Facile synthesis of micrometer-sized gold nanoplates through an aniline-assisted route in ethylene glycol solution. *Colloids and Surfaces A: Physicochemical and Engineering Aspects*, **2006**. 278 (1-3), pp. 33–38. ISSN 09277757. doi: 10.1016/j.colsurfa.2005.11.075.

[301] Kawasaki, H., Yonezawa, T., Nishimura, K., and Arakawa, R. Fabrication of Submillimeter-sized Gold Plates from Thermal Decomposition of HAuCl4 in Two-component Ionic Liquids. *Chemistry Letters*, **2007**. 36 (8), pp. 1038–1039. ISSN 0366-7022. doi: 10.1246/cl.2007.1038.

[302] Wu, X., Kullock, R., Krauss, E., and Hecht, B. Single-crystalline gold microplates grown on substrates by solution-phase synthesis. *Crystal Research and Technology*, **2015**. 50 (8), pp. 595–602. ISSN 02321300. doi: 10.1002/crat.201400429.

[303] Krauss, E., *et al.* Controlled Growth of High-Aspect-Ratio Single-Crystalline Gold Platelets. *Crystal Growth & Design*, **2018**. 18 (3), pp. 1297–1302. ISSN 1528-7483. doi: 10.1021/acs.cgd.7b00849.

[304] Kaltenecker, K. J., *et al.* Mono-crystalline gold platelets: a high-quality platform for surface plasmon polaritons. *Nanophotonics*, **2020**. 9 (2), pp. 509 – 522.

[305] Radha, B., Arif, M., Datta, R., Kundu, T. K., and Kulkarni, G. U. Movable Au microplates as fluorescence enhancing substrates for live cells. *Nano Research*, **2010**. 3 (10), pp. 738–747. ISSN 19980124. doi: 10.1007/s12274-010-0040-6.

[306] Radha, B. and Kulkarni, G. U. A Real Time Microscopy Study of the Growth of Giant Au Microplates. *Crystal Growth & Design*, **2011**. 11 (1), pp. 320–327. ISSN 1528-7483. doi: 10.1021/cg1015548.

[307] Radha, B. and Kulkarni, G. U. Giant single crystalline Au microplates. *Current Science*, **2012**. 102 (1), pp. 70–77. ISSN 00113891. doi: 10.2307/24080388.

[308] Olmon, R. L., *et al.* Optical dielectric function of gold. *Physical Review B*, **2012**. 86, p. 235147. doi: 10.1103/PhysRevB.86.235147.

[309] Prämassing, M., Liebtrau, M., Schill, H. J., Irsen, S., and Linden, S. Interferometric near-field characterization of plasmonic slot waveguides in single-and poly-crystalline gold films. *Optics Express*, **2020**. 28 (9), p. 12998. doi: 10.1364/OE.384629.

[310] See, K. M., Lin, F. C., and Huang, J. S. Design and characterization of a plasmonic Doppler grating for azimuthal angle-resolved surface plasmon resonances. *Nanoscale*, **2017**. 9 (30), pp. 10811–10819. ISSN 20403372. doi: 10.1039/c7nr01509g.

[311] Frank, B., *et al.* Short-range surface plasmonics: Localized electron emission dynamics from a 60-nm spot on an atomically flat single-crystalline gold surface. *Science Advances*, **2017**. 3 (7), p. e1700721. ISSN 23752548. doi: 10.1126/sciadv.1700721.

[312] Boroviks, S., Todisco, F., Asger Mortensen, N., and Bozhevolnyi, S. I. Use of monocrystalline gold flakes for gap plasmon-based metasurfaces operating in the visible. *Optical Materials Express*, **2019**. 9 (11), p. 4209. ISSN 2159-3930. doi: 10.1364/ome.9.004209.

[313] Siampour, H., *et al.* Ultrabright single-photon emission from germanium-vacancy zero-phonon lines: deterministic emitter-waveguide interfacing at plasmonic hot spots. *Nanophotonics*, **2020**. 9 (4), pp. 953 – 962.

[314] Boroviks, S., *et al.* Extremely confined gap plasmon modes: when nonlocality matters. *Nature Communications*, **2022**. 13 (1), p. 3105. ISSN 2041-1723. doi: 10.1038/s41467-022-30737-2.

[315] Hoffmann, B., *et al.* New insights into colloidal gold flakes: Structural investigation, micro-ellipsometry and thinning procedure towards ultrathin monocrystalline layers. *Nanoscale*, **2016**. 8 (8), pp. 4529–4536. ISSN 20403372. doi: 10.1039/c5nr04439a.

[316] Méjard, R., *et al.* Advanced engineering of single-crystal gold nanoantennas. *Optical Materials Express*, **2017**. 7 (4), p. 1157. ISSN 2159-3930. doi: 10.1364/ome.7.001157.

[317] Kalousek, R., Dub, P., Břínek, L., and Šikola, T. Response of plasmonic resonant nanorods: an analytical approach to optical antennas. *Optics Express*, **2012**. 20 (16), p. 17916. ISSN 1094-4087. doi: 10.1364/oe.20.017916.

[318] Shankar, S. S., *et al.* Biological synthesis of triangular gold nanoprisms. *Nature Materials*, **2004**. 3 (7), pp. 482–488. ISSN 1476-1122. doi: 10.1038/nmat1152.

[319] Golze, S. D., *et al.* Plasmon-Mediated Synthesis of Periodic Arrays of Gold Nanoplates Using Substrate-Immobilized Seeds Lined with Planar Defects. *Nano Letters*, **2019**. 19 (8), pp. 5653–5660. ISSN 1530-6984. doi: 10.1021/acs.nanolett.9b02215.

[320] Stark, Y., Frömter, R., Stickler, D., and Oepen, H. P. Sputter yields of single- and polycrystalline metals for application in focused ion beam technology. *Journal of Applied Physics*, **2009**. 105 (1), p. 013542. doi: 10.1063/1.3056161.

[321] Mitchell, D. R. G. Determination of mean free path for energy loss and surface oxide film thickness using convergent beam electron diffraction and thickness mapping: a case study using si and p91 steel. *Journal of microscopy*, **2006**. 224 (2), pp. 187–196. ISSN 1365-2818. doi: 10.1111/j.1365-2818.2006.01690.x.

[322] Iakoubovskii, K., Mitsuishi, K., Nakayama, Y., and Furuya, K. Thickness measurements with electron energy loss spectroscopy. *Microscopy Research and Technique*, **2008**. 71 (8), pp. 626–631. ISSN 1097-0029. doi: 10.1002/jemt.20597.

[323] García de Abajo, F. J. and Howie, A. Retarded field calculation of electron energy loss in inhomogeneous dielectrics. *Physical Review B*, **2002**. 65 (11), p. 1154181. ISSN 01631829. doi: 10.1103/PhysRevB.65.115418.

[324] Waxenegger, J., Trügler, A., and Hohenester, U. Plasmonics simulations with the mnpbem toolbox: Consideration of substrates and layer structures. *Computer Physics Communications*, **2015**. 193, pp. 138–150. ISSN 00104655. doi: 10.1016/j.cpc.2015.03.023.

[325] Pletcher, D. *Developments in electrochemistry : science inspired by Martin Fleischmann*. John Wiley & Sons, Chichester, West Sussex, **2014**. ISBN 978-1-118-69443-5.

[326] Bard, A. *Electrochemical methods : fundamentals and applications*. John Wiley & Sons, Inc, Hoboken, NJ, **2001**. ISBN 978-0-471-04372-0.

[327] Plieth, W. *Electrochemistry for materials science*. Elsevier, Amsterdam Boston, **2008**. ISBN 978-0-444-52792-9.

[328] Zoski, C. *Handbook of electrochemistry*. Elsevier, Amsterdam Boston, **2007**. ISBN 978-0-444-51958-0.

[329] Gerischer, H. *Semiconductor electrochemistry*. Lawrence Berkeley National Laboratory, **1968**.

[330] Gerischer, H. The impact of semiconductors on the concepts of electrochemistry. *Electrochimica Acta*, **1990**. 35 (11), pp. 1677–1699. ISSN 0013-4686. doi: https://doi.org/10.1016/0013-4686(90)87067-C.

[331] Willig, F. and Gundlach, L. *Redox Processes at Semiconductors–Gerischer Model and Beyond*, pp. 1786–1798. Springer New York, New York, NY. ISBN 978-1-4419-6996-5, **2014**. doi: 10.1007/978-1-4419-6996-5_41.

[332] Bagotsky, V. S. *Fundamentals of electrochemistry*. Wiley-Interscience, Hoboken, N.J, **2006**. ISBN 978-0-471-70058-6.

[333] PINEresearch instrumentation. https://pineresearch.com/shop/kb/theory/instrumentation/what-potentiostat-does/. Accessed: 2022-01-04.

[334] Agarwal, A. *Foundations of analog & digital electronic circuits*. Elsevier Morgan Kaufman Publishers, Amsterdam Boston, **2005**. ISBN 978-1558607354.

[335] Inzelt, G. *Chronoamperometry, Chronocoulometry, and Chronopotentiometry*, pp. 207–214. Springer New York, New York, NY. ISBN 978-1-4419-6996-5, **2014**. doi: 10.1007/978-1-4419-6996-5_217.

[336] Bilal, S. *Cyclic Voltammetry*, pp. 285–289. Springer New York, New York, NY. ISBN 978-1-4419-6996-5, **2014**. doi: 10.1007/978-1-4419-6996-5_220.

[337] Elgrishi, N., *et al.* A practical beginner's guide to cyclic voltammetry. *Journal of Chemical Education*, **2018**. 95 (2), pp. 197–206. ISSN 0021-9584. doi: 10.1021/acs.jchemed.7b00361.

[338] Compton, R. G. *Understanding voltammetry*. World Scientific, New Jersey-London, **2018**. ISBN 978-1786345295.

[339] Wang, J. *Analytical electrochemistry*. Wiley-VCH, Hoboken, N.J, **2006**. ISBN 978-0-471-67879-3.

[340] Lau, H. Y., *et al.* Specific and sensitive isothermal electrochemical biosensor for plant pathogen DNA detection with colloidal gold nanoparticles as probes. *Scientific Reports*, **2017**. 7 (1). doi: 10.1038/srep38896.

[341] Vesali-Naseh, M., Khodadadi, A. A., Mortazavi, Y., Moosavi-Movahedi, A. A., and Ostrikov, K. H2o/air plasma-functionalized carbon nanotubes decorated with MnO2 for glucose sensing. *RSC Advances*, **2016**. 6 (38), pp. 31807–31815. doi: 10.1039/c6ra00405a.

[342] Mirkin, M. V., Sun, T., Yu, Y., and Zhou, M. Electrochemistry at one nanoparticle. *Accounts of Chemical Research*, **2016**. 49 (10), pp. 2328–2335. doi: 10.1021/acs.accounts.6b00294.

[343] Manzeli, S., Ovchinnikov, D., Pasquier, D., Yazyev, O. V., and Kis, A. 2d transition metal dichalcogenides. *Nature Reviews Materials*, **2017**. 2 (8), p. 17033. ISSN 2058-8437. doi: 10.1038/natrevmats.2017.33.

[344] Novoselov, K. S., *et al.* Two-dimensional atomic crystals. *Proceedings of the National Academy of Sciences*, **2005**. 102 (30), pp. 10451–10453. ISSN 0027-8424. doi: 10.1073/pnas.0502848102.

[345] Chhowalla, M., *et al.* The chemistry of two-dimensional layered transition metal dichalcogenide nanosheets. *Nature Chemistry*, **2013**. 5 (4), pp. 263–275. ISSN 1755-4349. doi: 10.1038/nchem.1589.

[346] Voiry, D., Mohite, A., and Chhowalla, M. Phase engineering of transition metal dichalcogenides. *Chem. Soc. Rev.*, **2015**. 44, pp. 2702–2712. doi: 10.1039/C5CS00151J.

[347] Wang, R., *et al.* Strategies on phase control in transition metal dichalcogenides. *Advanced Functional Materials*, **2018**. 28 (47), p. 1802473. doi: https://doi.org/10.1002/adfm.201802473.

[348] Sokolikova, M. S. and Mattevi, C. Direct synthesis of metastable phases of 2d transition metal dichalcogenides. *Chem. Soc. Rev.*, **2020**. 49, pp. 3952–3980. doi: 10.1039/D0CS00143K.

[349] Zhang, Y. J., *et al.* Enhanced intrinsic photovoltaic effect in tungsten disulfide nanotubes. *Nature*, **2019**. 570 (7761), pp. 349–353. ISSN 1476-4687. doi: 10.1038/s41586-019-1303-3.

[350] Novoselov, K. S., *et al.* Electric field effect in atomically thin carbon films. *Science*, **2004**. 306 (5696), pp. 666–669. doi: 10.1126/science.1102896.

[351] Castro Neto, A. H., Guinea, F., Peres, N. M. R., Novoselov, K. S., and Geim, A. K. The electronic properties of graphene. *Rev. Mod. Phys.*, **2009**. 81, pp. 109–162. doi: 10.1103/RevModPhys.81.109.

[352] Bonaccorso, F., Sun, Z., Hasan, T., and Ferrari, A. C. Graphene photonics and optoelectronics. *Nature Photonics*, **2010**. 4 (9), pp. 611–622. ISSN 1749-4893. doi: 10.1038/nphoton.2010.186.

[353] Mak, K. F., *et al.* Measurement of the optical conductivity of graphene. *Phys. Rev. Lett.*, **2008**. 101, p. 196405. doi: 10.1103/PhysRevLett.101.196405.

[354] Yin, X., *et al.* Recent developments in 2d transition metal dichalcogenides: phase transition and applications of the (quasi-)metallic phases. *Chem. Soc. Rev.*, **2021**. 50, pp. 10087–10115. doi: 10.1039/D1CS00236H.

[355] Polcar, T. *Solid Lubricants, Layered-Hexagonal Transition Metal Dichalcogenides*. Springer US, Boston, MA, **2013**. ISBN 978-0-387-92897-5.

[356] Wang, Q. H., Kalantar-Zadeh, K., Kis, A., Coleman, J. N., and Strano, M. S. Electronics and optoelectronics of two-dimensional transition metal dichalcogenides. *Nature Nanotechnology*, **2012**. 7 (11), pp. 699–712. ISSN 1748-3395. doi: 10.1038/nnano.2012.193.

[357] Akinwande, D., *et al.* Graphene and two-dimensional materials for silicon technology. *Nature*, **2019**. 573 (7775), pp. 507–518. ISSN 1476-4687. doi: 10.1038/s41586-019-1573-9.

[358] Chakraborty, C., Kinnischtzke, L., Goodfellow, K. M., Beams, R., and Vamivakas, A. N. Voltage-controlled quantum light from an atomically thin semiconductor. *Nature Nanotechnology*, **2015**. 10 (6), pp. 507–511. ISSN 1748-3395. doi: 10.1038/nnano.2015.79.

[359] Chia, X., Eng, A. Y. S., Ambrosi, A., Tan, S. M., and Pumera, M. Electrochemistry of nanostructured layered transition-metal dichalcogenides. *Chemical Reviews*, **2015**. 115 (21), pp. 11941–11966. doi: 10.1021/acs.chemrev.5b00287.

[360] Tan, S. M., *et al.* Pristine basal- and edge-plane-oriented molybdenite MoS_2 exhibiting highly anisotropic properties. *Chemistry â€“ A European Journal*, **2015**. 21 (19), pp. 7170–7178. doi: https://doi.org/10.1002/chem.201500435.

[361] Chia, X., Ambrosi, A., Sofer, Z., Luxa, J., and Pumera, M. Catalytic and charge transfer properties of transition metal dichalcogenides arising from electrochemical pretreatment. *ACS Nano*, **2015**. 9 (5), pp. 5164–5179. doi: 10.1021/acsnano.5b00501.

[362] Tanwar, S., Arya, A., Gaur, A., and Sharma, A. L. Transition metal dichalcogenide (TMDs) electrodes for supercapacitors: a comprehensive review. *Journal of Physics: Condensed Matter*, **2021**. 33 (30), p. 303002. doi: 10.1088/1361-648x/abfb3c.

[363] Gan, X., Zhao, H., and Quan, X. Two-dimensional MoS2: A promising building block for biosensors. *Biosensors and Bioelectronics*, **2017**. 89, pp. 56–71. doi: 10.1016/j.bios.2016.03.042.

[364] Sang, Y., *et al.* From UV to near-infrared, WS2nanosheet: A novel photocatalyst for full solar light spectrum photodegradation. *Advanced Materials*, **2014**. 27 (2), pp. 363–369. doi: 10.1002/adma.201403264.

[365] Chowdhury, T., Sadler, E. C., and Kempa, T. J. Progress and prospects in transition-metal dichalcogenide research beyond 2d. *Chemical Reviews*, **2020**. 120 (22), pp. 12563–12591. ISSN 0009-2665. doi: 10.1021/acs.chemrev.0c00505.

[366] Tenne, R., Margulis, L., Genut, M., and Hodes, G. Polyhedral and cylindrical structures of tungsten disulphide. *Nature*, **1992**. 360 (6403), pp. 444–446. ISSN 1476-4687. doi: 10.1038/360444a0.

[367] Serra, M., Arenal, R., and Tenne, R. An overview of the recent advances in inorganic nanotubes. *Nanoscale*, **2019**. 11, pp. 8073–8090. doi: 10.1039/C9NR01880H.

[368] Qin, F., *et al.* Diameter-dependent superconductivity in individual WS_2 nanotubes. *Nano Letters*, **2018**. 18 (11), pp. 6789–6794. ISSN 1530-6984. doi: 10.1021/acs.nanolett.8b02647.

[369] Frey, G. L., Elani, S., Homyonfer, M., Feldman, Y., and Tenne, R. Optical-absorption spectra of inorganic fullerenelike ms_2 (m = Mo, w). *Phys. Rev. B*, **1998**. 57, pp. 6666–6671. doi: 10.1103/PhysRevB.57.6666.

[370] Piskunov, S., *et al.* First-principles evaluation of the morphology of WS_2 nanotubes for application as visible-light-driven water-splitting photocatalysts. *ACS Omega*, **2019**. 4 (1), pp. 1434–1442. doi: 10.1021/acsomega.8b03121.

[371] Ghosh, S., *et al.* Cathodoluminescence in single and multiwall WS_2 nanotubes: evidence for quantum confinement and strain effect. *Applied Physics Reviews*, **2020**. 7 (4), p. 041401. doi: 10.1063/5.0019913.

[372] Xia, H., *et al.* Probing the chiral domains and excitonic states in individual WS_2 tubes by second-harmonic generation. *Nano Letters*, **2021**. 21 (12), pp. 4937–4943. ISSN 1530-6984. doi: 10.1021/acs.nanolett.1c00497.

[373] Yadgarov, L., *et al.* Strong lightâ€“matter interaction in tungsten disulfide nanotubes. *Phys. Chem. Chem. Phys.*, **2018**. 20, pp. 20812–20820. doi: 10.1039/C8CP02245C.

[374] Sinha, S. S., *et al.* MoS_2 and WS_2 nanotubes: Synthesis, structural elucidation, and optical characterization. *The Journal of Physical Chemistry C*, **2021**. 125 (11), pp. 6324–6340. ISSN 1932-7447. doi: 10.1021/acs.jpcc.0c10784.

[375] Albu-Yaron, A., Sinha, S. S., and Tenne, R. Nanotubes from two-dimensional materials in contemporary energy research: Historical and perspective outlook. *ACS Energy Letters*, **2020**. 5 (5), pp. 1498–1511. doi: 10.1021/acsenergylett.0c00185.

[376] Zhang, C., *et al.* High-performance photodetectors for visible and near-infrared lights based on individual WS_2 nanotubes. *Applied Physics Letters*, **2012**. 100 (24), p. 243101. doi: 10.1063/1.4729144.

[377] Tenne, R., Rosentsveig, R., and Zak, A. Inorganic nanotubes and fullerene-like nanoparticles: Synthesis, mechanical properties, and applications. *physica status solidi (a)*, **2013**. 210 (11), pp. 2253–2258. doi: https://doi.org/10.1002/pssa.201329309.

[378] Solvent table. `https://people.chem.umass.edu/xray/solvent.html`. Accessed: 2022-02-04.

[379] You, Z. Z. Combined afm, xps, and contact angle studies on treated indiumâ€“tin-oxide films for organic light-emitting devices. *Materials Letters*, **2007**. 61 (18), pp. 3809–3814. ISSN 0167-577X. doi: https://doi.org/10.1016/j.matlet.2006.12.063.

[380] Polyakov, A. Y., *et al.* Optical properties of multilayer films of nanocomposites based on WS_2 nanotubes decorated with gold nanoparticles. *Journal of Physics: Conference Series*, **2015**. 643, p. 012046. doi: 10.1088/1742-6596/643/1/012046.

[381] Laloy, J., *et al.* Impact of functional inorganic nanotubes f-ints-WS_2 on hemolysis, platelet function and coagulation. *Nano convergence*, **2018**. 5 (1), pp. 31–31. ISSN 2196-5404. doi: 10.1186/s40580-018-0162-1.

[382] Geiger, S., Kasian, O., Mingers, A. M., Mayrhofer, K. J. J., and Cherevko, S. Stability limits of tin-based electrocatalyst supports. *Scientific Reports*, **2017**. 7 (1), p. 4595. ISSN 2045-2322. doi: 10.1038/s41598-017-04079-9.

[383] Benck, J. D., Pinaud, B. A., Gorlin, Y., and Jaramillo, T. F. Substrate selection for fundamental studies of electrocatalysts and photoelectrodes: Inert potential windows in acidic, neutral, and basic electrolyte. *PLOS ONE*, **2014**. 9 (10), pp. 1–13. doi: 10.1371/journal.pone.0107942.

[384] Zangeneh Kamali, K. and Moradi Golsheikh, A. Green and facile approach to synthesis of well-dispersed nitrogen-doped graphene without using surfactant or stabilizer with potential application for oxygen reduction reaction. *Colloids and Surfaces A: Physicochemical and Engineering Aspects*, **2016**. 509, pp. 574–582. ISSN 0927-7757. doi: https://doi.org/10.1016/j.colsurfa.2016.09.038.

[385] Cirocka, A., ZarzeczaĹ„ska, D., and WcisĹ‚o, A. Good choice of electrode material as the key to creating electrochemical sensorsâ€"characteristics of carbon materials and transparent conductive oxides (tco). *Materials*, **2021**. 14 (16). ISSN 1996-1944. doi: 10.3390/ma14164743.

[386] McCreery, R. L. Advanced carbon electrode materials for molecular electrochemistry. *Chemical Reviews*, **2008**. 108 (7), pp. 2646–2687. ISSN 0009-2665. doi: 10.1021/cr068076m.

[387] Chen, P. and McCreery, R. L. Control of electron transfer kinetics at glassy carbon electrodes by specific surface modification. *Analytical Chemistry*, **1996**. 68 (22), pp. 3958–3965. ISSN 0003-2700. doi: 10.1021/ac960492r.

[388] Marcus, R. and Sutin, N. Electron transfers in chemistry and biology. *Biochimica et Biophysica Acta (BBA) - Reviews on Bioenergetics*, **1985**. 811 (3), pp. 265–322. ISSN 0304-4173. doi: https://doi.org/10.1016/0304-4173(85)90014-X.

[389] Liu, A. T., *et al.* Solvent-induced electrochemistry at an electrically asymmetric carbon janus particle. *Nature Communications*, **2021**. 12 (1), p. 3415. ISSN 2041-1723. doi: 10.1038/s41467-021-23038-7.

[390] O'Reilly, J. E. Oxidation-reduction potential of the ferro-ferricyanide system in buffer solutions. *Biochimica et Biophysica Acta (BBA) - Bioenergetics*, **1973**. 292 (3), pp. 509–515. ISSN 0005-2728. doi: https://doi.org/10.1016/0005-2728(73)90001-7.

[391] Metzker, G., *et al.* Electrochemical and chemical aspects of ruthenium(ii) and (iii) ammines in basic solution: The role of the ruthenium(iv) species. *Inorganica Chimica Acta*, **2014**. 416, pp. 142–146. ISSN 0020-1693. doi: https://doi.org/10.1016/j.ica.2014.03.013.

[392] Mampallil, D., Mathwig, K., Kang, S., and Lemay, S. G. Reversible adsorption of outer-sphere redox molecules at pt electrodes. *The Journal of Physical Chemistry Letters*, **2014**. 5 (3), pp. 636–640. doi: 10.1021/jz402592n.

[393] Wu, C. C., Wu, C. I., Sturm, J. C., and Kahn, A. Surface modification of indium tin oxide by plasma treatment: An effective method to improve the efficiency, brightness, and reliability of organic light emitting devices. *Applied Physics Letters*, **1997**. 70 (11), pp. 1348–1350. doi: 10.1063/1.118575.

[394] You, Z. Z. and Dong, J. Y. Oxygen plasma treatment effects of indium-tin oxide in organic light-emitting devices. *Vacuum*, **2007**. 81 (7), pp. 819–825. ISSN 0042-207X. doi: https://doi.org/10.1016/j.vacuum.2006.09.004.

[395] Polyakov, A. Y., *et al.* Decoration of WS_2 nanotubes and fullerene-like MoS_2 with gold nanoparticles. *The Journal of Physical Chemistry C*, **2014**. 118 (4), pp. 2161–2169. ISSN 1932-7447. doi: 10.1021/jp407388h.

[396] Kong, M., *et al.* Tuning the relative concentration ratio of bulk defects to surface defects in tio2 nanocrystals leads to high photocatalytic efficiency. *Journal of the American Chemical Society*, **2011**. 133 (41), pp. 16414–16417. ISSN 0002-7863. doi: 10.1021/ja207826q.

[397] Polyakov, A. Y., *et al.* Gold decoration and photoresistive response to nitrogen dioxide of WS_2 nanotubes. *Chemistry â€“ A European Journal*, **2018**. 24 (71), pp. 18952–18962. doi: https://doi.org/10.1002/chem.201803502.

[398] Li, S., *et al.* Direct evidence of the efficient hole collection process of the coo x cocatalyst for photocatalytic reactions: a surface photovoltage study. *Journal of Materials Chemistry A*, **2015**. 3 (34), pp. 17820–17826.

[399] Fang, M., Zhang, C., and Chen, Q. Tuning the ito work function by capacitively coupled plasma and its application in inverted organic solar cells. *Applied Surface Science*, **2016**. 385, pp. 28–33. ISSN 0169-4332. doi: https://doi.org/10.1016/j.apsusc.2016.05.077.

[400] McMichael, S., FernĂˇndez-Ibáñez, P., and Byrne, J. A. A review of photoelectrocatalytic reactors for water and wastewater treatment. *Water*, **2021**. 13 (9). ISSN 2073-4441. doi: 10.3390/w13091198.

[401] Wu, X., Thrall, E. S., Liu, H., Steigerwald, M., and Brus, L. Plasmon induced photovoltage and charge separation in citrate-stabilized gold nanoparticles. *The Journal of Physical Chemistry C*, **2010**. 114 (30), pp. 12896–12899. ISSN 1932-7447. doi: 10.1021/jp102720r.

[402] Schlather, A. E., *et al.* Hot hole photoelectrochemistry on $Au@SiO_2@Au$ nanoparticles. *The Journal of Physical Chemistry Letters*, **2017**. 8 (9), pp. 2060–2067. doi: 10.1021/acs.jpclett.7b00563.

[403] Forcherio, G. T., *et al.* Gold nanoparticles physicochemically bonded onto tungsten disulfide nanosheet edges exhibit augmented plasmon damping. *AIP Advances*, **2017**. 7 (7), p. 075103. doi: 10.1063/1.4989774.

[404] Andriukonis, E., Ramanaviciene, A., and Ramanavicius, A. Synthesis of polypyrrole induced by $[Fe(CN)_6]^{3-}$ and redox cycling of $[Fe(CN)_6]^{4-}$ / $[Fe(CN)_6]^{3-}$. *Polymers*, **2018**. 10 (7). ISSN 2073-4360. doi: 10.3390/polym10070749.

[405] Iwanski, P., Curran, J. S., Gissler, W., and Memming, R. The photoelectrochemical behavior of ferric oxide in the presence of redox reagents. *Journal of The Electrochemical Society*, **1981**. 128 (10), pp. 2128–2133. doi: 10.1149/1.2127202.

[406] Le Formal, F., *et al.* Passivating surface states on water splitting hematite photoanodes with alumina overlayers. *Chem. Sci.*, **2011**. 2, pp. 737–743. doi: 10.1039/C0SC00578A.

[407] Schneider, J., *et al.* Understanding TiO_2 photocatalysis: Mechanisms and materials. *Chemical Reviews*, **2014**. 114 (19), pp. 9919–9986. ISSN 0009-2665. doi: 10.1021/cr5001892.

[408] Ni, M., Leung, M. K., Leung, D. Y., and Sumathy, K. A review and recent developments in photocatalytic water-splitting using tio2 for hydrogen production. *Renewable and Sustainable Energy Reviews*, **2007**. 11 (3), pp. 401–425. ISSN 1364-0321. doi: https://doi.org/10.1016/j.rser.2005.01.009.

[409] Gopinath, K. P., Madhav, N. V., Krishnan, A., Malolan, R., and Rangarajan, G. Present applications of titanium dioxide for the photocatalytic removal of pollutants from water: A review. *Journal of Environmental Management*, **2020**. 270, p. 110906. ISSN 0301-4797. doi: https://doi.org/10.1016/j.jenvman.2020.110906.

[410] Kreft, S., Wei, D., Junge, H., and Beller, M. Recent advances on tio2-based photocatalytic co2 reduction. *EnergyChem*, **2020**. 2 (6), p. 100044. ISSN 2589-7780. doi: https://doi.org/10.1016/j.enchem.2020.100044.

[411] Ma, Y., *et al.* Titanium dioxide-based nanomaterials for photocatalytic fuel generations. *Chemical Reviews*, **2014**. 114 (19), pp. 9987–10043. ISSN 0009-2665. doi: 10.1021/cr500008u.

[412] Wang, S., Ding, Z., Chang, X., Xu, J., and Wang, D.-H. Modified nano-tio2 based composites for environmental photocatalytic applications. *Catalysts*, **2020**. 10 (7). ISSN 2073-4344. doi: 10.3390/catal10070759.

[413] Diebold, U. The surface science of titanium dioxide. *Surface Science Reports*, **2003**. 48 (5), pp. 53–229. ISSN 0167-5729. doi: https://doi.org/10.1016/S0167-5729(02)00100-0.

[414] Nyamukamba, P., Okoh, O., Mungondori, H., Taziwa, R., and Zinya, S. Synthetic methods for titanium dioxide nanoparticles: A review. In D. Yang (ed.), *Titanium Dioxide*, chap. 8. IntechOpen, Rijeka, **2018**. doi: 10.5772/intechopen.75425.

[415] Guo, Q., Zhou, C., Ma, Z., and Yang, X. Fundamentals of TiO_2 photocatalysis: Concepts, mechanisms, and challenges. *Advanced Materials*, **2019**. 31 (50), p. 1901997. doi: https://doi.org/10.1002/adma.201901997.

[416] Mansfeldova, V., *et al.* Work function of TiO_2 (anatase, rutile, and brookite) single crystals: Effects of the environment. *The Journal of Physical Chemistry C*, **2021**. 125 (3), pp. 1902–1912. ISSN 1932-7447. doi: 10.1021/acs.jpcc.0c10519.

[417] Etacheri, V., Di Valentin, C., Schneider, J., Bahnemann, D., and Pillai, S. C. Visible-light activation of tio2 photocatalysts: Advances in theory and experiments. *Journal of Photochemistry and Photobiology C: Photochemistry Reviews*, **2015**. 25, pp. 1–29. ISSN 1389-5567. doi: https://doi.org/10.1016/j.jphotochemrev.2015.08.003.

[418] Kumar, S. G. and Devi, L. G. Review on modified TiO_2 photocatalysis under uv/visible light: Selected results and related mechanisms on interfacial charge carrier transfer dynamics. *The Journal of Physical Chemistry A*, **2011**. 115 (46), pp. 13211–13241. ISSN 1089-5639. doi: 10.1021/jp204364a.

[419] Linic, S., Aslam, U., Boerigter, C., and Morabito, M. Photochemical transformations on plasmonic metal nanoparticles. *Nature Materials*, **2015**. 14 (6), pp. 567–576. ISSN 1476-4660. doi: 10.1038/nmat4281.

[420] Park, J. Y., Lee, H., Renzas, J. R., Zhang, Y., and Somorjai, G. A. Probing hot electron flow generated on pt nanoparticles with au/tio2 schottky diodes during catalytic co oxidation. *Nano Letters*, **2008**. 8 (8), pp. 2388–2392. ISSN 1530-6984. doi: 10.1021/nl8012456.

[421] McFarland, E. W. and Tang, J. A photovoltaic device structure based on internal electron emission. *Nature*, **2003**. 421 (6923), pp. 616–618. ISSN 1476-4687. doi: 10.1038/nature01316.

[422] Tagliabue, G., DuChene, J. S., Habib, A., Sundararaman, R., and Atwater, H. A. Hot-hole versus hot-electron transport at cu/gan heterojunction interfaces. *ACS Nano*, **2020**. 14 (5), pp. 5788–5797. ISSN 1936-0851. doi: 10.1021/acsnano.0c00713.

[423] Challagulla, S., Tarafder, K., Ganesan, R., and Roy, S. Structure sensitive photocatalytic reduction of nitroarenes over tio2. *Scientific Reports*, **2017**. 7 (1), p. 8783. ISSN 2045-2322. doi: 10.1038/s41598-017-08599-2.

[424] Niilisk, A., *et al.* Structural study of tio2 thin films by micro-raman spectroscopy. *Open Physics*, **2006**. 4 (1), pp. 105–116. doi: doi:10.1007/s11534-005-0009-3.

[425] Jin, C., Liu, B., Lei, Z., and Sun, J. Structure and photoluminescence of the tio2 films grown by atomic layer deposition using tetrakis-dimethylamino titanium and ozone. *Nanoscale Research Letters*, **2015**. 10 (1), p. 95. ISSN 1556-276X. doi: 10.1186/s11671-015-0790-x.

[426] Boikanyo, D., Mishra, S. B., Ray, S., Mhlanga, S. D., and Mishra, A. K. Structure–activity relationships of er3+ and mwcnt-modified tio2: Enhancing the textural and optoelectronic properties of tio2. *The Journal of Physical Chemistry C*, **2019**. 123 (51), pp. 31246–31261. ISSN 1932-7447. doi: 10.1021/acs.jpcc.9b08420.

[427] Pallotti, D. K., Passoni, L., Maddalena, P., Di Fonzo, F., and Lettieri, S. Photoluminescence mechanisms in anatase and rutile TiO_2. *The Journal of Physical Chemistry C*, **2017**. 121 (16), pp. 9011–9021. ISSN 1932-7447. doi: 10.1021/acs.jpcc.7b00321.

[428] Janczarek, M. and Kowalska, E. Defective dopant-free tio2 as an efficient visible light-active photocatalyst. *Catalysts*, **2021**. 11 (8). ISSN 2073-4344. doi: 10.3390/catal11080978.

[429] Lee, C., Park, Y., and Park, J. Y. Hot electrons generated by intraband and interband transition detected using a plasmonic cu/tio2 nanodiode. *RSC Adv.*, **2019**. 9, pp. 18371–18376. doi: 10.1039/C9RA02601K.

[430] Kuznetsov, V. N. and Serpone, N. On the origin of the spectral bands in the visible absorption spectra of visible-light-active tio2 specimens analysis and assignments. *The Journal of Physical Chemistry C*, **2009**. 113 (34), pp. 15110–15123. ISSN 1932-7447. doi: 10.1021/jp901034t.

[431] Abdullah, S. A., *et al.* Photoluminescence study of trap-state defect on TiO2 thin films at different substrate temperature via RF magnetron sputtering. *Journal of Physics: Conference Series*, **2018**. 995, p. 012067. doi: 10.1088/1742-6596/995/1/012067.

[432] Wang, J., Ando, R. A., and Camargo, P. H. Controlling the selectivity of the surface plasmon resonance mediated oxidation of p-aminothiophenol on au nanoparticles by charge transfer from uv-excited tio2. *Angewandte Chemie*, **2015**. 127 (23), pp. 7013–7016.

[433] Qian, K., *et al.* Surface plasmon-driven water reduction: Gold nanoparticle size matters. *Journal of the American Chemical Society*, **2014**. 136 (28), pp. 9842–9845. ISSN 0002-7863. doi: 10.1021/ja504097v.

[434] Le Formal, F., Sivula, K., and Grätzel, M. The transient photocurrent and photovoltage behavior of a hematite photoanode under working conditions and the influence of surface treatments. *The Journal of Physical Chemistry C*, **2012**. 116 (51), pp. 26707–26720. ISSN 1932-7447. doi: 10.1021/jp308591k.

[435] Wang, G., *et al.* A mechanistic study into the catalytic effect of ni(oh)2 on hematite for photoelectrochemical water oxidation. *Nanoscale*, **2013**. 5, pp. 4129–4133. doi: 10.1039/C3NR00569K.

[436] Christopher, P., Xin, H., and Linic, S. Visible-light-enhanced catalytic oxidation reactions on plasmonic silver nanostructures. *Nature Chemistry*, **2011**. 3 (6), pp. 467–472. ISSN 1755-4349. doi: 10.1038/nchem.1032.